UNIVERSITA' DEGLI STUDI DI PADOVA

Università degli Studi di Padova

Dipartimento di Astronomia

DOTTORATO DI RICERCA IN : **ASTRONOMIA**

CICLO: **XVIII**

The search for extrasolar planets:
Study of line bisectors
from stellar spectra and its relation
with precise radial velocity measurements

Coordinatore: Ch.mo Prof. Giampaolo Piotto

Supervisore: Ch.mo Prof. Raffaele Gratton

Dottorando : Aldo Fabricio Martínez Fiorenzano

2 gennaio 2006

The search for extrasolar planets: Study of line bisectors from stellar spectra and its relation with precise radial velocity measurements

Aldo Fabricio Martínez Fiorenzano
Dipartimento di Astronomia
Università degli Studi di Padova

A thesis submitted for the degree of
Doctor of Philosophy
January 2nd, 2006

Acknowledgements

I thank heaven, literally.
In the past years, studying astronomy and preparing the PhD thesis, I met many people from whom I learned a lot, about science but specially about life.
Now, at the end of this path I thank all those I met during my stay in Padova, specially: Alessia Moretti, Eugenio Carretta, Andrea Pastorello, Luca Rizzi, Filomena Bufano, Silvano Desidera, Riccardo Claudi, Mauro Barbieri, Giancarlo Pace, Elena Rasia, Paola Mucciarelli, Stefano Berta, Jacopo Fritz, Demetrio Magrin, Enrico Maso. The people from abroad that for one way or another end up in Padova for a long or short time: Nancy Elías, Avet Harutyunyan, Jesús Varela, Jairo Méndez, Andreu Balastegui, Begoña Ascaso, Ruth Grützbauch.
From deep of my heart I thank Aida Fiorenzano and Jimena Martínez, whom I left to follow my path.
Thanks to my friends of soul, spread over the surface of this planet: Gloria, Manu, Yeyo and Mafe.
A special acknowledgement is due to Mikhail Varnoff, for support and advice coming from the place that does not exist but is there.
And to all the people that come and go, with whom there is always something to share.

Abstract

In recent years, the study of the mechanisms of formation and evolution of planetary systems has received a considerable boost from the discovery of more than a hundred extra-solar planets, mainly thanks to the analysis of the variations of radial velocities of the stars. While several general features of planetary systems are beginning to emerge, still little is known of several aspects, concerning e.g. the possible mechanisms that lead to the observed planet configurations (semimajor axis, orbital eccentricity, planetary masses, etc.). In particular, the impact of dynamical interactions in wide binary systems (a very common case among stars in the solar neighborhood) is still unknown. This has significant impact on e.g., the determination of the frequency of planets in general, and of those able to host life in particular.
With the aim to contribute to this field, a long term program has begun at INAF using the "Telescopio Nazionale Galileo" (TNG) on a sample of about 50 wide binary systems. The program searches for Jupiter-sized planets in these systems using variations of the radial velocities. A few detections would be expected, based on statistics for single stars. However, radial velocity variations of stars due to planets are small, typically of the order of a few tens of m/s, or even less. Apparent variations of similar size can be caused by effects other than Keplerian motion of the stellar barycentre. The purpose of this study is to develop a technique able to distinguish between radial velocity variations due to planets from the spurious variations due to stellar activity or spectral contamination, with the aim to search for planets around young/active stars, and to clean our sample from possible erroneous measures of radial velocities.
To this purpose, in the course of the thesis work we prepared a suitable software in order to use the same spectra acquired for radial velocity determinations (i.e., with the spectrum of the Iodine cell imprinted on) to measure variations of the stellar line profiles. This is a novel approach, that can be of general utility in all high precision radial velocity surveys based on iodine cell data. This software has then been extensively used on data acquired within our survey, allowing

a proper insight into a number of interesting cases, where spurious estimates of the radial velocities due to activity or contamination by light from the companions were revealed. The same technique can also be considered to correct the measured radial velocities, in order to search for planets around active stars.
The structure of the thesis is as follows. In Chapter 2 some general aspects about ongoing situation in the research field of extrasolar planets are exposed. Current theories about planet formation, like the core accretion and the disk instability, as well as proposed mechanisms of planet migration to explain the presence of massive planets in very close orbits around their host stars, are briefly presented and commented.
In Chapter 3, various detection techniques are described, with special emphasis on the Doppler or radial velocity technique, and the two methods employed for high precision measurements, through the Iodine cell and the simultaneous wavelength calibration with optical fiber fed spectrographs, are discussed.
Relevant aspects of stellar atmospheres are presented in Chapter 4, with a brief description of stellar activity and of the usefulness of line bisectors in the interpretation of physical processes through the study of spectral line asymmetries.
In Chapter 5, we present the current status of the Italian planet search program around wide binaries, ongoing at the TNG, with the radial velocity technique employing the Iodine cell with the high resolution spectrograph SARG. Some characteristics of the stellar sample, results, and future perspectives are given.
We developed a software able to read and analyze the stellar spectra with the Iodine lines. A description of the technique employed to remove the Iodine features from the stellar spectrum is given in Chapter 6: it exploits the spectrum of a rapidly rotating B-star spectrum, acquired within the same procedure adopted to measure precise radial velocities. This allows to deal with spectra free of Iodine lines to perform a detailed analysis of spectral line asymmetries. A solar catalog was employed to construct a mask, which is cross-correlated with the stellar spectra to obtain high S/N average absorption profiles; these were used to measure line bisectors (i.e. the middle point at constant flux between the blue and red sides of the profile). The constancy in time of the shape and orientation of line bisectors would ensure that radial velocity variations measured for a star are due to the barycentre motion, caused by a substellar companion orbiting the observed star. The difference of velocities given by an upper and lower zone

of the line bisectors, known as bisector velocity span, is employed in a plot against radial velocities to search for possible trends and thus correlations. Outliers (mainly due to contamination by light from companions) can also be identified on these plots.
In Chapter 7, the analysis of a subsample of the program stars is presented. Details about the chosen subsample and the motivations for the choice of upper and lower zones to determine the bisector velocity span in the search for possible correlations, are given. The instrumental profile characteristics are described, and its (negligible) influence on the asymmetries observed in the stellar spectra is discussed. Some statistical results are also presented.
In Chapter 8, the meaning of the correlations are discussed and explained for the specific cases of active stars and for the cases of the stellar spectra contaminated by light from a nearby object. A linear correlation with negative slope is found in the case of active stars, while for stars with their spectra contaminated by light from their companions the correlation is positive. For stars known to host planets, no correlation is found and line bisectors appear constant.
Finally in Chapter 9 we explored the possibility to apply corrections to the observed radial velocities in the case of stellar activity. These corrected radial velocities may be used to search for orbital motion, hidden by the activity variations, and/or to derive more stringent upper limits to possible substellar companions by Monte Carlo simulations. The success of such correction technique is discussed, as well as its usefulness in surveys looking for planets around young and active stars. Due to the intrinsic brightness of young planets, these represent important targets for direct imaging instruments.

Riassunto

Negli ultimi anni lo studio della formazione ed evoluzione di sistemi planetari ha avuto una forte spinta dalla scoperta di più di un centinaio di pianeti extrasolari, grazie principalmente alle analisi delle variazioni delle velocità radiali di stelle. Mentre alcune proprietà generali di sistemi planetari cominciano ad emergere, ancora si sà poco degli aspetti che riguardano i possibili meccanismi che portano alle configurazioni dei pianeti scoperti (semiasse maggiore, eccentricità orbitale, massa planetria, ecc.). In particolare l'influenza delle interazioni dinamiche in sistemi stellari binari di larga separazione (un caso molto comune tra le stelle nelle vicinanze del sole) è ancora sconosciuto. Questo ha una particolare rilevanza nella determinazione della frequenza di pianeti in generale, e quelli in grado di albergare vita in particolare.
Con il proposito di contribure in questo campo di ricerca, un programma di lungo termine è iniziato all'INAF adoperando il "Telescopio Nazionale Galileo" (TNG) con un campione di stelle di circa 50 sistemi binari di separazione larga. Il programma cerca pianeti della grandezza di Giove in questi sistemi, studiando le variazioni delle velocità radiali. Si aspettano pochi rilevamenti sulla base statistica dei rilevamenti fatti in stelle singole. Tuttavia, le variazioni di velocità radiali delle stelle dovute a pianeti è piccola, tipicamente dell'ordine di poche centinaia di m/s, o persino di meno. Variazioni apparenti di grandezza simile possono essere causate da altri effetti diversi dai moti gravitazionali del baricentro stellare. Il proposito di questo studio è sviluppare una tecnica in grado di distinguere le variazioni di velocità radiali dovute a pianeti, dalle variazioni spurie dovute ad attività stellare oppure contaminazione spettrale, allo scopo di cercare pianeti attorno a stelle giovani/attive e per eliminare dal nostro campione misure di velocità radiali possibilmente sbagliate.
Con questo proposito, nel corso del lavoro di tesi abbiamo preparato un software adeguato per utilizzare gli stessi spettri acquisiti per determinare velocità radiali (i.e., con lo spettro della cella di Iodio sovrapposto) per misurare variazioni dei profili delle righe stellari. Questo è un approcio innovativo che può essere di gran utilità in tutti

i programmi osservativi che misurano velocità radiali di alta precisione con la cella allo Iodio. Questo software è poi stato ampiamente utilizzato con dati acquisiti all'interno del nostro programma osservativo, permettendo una visione adeguata del numero di casi interessanti, dove sono state rilevate stime spurie di velocità radiale dovute ad attività o a contaminazione proveniente dalla luce di stelle compagne. La stessa tecnica può essere considerata per correggere le velocità radiali osservate nella ricerca di pianeti attorno a stelle attive.
La struttura della tesi è come segue. Nel Capitolo 2 sono esposti alcuni aspetti generali della situazione attuale nella ricerca di pianeti extrasolari. Breve presentazione e commenti delle teorie che riguardano la formazione di pianeti come "accrescimento di nucleo" e "instabilità di dischi", anche meccanismi di migrazione planetaria proposti per spiegare la presenza di pianeti giganti in orbite molto strette attorno alle stelle.
Nel Capitolo 3, sono descritte diverse tecniche di rilevamento, con particolare enfasi nella tecnica Doppler o della velocità radiale, e sono discussi i due metodi adoperati per misure di alta precisione, attraverso la cella allo Iodio e la calibrazione simultanea in lunghezza d'onda con spettrografi alimentati da fibre ottiche.
Apetti rilevanti delle atmosfere stellari sono presentati nel Capitolo 4, con una breve descrizione della attività stellare e dell'utilità dei bisettori nella interpretazione di processi fisici attraverso lo studio delle asimmetrie delle righe spettrali.
Nel Capitolo 5, c'è la presentazione della situazione attuale del programma italiano di ricerca di pianeti attorno a stelle binarie di larga separazione, in corso al TNG, attraverso la tecnica della velocità radiale utilizzando la cella allo Iodio con lo spettrografo ad alta risoluzione SARG. Sono presentate alcune caratteristiche del campione di stelle, risultati e prospettive future.
Abbiamo sviluppato un software in grado di leggere e analizzare gli spettri stellari con le righe dello Iodio. Nel Capitolo 6 è descritta la tecnica adoperata per rimuovere le righe dello Iodio dallo spettro stellare: si approfitta dello spettro di una stella ad alta rotazione (B-star), acquisito con la stessa procedura utilizzata per misurare velocità radiali di precisione. Questo permette avere spettri liberi di righe di Iodio per eseguire analisi dettagliati di asimmetrie di righe spettrali. Un catalogo solare è stato utilizzato per costruire la maschera che poi viene utilizzata nella "cross-correlation" con gli spettri stellari per ottenere profili medii di assorbimento ad alto rapporto S/N, che vengono utilizzati per misurare bisettori (i.e., il punto medio a flusso

costante tra i lati blu e rossi del profilo). Bisettori costanti in forma ed orientamento attraverso il tempo, assicurerebbero che le variazioni di velocità radiale misurate per una stella corrispondono al movimento del baricentro, causato dal moto di un compagno sub-stellare in orbita attorno alla stella osservata. La differenza di velocità, data da una zona superiore ed inferiore dei bisettori, nota come "bisector velocity span" è utilizzata in plot contro le velocità radiali per cercare possibili tendenze e così correlazioni. Valori erratici (principalmente dovuti a contaminazione di luce dalle stelle compagne) possono essere individuati in questi plot.
Nel Capitolo 7 è presentato l'analisi di un sotto campione delle stelle del programma di ricerca. Ci sono dettagli che riguardano la selezione del sotto campione e le motivazioni nella scelta delle zone superiori ed inferiori per determinare il "bisector velocity span" in cerca di possibili correlazioni. Sono descritte e discusse le caratteristiche del profilo strumentale e la loro influenza (trascurabile) nelle asimmetrie osservate sugli spettri osservati. Alcuni risultati statistici sono anche presentati.
Nel Capitolo 8 è discusso il significato delle correlazioni e sono spiegate per i casi specifici di stelle attive e per i casi di spettri contaminati da luce proveniente da oggetti vicini. Correlazioni con pendenza negativa è stata individuata nel caso di stelle attive, mentre per le stelle con spettri contaminati da luce delle loro compagne le correlazioni mostrano pendenze positive. Per stelle note per avere un pianeta attorno, nessuna correlazione è stata individuata e i bisettori appaiono costanti.
In fine nel Capitolo 9 si esplora la possibilità di applicare correzioni alle velocità radiali osservate nel caso di attività stellare. Le velocità radiali corrette possono essere utilizzate in cerca di moti orbitali che le variazioni dovute all'attività possono nascondere ed anche per derivare limiti superiori più stringenti per possibili compagni sub-stellari attraverso simulazioni di Monte Carlo. Il successo di questa tecnica di correzione è discusso ed anche la sua utilità in programmi di osservazione nella ricerca di pianeti extrasolari attorno a stelle giovani e attive. Data la luminosità intrinseca dei pianeti giovani, questi rappresentano obbiettivi importanti per progetti che mirano a risolvere direttamente l'immagine dei pianeti.

Contents

List of Figures

List of Tables

Chapter 1

Introduction

In the past decade more than 150 planets outside our Solar System were found, mainly by the measurement of perturbation to the barycentre motion produced by an orbiting body around the observed star.
The Doppler technique, based on the high precision measurement of radial velocity of stars, is more sensitive to massive objects in close orbits. Furthermore, present researches focus on main sequence stars of spectral types F–G–K, because the characteristics of their spectra and atmospheres allow to perform velocity measurements of higher precision. Even for these stars, however, the study of activity jitter is mandatory in the search for exoplanets using the radial velocity technique because it represents an important (often dominant) source of noise, and a proper analysis is required to discard false alarms. Simultaneous determination of radial velocity, chromospheric emission and/or photometry is even more powerful in disentangling the origin of the observed radial velocity variations (Keplerian motion vs. stellar activity). However these techniques cannot be considered as direct measurements of the alterations of the spectral line profiles, that are the origin of the spurious radial velocity variations. This can be directly addressed by considering variations of line bisectors, that may be thought of as direct measures of activity jitter through the evidence of variations of the profiles of the spectral lines.
The present work is dedicated to the analysis of line bisectors extracted from high resolution stellar spectra, as an attempt to evaluate if the radial velocity variations observed from a star truly correspond to the effects of a substellar companion or rather to processes in the stellar atmospheres or other effects (like contamination of spectra from light from other sources, a possible important effect when considering binaries).
The scientific motivation of this project is to understand the causes and nature of the observed radial velocity variations from stellar spectra. The analysis of spectral line asymmetries through line bisectors helps in this task because bisec-

tors give an idea about the variations of the line centroids involved in the radial velocity measurements. We explore if there is a correlation between radial velocity and line bisector variations; if any, then the possibility exists to employ such a correlation to "correct" the radial velocities and remove the undesired spurious effect.

The first part of the thesis is dedicated to present the ongoing status of extrasolar planet researches, the formation theories of planetary systems and planet formation like the core accretion and the disk instability scenarios, as well as migration mechanisms, attempting to explain the presence of massive planets in very close orbits around their parent stars, commonly observed. Brief descriptions of the most important detection techniques, of the observed properties of stars hosting planets, and of the inferred/observed properties of known extrasolar planets, follow. There is a special emphasis on the radial velocity technique and a more extensive description of the measurements through the Iodine cell and the simultaneous wavelength calibration with the fiber fed spectrographs and ThAr lamps. Relevant features of stellar atmospheres, active regions and activity indicators of solar type stars are also described, with a discussion of the information that line bisectors may provide about stellar photospheres.

The second part of the thesis begins with a description of the current status of the Italian search program for planets around stars in wide binaries, ongoing at the "Telescopio Nazionale Galileo". A complete chapter is devoted to explain how line bisectors are measured from the same spectra employed in the high precision radial velocity measurements. The method used to remove the Iodine lines by means of the B-star spectra, involved in the radial velocity determinations, is described. Average absorption profiles are then determined by cross-correlating the spectra with masks constructed with suitable lines from a solar catalogue. Line bisectors are computed from these average profiles, and the errors in these estimates determined. This is the first time, to our knowledge, that the same stellar spectra, with superposed Iodine lines employed for precise radial velocity measurements, are used to compute line bisectors, after removal of the Iodine features, in order to study line asymmetries quantitatively.

The next chapter contains a presentation and discussion of the analysis: the subsample of stars selected to measure line bisectors, as well as the main steps followed to determine the existence and significance of correlations between bisector velocity spans and radial velocities, with a description of the impact of the instrumental profiles. The results are then discussed, and explanations are given for the observed correlations. The most interesting cases are presented: the correlations found for active stars; the stars with spectra contaminated by light from their companions; and the lack of correlation for stars already known to host planets.

The possibility to apply corrections to the observed radial velocities in the spe-

cific case of stellar activity is explored in the final chapter of the thesis. This is done by using the linear correlation found between radial velocities and bisector velocity spans. We discuss the importance of such a technique and its application to the surveys for planets around young/active stars. The development of such a technique may shed light into controversial cases of planets in active stars, like the cases of HD192263, ϵ Eri, and HD219542B. Most of the current exoplanet surveys indeed do not consider young stars, that are generally active, and thus restrict the study of planetary systems to old, quiet stars. Young stars are however important to study the evolution of planetary systems: to study whether the properties of planets change with age (planet evolution); to test theoretical models of orbital migration in protoplanetary disks; to find best targets for direct imaging (young planets are in fact expected to be much brighter than old ones, and then more easily detectable); and to study the star-planet interaction processes through tidal forces and magnetic fields.

Chapter 2

The exoplanets research

The discovery of three Earth masses companions around the pulsar PSR 1257+12 (Wolszczan and Frail 1992 and Goździewski et al. 2005) during an accurate pulsar timing survey, opened the way to the search for extrasolar planets. However, it was the discovery of an object of jovian mass around the solar-type star 51 Peg (Mayor and Queloz 1995) that gave a strong motivation to the scientific community in the study of planetary systems beyond our own. The following decade has seen a real explosion in the science of extrasolar planets through the development of techniques to detect exoplanets and the development of models to explain the unexpected features shown by these objects.

2.1 Theories on planetary systems formation

Up to ten years ago, our knowledge of planets and planetary systems was based on the observed characteristics and study of the Solar system alone. The new exoplanets found so far around stars other than the Sun, showed a different and more general picture of planetary systems and planet formation.
Among the first models attempting to explain the formation of the Solar system and thus of planetary systems, those by Pierre Laplace (1796) and James Jeans (1917) should be mentioned (see Woolfson 2000). The former, the Laplace nebula theory, was based on ideas and observations from Descartes, Kant and Herschel, describing a slow rotating cloud which increases its rotation as gas and dust get cold and collapses under gravity, producing a lenticular shape from where rings form in the equatorial plane and the clumpling material produces protoplanets in each ring. The Sun is produced by the collapsed material at the center of the original cloud.
The latter, the Jeans' theory, suggests that a star passing close to the Sun drags

from it tidal filaments, which are gravitationally unstable and break in pieces forming protoplanets. These, attracted by the passing star, would occupy heliocentric orbits. At first perihelion passage, a small scale process similar to the previous one would produce tidal filaments leading to protosatellites.
These theories did not overcome scientific criticism, in particular those associated with problems about conservation and distribution of angular momentum. Nevertheless, new theories developed later came as evolution of these original ideas introduced by Laplace and Jeans.
The Solar Nebula Theory considers the idea that material in the early Solar system was embebbed in a hot gaseous environment. In this proposed scenario a process with different stages emerges from a disk of mass between $0.01\,M_\odot$ and $0.1\,M_\odot$: dust in the disk locates in the mean plane and grains stick together to form large particles (Weidenschilling et al. 1989). The dust disk breaks up due to gravitational instability to form "planetesimals": bodies of about a few kilometers radius (over $10^4 - 10^5$ years) which, through gravitational interaction, changing their Keplerian orbits and colliding, form single objects or embryos of about 10^{23}kg (the size of the Moon) in the terrestrial plane region and of larger masses in outer zones (over 10^7 to few times 10^8 years, Wetherill 1990). Successively, planetary cores of large enough mass ($> 10^{26}$kg) may accrete gaseous envelopes and eventually satellite formation arises as a very small scale process of planet formation.
The other proposed scenario, the Capture Theory, considers tidal interaction between the Sun and a diffuse cold protostar which distorts, and may escape a filament of material. Dormand and Woolfson (1971) confirmed the validity of the capture process and showed, from simulations, the agreement of the calculated distribution of planetary material with that of the Solar system. Later, Dormand and Woolfson (1988) modeled filament fragmentation (by smoothed particle hydrodinamics), showing that protoplanets move toward the aphelia of eccentric orbits and if the collapse time of a protoplanet is less than its orbital period (more that 100 years), then it would condense before the action of tidal forces at perihelion. In this scenario, planets are formed from cold material satisfying chemical constraints, in almost coplanar orbits close to the Sun-protostar orbital plane, and surrounded by satellites.
These scenarios succeed to explain some characteristics observed in the Solar system but still fail to explain other features, namely: the distribution of angular momentum in the system and the slow rotation of the Sun.
The discovery of many exoplanets with very particular characteristics in comparison to the known Solar system, like the exoplanets of Jupiter masses with low eccentric orbits (47 UMa), with high eccentric orbits (70 Vir), and close-in giant planets ("hot Jupiters") in almost circular orbits (51 Peg), pointed out the need to revise former theories and develop suitable models to explain planet origin. In

this context two mechanisms for planet formation are evoked: the core accretion and the disk instability.
The gas giant planets may be formed by the core accretion mechanism, where colliding elements inside a solar nebula give origin to growing solid objects. Solid cores of about 10 Earth masses in the outer solar nebula in approximately circular orbits, can accrete massive gaseous envelopes from the disk (Mizuno 1980). The protoplanet forms an atmosphere, grows accreting gas and planetesimals until the hydrostatic equilibrium is broken and the atmosphere contracts during a short period of collapse in which the protoplanet gains the majority of its final mass (Pollack et al. 1996).
The disk instability mechanism suggests the formation of protoplanets through gravitational instabilities. An unstable disk may give rise to trailing spiral arms, which can form high density clumps with sufficient mass to be self gravitating and tidally stable, forming protoplanets in about 10^3 years (Boss 2002a).
In all scenarios it is very difficult to form giant planets at very small distances from the central star, as it is observed in an entire class of exoplanets, the so-called Hot Jupiters which first example was 51 Peg. This is due to the very hot temperatures and the presence of magnetic fields in these regions, that prevent gas accretion. To overcome the difficult met by in-situ formation mechanisms, it was suggested that planets might have formed at much large distances, and later have migrated to the presently observed short period orbits. However, planets could be formed near the parent star when the disk density is particularly high.
In order to understand this migration process it should be considered that the gravitational interactions between the formed protoplanet and the rest of the disk not yet captured by planets produce a net torque, taking away angular momentum from the orbit of the protoplanet. A spiral density wave propagates away and the attraction of the protoplanet on these density perturbations results in the torque. Density wave torques repel material on both sides of the orbit and two modes of migration are possible depending on the strength of the interaction between protoplanet and disk.
Type I migration occurs when the protoplanet is not large enough to open and sustain a gap. The drift relative to the gas disk has a linear rate in both the protoplanet and disk masses. If the orbital decay time is faster than the life time of the disk, the protoplanet is in danger to fall into the central star.
Type II migration occurs when the protoplanet is large enough to form a gap, creating a barrier that prevents radial disk flow due to viscous diffusion. The protoplanet is then locked to and coevolving with the disk, its drift is set by the viscosity of the disk, with a rate independent of the protoplanet mass. The protoplanet may fall into the central star but after a longer time in comparison to type I migration (Ward 1997).
An important remark is the possibility that migration can occurs outwards as

well as inwards, depending on the initial disk density distribution. Through two-dimensional fully nonlinear disk models, Artymowicz (2004) introduces a third very rapid migration mechanism, as a result of a process driven by corotational gas flows and orbital libration of underdense disk gas, with characteristic time scale lower than a hundred orbital periods. This type of migration can be stopped by density gradients, like at the inner boundary of the magnetically inactive "dead zone" of a protoplanetary disk.
Masset and Papaloizou (2003) obtained similar results through the analysis of the torque exerted on a planet embedded in a gaseous disk, produced by the fluid elements as they perform a horseshoe U-turn in the planet vicinity. This so called "runaway" (or type III) migration, would give light to the processes intervening between the disk, the gap a planet can form within the disk and the magnetic forces at the disk boundaries, that may lie between 0.1 to 10 AU, and where exoplanets are commonly found.
Migration may arise also after the formation of the giant planet, after close encounters in unstable planetary systems.
The "Jumping Jupiter Model" by Marzari and Weidenschilling (2002), studies the stability of a planetary system composed by one solar mass star and three more objects of Jupiter masses by integration of their orbits in three dimensions. The most common result of gravitational scattering by close encounters is hyperbolic ejection of one planet. From the two remaining, one is moved closer to the star and the other to a distant orbit. Eccentric orbits are the typical product of such events.

2.2 Detection techniques

There are many different techniques to search for exoplanets and many of those rely on the measure of interactions between the exoplanet and its parent star. Efforts are ongoing to construct instruments for direct imaging the exoplanets, nevertheless some sub-stellar companions were already observed directly. The most exciting cases are the transiting exoplanets HD 209458b and TrES-1 from which the second eclipse was observed, by thermal emission measured in the infrared band with the satellite *Spitzer* (Deming et al. 2005 and Charbonneau et al. 2005). Three exoplanets candidates were also resolved directly by adaptive optics: 2M1207 b around a brown dwarf (Chauvin et al. 2004), AB Pic b (actually at the planet/brown dwarf boundary Chauvin et al. 2005b) and GQ Lup b (Neuhäuser et al. 2005).

Table 2.1: Basic quantities for planets.

	Sun	Jupiter	Earth	HD 209458b
Mass (kg)	1.99×10^{30}	1.9×10^{27}	5.98×10^{24}	1.31×10^{27}
M_v	4.85	25.5	27.8	–
Radius (km)	696000	71474	6378	94346
P (days)	–	4329	365	3.52
Semimajor Axis (AU)	–	5.2	1	0.045
RV semiamplitude of reflex motion (m/s)	–	12.5	0.09	86.52
Projected semimajor axis at 10pc (milliarcsec)	–	520	100	4.5
Contrast ($L_\odot$/L)	1	1.82×10^8	1.5×10^9	–
Transit lightcurve depth (%)	–	1.01	0.0084	1.7

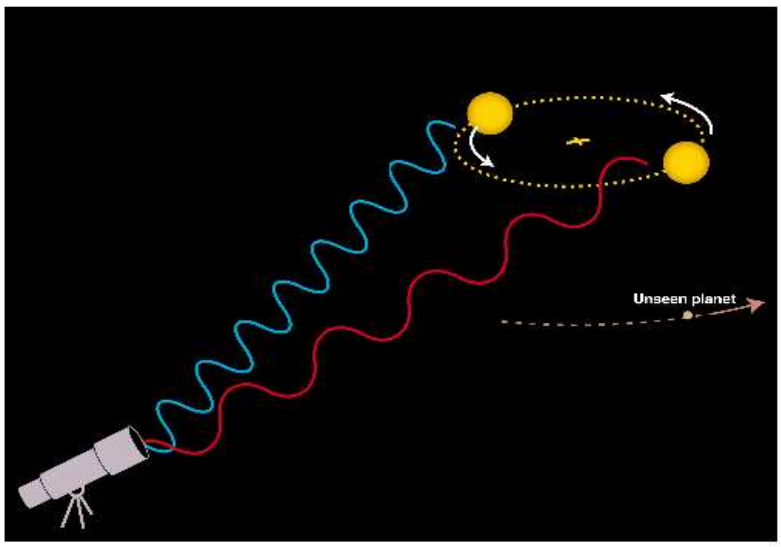

Figure 2.1: Schematic view of the wobble of a star due to an orbiting planet as observed from Earth. The star moves around the barycenter of the planetary system and its spectrum appears blue-shifted as it approaches the observer and red-shifted when it moves away.

2.2.1 Radial velocity

The radial velocity (RV) or Doppler technique is the most successful in the search for exoplanets. Almost all the known exoplanets have been discovered (confirmed) by measuring the variation of the RV of the star, when it orbits around the barycenter of the star-planet system (see Figures 2.1 and 2.2).
Typical RV accuracies required to detect exoplanets using this technique can be obtained from Table 2.1. Semi amplitudes of the RV curves are ∼50-100 m/s for hot Jupiters (like the transiting planet HD 209458b or 51 Peg b, see Figure 3.1 in the next Chapter) a few m/s for Jupiter-like planets in long orbits and a few cm/s for Earth-like planets.
Stellar spectra of both high resolution and high S/N are necessary to determine the wavelength shifts resulting from the relative motion of the star seen from Earth, even for the easiest cases. The very accurate wavelength calibration is carried out through simultaneous Thorium calibration or the use of a Iodine cell which superpose many absorption lines in the spectrum, producing accurate reference features.
The velocity amplitude is related to the stellar mass, the mass of the exoplanet, the period and eccentricity of the orbit. Using the Kepler's third law it is possible to establish the orbit semimajor axis a. However the exoplanet mass depends on the orbital inclination through a factor $\sin i$; hence, RV provides only lower limits to the masses.
This method favors the detection of exoplanets with high mass as well as short periods. Most of the planets discovered by the RV technique have masses of the order of Jupiter, semimajor axes a as low as 0.05 AU and periods of the order of days to a few years.
Most of the targets surveyed in the search for exoplanets are main sequence stars, typically of spectral type F-G-K, because their spectra are more suitable for analysis. In fact, stars earlier than F5 are fast rotators with broad spectral features, preventing precise RV measurements (Perryman 2000). Young or giant stars display rather large RV variations, due to spots, plages, chromospheric active zones, convective inhomogeneities and photometric variations that may mimic a stellar baricentric motion. Analyses of active stars require then the development of suitable techniques to correct radial velocities for such effects (Saar and Donahue 1997).
To date, the current instruments and technology allow measurements with accuracies even below 1 m/s (Mayor et al. 2003). Exoplanets with masses of about 21, 14 and 7.5 times the Earth mass (in short period orbits) were found recently (Butler et al. 2004, Santos et al. 2004 and Rivera et al. 2005).
However, increasing the accuracy of RV measurements would lead to a natural limit: the jitter of RV due to intrinsic stellar "noise".

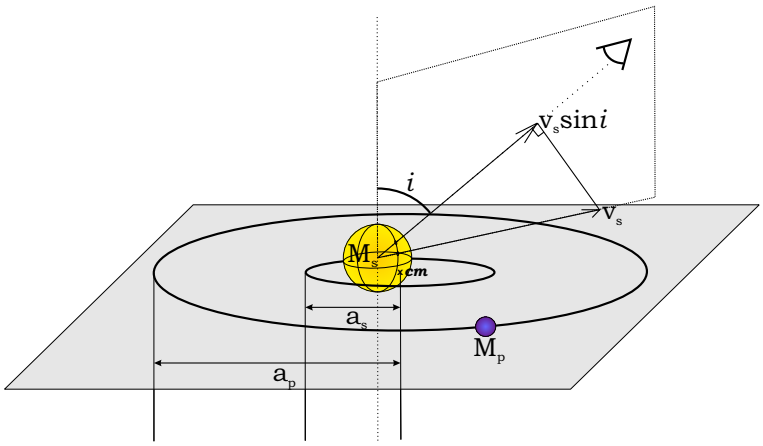

Figure 2.2: Orbital parameters of a planet-star system. The star s and the planet p are in circular orbit around the center of mass cm of the system. The orbital radii are a_s for the star and a_p for the planet, these are plotted along the orbital plane. The angle i between the normal to the orbital plane and the line of sight determines the orbital inclination angle. The radial velocity V_s of the star as measured along the line of sight (from the upper right in the diagram) depends on the sine of the orbital inclination angle (from Alonso 2006).

2.2.2 Transits

The exoplanet may cause an eclipse if it crosses the stellar disk, diminishing the observed light from the star; the result is a dip in the light curve, whose amplitude and length are determined by the ratio between the exoplanet and stellar radii, the stellar mass, the stellar disk limb-darkening parameter and the orbital inclination i. To reveal a transit, the observing direction must be close to the orbital plane of the planet ($i \approx 90°$); the probability of observe a system in such a configuration depends on the semimajor axis of the planet orbit. For close-in orbits ($P \sim 3\,d$) it is about 10% and decreases linearly with the semimajor axis for more distant exoplanets (see Figure 2.3).
The available photometric precision from ground is able to reach 0.2% (see Perryman and Hainaut 2005 and references therein). This is enough to reveal planets of the size of Jupiter but not of the size of the Earth (see Table 2.1). For terrestrial planets, space observations are mandatory.
If it is possible to obtain a mass from RV data then from the light curve it is possible to determine physical parameters of the exoplanet, namely: the radius, the orbital inclination i, the density, the surface gravity.
The planet surface temperature can be obtained by assuming equilibrium between the radiation from the star and emission by the planet, if a value for the albedo

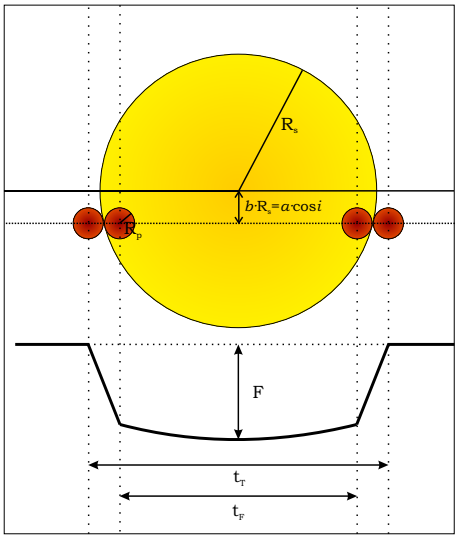

Figure 2.3: Schematic representation of a transiting planet across the stellar disk. The planet is shown from first to fourth contact. The stellar flux (solid line) diminishes by ΔF during a transit for a total time of t_T and t_F is the duration between ingress and egress. The curvature seen on the light curve is consequence of the star's limb darkening. The impact parameter b is shown also, in terms of the inclination angle i and the semimajor axis a of the planet's orbit (from Alonso 2006).

can be assumed. Alternatively, if the secondary transit is also observed in the mid-IR, the effective temperature can be directly obtained from the measured flux due to the planet, and its radius determined from the primary transit.
Since transits are quite rare, transit surveys must be performed over wide fields for long periods of time. In this way it should be possible to search for massive (Jupiter) exoplanets from the ground; detection of less massive planets of Earth masses require photometric accuracies of $\sim 10^{-5}$ mag, only possible from space. Anyhow it is important to set up suitable strategies of data analysis to discard false alarm detections, that can be caused by stellar effects like flares, spots, coronal effects or intrinsic stellar variation, as well as photometric binaries with grazing eclipses or whose image is blended with another constant star. For the case of ground based observations, attention must also be payed to atmospheric effects like air mass, absorption bands, seeing and scintillation. But transits may be caused by binary stars or brown dwarfs instead of exoplanets. All these are motivations for spectroscopic follow up observations, in order to confirm the real detection of a transiting planet.
Examples of exoplanets discovered by their transit are: TrES-1, OGLE-TR-10, OGLE-TR-56, OGLE-TR-111, OGLE-TR-113, OGLE-TR-132 and some other candidates of the OGLE project. Exoplanets discovered by the radial velocity technique and transiting their parent star are: HD 209458b, HD 149026 and

HD 189733 (Bouchy et al. 2005 and Hébrard and Lecavelier Des Etangs 2006). Among these, the most observed and well studied are HD 209458b (Charbonneau et al. 2000 (see Figure 2.4) and Henry et al. 2000b) and TrES-1 (Alonso et al. 2004). The transit observed towards HD 149026 suggest an object with a large and heavy core, inferred from the observed radius and mass deduced from the velocity semiamplitude (Sato et al. 2005).

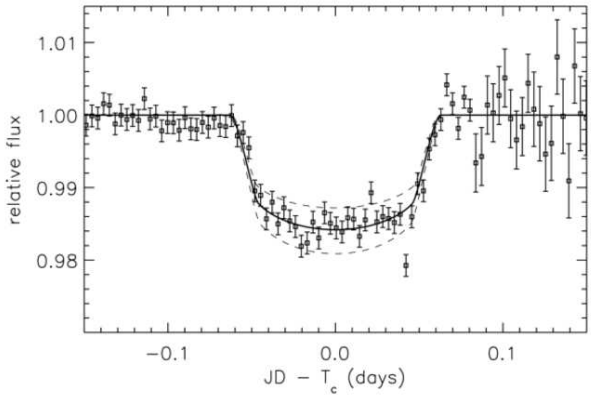

Figure 2.4: The observed transit of HD 209458b (Charbonneau et al. 2000).

2.2.3 Gravitational microlensing

The gravitational field produced by a mass, may deflect light from a background source and in some cases magnify it through a lens effect. The microlensing is a gravitational lensing, where the observable is the intensity variation of the light of a source (generally a background star) caused by an object (lens) passing between the observer and the source.
It is common to use the "Einstein ring radius", to express separations; this is a quantity that depends on the mass of the lens, the distance toward the lens and the distance toward the source.
A lensing event displays a characteristic light curve due to the magnification caused by the not resolved lens object, and on the relative motion of the lensing object and the background star. In the case of a binary system the lens determines a "caustic" (closed curve made of points in the source plane with (formally) infinite amplification) yielding the amplification pattern and displaying a characteristic light curve with sharp peaks due to the binary nature of the lens. In this manner it is possible to determine properties of the lensing object; if it is composed of two-point like objects, the light curve depends on the mass ratio

between the two objects (e.g., exoplanet/star) and their projected separation.
Since gravitational microlensing depends on the random alignment between the lensing object and the background star, probability of occurrence depends on the square of the field density. The fields surveyed by this kind of programs consider then zones with many sources, like our Galactic Bulge and the Large Magellanic Cloud, providing a high, not (strongly) biased, sample of stars.
In principle, it is possible to detect exoplanets of masses as low as a few Earth masses, though achieving the required photometric precision and observing frequency is a challenging task. At least, in principle, it is possible to detect multiple exoplanet systems as well as free floating exoplanets possibly providing a detailed statistics of the galactic population of planets.
There are some weaknesses of microlensing surveys: the probability to find exoplanets is very small, the duration of the event may be small (about hours or days), the event is not repeatable and light curves may not always yield a unique mass/separation fit. Additionally, rather than the exoplanet mass only the mass ratio of the system is determined. Finally the exoplanets discovered by microlens events are very distant, further complicating the analyses.
There are only two microlensing events that have been identified as exoplanet sources so far: OGLE 2003-BLG-235/MOA 2003-BLG-53 (Bond et al. 2004) (see Figure 2.5) and OGLE-2005-BLG-071 (Udalski et al. 2005).

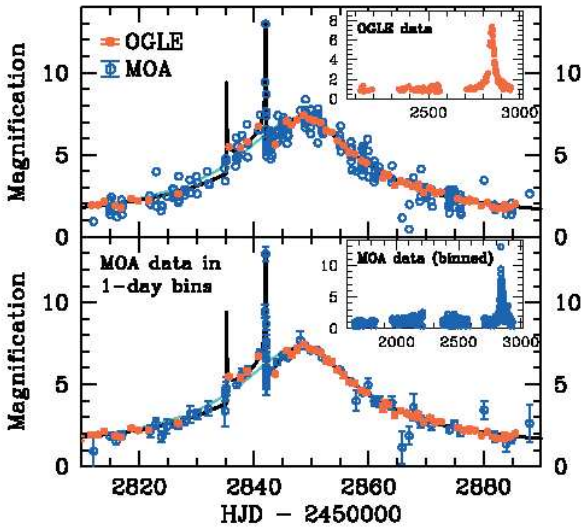

Figure 2.5: Light curve of the microlensing event OGLE 2003-BLG-235/MOA 2003-BLG-53 and best fit model for single lens (Bond et al. 2004).

2.2.4 Astrometry

A star in a planetary system would move around the barycenter in a circular or elliptical path projected on the plane of the sky. This motion can be observed and measured. The angular semimajor axis can be expressed in terms of the masses of the star and exoplanet, the semimajor axis of the orbit a in AU and the distance to the star d in pc.
Measuring the components of the orbital motion, it is possible to determine the inclination i, hence combining it with radial velocities data it is possible to determine the mass of the exoplanet without ambiguity. It is also possible to determine relative orbital inclinations, in the study of co-planar orbits, for analyses of dynamical stability and formation theories.
Through astrometry, it is possible to survey a bigger sample of stars (i.e., more massive, young, pre main sequence) and to overcome some of the limits in the RV surveys, e.g., those due to stars with complex (few or broad) spectral features. It would be also possible to detect exoplanets around young stars, to probe the time scale of planet formation and migration processes.
Because the astrometric signal increases linearly with the semimajor axis a of the planetary orbit, systems with even rather small masses would be more easily detectable at large enough values of a. Besides, astrometry would help to confirm long period exoplanets in the cases of long term RV residuals found in some surveys (Perryman and Hainaut 2005).
The astrometric technique requires very accurate measurements of positions, in a well defined reference system, and at a number of epochs. An observer located at 10 pc from the Sun would observe an angular amplitude of 500 microarcsec due to the motion of Jupiter and an amplitude of 0.3 microarcsec in the case of the Earth. Thus, measurements require accuracy below 0.1 milliarcsec to detect objects smaller than Jupiter at distances of 50-200 pc.
Measuring displacements of the order of a few milliarcsecs are impossible using standard imaging techniques from ground based observatories, due to effects of the atmosphere like turbulence and refraction that prevents the precise centering of images. Thus, interferometric techniques and space missions are ongoing to overcome these difficulties.
No exoplanets have been detected so far by this technique, however the mass for a companion of Gliese 876 was determined astrometrically (Benedict et al. 2002). There are projects under development carried out by ESO: PRIMA (Phase-Reference Imaging and Micro-Arcsecond Astrometry); ESA: Gaia; and NASA: SIM (Space interferometry Mission), just to cite a few.

2.2.5 Direct detection

The techniques discussed above are all indirect ways to determine the presence of exoplanets through the influence they exert on the host or background stars. Efforts are ongoing to make possible the direct detection of exoplanets and a successful result is the direct imaging of the exoplanet 2M1207 b around the brown dwarf 2MASSWJ1207334-393254. For this recent discovery, Chauvin et al. (2005a) employed VLT/NACO and confirmed that the exoplanet shares the same proper motion of the star, has about five Jupiter masses and with a high confidence it is not a stationary background object (see Figure 2.6).
Other successful results were the detection of the thermal radiation from the secondary eclipses of two known transiting exoplanets: HD 209458b and TrES-1 by the infrared satellite *Spitzer*. Deming et al. (2005) studied the secondary eclipse of HD 209458b (i.e., when the exoplanet passes behind the star) measuring radiation at $24\,\mu m$; for TrES-1, Charbonneau et al. (2005) performed analysis at $4.5\,\mu m$ and $8\,\mu m$.
Direct detection remains the most difficult technique to search for exoplanets due to the enormous brightness contrast between the star and the planet. Instruments able to provide high contrast and spatial resolution are under development.
Various approaches are considered. A careful selection of the wavelength of observation may reduce the star-planet contrast. This is minimum in the thermal IR ($\lambda > 5\mu m$) and may be better exploited from space due to the strong atmospheric background in ground-based observatories. The James Webb Space Telescope (JWST) will exploit this fact. From ground, use of high order Adaptive Optics is mandatory, in order to enhance the central peak of the planet image with respect to the stellar image. Also, coronography is very useful, to both reduce saturation of the central peak of the stellar image, and the halo of the diffraction image of the star. Differential imaging, that is comparison between similar images taken at wavelengths where the planet has, or has not, a strong spectral feature, can also be considered. By interferometry, it is possible to adjust the baseline and combine the stellar light out of phase to produce destructive interference, while the planet signal interferes constructively (nulling interferometry).
Probably the most suitable targets for the next instruments are young stars, since young exoplanets are expected to have an internal luminosity greater than the reflected light from the star (see Figure 2.7) (Burrows and et al. 1997).
Among the various projects aimed to direct imaging of exoplanets, there are the NASA Terrestrial Planet Finder (TPF); the ESO Planet Finder for VLT and EPICS for OWL; and the ESA Darwin mission.

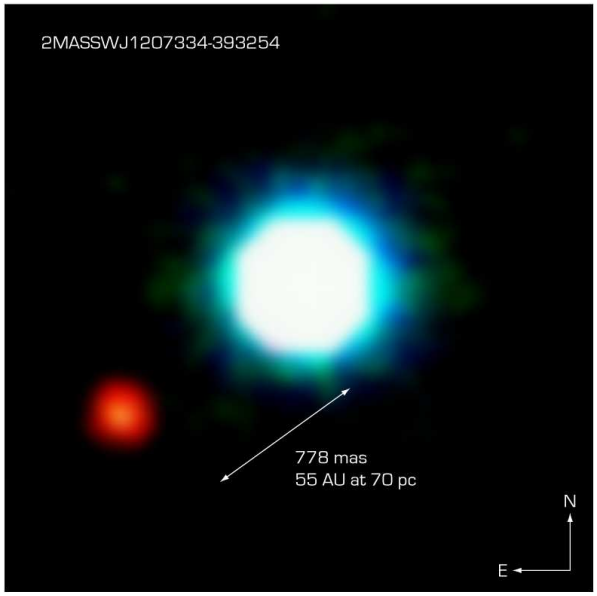

Figure 2.6: Image of the object 2MASSWJ1207334-393254 and its companion, from NACO/VLT.

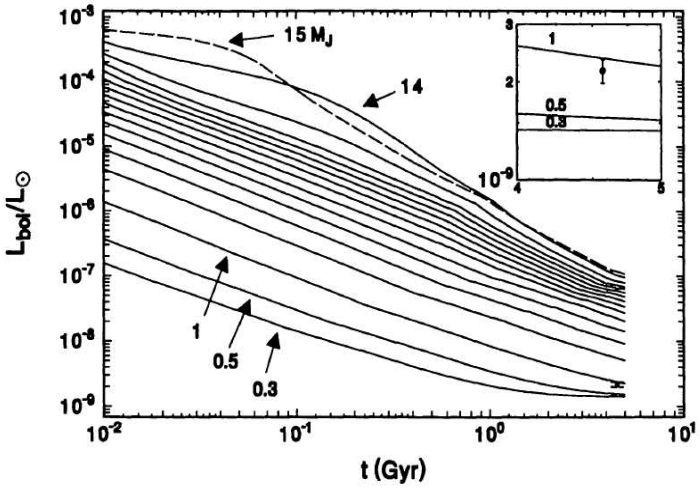

Figure 2.7: Bolometric luminosity, in solar units, of a sample of exoplanets versus time in Gyr. Planets are around an G2V star and at 5.2 AU. The data point at 4.33 Gyr shows the observed luminosity of Jupiter. In the small window, on an expanded scale, there is the comparison of the lowest mass evolutionary trajectories with the present Jupiter luminosity. Note that younger and more massive objects are brighter and more easily detected (from Burrows and et al. 1997).

2.3 Properties of stars and exoplanets

To date more than a thousand stars have been surveyed for planets and more than a hundred of exoplanets have been discovered only considering RV surveys. It is then possible to do statistical considerations about the stars hosting exoplanets, as well as the exoplanets themselves. However, the statistical significance of some features is limited by the available sample of stars (mainly biased to the main sequence and spectral types F-G-K) and to the observed properties of the exoplanets sensible to be discovered by the Doppler technique (e.g., higher velocity amplitudes with consequent smaller separations and higher masses).

2.3.1 Stellar properties

The RV technique is so far the most successful to reveal substellar companions. The stars surveyed are those with the spectra more suitable to perform accurate measurements, mainly stars of spectral type F-G-K.
One of the most remarkable feature of stars hosting exoplanets is their metallicity, which is higher in comparison to that of stars without exoplanets (see Figure 2.8 Fischer and Valenti 2005 and Santos et al. 2005 and references therein).
A power law can express the correlation between the frequency of exoplanets and metallicities (Fischer and Valenti 2005), with the probability of exoplanets formation approximately proportional to the square of the number of iron atoms. In particle collision rates there is a similar proportionality to the square number of particles, leading to think about a physical relation between dust particle collision rates in the disk and the formation rate of gas giant planets.
This supports the argument that the high metallicity of stars with exoplanets is due to a metal rich primordial cloud instead of a successive metal enrichment, and that gas giant planets form by core accretion rather than gravitational instabilities in a disk (Fischer and Valenti 2005 and Marcy et al. 2005). In fact planet formation is not expected to depend on metallicity in the disk instability scenario (Boss 2002b), while a larger availability of solid material should make easier the formation of the rocky cores of giant planets in the core accretion scenario.
Many stars are being surveyed in the search for exoplanets and a detailed astrophysical characterization is needed. Usually, it is carried out through photometry and spectroscopy, to determine luminosity, temperature, local surface gravity, metallicity, as well as spatial distribution and kinematical parameters like distance, rotation velocity, etc. (see e.g., Valenti and Fischer 2005).
There are ongoing surveys looking for planets around M dwarfs to set constrains on the frequency of planets as a function of stellar mass and metallicity in the comparison with solar type stars (Bonfils et al. 2005 and references therein).

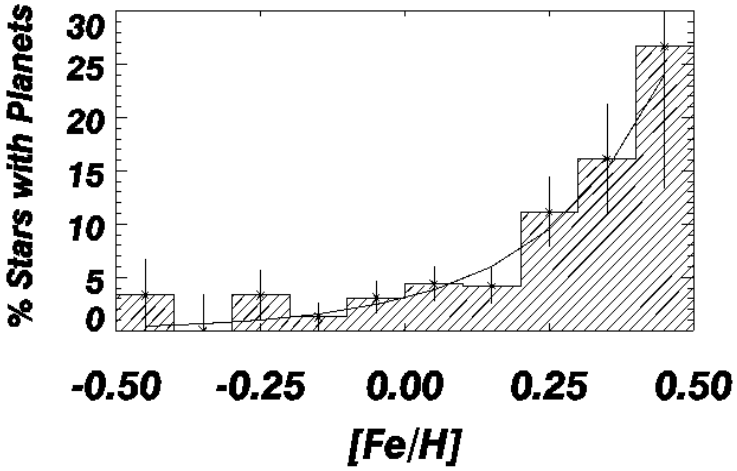

Figure 2.8: The percentage of stars with planets as a function of metallicity (from Fischer and Valenti 2005).

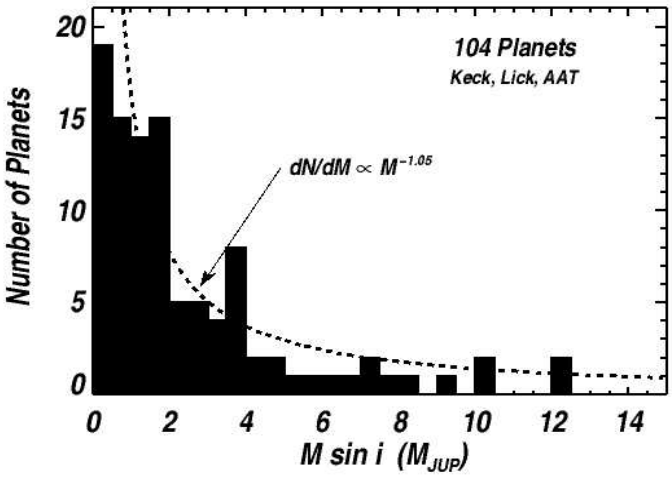

Figure 2.9: The distribution of 104 planet masses and its dependence on $M^{-1.05}$ from Marcy et al. (2005).

2.3.2 Exoplanets properties

From the more than one hundred exoplanets found so far, it is possible to derive some statistical properties. In the sample studied by Marcy et al. (2005) (1330 F-G-K-M stars and 104 exoplanets) the exoplanet masses ($M \sin i$) lie in an interval that ranges from around $15 M_{Earth}$ to $15 M_{Jupiter}$. Once selection effects are taken into account, the distribution with mass can be expressed by a power law proportional to $M^{-1.05}$ (see Figure 2.9). In more than 7% of the stars there are giant planets inside orbits with semimajor axis smaller than 5 AU, most beyond 1 AU.

A wide range of eccentricities e are observed: low values of e (almost circular orbits) occur for exoplanets with semimajor axis around 0.1 AU or less, due to tidal circularization. Those beyond 0.1 AU show $< e >= 0.25$, indicating that giant planets within 5 AU have higher e than the giant planets in our Solar system. Massive planets ($> 5\, M_{Jupiter}$) show systematically higher values of e.

The observed orbits with low e may be explained by tidal interactions between the planet and the star, at least for $\mathrm{P} < 10 - 20$ days, because there are exoplanets with long P and low e. The higher e values may be due to dynamical interactions like tidal interactions between the protoplanet and the disk, gravitational scattering between growing planetesimals, and resonant gravitational interactions between planets or planetesimals in the disk (see Fischer et al. 2004 and references therein).

There is no strong evidence for a dependence of the mass distribution on orbital distance; there are few massive planets in orbit close to stars, but the mass distribution appears similar for planets in orbits within 1 AU as well as beyond 1 AU.

Multi-planet systems are found around 18 stars; in these systems, the less massive planets appear in smaller orbits than the more massive ones.

In other statistical studies, Udry et al. (2003) concluded that no massive planets ($> 2\, M_{Jupiter}$) are found in short period orbits ($P < 100$ days) around single stars, although massive planets would be easier to detect closer to the star, suggesting that the migration rate of planets decrease with increasing masses. Additionally, there should be a large number of massive planets in orbits with long period not yet detected because of the short duration of the present surveys.

The period distribution of exoplanets can be expressed by a power law proportional to $P^{-\beta}$, with $\beta = 0.73 \pm 0.06$ or $\beta \simeq 1$ without correcting for selection effects. Besides, the period distributions and the eccentricity of extrasolar planets are almost equal to the low mass secondaries of spectroscopic binaries; an observation that leads to think the exoplanets can be formed in collapsing protostellar clouds like binary stars (see Tremaine and Zakamska (2004) and references therein).

In general, the presence of planets in close (2:1) resonance is the best observational proof of the occurrence of orbital migration.
Exoplanets have been found also around binary or multiple star systems (e.g., the giant planet in a close triple system (Konacki 2005)), showing different characteristics than planets found around single stars. This is the case of the most massive planets ($\geq 2\,M_{Jupiter}$) with short periods, and those with periods shorter than 40 days having very low eccentricities (Eggenberger et al. 2004). In Chapter 5 will appear a presentation and discussion of our exoplanets survey around wide binary stars, ongoing at the "Telescopio Nazionale Galileo".

Chapter 3

The radial velocity technique

In stellar and planetary systems there are gravitational interactions among their members that may appear as oscillating motions of the center of mass.
A planet orbiting a star would produce a wobble of the star around the barycenter of the system and this oscillation is what the RV surveys mean to measure in the search for exoplanets (see Figure 3.1). In cases where more than one object orbits the observed star, the oscillations may show modulations.
The RV semi-amplitude K, may be expressed by

$$K = \left(\frac{2\pi G}{P}\right)^{1/3} \frac{M_p \sin i}{(M_\star + M_p)^{2/3}} \frac{1}{\sqrt{1-e^2}}, \tag{3.1}$$

with G the Newton's gravitational constant, P the orbital period of the planet, M_p the planetary mass, $M_\star$ the stellar mass and e the orbital eccentricity. By Kepler's third law, the period may be expressed as

$$P = \left[\frac{4\pi^2 a^3}{G(M_\star + M_p)}\right]^{1/2}, \tag{3.2}$$

with a the semimajor axis of the planetary orbit.
Considering a circular orbit seen edge-on (e=0 and $\sin i = 1$, respectively) the semi-amplitude equation becomes

$$K = M_p \sqrt{\frac{G}{a(M_\star + M_p)}}, \tag{3.3}$$

for quantities in mks units. It helps to give an idea about the magnitude of the semi-amplitudes in our Solar system: $K = 12.5$ m/s for the case of Jupiter and $K = 0.09$ m/s for the Earth (see Table 2.1). Thus, giant planets (few Jupiter masses) in close-in orbits (smaller than 1 AU) produce larger K values, easier to be measured.

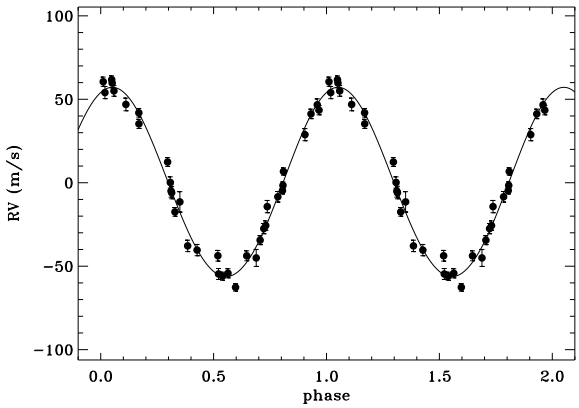

Figure 3.1: Radial velocity curve of 51 Peg as measured with SARG.

In order to reveal RV semi-amplitudes of few tens of m/s, to detect exoplanets with low mass or in large orbits, it is necessary to set suitable procedures of data acquisition and data analysis (see Butler et al. 1996 and Mayor et al. 2003 for precisions of 3 m/s and 1 m/s respectively).
The most successful approaches are the use of spectrographs fed by optical fibers, employing a Thorium Argon lamp for simultaneous wavelength calibration and on the other hand, a molecular Iodine (I_2) cell superposed to the stellar spectrum to use its many and sharp absorption lines as wavelength reference for calibration.
A novel technique for RV measurements consist in fixed delay interferometry (Ge 2002). A Michelson interferometer with a fixed delay and a medium-resolution grating postdisperser is employed to determine Doppler shifts by the phase shifts of the fringes in the spectrum. Using this approach van Eyken et al. (2004) achieved 11.5 m/s RV precision for 51 Peg and a wide field multiobject mode would allow to survey many stars in wide fields.
The accuracy in RV measurements depends on instrumental fluctuations as well as on external factors.
Ultimately, RV measurements rely on spectroscopic observations which uses an optical detector, generally a CCD. A CCD detector converts photons in photo-electrons which carry the signal and a statistical variation of fluctuations in the photon arrival rate. This phenomenon follows Poisson statistics and is known as photon noise. It is the intrinsic natural variation of the incident photon flux and the noise is proportional to the square root of the signal. This natural limit can be constrained by adequate modeling of the procedures of RV measurements in stellar spectra (see Bouchy et al. 2001 and Butler et al. 1996).
In addition, there are different sources of noise in the CCD to be considered: the read out noise which appears during the process of quantifying the electronic sig-

nal; the dark current produced by thermal electrons and non uniform structure within the pixels to cite a few.
Additionally, there are systematic errors coming from the slit illumination in the spectrograph, which depends on seeing conditions, guiding of the telescope and contamination from light different from the star being observed. These errors cause shifts of the monochromatic images on the spectrograph detection, mimicking variations in wavelengths similar to those due to RV variations. Other similar errors arise from instrument instabilities related to the spectrograph and its coupling with the telescope, such as mechanical flexures altering the optical path and temperature and pressure variations altering the refraction index of light and the CCD response.
The above considerations not only change the barycenter position of monochromatic images, but also influence the characteristics of the shape of the instrumental profile (IP), which is the instrumental point spread function in the direction of dispersion.
Diffraction and optical imperfections modify at some extent the stellar light from which is recorded the spectrum. This process can be thought of as the convolution of two functions, one representing the "intrinsic" stellar spectrum and the other the IP. The function of the IP can be determined by describing the observation with an appropriate model, considering the IP as a functional form of one or many free parameters. To know the IP shape is very important because its asymmetries, causing shifts of spectral lines, must be appropriately corrected to achieve precise RV measures.
The Earth atmosphere is also responsible of external errors in RV determination due to its dispersion and because the telluric absorption lines may vary in relative position and intensity compared to the stellar spectra. Finally the intrinsic variability of a star, hence its jitter, is also a source of noise.
To attain a precision of few m/s, needed for planetary and asteroseismology research, it is necessary to correct effects such as the velocity vector of the observer relative to the solar system barycenter, time dilation, general relativistic blueshifts due to the solar gravitational field, rotation of the Earth, changes of stellar coordinates due to proper motion and the apparent secular acceleration due to the transverse component of the stellar velocity vector, although some of these effects cause near constant offset in RV, that can be neglected when differential measurements are considered. Moreover the search for planets requires surveys extended over years, thus demanding long-term stability in order to ensure the good performance of instruments.
For a dispersing spectrograph having a resolution of R = 100.000 (2 pixels) and pixel size of 15 μm (typical of CCD detectors), RV precision of 1 m/s implies that the monochromatic images are stable (or their position can be calibrated) with an accuracy of 10 nm. Such an enormous stability requires special techniques,

that have been developed only in the last two decades.
In the following sections, techniques involving the Iodine cell and the use of optical fibers with the ThAr lamp will be discussed in more detail.

3.1 The Iodine cell

When this approach is considered, a cell with molecular Iodine gas is placed in the path of the stellar light, so that the spectrum recorded by the CCD has the Iodine features superposed. The many and sharp absorption lines of Iodine provide a very good reference for wavelength calibration.
Iodine has a strong absorption coefficient and requires path lengths of few centimeters at pressures lower than 1 atm. It is chemically stable and the sealed cell ensures the constant number of molecules. The wavelength range from 5000-6300 Å displays absorption features of high density.
A temperature of about 50 C is sufficient for Iodine to be in gaseous form and keep small thermal losses from the cell to the spectrograph. In the recorded stellar spectrum there is a shift corresponding to the Doppler effect of the star itself and a small spurious shift due to instrumental effects. The spurious shift is represented completely by the shifts of the Iodine lines, which are at rest relative to the observatory. Once the instrumental shift is determined, it is employed as correction to the shift observed in the stellar spectrum, yielding the Doppler shift relative to a stellar spectrum.
The RV determination is performed by an analysis consisting of different steps. As pointed out before, a spectroscopic observation can be described by the convolution of two functions, one representing the "intrinsic" source spectrum and the other the IP.
We briefly describe the analysis procedure to derive RV from spectra taken with the Iodine cell (see diagram on Figure 3.2), taking as reference the code AUSTRAL by Endl et al. (2000), which is used for the analysis of the SARG spectra (see Section 5.3.2). Other packages for analysis (e.g., Butler et al. 1996) differ only in details.
In the first step, the IP is determined from the observed spectrum and a very high resolution Iodine spectrum, which is obtained by a Fourier Transform Spectrometer (FTS) conveniently sampled and resolved.
To model adequately the IP, different types of functions can be considered, like a single Gaussian, a convolution of box-function with a single Gaussian, multi Gaussian or Lorentz functions. Bearing in mind the possible changes of IP along the spectrum, this is divided in several pieces of about 2 Å (80-120 pixels) each, to model the IP in a sub-pixel grid for every chunk. Finally, through a multi pa-

rameter χ^2 optimization it is possible to obtain information about the IP shape, dispersion solution, continuum tilt and line depth for every chunk.
In the second step, the stellar spectrum with the superposed Iodine spectrum is modelled. For this task the very high resolution Iodine spectrum and a spectrum of the star free of the Iodine features (called template) are employed; the last is deconvolved by using the IP derived formerly. To safely employ the IP in this step and minimize possible IP variations, it is better to get the Iodine spectrum as close as possible to the stellar spectrum. This is accomplished by acquiring a featureless star (e.g., early-type, fast rotator) spectrum with the Iodine cell rather than a flat field lamp to avoid differences in the spectrograph illumination.
Deconvolution can be performed by using the Maximum Entropy Method (MEM), as explained by Endl et al. (2000).
The final step is the same as the first step but using the spectrum of the star with the superposed Iodine spectrum instead of the pure Iodine spectrum. The very high resolution Iodine spectrum and the deconvolved stellar spectrum derived in the previous step are employed as "intrinsic" spectra.
In the fitting procedure the most important output is the Doppler shift and the model by chunks yield 20-30 RV measurements for a spectral order; in the case of cross dispersed spectrographs some 400-600 chunks allow to do detailed statistical analysis, giving an accurate estimate of the internal (measuring) error.

3.2 Optical fibers fed spectrographs

An optical fiber is a waveguide where only specific modes (eigenvalue solutions to Maxwell's equations) can propagate. For application to high precision radial velocities see e.g., Queloz et al. (1999). Small section fibers, with diameters of about 10μm or less, are called single-mode fibers because only one mode can propagate. The multi-mode fibers are those with larger diameters ($50 - 500\mu$m), usually employed in spectrographs.
The optical fibers have the advantage of bringing the light from the telescope to any desired place, like a suitable isolated environment where the spectrograph can be continuously monitored to ensure stability.
Inside an optical fiber, the convolution of ray trajectories of different optical path lengths by multiple total internal reflections is the basis of image scrambling. This results in an illumination of the output end of the fiber that maps more reliably the pupil of the input beam than it does the image (Heacox 1988). Moreover, multi-mode fibers are better beam scramblers in the azimuthal than in the radial fiber section.
Another property of optical fibers is an increase of the divergence of the beam

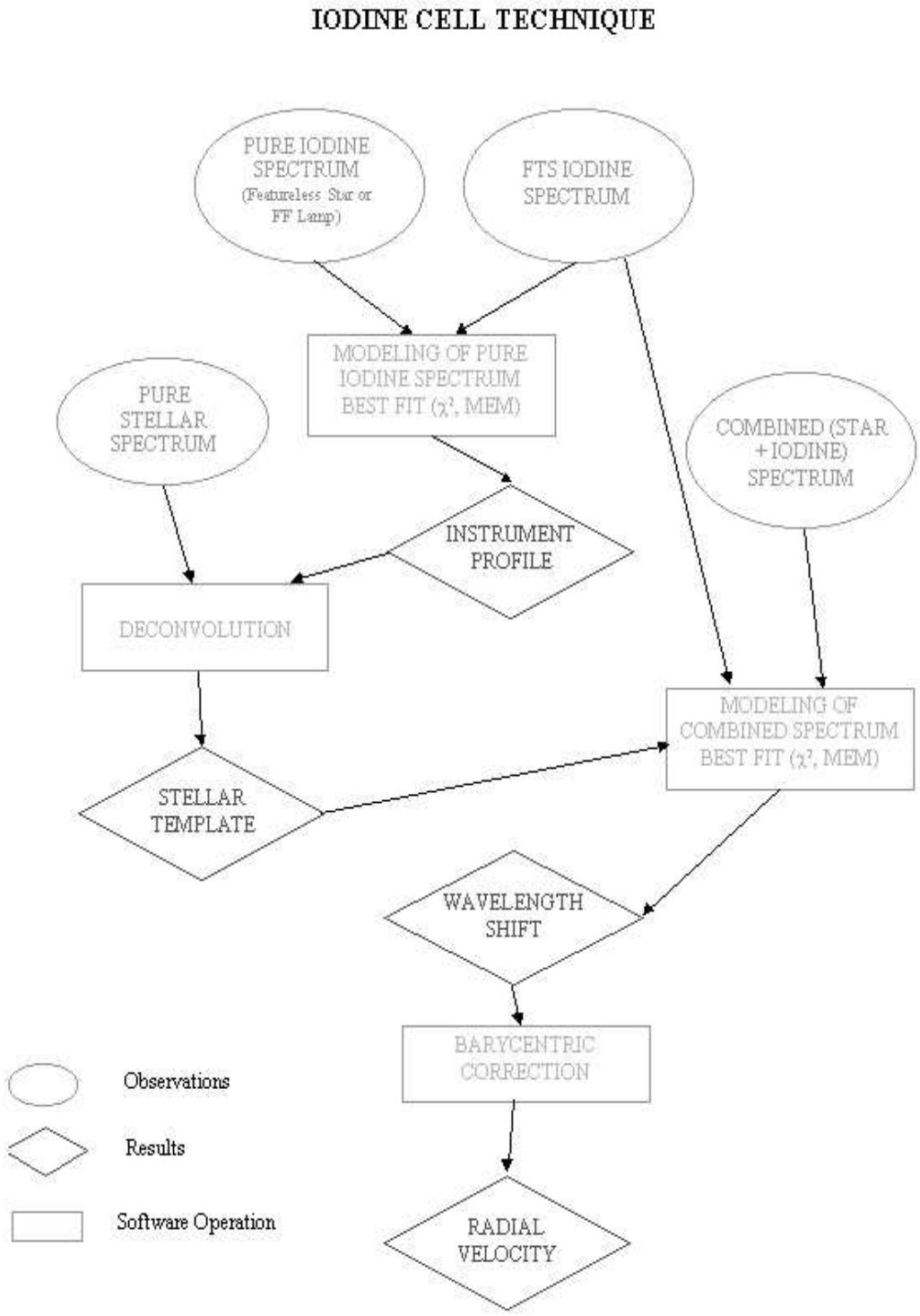

Figure 3.2: Diagram of the analysis in the process to measure radial velocities from stellar spectra (from Desidera 1996).

it carries (see e.g., Bouchy and Connes 1999). Various fiber imperfections and microbendings lead to the focal ratio degradation (FRD) effect, which increases the output beam aperture, due to random walk phenomena (see e.g., Queloz et al. 1999). The image scrambling improves with an increase of FRD.
The brightness distribution across the output side of the fiber, defines the near-field pattern of a fiber. The cross section of the beam far from the output side, defines the far-field pattern.
A double fiber scrambler may be employed to increase image scrambling. It couples two fibers by a pair of microlenses separated by their common focal lengths. In this manner the fibers see each other at infinity, causing the near and far field to be interchanged.
Exploiting the scrambling properties of fibers and double sclamber devices, a spectrograph can have very stable slit illumination. Minimizing the stresses and micro bends, with optimal focal lengths the fibers can be sufficiently bright with about 80% transmission.
The use of optical fibers to feed spectrographs with starlight and a reference lamp for wavelength calibration, avoids the higher photon noise in RV errors that appears when the stellar and reference spectra are recorded from the same beam.
ELODIE (OHP-France), CORALIE (OG-Switzerland) and HARPS (ESO) are fibre-fed, cross-dispersed echelle spectrographs presently employed for the measurement of radial velocities. The last is the most stable instrument, inside a vacuum vessel on a temperature controlled room to keep at minimum pressure and thermic fluctuations.
Usually two optical fibers are used: the first with starlight from the telescope focus and the second with the light of a ThAr lamp for simultaneous calibration or with light from the sky for better sky subtraction.
For the case of HARPS, the light is coupled into a fiber by means of two microlens doublets. The image is projected on the fibre input so that the telescope pupil is at infinity. This design provides excellent image quality, not critical and simple alignment with minimum FRD.
A double image scrambler is set at the entrance of the fibre going into the vacuum vessel, in order to stabilize the spectrograph illumination, because the object light may move at the fibre input due to guiding problems or seeing conditions. Inside the vacuum vessel, a pair of doublet microlens helps to couple the fiber to the spectrograph. This is done by two fibers, one carrying light from the star and the other carrying light from the ThAr lamp (Pepe et al. 2002).
The simultaneous ThAr technique provides an easy and efficient way to measure any zero point shifts occurring during the exposure. Each beam has its own wavelength calibration but their wavelength variations are correlated. The zero point variation, measured with the ThAr spectrum, is applied to correct the stellar spectrum which is taken at the same time (Queloz et al. 1999).

A cross correlation function is computed between the observed stellar spectrum and a template spectrum, made from box-shaped emission lines, to determine the radial velocities (Baranne et al. 1996). The technique is suitable for a large wavelength range, with a large number of lines (about 1000) in the stellar spectrum (e.g., a cool star), because the template is efficient if the number of lines is statistically significant (Queloz 1995).

3.3 Throughput and characteristics

The methods described above are implemented in different survey programs to guarantee an instrumental stability over years; however each technique has its advantages and disadvantages.
RV values can be obtained after few minutes of the observation when using the simultaneous calibration by the ThAr lamp due to the less complex analysis required in comparison to the one for Iodine cell.
In the case of the Iodine cell, there is a loss of efficiency due to the presence of the cell in the optical path, thus the stellar spectrum is scaled by the effective throughput of the absorption cell. The mean throughput is about 50% on average (Pepe et al. 2003). The wavelength range coverage, of about 1300 Å, does not allow to use entirely the stellar spectrum for RV measurements. With the above considerations, when using the Iodine cell in place of the ThAr lamp, the radial velocity efficiency is about 6 times lower (Pepe et al. 2003).
Nevertheless, employing an FTS, the Iodine spectrum obtained has very high resolution and high signal-to-noise ratio ($R = 400000$ and $S/N = 1000$) providing a wavelength scale accurate to $1 : 10^8$ (Marcy and Butler 1992).
The use of an Iodine cell is suitable for any kind of high resolution spectrograph and the instrument can be employed also for tasks different from planet search. It is also a good choice in terms of cost, which is higher when constructing a dedicated and stabilized instrument. In a direct illumination slit spectrograph, there is the possibility of slit orientation and light contamination by a nearby companion of the target can be minimized by using narrow slit apertures.
Fiber fed spectrographs have to be intrinsically stable without moving parts; with a fixed set-up they can be used for specific (limited) types of scientific goals. When using fibers, scrambling of circular apertures of 1-2 arcsec on the sky, does not allow to have spatial information.
The fibers provide a constant, roughly symmetric illumination of the slit. Furthermore, spectra are generally acquired with simultaneous wavelength calibration lamps. For the study of spectral line asymmetries (that will be discussed in Chapter 6), no attempt has been made to our knowledge to study line bisectors

on spectra obtained through an Iodine cell. One disadvantage is the necessity to remove the iodine lines from the stellar spectra; but on the other hand, the Iodine lines allow a fine wavelength calibration and the possibility of monitoring the instrumental profile. In the rest of this Dissertation, we will discuss how spectral lines asymmetries can be determined from spectra acquired with an Iodine cell.

Chapter 4

Magnetic activity in stellar atmospheres

A stellar atmosphere is the transition region from the interior of a star and the outside or interstellar medium region. It can be described as composed of different subregions. From the interior outward, they are: the subphotosphere, the photosphere, the chromosphere and the corona.
The subphotosphere or convective zone is a region where the energy is transported mainly by convection. In low mass stars, it reaches large depths and energy transport can be totally convective. In higher mass main sequence stars the convective zone is less deep and may be replaced by a radiative zone. The photosphere is the region where almost all the visible spectrum of a star originates. The chromosphere is a thin region hotter than the photosphere and above it, the higher zone being the transition region where temperature increases very rapidly with radius. The corona is an external layer of extremely hot and low density gas extending for millions of kilometers. This thesis focuses the study on solar type, main sequence stars, that are the stars for which higher precision in RV can be obtained.

4.1 The photosphere

Almost all features seen in the visible light spectrum of stars have origin in their photospheres. There, the hot gas produce rising convective cells in a process called granulation, giving the stars its particular surface texture. The intergranular lanes are relatively cool dark zones where material descends between granules. Dark zones of lower temperature than their surroundings give rise to spots; they are accompanied by brighter zones known as faculae. Filigrees are strings

of bright points seen in the intergranular lanes. Spots, faculae and filigrees are associated with strong magnetic fields, which interact with the convective motion, slowing down or accelerating the heat transport, and then causing the presence of cooler (darker) or warmer (brighter) regions.

4.2 Convective motions in a stellar atmosphere

In a solar type star, the major contribution to the spectral profile comes from the hot rising granules: spectral lines appear blue-shifted with respect to the stellar barycenter velocity. A lower contribution come from the cooler, descending material of intergranular regions and it appears red-shifted with respect to the stellar barycenter velocity. There are different amount of photons coming from the rising and descending material measured in the flux spectrum and this is a cause of spectral line asymmetry.

4.2.1 Line bisectors to study asymmetries

A line bisector of a spectral line is made by the mid points of the horizontal segments joining both sides of the profile, from the core toward the wings.
There are different factors that produce asymmetries in stellar spectral lines: blends of lines, dark spots on stellar surface, oscillations, pulsations and granulation, among others. These asymmetries can provide information on photospheric velocity fields and for this study the bisectors are employed.
Among the different techniques to study asymmetries in spectral profiles, the line bisectors are the most powerful because the shift and curvature along the points of the bisector indicate the velocity and flux contrast at different depths of line formation, something that reversed profiles can not provide. A line profile can be reversed on itself to detect asymmetry, but it does not provide physical information as line bisector does. The Fourier transform can also be applied to spectral profiles and the imaginary components gives a measure of non symmetry, however large imaginary components may arise from minor blends in the line wings which is a very common feature (Gray 1988).

4.2.2 Line bisectors across the HR diagram

Temperature is one of the different factors changing the bisector shape for stars of different spectral types (see Figure 4.1). In normal cool stars, like the Sun, the

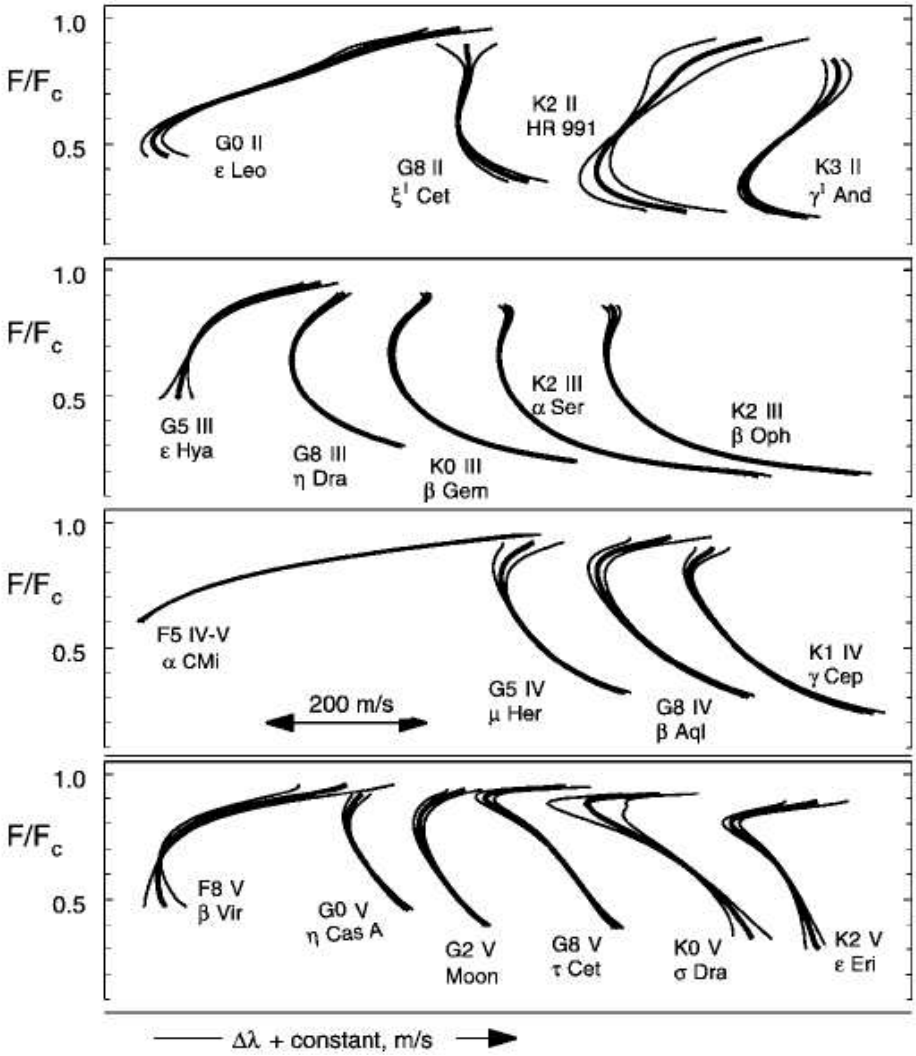

Figure 4.1: Bisector shape and its dependence on effective temperature. Each panel corresponds to a different luminosity class. Thin lines represent the rms uncertainty in the measurements of the mean bisectors (thick lines). Moving toward cooler stars, the upper portion of the bisectors are slowly blue-shifted, while the lower portion are slowly red-shifted. These are all relative changes (from Gray 2005).

typical "C" shape of bisectors comes from motions mainly due to granulation. Hotter stars display highly asymmetric bisectors, indicating velocities larger than those for cool stars, with slope and curvature in the opposite direction (inverted "C"). This leads to deduce that a low percentage ($\lesssim 10\%$) of photons are associated with rising material and it is not clear if velocities are generated by thin convective zones (as thought for hot stars) or by different mechanisms (Gray 1992).
The zone in the HR diagram where the line bisector of stars changes its curvature from one direction to the other, passing through a straight line bisector, corresponds to the granulation boundary. Besides, the magnetic activity increases from the hot side toward the cool side of the granulation boundary, as consequence of convection and rotation that generates magnetism through the dynamo effect.
Luminosity also contributes to changes in line bisectors. Gray (2005) shows how the line bisector varies in early K stars of different luminosity class. When luminosity increases, there are two remarkable features: first, the curvature of the lower portion of the bisector turns from an inverted "C" to the typical "C" shape. Second, the blue-most point of the bisector decrease in the flux scale. In the plot of the blue-most point of bisectors against absolute magnitude, for a sample of late G and early K stars, but in particular for the class III giant portion, there is evidence for a nearly unique relation between bisector shape and luminosity (see Gray 2005 for details).
Rotation, broadening the spectral profiles, changes the shape of line bisectors. The center of the stellar disk is unaffected but rotation introduces the largest Doppler shifts at the limb. Therefore, some of those shifts near the peak of the distribution are displaced to the edges, resulting in an enhancement or even reversal of the skewness of their distribution, provided the presence of asymmetries. These change as $v \sin i$ increases; for large rotational velocities, the lower part of the line bisector appear blue-shifted (Gray 1988).
From computed models of the Sun, Smith et al. (1987) concluded that rotation exaggerates any curvature on line bisectors and deviations from symmetry increase roughly as the square of rotational velocity.
The effects of active regions on line bisectors are discussed in Sec. 4.3.4.

4.3 Stellar activity

Motions of mass inside a star can increase the energy of magnetic fields above its mean static value. As a consequence, the magnetic energy can be converted into heat, in non-thermal particles or kinetic energy. All these processes, where the interactions between magnetic fields and turbulent plasmas cause different

phenomena, are termed stellar activity.

4.3.1 Active regions

An active region of a star is a zone where very strong magnetic fields produce different temporary features, which appear in different zones of the stellar atmosphere. From observations of the Sun these features can be described as follows:
In the photosphere, spots appear as dark zones due to their temperature lower than their surroundings. These are concentrations of magnetic flux that move across the stellar surface as it rotates, appear in pairs of opposite polarity and are connected by loops of magnetic fields in archs through the stellar corona. The high intensity of magnetic flux restricts the rise of convective heat and keeps the spot at a lower temperature, cooler than the rest of the photosphere. Lifetime of spots varies; in the Sun they last from some hours to few days or even months.
Faculae, are bright zones commonly seen near spots; they are thought to be caused by luminous hydrogen clouds close to the photosphere. Faculae are best observed in blue light and they are not visible in Hα.
In the chromosphere, plages appear as bright zones near spots visible in the monochromatic light of spectral lines, like Hα or Ca II. They can last for various days and mark areas of almost vertical emerging or connecting magnetic fields.
Fibrils are fine dark lines seen in Hα light in the low chromosphere. They form whirls near spots and plages, connect spots and plages of opposite polarities along magnetic field lines and surround spots in a radial pattern. They last for few minutes.
Filaments are strings of cool gas above the photosphere due to magnetic fields and appear as dark lines over the stellar disk. On the limb of the star they appear as emissions known as prominences. Filaments can be seen only in the centers of strong spectral lines like Hα or H-K lines of Ca II.
Flares are sudden and impressive release of energy through a break in the stellar chromosphere, close to a spot and lasting from a few minutes to a few hours.
In the corona, coronal condensations appear as very hot zones, denser than their surroundings. They are seen at the limb above groups of spots and display loop structures delineating magnetic field lines.

4.3.2 Time scales of variations

The activity phenomena described in Sec. 4.3.1 show temporal variations with different timescales. Flares have typical duration of few minutes or few hours, without periodicities. The presence of spots and plages on the photosphere, cou-

pled with the stellar rotation causes a modulation of the flux with the same period of the stellar rotation. Such rotational modulations, usually are not constant in amplitude and phase because the typical lifetime of spots and plages is of the order of weeks or months. However, there are observations of special cases of stars that keep their spots distribution fairly constant even on timescales of several years (ξ Boo A).
Magnetic activity of solar type stars shows cyclic variations with timescales of several years (Baliunas et al. 1995). During maximum phases, the spot and the plage coverage is larger, making easier the detection of rotational modulations. Stable activity cycles were detected for several stars and in the case of the Sun it last about 11 years.
It appears that stable cyclic variations occur more easily for stars of low activity.

4.3.3 Activity indicators

Following Gray (1988), there are two approaches to study magnetism in stars: the direct measurements and the use of indirect indicators of magnetic fields.
The first approach relies on direct measurements like Zeeman splitting of spectral lines. The Zeeman effect occurs when a strong magnetic field pervades a gas and provokes the division of a spectral line in many components, a rarely observed phenomena in stellar spectra. In cool stars the split is generally a small fraction of the Doppler broadening due to rotation and granulation. In fact, it can be considered as another component of line broadening.
Polarization can be used to detect weak Zeeman broadening but one inconvenience is the small net polarization to be measured, at least in F, G and K stars. For this reason, Zeeman broadening has been studied only in G dwarfs and cooler stars, where the Doppler broadening is small.
The second approach exploits the properties of some spectral lines as indicators of magnetic fields (see Montes et al. 2000 and references therein). Typical examples are the Ca II H and K lines. In the profile of these lines we may consider a main absorption feature K1, formed in the higher photosphere; the emission features K2 formed in the chromosphere, with asymmetries due to upper flows in the plage regions; and finally a central absorption feature K3, that can appear as an emission reversal and form in even outer regions of the chromosphere. These optical lines represent an important cooling mechanism for the outer atmospheric regions.
A second example are the Ca II infrared triplet (IRT) lines: formed in the lower chromosphere, the equivalent width ratios of their emissions are employed as indicators of the type of chromospheric structure, like plages or prominences.
The core of the Hα and Balmer lines, formed in the middle chromosphere, appear

as emission above the continuum in very active stars and as filling-in absorption features in less active stars. The equivalent width ratio of Hα and Hβ helps to discriminate between plages or prominences in the stellar surface.
The cores of the Na I D_1, D_2 lines and of the Mg I b triplet are good indicators of changes in the upper photosphere and lower chromosphere. They appear as emission reversals or filling-in during flares.
Finally, the He I D_3 line has origin in the upper chromosphere and is an indicator of flare events.
The X-ray radiation from stars may have origin in the corona, which is heated and enclosed by magnetic fields generated by a dynamo process (see e.g., Randich 2000). Indeed, X-ray emission from coronae of late type stars is a good indicator of magnetic heating mechanism (Stepien and Ulmschneider 1989) and X-rays originated from solar flares can heat the chromosphere (Linsky 1980).
As a star evolves, the dependence on height of the magnetic fields changes because the dynamo process weakens with age. Evidence of this effect is observed when the decrease of coronal X-ray emission is followed by changes in asymmetry of the Mg II h and k emission lines and similar changes in Ca II H and K asymmetry (Gray 1988).
Hempelmann et al. (1996) studied the relation of coronal X-ray emission of main sequence F-K stars and the characteristics of their magnetic cycles, through X-ray data from the ROSAT all-sky survey (RASS) and data of the Mt. Wilson Ca II H+K monitoring program. The authors demonstrated (in a statistical sense) that cyclic chromospheric activity also implies cyclic coronal activity.

4.3.4 Variation of line profiles caused by stellar activity

Different stellar activity features can change the spectral line profiles; this is e.g. the case of plages that alter the granulation pattern, and of spots that alter the rotation profile. Both effects may be studied through the analysis of line bisectors.
For the case of plages altering the granulation or convection, it is useful to consider specific lines of the stellar spectra, to deal with species of the same strength, formed more or less at the same depth of the photosphere, to study the asymmetries of their "absolute" line bisectors.
For the case of spots and their influence on a rotation profile, an average of suitable lines yielding an average absorption profile provide a useful line bisector. This procedure is reliable because spots, obscuring the photosphere, act more or less uniformly on all species and the asymmetries, measured from the line bisector of the average profile, reflect the distortion due to obscure zones over the stellar surface. Thus, as sources of changes can be considered different cases like: spots

moving over the star as it rotates e.g., HD 166435 (see Queloz et al. 2001 and Martínez Fiorenzano et al. 2005) and the "starpatch" on ξ Boo A (see Toner and Gray 1988); pulsation or motions across the stellar surface e.g., non-radial oscillation in α Hya (see Setiawan et al. 2005 (in press)) and variations of the granulation and magnetic activity cicles.
The variations of line profiles described here follow the timescales of the variations of the magnetic activity and their coupling with the rotation.

4.4 Analysis from stellar spectra

Considering the procedures explained in the previous chapter and some characteristics of stars described in the previous sections, it is necessary to be cautious about the interpretation of the differential radial velocities measured from stellar spectra in the search for planets.
Most of the thousands of stars surveyed in the RV programs belong to the main sequence and are of solar-type, hence objects sufficiently stable, bright and with suitable features to record high quality spectra. Nevertheless the reliability of the RV variations that give a Keplerian curve must be supported by further analysis, i.e., by the study of spectral line asymmetries, by monitoring of activity indicators and by photometric observations.
The purpose of this thesis is to present a method to analyze the line asymmetries, through line bisectors, from the same stellar spectra employed in the RV calculations.
If a constancy in shape and orientation is observed in line bisectors, it would ensure a uniform pattern of the spectral absorption features and the measured Doppler shift surely corresponds to the motion of the star.
It is interesting to study the relationship of line bisectors and radial velocities. A lack of correlation among the velocity span, given by the bisectors, and the radial velocities measured from the spectra, supports the mechanical nature of the recorded variations. However, if a correlation appears, the interpretation of the RV variation would be different than a pure mechanical motion around the barycenter of a star-planet system. The variations recorded from the spectra, may be due to stellar activity, like spots covering the stellar surface as it rotates or may be due to light contamination from an unseen stellar companion of the target. Both phenomena leave a particular imprint on the spectral lines that an accurate study of asymmetries, through line bisectors, can reveal. The cases where a correlation is found are of particular interest because the observed trend can be employed as a quantitative tool, to remove the activity or the contamination, aiming to correct the radial velocities measured from the spectra in the

search for sub-stellar companions.
The activity jitter of a star may be predicted by means of statistical relations from its chromospheric emission, rotational velocity or amplitude of photometric variations (Saar et al. 1998 and Paulson et al. 2004). Simultaneous determination of RV, chromospheric emission and/or photometry is even more powerful in disentangling the origin of the observed RV variations (Keplerian vs. stellar activity). However these techniques cannot be considered as a direct measurement of the alterations of the spectral line profiles that are the origin of the spurious RV variations.
This type of study can be carried out by considering variations of line bisectors, that may be thought of as direct measures of activity jitter through the evidence of variations of the asymmetries which appear in spectral lines.
Complementary observations such as the record of activity indicators and photometry observations would enhance our knowledge about RV variations.

Chapter 5

The SARG planet search

The data discussed in the present thesis are part of the RV survey aimed to find planets around stars in wide binary systems (Desidera et al. 2004a), ongoing at "Telescopio Nazionale Galileo" (TNG) in La Palma (Canary Islands, Spain) using the "Spettrografo ad Alta Risoluzione per Galileo" (SARG) (Gratton et al. 2001).

5.1 Scientific motivations and goals

Our study of the presence of giant planets in wide binary systems is motivated by two specific aims:
-The study of dynamical effects due to the presence of a stellar companion on the formation and evolution of planetary systems, e.g., the minimum binary separation for the formation of planets and perturbations due to planetary orbits.
-The study of chemical composition to identify possible alterations related to the presence of planets, not viable when considering single stars.
In detail, studying the properties of planets in binary stars and the differences of those around single stars would help to understand the effects caused by the presence of other components in binary systems. The occurrence of some difference on the period-mass relation was suggested (Zucker and Mazeh 2002). It is also possible that a stellar companion to a planet host, forces the planet to reach high eccentricities through the Kozai mechanism (Wu and Murray 2003). In general it seems difficult to form planets in tight binary systems (see Hatzes and Wuchterl 2005), but some cases are actually observed (HD 188753A, Konacki 2005 and γ Cep, Hatzes et al. 2003).
Theoretical models indicate that planets might form in wide enough binary systems and discoveries of planets in those systems with different mass ratios and separations support these models (Eggenberger et al. 2004). Studies on the dy-

namical stability of planets in binary systems can be performed by means of numerical simulations (Holman and Wiegert 1999 and references therein).
To analyze our stellar sample, suitable tools are being developed to derive clues on the orbits of the stellar pairs in case of significant trends in position angle and separation (about 25% of the pairs) and possible dynamical situations for various binary orbits. N-body simulations were perfomred, to explore the long term stability of the system and possible terrestrial planets. The infall of material during the accretion of planetary companions from a protostellar disk is also explored.
An adequate procedure for the analysis of the chemical abundances and the very good quality of data, allows a precision of about 0.01-0.02 dex (1σ) in the differential measurement of the metallicity. From the analysis of 23 pairs there is no pair with abundance differences larger than 0.07 dex. The four cases of differences larger than 0.02 dex may be spurious due to large error bars affecting pairs with large temperature differences, rotating and cold stars (Desidera et al. 2004c).
For non rotating stars with temperatures higher than 5500 K, characterized by thin convective envelopes and for which the analysis appears to be of higher accuracy, it is possible to exclude in most cases the consumption of more than one Earth mass of iron (about 5 Earth masses of meteoritic material) during the main sequence lifetime of the stars, placing more stringent limits (about 0.4 Earth masses of iron) in five cases of warm stars, a limit similar to the estimates of rocky material accreted by the Sun during its main sequence lifetime (Murray et al. 2001).

5.2 The stellar sample

5.2.1 Selection criteria

The stars in our sample were selected from the Hipparcos Multiple Stars Catalog. The selection criteria considered were: separation greater than 2 arcsec to avoid contamination of the spectra[1]; magnitude differences less than 1 mag (see Figure 5.1) because a small magnitude (and temperature) difference is useful when comparing the chemical composition of the components and avoids systematic effects due to different temperatures and gravities; colors in the range $0.45 <$ (B-V) < 1.1; and parallaxes larger than 10 mas, with errors smaller than 5 mas[2];

[1] As we will discuss in Chapter 7, contamination by light from the companion is a major source of concern for the closest pairs in our sample. This is one of the motivations of the line bisector analysis presented in this thesis

[2] Parallax errors for visual binaries are generally much larger than the typical errors in the Hipparcos parallaxes (about 1 mas)

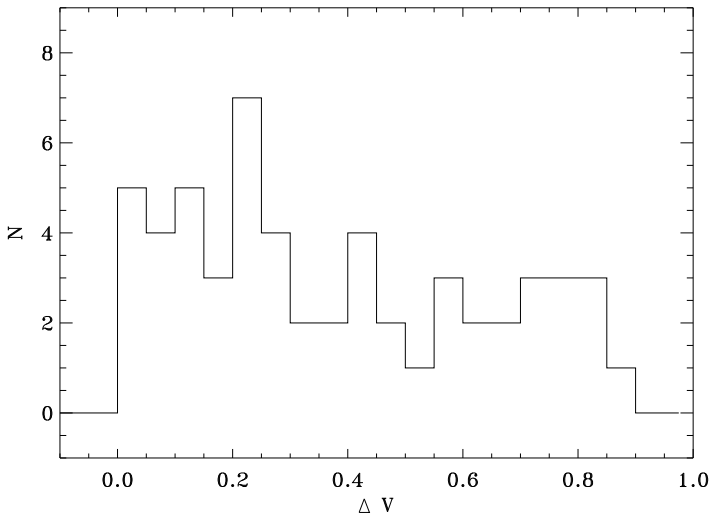

Figure 5.1: Histogram of the visual magnitude difference between components of the binaries.

declination $\delta >$ -20 to be observable from Canary Islands.
Projected separations are in the range 40-1000 AU (see Figure 5.2). In our systems, dynamical stability for a planet up to 20-30 AU from the star is possible according to the simulations of Holman and Wiegert (1999).
We excluded from the sample known spectroscopic binaries, stars with known additional companions within 2 arcsec and stars of spectral type earlier than F7, because their spectra have too shallow features to perform high precision RV measurements.

5.2.2 Sample characteristics

All the stars in the sample appear to be normal main sequence stars. The mean visual magnitude is V=8.7. The magnitude vs. color difference between components of the pairs indicates that the selected binaries are composed of similar stars, as expected.
Stellar masses, calculated from the table by Gray (1992) yield values for the masses of the stars in our sample in the range 0.60–1.25 $M_{\odot}$. Results from the M_V vs. stellar mass and (B-V) vs. stellar mass relations after averaged, yield values for the masses of stars in our sample in the range $0.68 \lesssim M_{\odot} \lesssim 1.25$.
Strömgren photometry from the catalog of Hauck and Mermilliod (1998), when available for the stars of the sample, was employed to estimate metallicities using the calibration of Schuster and Nissen (1989). However these results were recal-

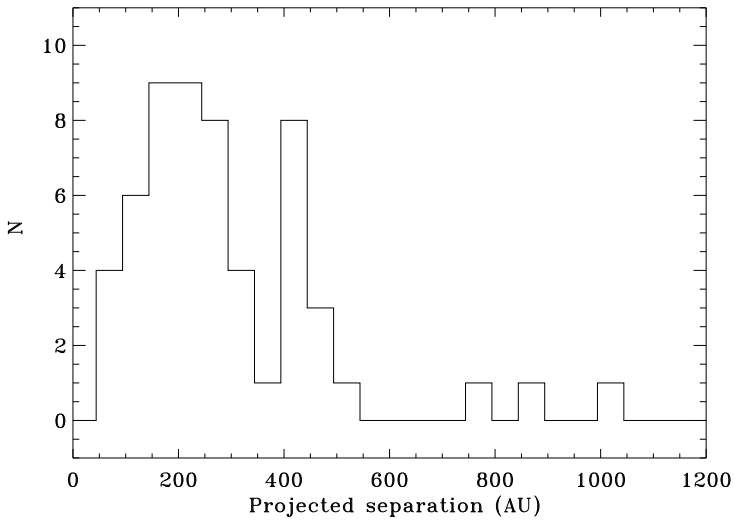

Figure 5.2: Histogram of the projected separation between components of the binaries.

ibrated following Gratton et al. (1997) by a constant offset of 0.102 dex. The rms for individual stars of this metal abundance is of 0.151 dex. The metallicities measured from our high resolution spectra of the 23 pairs in Desidera et al. (2004c) lie in the range -0.195 $\leq$ [Fe/H] $\leq$ +0.267.
Some moderately active stars were kept in the sample for the purpose to study in detail the RV variations related to activity and their diagnostics.

5.3 Survey status

5.3.1 Observations and spectra characteristics

The spectra, taken since September 2000, have a resolution of $R \sim 150000$; they cover the spectral range 4580 Å - 7900 Å in 55 echelle orders, with S/N values per pixel in the range 50 - 200 depending on stellar magnitude and observing conditions. They were acquired with typical exposures times of 15 minutes in order to avoid too large uncertainties in the timing of the mid-exposure of observations. The lowest S/N corresponds either to the faintest stars or to not optimal observing conditions. Slit width was set at 0.27 arcsec (the smallest value available with SARG), much smaller than the typical seeing Full Width Half Maximum (FWHM)[1]. The slit was oriented perpendicular to the stars separation to mini-

[1]It can be shown that adoption of the highest possible resolution yield the smallest error in the radial velocities and bisectors measured using the Iodine cell technique, even if more

mize light contamination by the companion. Furthermore, an autoguider system, viewing the slit by means of a detector and with its wavelength response peaked at the wavelength of the Iodine cell lines, is employed, keeping the instrumental profile stable and fairly independent of illumination effects. Guiding is generally performed using the image of the binary companion on the slit viewer.
The stellar spectra without the Iodine features used as templates for the RV determination, were acquired between the two B star (or flat lamp) plus Iodine cell exposures (see next sub section), to derive instrument profile as close as possible to the template spectra. Additionally, a star plus Iodine cell was acquired after or before the templates acquisitions, reducing overheads due to telescope pointing.

5.3.2 Data analysis

Data reduction is performed before the following observing run to optimize the observational sequence depending on results. Spectrum extraction and calibration is performed in a standard way using IRAF[1].
High precision radial velocities are measured on these spectra with the AUSTRAL code (Endl et al. 2000) as described in Desidera et al. (2003).
The Iodine cell technique includes the acquisition of spectra from a featureless source (a fast rotating B-star or the flat field lamp) taken with the Iodine cell inserted in the optical path (Butler et al. 1996). This kind of spectra is necessary only for the deconvolution of stellar templates (taken without the cell), but they were acquired also in most of the observing nights of the survey to monitor instrument performances. They are extensively used for the removal of Iodine lines (see Chapter 6).
The results, with internal errors of about 3 m/s for standard stars and 5 m/s for program stars, indicate that SARG allows to achieve a RV precision similar to the best instruments worldwide[2].

photons are lost in the slit entrance. In our observations a further advantage is given by the possibility to minimize the contamination by the companion.

[1]IRAF is distributed by the National Optical Observatory, which is operated by the Association of Universities for research in Astronomy, Inc., under contract with the National Science Fundation.

[2]A series of spectra of Procyon taken for a different program (asteroseismology) shows that RV with precision better than 1 m/s can be attained with SARG (Claudi et al. 2005)

5.4 Results and future perspectives

During the first years of the survey each object was observed the maximum possible times per year, at least in the cases of suitable observing conditions (good weather and no technical problems) and prompt identification of targets with short term variability were obtained. These targets are currently being observed with the required frequency to understand the origin of the radial velocity variation and in case of Keplerian motion to derive precise orbital elements.
From the original stellar sample, including about 100 objects, 78 objects have now more than ten values of the radial velocities measured. Within this subsample, 6 have a very low false alarm probability (FAP < 0.05)[1], thus a high probability that the best Keplerian curve given by the radial velocities is not a random result but may indeed correspond to the effect of a substellar companion. A statistical analysis of the excess of stars with low values of the FAP shows that we may conclude that at least three stars within the observed sample have statistical significant periods. However to achieve a relevant significance of the Keplerian curve for each given star additional spectra are required. These data will be obtained in the next observing seasons, giving priority to the best candidates.
There is an estimation of upper limits on planetary companions compatible with the data, derived for all the surveyed stars as in Desidera et al. (2003). The procedure, based on a Monte Carlo approach, considers circular and eccentric orbits. This calculations can be used to evaluate statistically the null detections up to now in the survey, in terms of lower frequency of planets around binaries. In Figure 5.3 appear the results of the upper limits for the case of circular orbits. As stated above, chemical abundances and differences were studied for 23 pairs of the binaries and mesurement of the other pairs is in progress. Note that the technique used for the differential analysis is not optimal for the determination of absolute metallicities.
The null planet detection up to now in the survey is becoming not compatible (currently at slightly more than 1σ level) with the planet frequency derived for general samples composed mostly of single stars (e.g., Fischer and Valenti 2005). A statistical confirmation of this results require more data, as the upper limits on planets masses compatible with the data depend on the number of data itself and the temporal baseline.
If confirmed, this result would imply a lower frequency of planets around wide binaries with similar components. A similar result is emerging from preliminary results by Eggenberger et al. 2005 (ESO workshop in press), focused on different types of binaries and then complementary to the survey SARG.

[1] A Scargle periodogram analysis is employed, that allows a reliable and faster estimation of the False Alarm Probability, which is determined using a bootstrap approach.

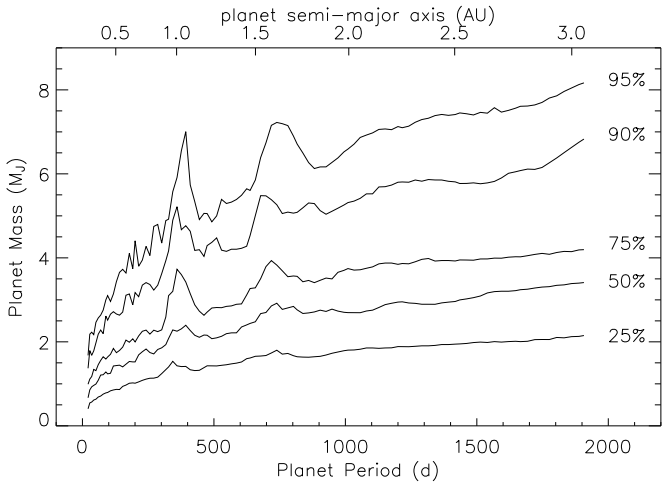

Figure 5.3: Summary of the upper limits estimations for the stars with at least 10 observations. For each period, the mass of the upper limits of 25%, 50%, 75%, 90%, and 95% of the stars is shown for the case of circular orbits.

Is worth to mention that a statistically significant demonstration of a lower frequency of planets around binaries would represent the full achievement of the main scientific goal of the survey project, even in the case of null planet detection.
Of the 78 objects with enough observations for a preliminary analysis of the radial velocity curve 44 have detailed analysis of spectral line bisectors in order to study the reliability of their radial velocities done within the present study. A few cases present a correlation between the RV and the line bisector, due to stellar activity or to contamination by light from a resolved stellar companion and an unresolved stellar companion.
As described in Chapter 4, the measurement of line bisectors and the search for correlation between radial velocities and line profile variations is a powerful tool to identify spurious RV variations due to stellar activity and not to Keplerian motion. Furthermore, line bisectors can be used also to identify spectra with significant contamination by the companion, an important issue for our survey because all the targets are visual binaries. Therefore, we developed a tool to measure the line bisector of average absorption profiles from the stellar spectra, which is described in detail in the next Chapter.

Chapter 6

Line bisectors from the stellar spectra

As discussed in the previous chapters, the analysis of line bisectors is a basic tool to study the origin of RV variations measured on stellar spectra. In this chapter we will present our original analysis procedure, that allows to measure line bisectors from the same spectra used for the RV determination. This has several advantages with respect to use specially acquired spectra:
(1) No additional observing time is required.
(2) The line bisector data are simultaneous with the RV ones.
(3) The Iodine cell provides an accurate wavelength calibration, removing uncertainties due to various causes (slit illumination, light and pressure variations, etc.) Additionally, line bisectors are much more powerful to understand the cause of RV variations than other, more indirect observables (like activity indicators), because they are strictly related to the same data (the profile of the spectral lines) used to measure radial velocities. For instance contamination by the companion can be revealed by line bisectors, but cannot be obtained from activity indicators. On the other hand, obtaining line bisectors from spectra taken through the Iodine cell requires a special technique.
This task is accomplished by a dedicated code developed under Interactive Data Language (IDL) that removes the Iodine lines from the stellar spectra, cross correlates them with a suitable mask of lines obtained from a solar catalogue, adds the computed profiles to get an average absorption profile from which finally, the line bisector is computed.

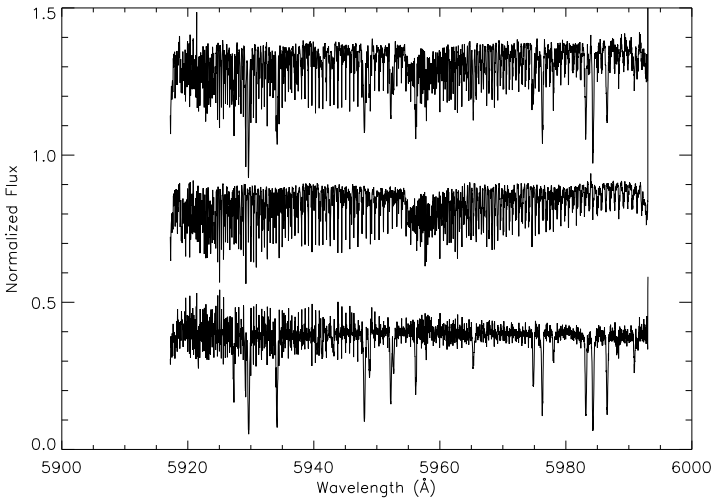

Figure 6.1: A spectral order of HD 166435. The spectrum on top corresponds to the target star with Iodine lines, in the middle is the spectrum of the B-star with Iodine lines and on the bottom is the target star spectrum after the division by the B-star spectrum. The division was computed for the whole order: the poor result is due to errors in the wavelength calibration along the order. In this case the Iodine lines are better removed in the right half than in the left half of the order.

6.1 Data analysis

6.1.1 Reading and handling of the spectra (removal of Iodine lines)

As a first step, the code reads the FITS files and extracts from the headers the spectral information needed to characterize the spectrum, namely: the order number, the starting wavelength, the step or pixel size for this order and the number of points determining the order length.
To handle the spectra, every order is divided into 7 chunks of 500 spectral points each, corresponding to a wavelength width of $\sim 10\,\text{Å}$, overlapped by 60 points ($\sim 1\,\text{Å}$) to eventually recover any absorption lying at the edges. The procedure of cutting the spectra in pieces is advantageous, because the division of complete orders displayed not optimal results, related to errors in the wavelength calibration of the spectra (see Figure 6.1).

The Iodine cell lines, superposed to the stellar spectrum for wavelength calibration and RV determination, must be eliminated because the line bisector is intended to study the asymmetry features of the stellar spectral lines only. For this task, the featureless spectrum of a fast rotating ($\geq 200\,\text{km}\,\text{s}^{-1}$) B-star is employed. The analysis is performed only for the wavelength range where reasonably

strong Iodine lines appear in the spectra (5036 Å - 6108 Å along 21 orders, corresponding to 147 chunks).
A cross correlation is computed between the chunks of the B-star and the program star, to determine the offset in wavelength between the Iodine lines common to both spectra. The B-star flux is adjusted to the new wavelength scale, adding or subtracting the offset previously determined, by using a Hermite spline interpolation (INTEP, see Hill 1982). Finally the chunks of the star spectrum are divided by the chunks of the B-star spectrum and the result is the stellar spectrum without the Iodine features (see Figure 6.2).
However, in some cases the offsets determined by this procedure are very different than the overall values for a spectral order, due to noisy chunks, cosmic rays (spikes) or defects in the spectrum. This results in poor removal of the Iodine lines. To overcome this problem, offsets computed along every spectral order are compared each other; then a "clipping" sub-routine is applied to check for outliers and those discrepant values (with a difference greater than 2σ with respect to the remaining chunks) are replaced by the median value of the reliable offsets computed first (see Figure 6.3).
Spikes due to cosmic rays or hot pixels were removed by replacing the spectral values within them by the averaged flux of adjacent spectral points [1].
The resulting S/N was determined by: $((N/S)^2_{star} + (N/S)^2_{B-star})^{-1/2}$, leading to values generally between 65 - 300. The S/N of these spectra is generally very close to that estimated from the photon flux, showing that the adopted procedure efficiently removed the Iodine lines without reducing significantly the quality of the observational material. This is possible because the B-star spectra have generally high S/N[2].

6.1.2 The cross correlation function (CCF)

Once the spectra were "cleaned" from the Iodine lines and accurately calibrated in wavelength using the same Iodine lines, they are ready to be used to estimate the line bisectors. These could be derived from individual lines. However the S/N of our spectra is generally not high enough for such an analysis. We may however improve the S/N of the line profile by combining data for several lines. While

[1] The S/N for each spectrum here is simply the square root of the number of photons detected within each pixel.

[2] It must be noticed that the offset between the program spectrum and that of the B-star is not constant along one order (even in RV). This is due to a scale factor, likely related to temperature and pressure variations in the spectrograph, that causes variations in the dispersion given by the echelle grating. Note however that the Iodine lines allows to calibrate properly each spectrum, so that accurate radial velocities and line profiles can be obtained.

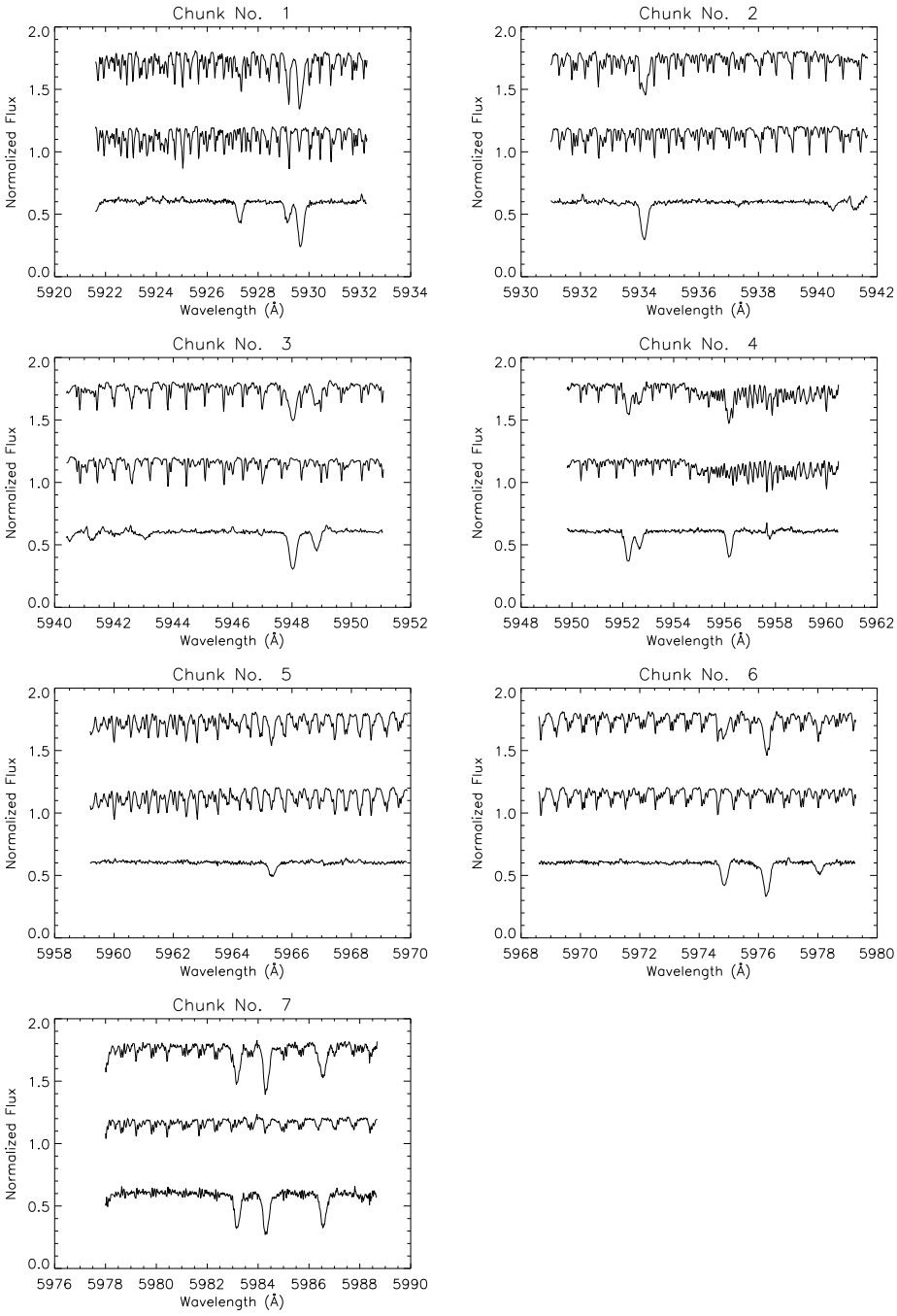

Figure 6.2: The same protion of a spectrum of HD 166435 (wavelength range 5921 - 5989 Å) shown in Figure 6.1. The order was divided into 7 chunks. The spectra are shifted arbitrarily in flux to show: on top the stellar spectra with Iodine lines, in the middle the B-star spectra (adjusted to the wavelength offset) with the Iodine lines and on the bottom the clean stellar spectra after dividing the target star spectrum by the B-star spectrum. Note the noisy chunk No. 7 and see Figure 6.3.

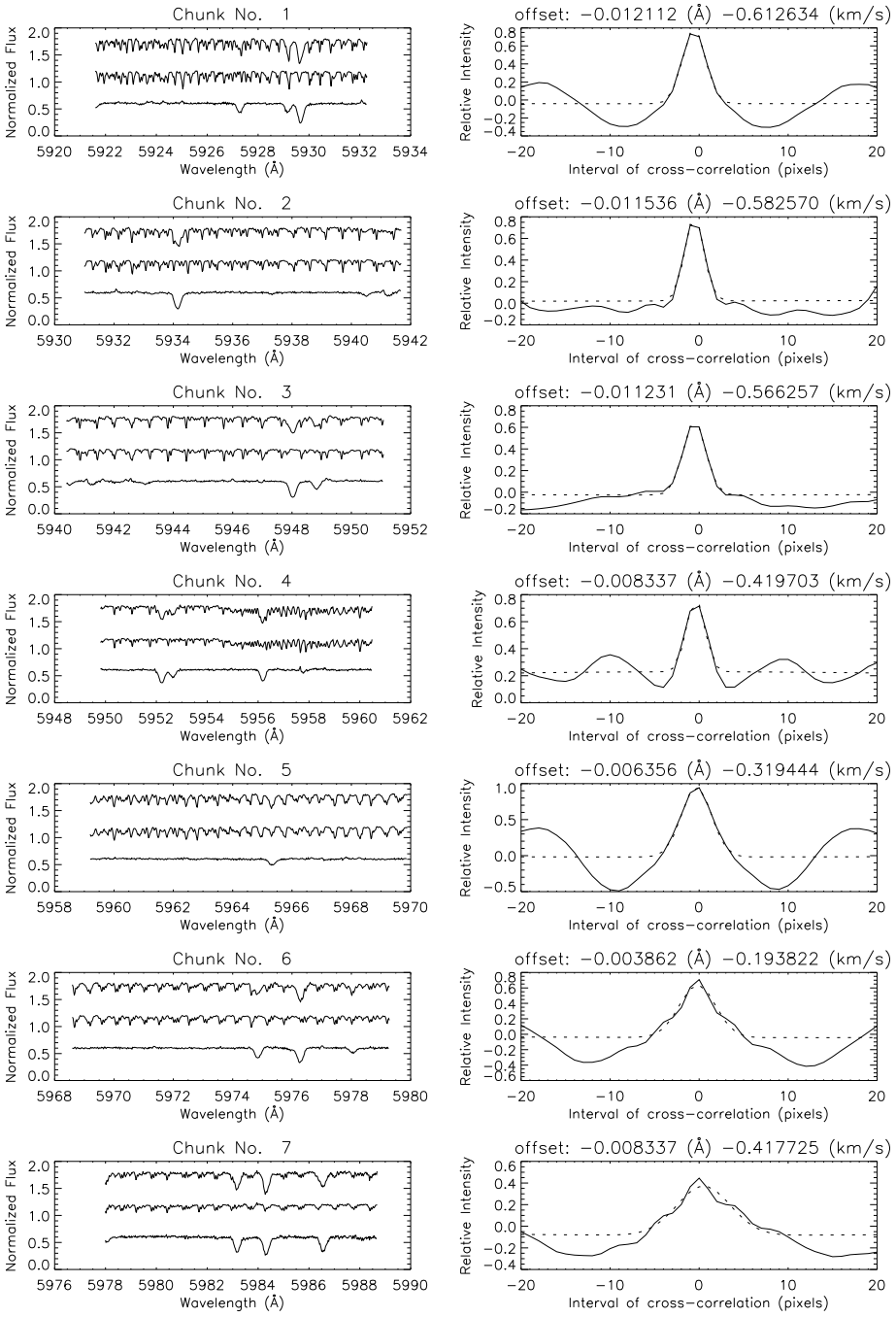

Figure 6.3: In the left column is the same spectrum of HD 166435 shown in Figure 6.2. In the right column appear the cross correlation computed between the B-star spectrum and the star spectrum. The dotted line is the Gaussian fit computed to determine the offset (maximum) to adjust the B-star spectrum wavelength scale before the division. The offset expressed in wavelength and velocity appears in the top of every window. The clipping sub-routine was active to check for outliers. Note the quality improvement of the Iodine removal in chunk No. 7, compared with the case without the clipping in Figure 6.2.

this complicates the physical interpretation of the profiles, it still contains the full data required to discuss their temporal variations. In order to combine data for many lines, we used the cross correlation function (CCF) obtained by cross correlating the observed spectra with masks obtained by suitable lines lists using the same approach considered by Queloz et al. (2001). Since these templates are mathematical functions they do not add noise to the data.

6.1.2.1 The solar catalogue and line selection for the mask

The list of spectral lines by Moore et al. (1966) was used to prepare the spectral mask needed for the computation of the CCF. A preliminary line list was obtained by selecting those lines that do not have possible contaminants (wavelength separation $\gtrsim 0.1$ Å), and have reduced width between 3 and 30 F. F (Fraunhofer) is defined as the dimensionless quantity $\Delta\lambda/\lambda \times 10^6$, where $\Delta\lambda$ is the equivalent width (see Moore et al. 1966). The range of reduced width chosen here corresponds to a range of central line depths from 0.14 to 0.75 in continuum units (in the solar spectrum). The CCFs derived, thus represent average profile for lines of intermediate strength.
Once a preliminary list of lines was determined for the wavelength range of interest (5036 Å to 6108 Å), a further selection was made by inspecting the "The Sacramento Peak Atlas of the Solar Flux Spectrum" (Beckers et al. 1976). Lines were labeled according to their appearance: "y" (*very good*): sharp, clear, with weak wings; "y:" (*good*): clear but near other lines altering their wings; "?" (*not very good*): with small blends or strong wings. Many other lines, blended or too close to other spectral lines, were removed from the list. The full list of lines used in the present analysis is given in the Appendix A. In Figure 6.4 is shown the histogram of the distribution of line strengths on the Solar spectrum. The mask used to compute the CCF is a sum of δ-function profiles corresponding to 1 for the line wavelength, with a base of two (spectral) points, and 0 elsewhere. The extensive line list (including *very good*, *good* and *not very good* lines: a total of 412 lines) are used to determine the centroid value of the average absorption profile obtained by the CCF. It corresponds somehow to a local minimum, indeed a RV not corrected to the barycenter. Once this point is established, which helps to properly locate the profiles for the addition, a new computation of the CCF is performed only with the *very good* lines (113 lines) to obtain an improved average profile, to calculate reliable average line bisectors (see Figure 6.5).

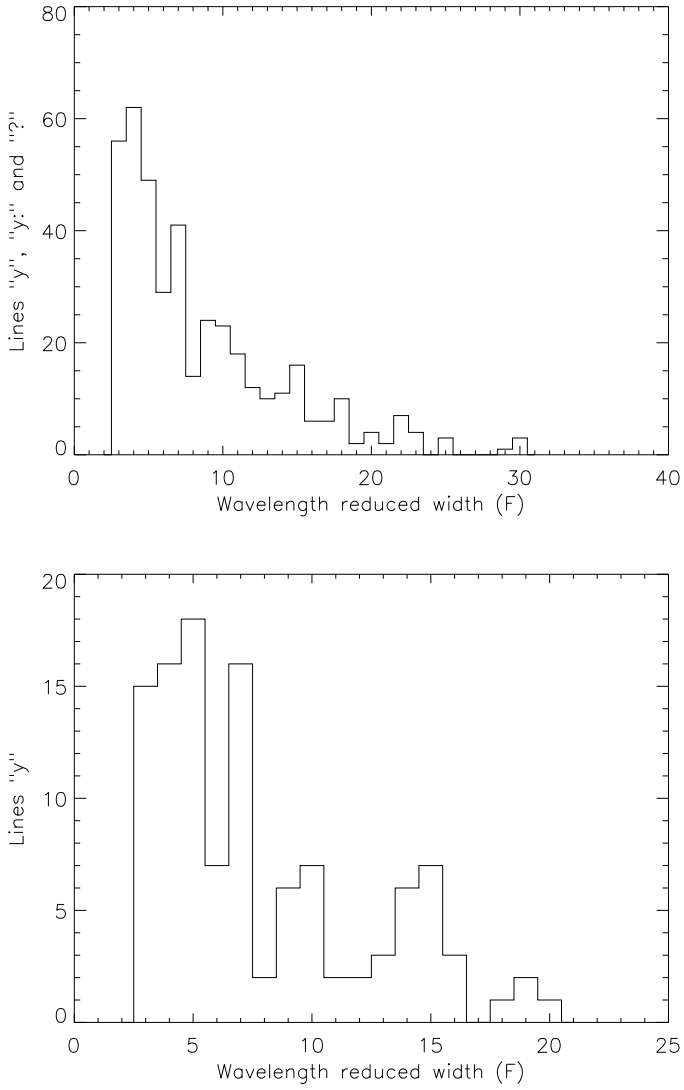

Figure 6.4: Distribution of line strength on the solar spectrum. Number of lines and wavelength reduced width (Fraunhofer). In the upper panel is the histogram for all the lines (including *very good*, *good* and *not very good*). In the lower panel is the histogram only for the *very good* lines.

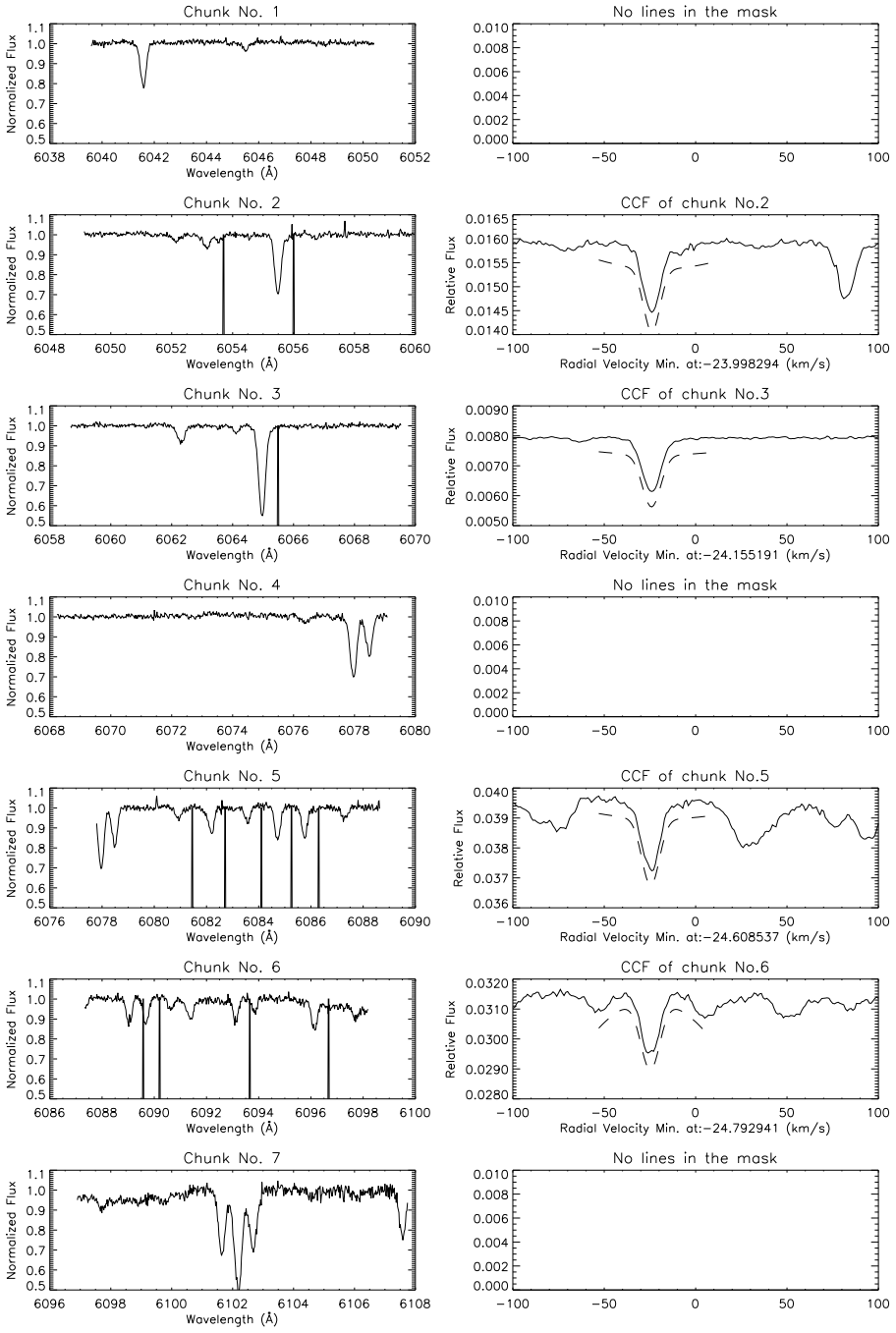

Figure 6.5: An order of a spectrum of HD 166435. The left column shows chunks of the spectrum, after removal of the Iodine cell lines. In the same windows appear the mask used for the determination of the CCF (only lines classified as *very good* are shown here). It is made of a sum of $\delta-$functions centered on the rest wavelengths of the selected lines. Note the wavelength shifts between the stellar lines and the mask peaks due to the non-zero RV of the star. The CCF for individual chunks computed by cross-correlating the spectra with the masks given on the left panels are shown in the right panels. The dashed lines, shifted slightly below the profiles for clarity, represent the Gaussian fits computed to determine the local minima of the CCF for each chunk. There are no CCF profiles for chunks 1, 4 and 7 due to the lack of suitable lines for the mask in these wavelength ranges.

6.1.2.2 The cross correlation and addition of profiles

A cross correlation between the mask and the stellar spectrum is computed for each chunk; the addition of all these cross correlations give the average profile. Due to the relatively low S/N of some spectra, use of the average of many lines is appropriate for study the variations of line bisectors with time. On the other hand, the actual line bisector depends on the line depth, so that the "average" line bisector does not rigorously correspond to the line bisector of a line with similar depth of the CCF. Therefore, the use of the average profile would be misleading for some scientific goals such as the study of convection in stellar atmospheres.
Due to different illumination of the CCD, each chunk along an order has different flux values, those close to the center of the orders being more luminous and yielding then results of higher S/N (see Figure 6.6). To account for this, before summing the individual cross correlations, each of them was multiplied by an appropriate weight, proportional to the instrumental flux at the center of the chunk. The weights were determined by the flux recorded in a central order of the echelle spectrum, namely: $w_1 = 1.08$, $w_2 = 1.26$, $w_3 = 1.36$, $w_4 = 1.24$, $w_5 = 0.98$, $w_6 = 0.67$, $w_7 = 0.41$ (Note that $\sum_{i=1}^{7} w_i = 7$, the number of chunks) (see Figure 6.6).

Once adjusted to a common reference frame, which may be thought of as a centering procedure, and multiplied by its weight, all CCF profiles are added to get the final profile for the spectrum. This is normalized to determine the finally adopted average line profiles using the reference continuum determined in the IRAF reduction. This is obtained by interpolating a polynome throughout the spectra with a suitable clipping rejection procedure. Note that this reference continuum may contain significant errors, so that there may be points in the normalized CCFs that are well above unity. However, all procedures are kept strictly uniform throughout the analysis of different spectra; then it is expected that these errors in the location of the reference continuum mainly affect absolute profiles and bisector estimates, but only marginally their spectrum-to-spectrum variations, which are of interest for the present discussion.

6.2 The line bisector calculation

The bisector of an absorption line is the middle point of the horizontal segment joining points on the left and right sides of the profile with the same flux value. The line bisector is obtained by combining bisector points ranging from just above the core toward the wings of the line.
To determine the bisector of an absorption profile it is necessary to adjust the ordinate axis of the profile to a convenient scale and to determine the values in

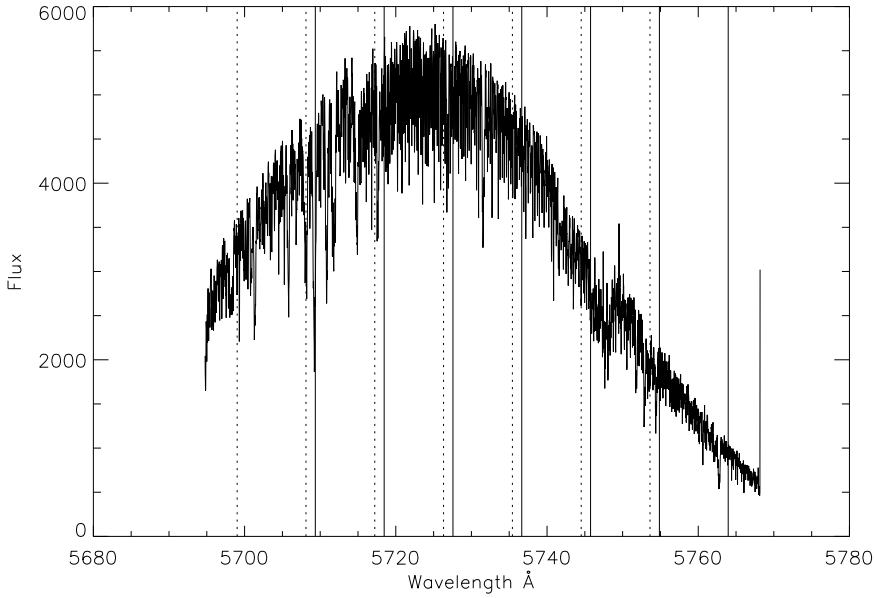

Figure 6.6: A spectral order close to the center of the echelle from a spectrum of HD 166435. Dotted and solid lines indicate the beginning and ending, respectively, of the chunks. Due to the blaze function of the echelle grating, chunks 2, 3, and 4 near the maximum have the greater weight values.

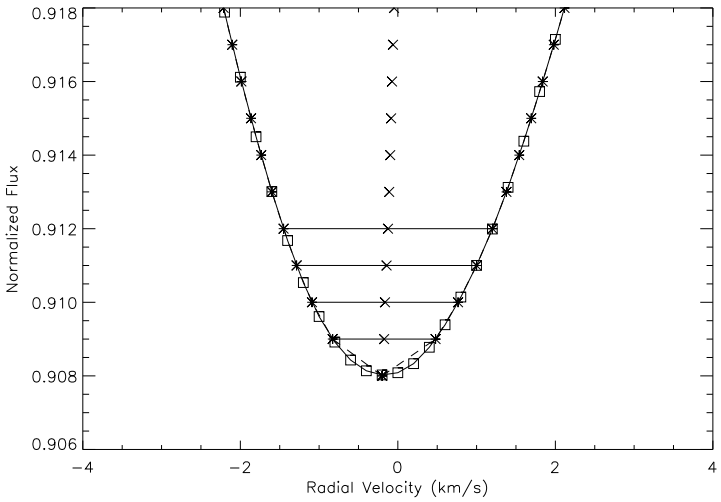

Figure 6.7: Spectrum of HD 166435. Construction of line bisector. Empty squares joined by the solid line, correspond to the normalized cross correlation profile. Asterisks joined by the dashed line, correspond to the interpolation computed to deal with a convenient flux scale. The bisectors are the crosses in the middle of the horizontal lines (for the first four cases) joining the left and right points of the profile.

velocity belonging to the left and right points for a given flux value. This is accomplished by interpolating (using INTEP, see Hill 1982) the absorption profile to the desired scale.
The code performs the interpolation by halves; for the left half of the profile, all velocity points are determined for a flux scale ranging from a high arbitrary point between the wings and the normalized continuum, toward the minimum flux point in steps of 0.001. For the right half, the interpolation determines the velocity points to the flux ranging from its minimum value toward the high arbitrary flux (set before in the left side computation) in the same amount of steps. Then the code verifies which values in velocity correspond to each value of flux being analyzed, the center between these is established as the bisector point (see Figure 6.7).

6.3 The bisector velocity span

The line bisector presents particular features to be studied, the slope and the curvature.
In the absorption profile there is a high zone near the wings and a low zone above the core which represent interesting places to study the velocity given by the bisector. These zones are located between initial and final flux values: (top_i, top_f) for the Top and (bot_i, bot_f) for the Bottom (see Figure 6.8).
The difference of the average values of velocities in the Top and Bottom zones, V_T and V_B respectively, determine the bisector velocity span (BVS) (see Toner and Gray 1988).

6.4 Error determination

Errors in our estimates of the BVS were obtained as follows. We start with the expression given by Gray (1988) to determine the bisector error coming from photometric error:

$$\delta V = \frac{1}{\sqrt{2}}\,\delta F/(dF/dV), \tag{6.1}$$

where δV is the wavelength error in velocity scale, δF represents the photometric error of the flux F, dF/dV yields the slope of the profile. The factor $2^{-1/2}$ comes from assuming that the errors of each side of the profile are the same, which gives a $2^{1/2}$ increase over the error of one side, but since the midpoint of the line segment is the bisector point, this error is cut in half.

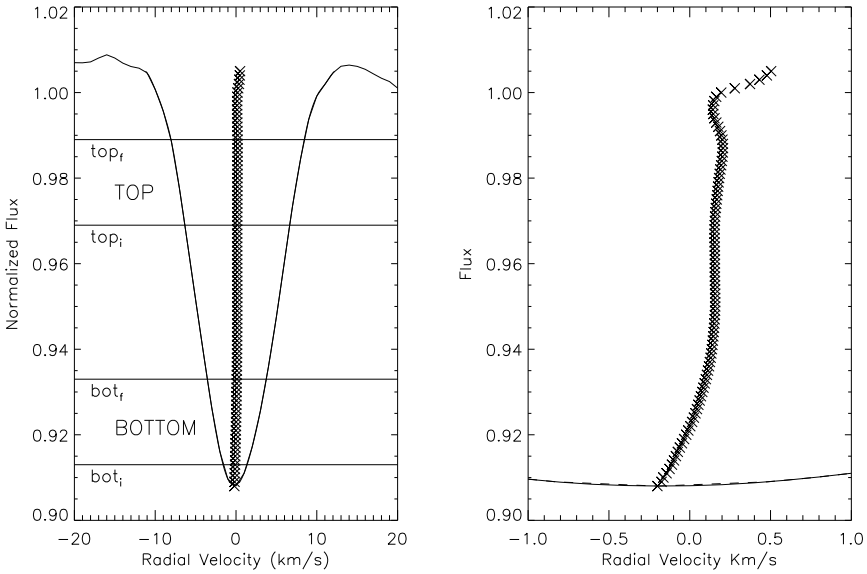

Figure 6.8: Spectrum of HD 166435. In the left panel we showed the normalized cross correlation profile, the line bisector, the top and bottom zones where $\Delta F = top_f - top_i = bot_f - bot_i$ (see text). In the right panel we showed a zoom of the profile with the RV scale increased to better display the asymmetries of the line bisector.

To determine an expression for the photometric error first consider in a spectrum the following quantity:

$$\frac{1}{\frac{S}{N}\sqrt{F}} \tag{6.2}$$

which gives the noise in the zone of an absorption line. The quantity

$$\frac{\Delta F}{x\frac{dF}{dV}} \tag{6.3}$$

gives a fraction of pixel, ΔF being the interval flux where the bisector is being computed and x represents the linear dispersion of the spectrograph. Thus the final expression for the photometric error becomes

$$\delta F = \frac{1}{\frac{S}{N}} \frac{1}{\sqrt{n\frac{\Delta F}{x\frac{dF}{dV}}F}} \tag{6.4}$$

which depends on the number of lines n employed in the mask for the CCF. Replacing this equation in equation 6.1 gives the expression

$$\delta V = \left(\frac{S}{N}\right)^{-1} \left(2nF\frac{\Delta F}{x}\frac{dF}{dV}\right)^{-1/2}, \tag{6.5}$$

where F is the central flux of the zone of analysis (Top or Bottom, see Figure 6.8) and x is 1.04 $\mathrm{km\,s^{-1}pix^{-1}}$ for the specific case of SARG.
In this manner it is possible to compute the errors for V_T and V_B from the absorption profile and set an appropriate error bar for the BVS by assuming that this is given by $\sqrt{\delta V_T^2 + \delta V_B^2}$ (see Figure 6.8).

6.5 Instrument profile asymmetries

The instrument profile IP was determined by AUSTRAL as part of the RV determination and line bisectors were computed from it as for stellar spectra. This was done to determine to which extent the asymmetries and the BVS computed for stars were real and not an instrumental effect.
Generally the IP shows line bisector variations but these are typically much smaller than the errors in the line bisectors determined from the stellar spectra. Corrections due to asymmetries of line profiles require complex convolution, which should take into account the real stellar profile. Actually, since the IP is much narrower than the intrinsic stellar line profiles (the case of SARG spectra), corrections due to IPs are much smaller than the IP asymmetries themselves. Therefore corrections to the stellar BVS were not considered.
This subject will be discussed in more detail in the next chapter for the specific case of HD 166435.

6.6 Error analysis

An analytic study of errors can be performed starting by considering the rms of BVS errors. The expected errors of BVS are computed for absorption profiles obtained by "theoretical profiles", computed from convolution of Gaussian and rotational profiles. The former are determined with a thermal broadening and a macroturbulence factors estimated from the colors (B-V) and then temperatures of each star, the latter with a v sin i factor determined by the Fast Fourier Transform (FFT) analysis of each star's absorption profile (Gray 1992).
To determine the v sin i, the observed profile of a star is made symmetric by mirroring one of its halves, with the purpose to reduce the noise of the FFT. A new profile is calculated by the convolution of a macroturbulence profile (Gaussian) and a rotational one, to compare the FFTs of the symmetric and the calculated (model) profiles. In this manner it is possible to determine the projected rotation velocity of stars.
The v sin i value of the rotation profile, is set as variable parameter until the first

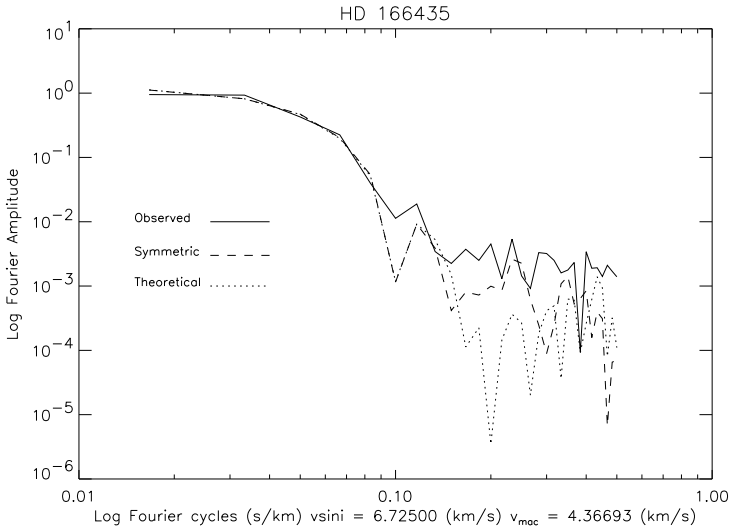

Figure 6.9: The FFT of HD 166435 for three absorption profiles: the solid line for the observed profile; the dashed line for the symmetric profile where the FFT appears less noisy; and the dotted line for the calculated (model) profile.

minimum of the FFT from the calculated profile coincides with the minimum of the FFT from the symmetric one.
Figures 6.9 and 6.10 shows the FFT of the absorption profiles corresponding to HD 166435 and HD 126246A, respectively.

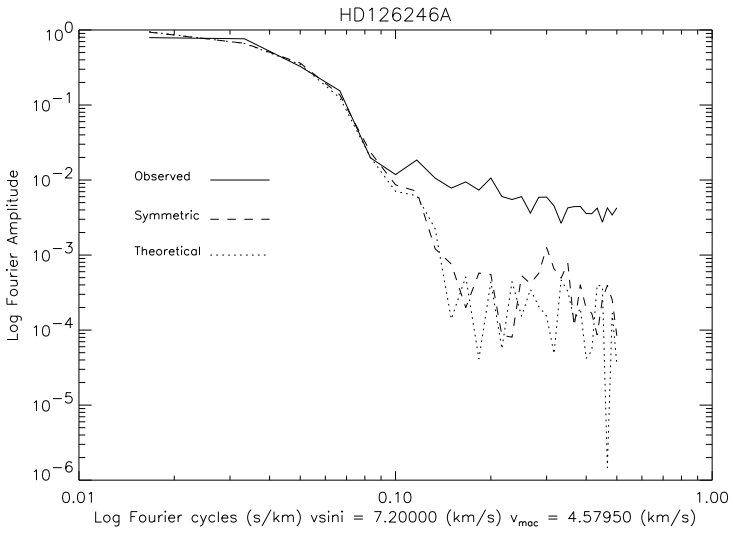

Figure 6.10: The FFT of HD 126246A for three absorption profiles: the solid line for the observed profile; the dashed line for the symmetric profile where the FFT appears less noisy; and the dotted line for the calculated (model) profile.

Chapter 7

Presentation and discussion of the analysis

In the following chapter we present the line bisector analysis for 44 objects from the SARG survey. For this task the most interesting stars were considered through a merit function.

7.1 The stellar subsample

In order to identify the objects most likely to show correlations between radial velocities and BVS, a merit function was employed in the form of $f = (S/N)(rms)\sqrt{N_{spec}}$, where S/N is the median of the signal to noise ratios of the spectra for each star, rms is the root mean square scatter of the measured radial velocities and N_{spec} the number of spectra available for each object.
By this approach the analysis focuses on the cases of stars with better S/N to reduce error bars, larger number of spectra to deal with many points (to see possible trends) and higher RV amplitudes to increase the possibility to see correlations if any.

7.2 Settings of the analysis

To analyze the big set of stars from the subsample and in general for the growing data that will be available during the survey program, it is necessary to define a suitable procedure to perform an homogeneous and consistent analysis for all objects. In this framework, the star HD 166435 is of particular interest, since it is an active star with an established correlation between the RV variation and BVS

due to the change in shape of line bisectors caused by apparent shifts of spots over the surface due to the stellar rotation (see Queloz et al. 2001 and Martínez Fiorenzano et al. 2005).
We have measured the line bisectors from the available spectra of HD 166435 obtained with SARG. SARG is very well suited to show variations of the line bisectors due to the high spectral resolution provided by the spectrograph (R $\sim$ 150000).
To determine the best line fitting the points relative to each observation in the RV-BVS plane, the Top and Bottom zones were moved along the absorption profile scanning the line bisectors. For each couple of Top and Bottom zones we computed values for BVS, and the ratio between the slope m and its uncertainty σ of the best line fitting the relation between BVS and RV. The quantity m/σ is an indicator of the significance of the linear term in the straight line fitting and helps in the diagnostic of the goodness of the fit: i.e., a higher absolute value of m/σ may be interpreted as a highly significant correlation.
The scan of the profile was made considering zones of the same flux width for both the Top and the Bottom region ($\Delta F = top_f - top_i = bot_f - bot_i$); this flux width was set at approximately 25% of the absorption depth (see Figure 6.8).
The fitting procedure started with the Bottom zone at the minimum possible place near the core, and the Top zone above it, separated by an interval of 0.005 in flux. Keeping fixed the Bottom zone, the Top zone was raised in steps of 0.001 in flux, scanning the whole absorption toward the maximum value near the continuum, computing every time the BVS, the line fit and taking account the ratio of slope to uncertainty (m/σ).
Once the Top zone scanned the absorption profile, the procedure started again with both zones, Top and Bottom, raised by 0.001 in flux from the previous positions, with the Bottom zone kept fixed again and the Top one scanning the absorption profile. This procedure stopped in the case where the upper limit of the bottom zone (bot_f) reached the middle of the absorption profile.
After the analysis of 12 spectra of HD 166435, the most significant correlation between the measured radial velocity and BVS was found for the BVS given by the Top and Bottom zones centered at $\sim$25% and $\sim$87%, respectively, of the absorption depth of the average profile given by the CCF (see Figure 7.1).
The above values of absorption percentages, were considered for all objects to establish the Top and Bottom zones, in order to compute the BVS in an homogeneous way for all the subsample and perform a consistent analysis.

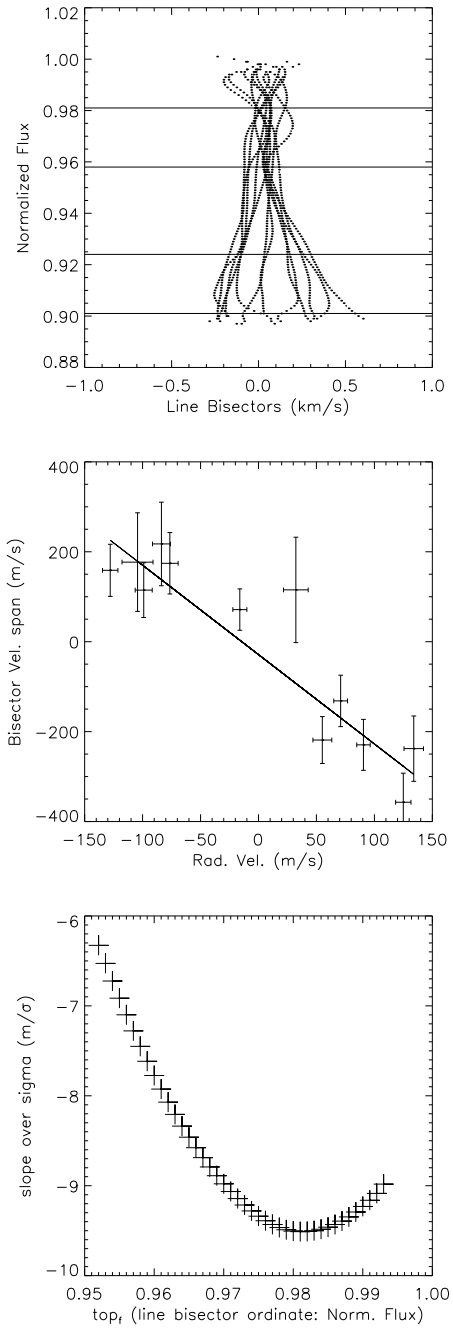

Figure 7.1: In the upper panel are shown the 12 line bisectors computed for HD 166435, the horizontal lines indicate the Top zone at ∼25% of absorption depth and the Bottom zone at ∼87% of absorption depth, where the BVS was computed. In the middle panel appear the linear fit of RV vs. BVS (computed for the zones shown above). The lower panel shows the behaviour of m/σ along the different Top zones considered while the Bottom zone was kept fix. Note that the value $m/\sigma = -9.51$ (for $top_f = 0.981$) corresponds to the maximum, in absolute value, for the configuration shown in the first two panels. It appears negative due to the negative slope of the correlation and allow us to consider this as the configuration which yield the most significant linear fit.

7.2.1 Instrument profile performance

As mentioned in the previous chapter, the instrument profile IP determined as part of the RV measurements was checked to rule out its influence on the observed variations of stellar line bisectors.
Line bisectors were computed from the IP determined for every spectrum in the measurement of RV and the BVS was computed over the Top and Bottom zones determined above.
The radial velocities were computed from portions (chunks) of spectra along every spectral order and line bisectors were then computed for these several IPs. Figure 7.2 shows the line bisectors from the central orders corresponding to three spectra in the analysis of HD 166435. The variation of line bisectors for the IP of a single spectrum is evident; nevertheless it is very small in comparison to the line bisector variation observed from the stellar spectra.
The rms of the observed BVS error in the case of spectra of HD 166435 is 74.5 m/s[1], while the rms of the observed BVS error in the case of the IPs corresponds to 35.4 m/s (see Figures 7.1 and 7.3).
To study further the influence of IP in the line bisectors and BVS variation we performed more checks like those shown in Figure 7.4, looking for trends in the plots of the IP BVS vs. RV, and of the IP BVS vs. stellar BVS. Since no evident correlation can be determined, we neglected hereinafter the influence of the IP on the line bisectors variation.
Is worth to mention that the detailed IP analysis leading us to rule out the influence of the IP on stellar results was carried out for three different stars (HD 166435, HD 8071B and ρ CrB).

7.3 Measurements and statistical analysis

Measurements of line bisectors were performed for all the available spectra of the stellar subsample. The BVS for all stars were computed in the Top and Bottom zones equivalent to those where the most significant correlation was found in the analysis of HD 166435 (i.e., Top centered at ∼25% and Bottom centered at ∼87% of the absorption depth of the CCF profile).
The number of spectra analyzed lies between 7 and 9 for eight stars, more than 20 for five stars and between 10 and 20 for the rest of the stars. Some numbers and computed quantities can be seen in Table 7.1, where the stars appear sorted according to the increasing value of the significance in the non parametric Spearman rank parameter for the correlation between BVS and RV.
For some columns the median was computed, namely:

[1]Computed from the error bars of the second column of Table 8.1 in the next Chapter.

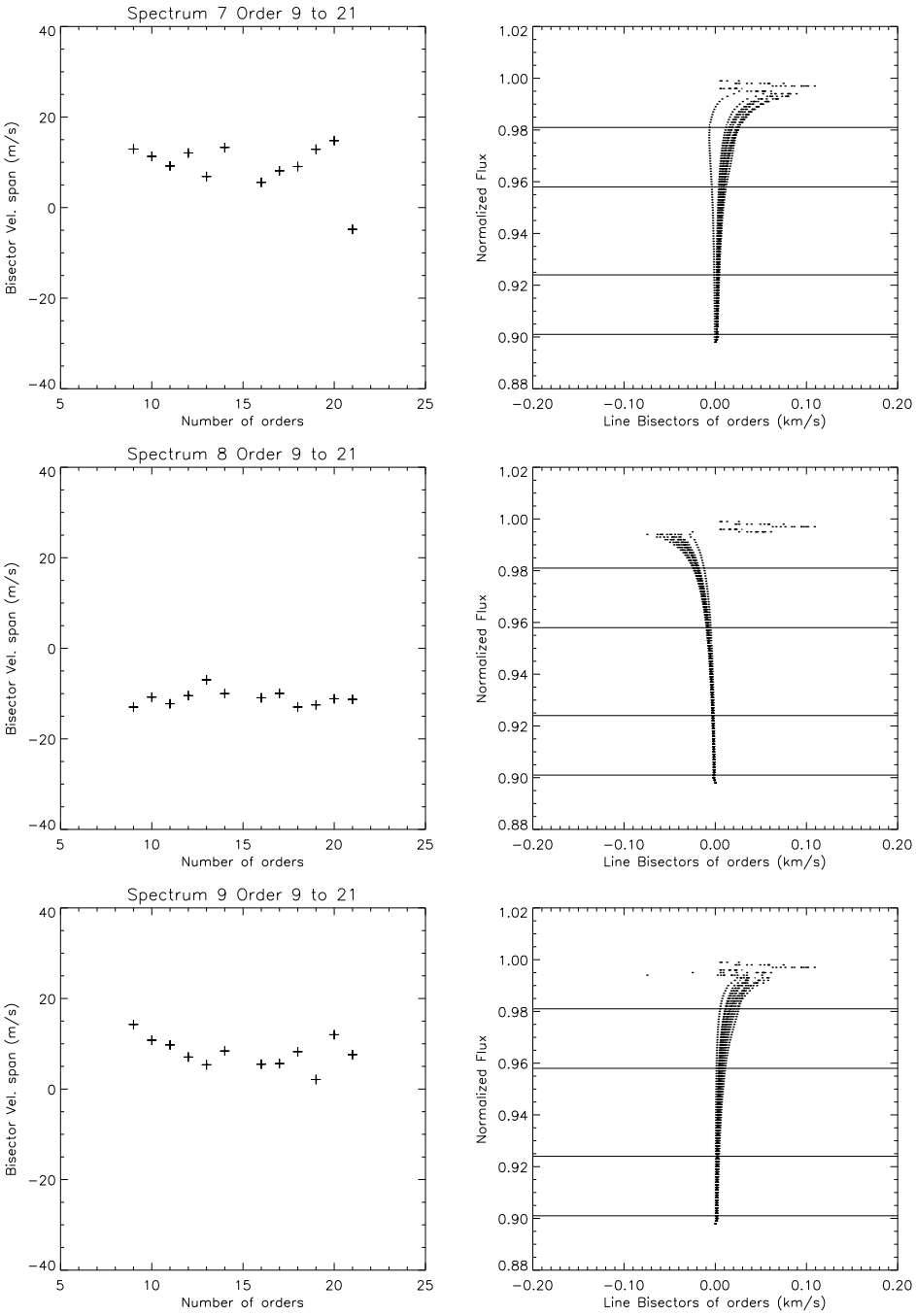

Figure 7.2: In the left column are the BVS computed from the line bisector, given by the sum of IP from the chunks along an order of a spectrum. In the right column are the corresponding line bisectors. A variation of orientation can be seen near the wings (toward the continuum) of the profiles.

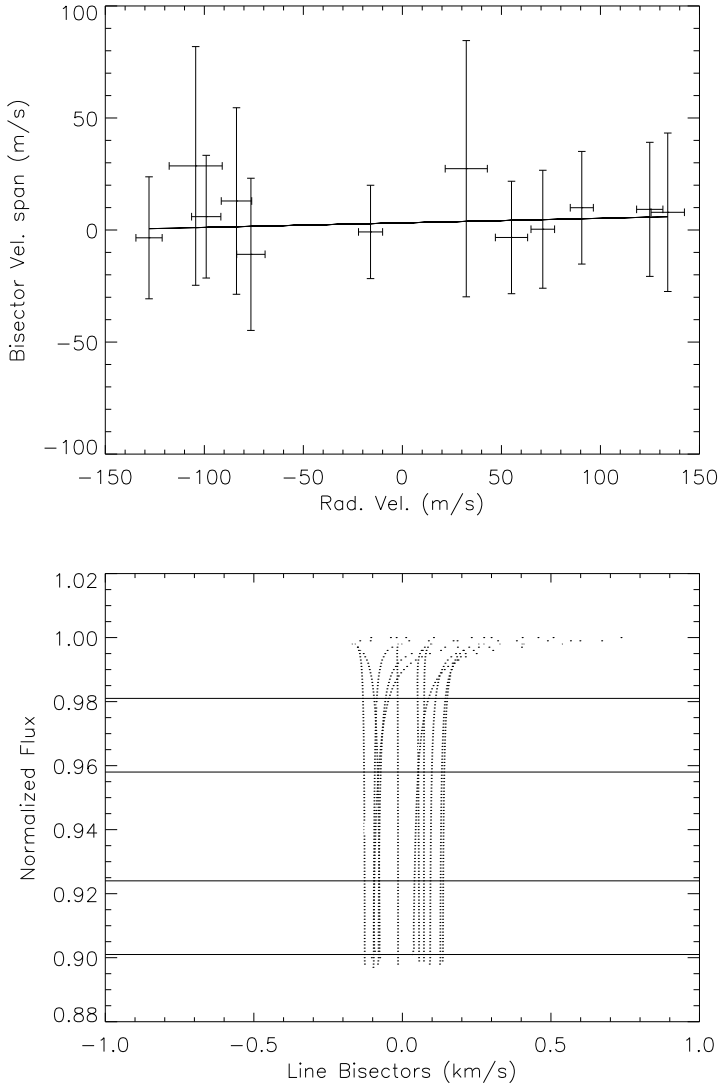

Figure 7.3: In the upper panel is the plot of BVS given by the IP vs. the RV measured from spectra of HD 166435. Error bars for BVS were determined by the rms of BVS itself, divided by the square root of the number of spectra (12). Note the lack of correlation and BVS variation consistent with zero. In the lower panel are the line bisectors computed from the IP of every spectrum analyzed.

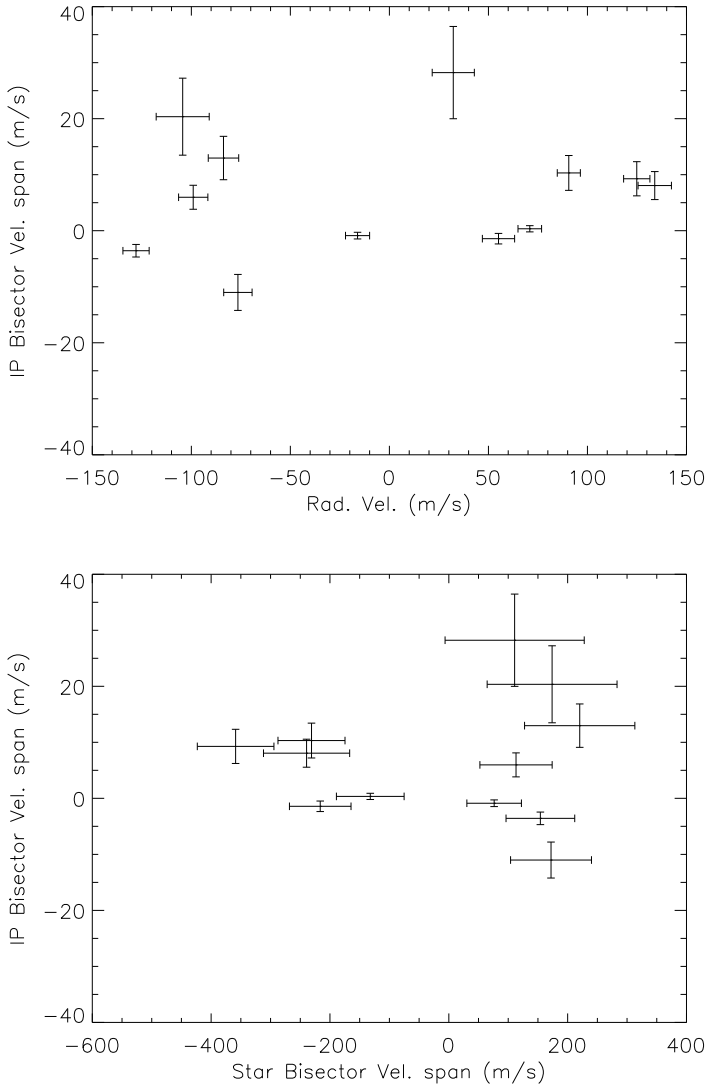

Figure 7.4: In the upper panel is a plot of IP BVS vs. radial velocities of HD 166435. In the lower panel is a plot of IP BVS vs. BVS of HD 166435. No evidence of trends were found.

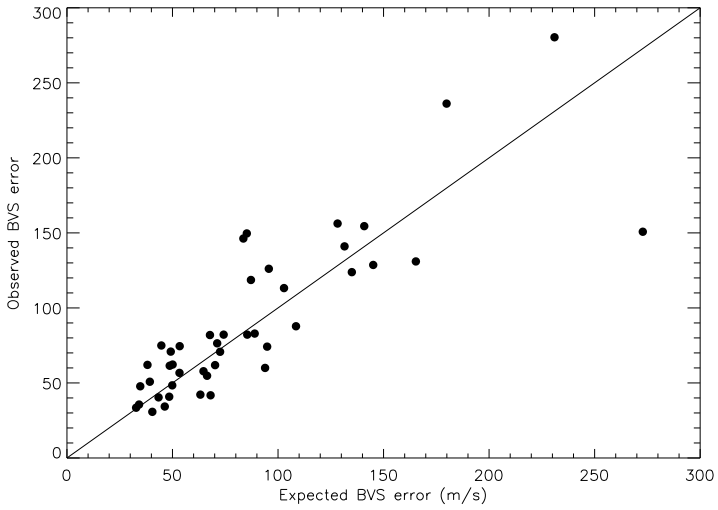

Figure 7.5: Plot of the observed errors of BVS Vs. the expected errors of BVS. The discrepant point, with highest expected error, corresponds to the special case of HD 76037A that will be discussed in Sec. 8.1.5.

Standard deviation of BVS = 70.67 (m/s);
Mean of the ratio of BVS and RV errors = 11.7;
Standard deviation of the previous quantity = 1.7;
rms of the BVS errors = 74.35 (m/s);
rms of the N/S = 73.1.
A comparison between the predicted internal error and scatter of observations for the stars analyzed can be seen in Figure 7.5. The plot of the observed errors of BVS against the expected errors of BVS show a good agreement along the identity line, which indicates the goodness of the model in the errors treatment. The discrepant point with highest expected error, corresponds to the special case of the star HD 76037A that will be discussed in Sec. 8.1.5.
A detailed discussion of these results, its interpretation and significance with a presentation of the most interesting objects, will appear in the next Chapter.

Table 7.1: Relevant quantities computed from the 44 stars of the subsample. The columns correspond to: catalog number; number of spectra; standard deviation of BVS; mean of the ratio of BVS and RV errors; standard deviation of the previous quantity; rms of the BVS errors; rms of the N/S; R is the linear Pearson correlation coefficient; ρ is the Separman non-parametric rank correlation coefficient; the significance of ρ is a value in the interval (0, 1), a small value indicates a significant correlation; the slope-uncertainty (m/σ) relation of the linear fit; the v sin i for rotation; the angular separation (Sep.) between components and the residual spread in RVs (jitter). The stars are sorted by increasing value of significance.

Star	$N_{sp.}$	std. dev. BVS (m/s)	$\langle \frac{\text{BVS er.}}{\text{RV er.}} \rangle$	std. dev. $\langle \frac{\text{BVS er.}}{\text{RV er.}} \rangle$	rms BVS er. (m/s)	rms N/S	R	ρ	Sig.	$\frac{m}{\sigma}$	$v \sin i$ (km/s)	Sep. arcsec	Jit. (m/s)
HD 200466B	18	43.40	11.31	2.49	40.38	81.78	−0.71	−0.70	0.001	−3.01	2.19	4.66	7.0
HD 76037A	16	272.83	16.49	1.69	150.76	84.31	0.71	0.70	0.003	5.03	–	9.80	133.1
HD 8071B	7	48.45	6.87	1.51	40.82	117.62	0.90	0.86	0.014	2.22	1.93	2.18	64.5
HD 126246A	13	102.84	13.77	2.44	113.21	96.28	−0.69	−0.57	0.044	−1.25	7.20	9.31	26.9
HD 209965B	12	44.72	14.39	2.62	74.96	71.57	0.56	0.59	0.045	1.61	$\leq$ 1.0	2.52	22.2
HD 216122B	12	74.24	13.68	5.10	82.19	76.40	0.39	0.57	0.055	1.47	3.05	5.33	19.3
HD 33334B	22	93.87	11.30	2.02	60.01	58.29	0.37	0.39	0.072	1.88	3.20	4.72	16.5
HD 139569A	16	165.31	12.92	2.41	130.97	74.63	−0.45	−0.40	0.125	−2.08	7.65	5.16	23.6
HD 132563A	10	145.10	14.10	3.67	128.63	56.82	−0.42	−0.50	0.138	−1.88	2.85	4.16	13.4
HD 209965A	15	50.06	13.22	2.30	62.26	85.51	−0.39	−0.40	0.143	−0.99	1.55	2.52	19.5
HD 099121A	22	128.22	17.74	1.93	156.23	75.59	0.05	0.31	0.164	0.14	$\leq$ 3.75	2.31	28.2
HD 215812A	11	40.45	11.54	3.10	30.75	131.74	0.43	0.45	0.170	1.71	$\leq$ 1.0	2.18	44.1
HD 108574	9	49.18	14.08	3.20	70.88	96.12	0.39	0.50	0.170	1.05	–	9.81	18.3
HD 099121B	15	140.85	15.87	1.72	154.49	56.11	0.24	0.37	0.177	0.60	2.69	2.31	26.5
HD 128041B	15	49.88	10.51	1.18	48.40	60.20	0.13	0.34	0.211	1.30	1.00	3.02	21.2
HD 66491B	15	71.17	9.46	1.21	76.41	48.01	−0.38	−0.34	0.216	−1.15	$\leq$ 0.9	5.14	25.4
HD 66491A	16	72.55	9.58	1.04	70.76	51.50	0.34	0.32	0.222	1.02	1.40	5.14	18.2
HD 213013A	16	34.73	10.10	1.45	47.77	62.95	0.41	0.32	0.222	0.96	3.00	5.51	11.8
HD 86057A	11	87.17	11.55	1.08	118.62	59.04	0.05	0.39	0.235	0.23	4.98	4.43	19.4
HD 139569B	17	134.97	14.46	2.94	123.84	60.48	0.24	0.29	0.256	1.05	5.00	5.16	26.6
HD 106515B	14	32.77	10.81	1.19	33.49	80.77	−0.49	−0.30	0.296	−1.40	$\leq$ 1.4	6.98	8.8
HD 87743A	13	95.64	10.88	1.53	126.09	42.97	−0.36	−0.31	0.297	−0.25	1.24	9.56	22.7
HD 19440A	11	67.75	14.52	3.43	81.93	88.56	0.27	0.34	0.312	1.24	$\leq$ 2.5	5.97	7.5
HD 76037B	10	230.99	20.22	2.04	280.36	76.29	−0.40	−0.33	0.347	−0.29	–	9.80	45.4
HD 126246B	13	39.27	11.95	1.99	50.81	89.34	0.32	0.28	0.354	0.60	$\leq$ 2.0	9.31	12.2
HD 215812B	13	34.16	11.76	2.70	35.61	106.25	0.47	0.27	0.374	0.76	1.20	2.18	28.6
HD 106515A	14	46.34	11.46	1.40	34.28	83.50	0.30	0.23	0.427	0.51	3.20	6.98	6.6
HD 87743B	12	83.58	10.43	1.08	146.25	42.60	−0.36	−0.25	0.430	−1.38	1.05	9.56	8.7
HD 30101B	20	70.18	13.15	2.55	61.87	60.27	0.21	−0.17	0.478	0.32	2.30	4.63	12.3
HIP 104687B	13	38.15	11.95	1.56	62.04	75.69	−0.24	−0.21	0.482	−0.49	2.56	4.01	13.3
HD 132563B	10	85.21	12.41	1.41	149.63	48.46	0.38	0.25	0.489	0.89	$\leq$ 2.0	4.16	15.8
HD 201936A	8	179.87	15.85	1.63	236.15	68.22	−0.29	−0.29	0.493	−0.11	8.31	2.73	41.9
HD 216122A	13	108.52	12.30	2.40	87.78	86.44	0.23	0.19	0.529	0.89	6.15	5.33	15.1
BD 231978A	10	53.41	8.23	0.83	74.50	51.74	0.06	−0.21	0.556	0.17	2.43	2.62	28.1
HD 30101A	21	66.38	10.91	2.00	54.78	59.05	−0.02	−0.14	0.569	−0.01	1.82	4.63	16.7
HD 86057B	10	131.51	11.27	1.38	141.02	43.17	0.18	0.19	0.603	0.22	4.00	4.43	33.6
HD 8071A	9	64.69	9.92	2.00	57.81	110.68	−0.05	−0.20	0.606	0.07	4.50	2.18	4714.4
HD 108575	14	85.42	11.50	1.65	82.19	67.58	−0.09	−0.10	0.725	−1.16	4.60	9.81	36.0
BD 231978B	10	94.85	9.18	0.95	74.19	52.91	−0.09	−0.13	0.726	−0.72	4.00	2.62	39.6
HD 33334A	19	63.21	11.64	1.59	42.21	86.34	−0.10	−0.09	0.726	0.55	1.65	4.72	10.3
HIP 104687A	23	53.32	11.36	1.19	56.71	76.82	0.08	0.07	0.740	0.36	$\leq$ 3.0	4.01	26.7
HD 200466A	21	68.05	11.90	1.44	41.77	83.94	0.26	0.08	0.746	2.50	$\leq$ 1.4	4.66	6.8
HD 19440B	13	88.95	13.51	2.10	82.90	66.72	0.03	−0.04	0.901	0.07	$\leq$ 1.0	5.97	8.3
HD 213013B	16	48.69	9.82	1.18	61.46	48.14	−0.03	0.02	0.948	−0.12	4.10	5.51	10.8

Chapter 8

Astrophysical discussion of results

From the analyses presented in the previous chapter, there are interesting results deserving a detailed discussion, these are the correlation between BVS with RV due to stellar activity and the correlation due to contamination of the stellar spectra by light from a nearby object.

8.1 The correlation and its interpretation

The study of asymmetries of the spectral lines and specifically the measurement of BVS from line bisectors, provide a quantity related with the line centroids involved in the determination of radial velocities. If any variation of the BVS determined for every spectrum is correlated with the radial velocities recorded for a star, the hypothesis of a center of mass motion may be discarded because very likely a different process (intrinsic or not to the star) is the responsible of the observed Doppler shifts leading to RV variations.
From the analyzes presented formerly, two types of linear correlation were found between the BVS and RV variation. One type, is the correlation with negative slope, observed for an active star, due in particular to star spots crossing the stellar surface as it rotates.
A second type, is a correlation with positive slope, caused by contamination of the spectra due to light coming from a nearby object, in our specific case from the stellar companion of the binary system being observed.
In Figure 8.1 there is a schematic representation of the different cases of absorption profiles and line bisectors for the cases of anticorrelation and correlation in the plots of BVS-RV.

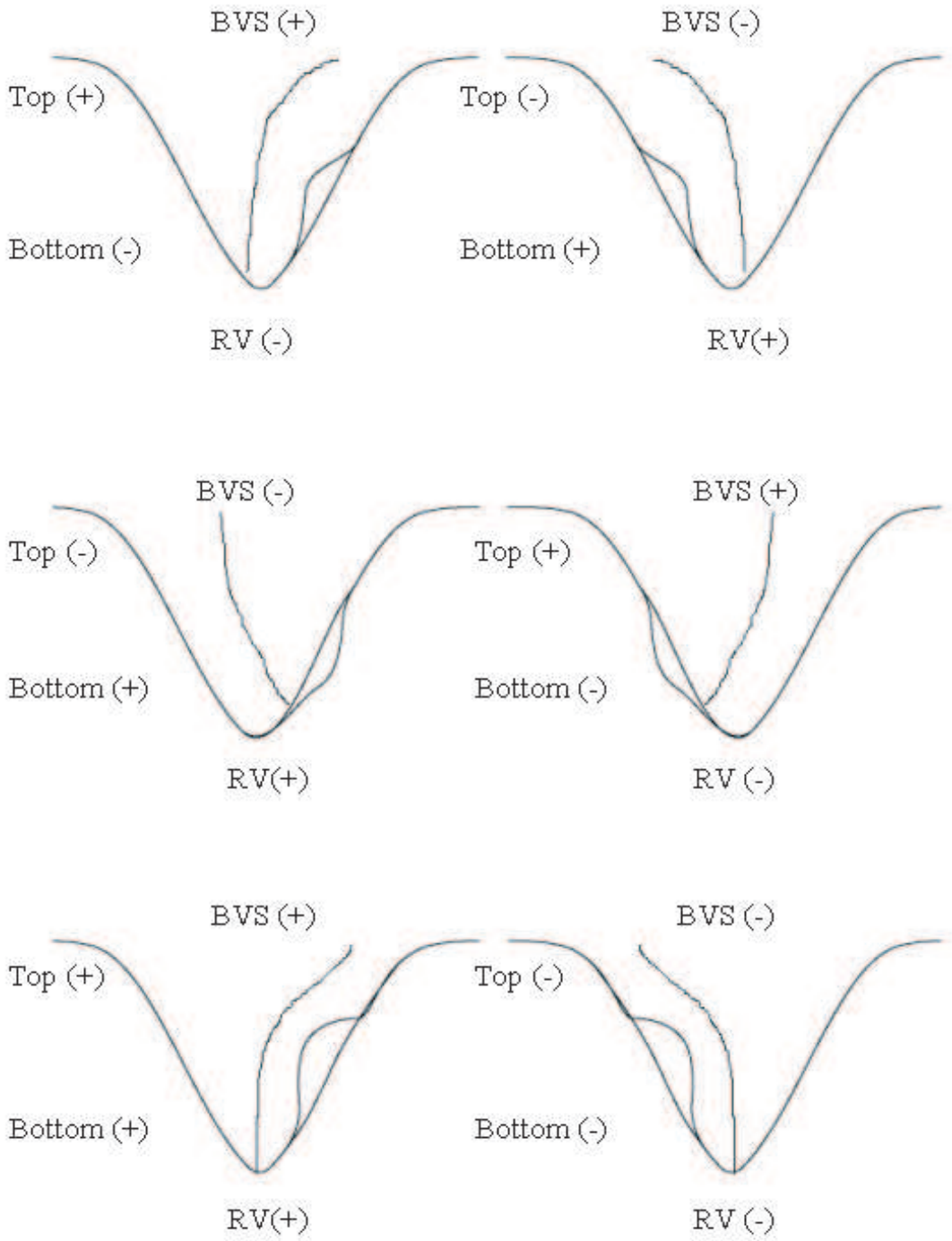

Figure 8.1: Schematic representation of different absorption profiles and their line bisectors, see text. Up: asymmetric absorptions due to spots (upward dip). Middle: asymmetric absorptions due to feculae (downward dip). Low: asymmetric absorptions due to light from a nearby object contaminating the spectrum os the star being observed (upward dip).

The RV is computed from the Doppler shift given by the measurement of the spectral line centroids and these can be altered by spots (dark zones altering the rotation profile) or by feculae (bright zones altering the absorption profiles).
In the case of spots, these appear as upward dips in the absorption profile. A spot in the red wing of the profile (in the upper left of Figure 8.1), will shift to the blue the line centroif, to more negative RV values. Due to the shape of the LB, the BVS = $(V_T - V_B)$ will be mainly positive, yielding an anticorrelation in the BVS-RV plot. A similar behaviour, with opposite sign, will occur if the spot is located in the blue wing of the profile.
For the case of feculae these appear as downward dips in the absorption profile. A fecula in the red wing of the profile (in the middle left of Figure 8.1), will produce a positve shift of the line centroid, yielding positive RV values. The LB will give negative BVS values with the consequence of an anticorrelation in the BVS-RV plot. A similar behaviour, with opposite sign, will occur if the fecula is located in the blue wing of the profile.
In the case of contamination, for the case of light from a nearby star companion, the absorption profile of the star being observed will display a weak superposed extra absorption feature in the profile (see Sec. 8.1.5 for the case of HD 76037A). If it appears in the red wing (as can be seen in the lower left of Figure 8.1), the line centroid will be shifted toward the red, yielding positive RV values and the LB shape will produce BVS of the same sign, resulting in a correlation of the BVS-RV plot.
The lack of correlation in stars known to host planets and the constancy in shape and orientation of the line bisectors computed from every spectra, is proof of the constancy of the line centroids involved in the RV determination and supports the hypothesis of a center of mass motion due to orbiting bodies perturbing the barycenter of the system.
In the following subsections some interesting cases of stars for which a correlation was found are presented and discussed. Besides the objects belonging to the subsample of wide binaries discussed in the previous chapter, there are analyzes for single stars, namely the case of an active one and two stars well known to host a planet.

8.1.1 HD 166435

The dwarf star HD 166435, of spectral type G0 and visual magnitude $m_V = 6.8$, shows evidence of RV variations, photometric variability and magnetic activity. Furthermore, previous analysis of the variation of the line bisectors revealed a correlation between RV and line bisector orientation (Queloz et al. 2001).
The large amplitude of the activity-induced variations and their stability make

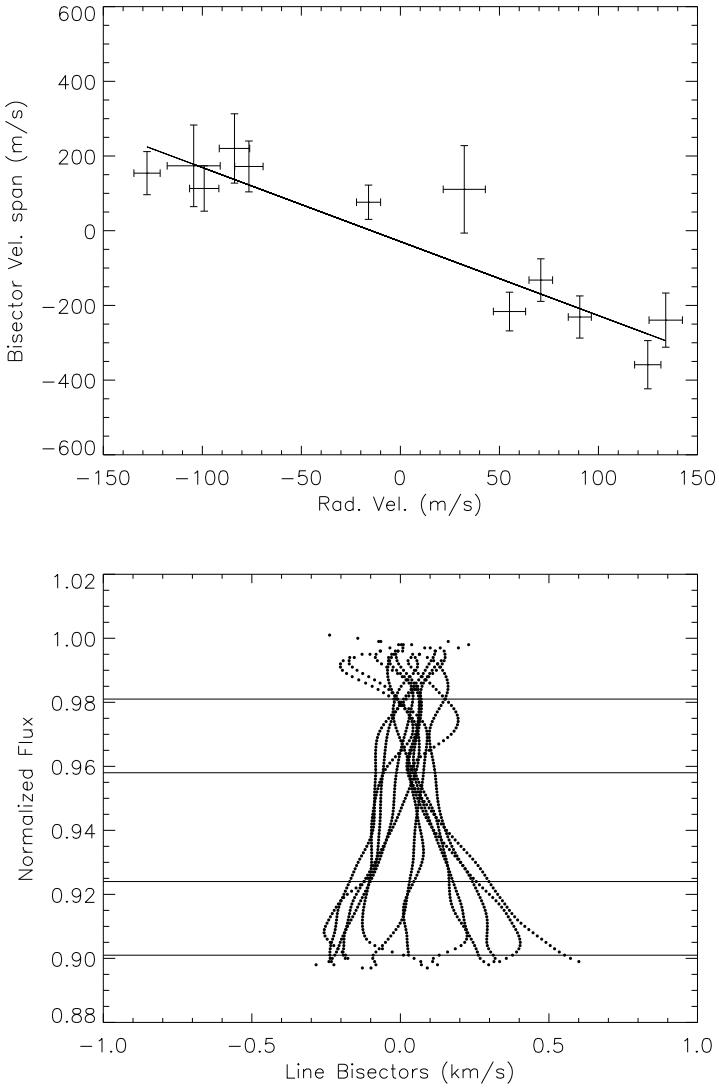

Figure 8.2: Upper panel: plot of BVS vs. RV for HD 166435 and the best fit to a straight line. Lower panel: line bisectors for individual spectra adjusted to their corresponding RV. The horizontal lines enclose the Top and Bottom zones considered for the fitting analysis.

Table 8.1: Bisector velocity span from spectra of HD 166435.

JD − 2450000	$(V_T - V_B)$ $\mathrm{m\,s^{-1}}$	V_r $\mathrm{m\,s^{-1}}$	S/N
2775.65	-231.1 ± 56.4	90.6 ± 5.8	164
2776.68	154.1 ± 57.8	-127.9 ± 6.6	156
2809.62	-216.4 ± 51.8	55.1 ± 8.2	178
2818.62	173.8 ± 109.3	-104.4 ± 13.4	86
2860.40	220.3 ± 92.8	-83.8 ± 7.7	98
2861.42	110.8 ± 117.1	32.3 ± 10.6	81
2862.42	-358.8 ± 64.5	124.9 ± 6.6	140
2891.37	172.0 ± 68.1	-76.5 ± 7.2	138
2892.35	-239.4 ± 72.5	134.0 ± 8.4	126
3129.74	113.1 ± 60.8	-99.0 ± 7.4	149
3130.73	76.3 ± 45.9	-16.1 ± 6.1	201
3131.74	-132.2 ± 57.0	70.9 ± 6.0	164

this star an ideal target to test new procedures like those presented in this thesis. Twelve spectra of HD 166435 were acquired between May 2003 and May 2004. The line bisectors, derived from the spectra, were used to study the correlation between the BVS and the radial velocities.
The location and extension of Top and Bottom zones of the line profiles used in the derivation of the BVS as well as the procedure to determine the best linear fit was discussed in the previous chapter. The upper panel of Figure 8.2 (middle pannel of Figure 7.1) displays the plot of BVS against RV; superimposed is the best fitting straight line, with:

$$(V_T - V_B) = (-1.98 \pm 0.21) \times V_r + (-29.03 \pm 18.45)\mathrm{m/s}\,. \qquad (8.1)$$

The Spearman rank correlation coefficient is -0.89 and the significance is of 99.99%. The lower panel of the same figure (upper pannel of Figure 7.1) shows the line bisectors computed for all spectra of HD 166435, corrected for their RV and plotted on a common reference frame. Values of bisector velocity span and RV for individual spectra are listed in Table 8.1. The trend of the BVS obtained in this work is similar to that of Queloz et al. (2001); the larger value we found for the slope can be attributed to the higher resolution of the SARG spectra.
A detailed discussion of this correlation, its implications and some important considerations will be discussed in the next Chapter.
Considering the quantities of BVS and RV (second and third columns of Table

Table 8.2: Bisector velocity span from spectra of HD 200466B.

JD − 2450000	$(V_T - V_B)$ $\mathrm{m\,s^{-1}}$	V_r $\mathrm{m\,s^{-1}}$	S/N
1801.59	-107.0 ± 38.9	6.6 ± 4.5	94
2042.69	-3.6 ± 41.1	-10.0 ± 3.8	77
2115.65	-16.7 ± 47.0	3.5 ± 3.8	72
2190.51	-82.8 ± 49.0	17.3 ± 2.9	67
2423.68	10.4 ± 34.4	-2.7 ± 3.4	93
2504.63	29.2 ± 39.0	-10.9 ± 3.1	83
2538.39	-7.6 ± 28.8	-7.0 ± 3.9	115
2605.33	-15.5 ± 44.5	-0.7 ± 3.4	73
2775.72	-1.2 ± 35.3	0.4 ± 3.5	90
2892.48	3.7 ± 38.9	-0.5 ± 3.1	84
2945.41	-45.2 ± 31.7	14.1 ± 3.5	99
3128.75	16.7 ± 37.5	2.9 ± 4.0	83
3129.73	-15.0 ± 42.4	-4.9 ± 2.9	82
3130.70	38.9 ± 34.8	-3.7 ± 3.2	94
3131.72	-60.4 ± 44.9	3.7 ± 3.2	83
3166.64	-4.9 ± 37.4	-2.9 ± 3.1	89
3305.40	75.3 ± 42.0	-6.9 ± 5.5	78
3625.40	-39.9 ± 51.6	10.6 ± 4.4	62

8.1 respectively) in a Scargle periodogram analysis (which allows a faster estimation of the false alarm probability as mentioned in Section 5.4) the results are: a period of 3.796 days with a FAP= 0.066 for the BVS and a period of 3.796 days with a FAP= 0.041 for the observed RVs (see Figure 9.3 in the next Chapter), values consistent with the rotation period of such an active star (Queloz et al. 2001 and Noyes et al. 1984). Indeed, this supports the scenario of rotating spots over the stellar surface, as source of the periodic variation of the spectral lines observed through the line bisectors.

8.1.2 HD 200466B

The star HD 200466B, has spectral type G5, visual magnitude $m_V = 7.6$ and 204 AU of separation between components. Eighteen spectra were acquired between September 2000 and October 2004. The line bisectors, derived from the spectra, were used to study the correlation between the BVS and the radial velocities.

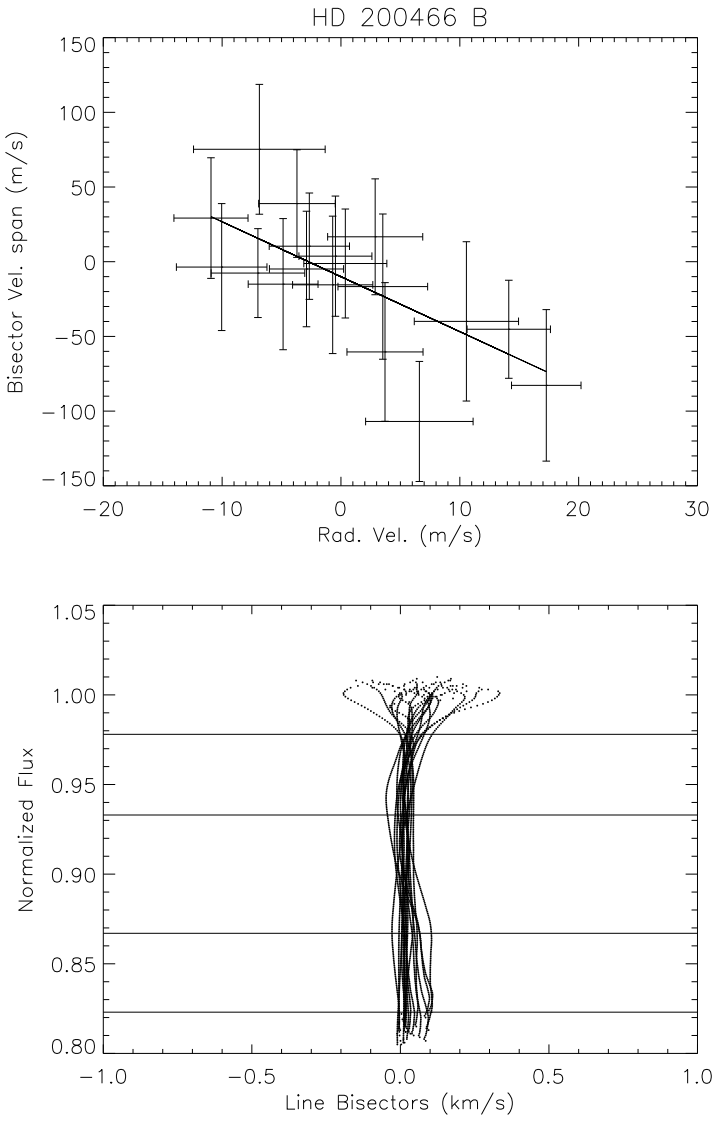

Figure 8.3: Upper panel: plot of BVS vs. RV for HD 200466B and the best fit to a straight line. Lower panel: line bisectors for individual spectra adjusted to their corresponding RV. The horizontal lines enclose the Top and Bottom zones considered for the fitting analysis.

Table 8.3: Bisector velocity span from spectra of HD 126246A.

JD − 2450000	$(V_T - V_B)$ $\mathrm{m\,s^{-1}}$	V_r $\mathrm{m\,s^{-1}}$	S/N
2012.58	19.0 ± 89.4	3.6 ± 7.7	122
2072.56	-243.0 ± 174.1	52.1 ± 9.6	62
2297.76	-77.4 ± 86.9	18.0 ± 8.9	129
2356.66	166.5 ± 126.3	-64.5 ± 8.7	94
2424.48	-12.7 ± 103.1	0.9 ± 7.5	104
2446.48	15.1 ± 92.8	-10.0 ± 6.8	117
2775.61	-11.7 ± 79.2	-14.0 ± 5.4	137
2781.53	9.5 ± 104.8	5.2 ± 7.2	106
3128.60	-99.3 ± 81.6	-30.5 ± 6.4	130
3129.61	116.3 ± 146.0	-0.8 ± 8.2	74
3130.55	-19.0 ± 78.8	-0.2 ± 5.9	138
3372.75	-121.7 ± 164.9	10.4 ± 11.6	65
3575.40	-35.4 ± 83.5	29.7 ± 8.1	126

The upper panel of Figure 8.3 displays the plot of BVS against RV, superposed is the best fitting straight line, with:

$$(V_T - V_B) = (-3.68 \pm 1.22) \times V_r + (-10.05 \pm 9.11)\mathrm{m/s}\,. \tag{8.2}$$

The Spearman rank correlation coefficient is -0.7 and the significance is of 99.88%. The lower panel of the same figure shows the line bisectors computed for all spectra, corrected for their RV and plotted on a common reference frame. Values of bisector velocity span and RV for individual spectra are listed in Table 8.2. The correlation with negative slope lead to think in a case of moderate activity, bearing in mind the low RV amplitude and low $v \sin i = 2.19\mathrm{km/s}$.

8.1.3 HD 126246A

The star HD 126246A, has spectral type G0V, visual magnitude $m_V = 6.7$ and 334 AU of separation between components. Thirteen spectra were acquired between May 2000 and July 2005. The line bisectors, derived from the spectra, were used to study the correlation between the BVS and the radial velocities. The upper panel of Figure 8.4 displays the plot of BVS against RV, superposed is the best fitting straight line, with:

$$(V_T - V_B) = (-1.49 \pm 1.19) \times V_r + (-23.19 \pm 27.27)\mathrm{m/s}\,. \tag{8.3}$$

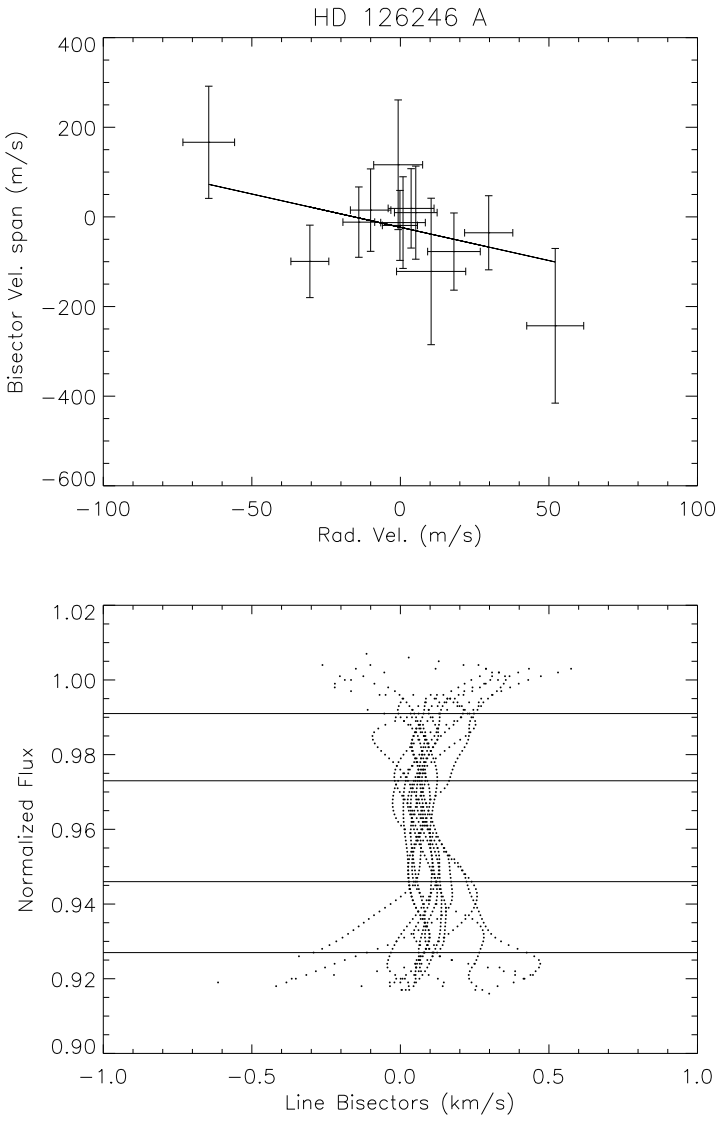

Figure 8.4: Upper panel: plot of BVS vs. RV for HD 126246A and the best fit to a straight line. Lower panel: line bisectors for individual spectra adjusted to their corresponding RV. The horizontal lines enclose the Top and Bottom zones considered for the fitting analysis.

Table 8.4: Bisector velocity span from spectra of HD 8071B.

JD − 2450000	$(V_T - V_B)$ $\mathrm{m\,s^{-1}}$	V_r $\mathrm{m\,s^{-1}}$	S/N
1797.64	110.3 ± 34.0	-9.2 ± 7.0	137
1854.54	146.7 ± 52.8	111.9 ± 5.6	91
2145.71	71.6 ± 34.9	23.2 ± 5.6	140
2297.38	-1.0 ± 44.4	-98.6 ± 5.9	110
2892.61	48.1 ± 42.0	-36.0 ± 6.1	112
3216.73	39.9 ± 33.8	-17.9 ± 6.1	141
3246.68	82.7 ± 40.3	26.7 ± 5.2	121

The Spearman rank correlation coefficient is −0.57 and the significance is 95.6%. The lower panel of the same figure shows the line bisectors computed for all spectra, corrected for their RV and plotted on a common reference frame. Values of bisector velocity span and RV for individual spectra are listed in Table 8.3. The correlation with negative slope and the observed shape of the line bisectors, sweeping a large interval of RV in the Bottom zone, lead to think in a case of stellar activity because these features are observed for HD 166435, moreover it has values of $\log R'_{HK} = -4.4$ and $v \sin i = 7.3$km/s. It was also shown to be photometrically variable by Skiff (1993), his photometry, that refers to the composite light of the components, shows night-to-night and season-to-season variability, but the data do not allow a photometric determination of the rotational period. The rather large projected separation between the components (9.3 arcsec) excludes the possibility of contamination as the source of the observed correlation.

8.1.4 HD 8071B

The star HD 8071B, of spectral type G0V, visual magnitude $m_V = 7.6$ and separation of 111 AU between components, is a member of a visual binary system. The primary HD 8071A is brighter by 0.3 mag and the system has a projected separation of 2.1 arcsec, the smallest in the sample of the SARG survey. Pairs with such small separation are typically not observed in cases of bad seeing; furthermore the slit was oriented perpendicularly to the separation of the components during all observations. Nevertheless, some contamination of the spectra is still possible, especially for the secondary component. Our velocity measures show that HD 8071A is itself a single lined spectroscopic binary with semiamplitude of $\sim 7\,\mathrm{km\,s^{-1}}$, Period of 576 days and fairly large eccentricity ($e \sim 0.4$) (see Desidera

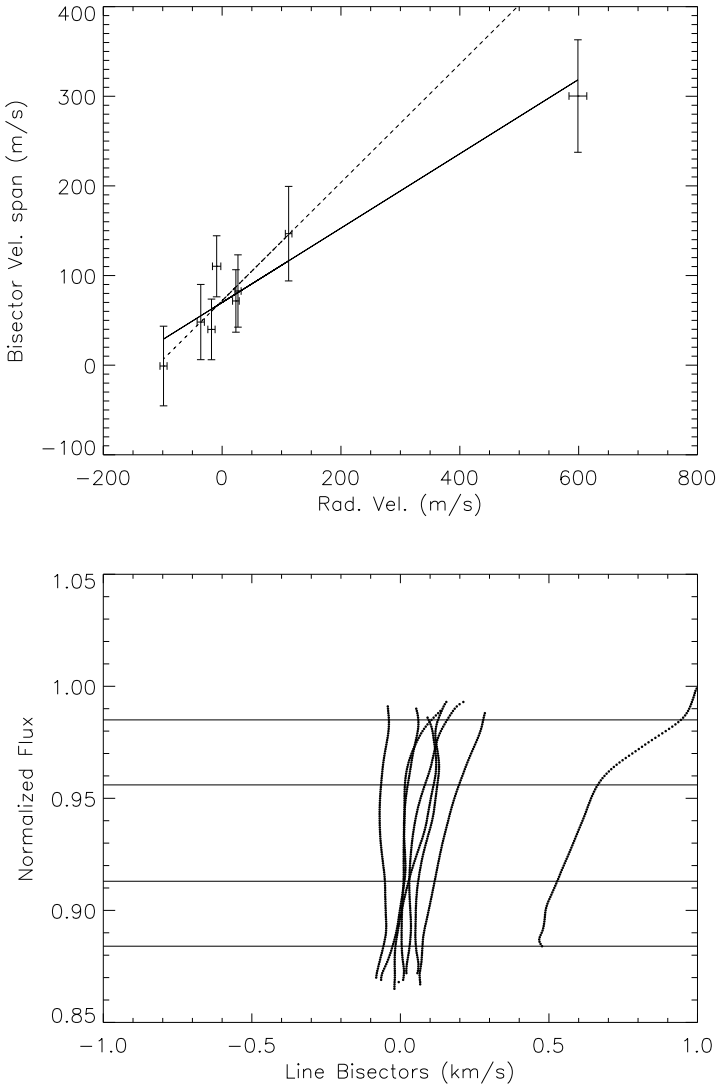

Figure 8.5: Upper panel: plot of BVS vs. RV for HD 8071B and the best fit to a straight line. The dotted line corresponds to the best fit discarding the spectrum with higher RV. Lower panel: line bisectors for individual spectra adjusted to their corresponding RV. The horizontal lines enclose the Top and Bottom zones considered in the fitting analysis.

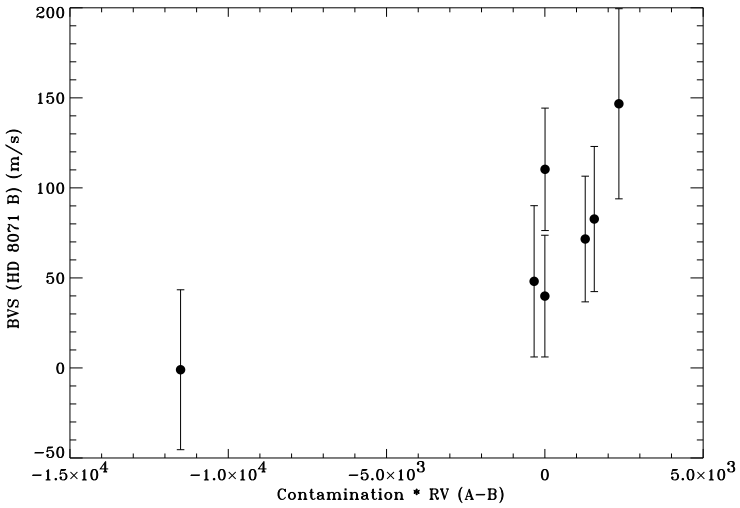

Figure 8.6: BVS of HD 8071B vs. the "effective contamination" of radial velocity, defined as the product of the light contamination from the companion HD 8071A and the RV difference between the components, variable with time because HD 8071A is itself a spectroscopic binary. The highly discrepant spectrum obtained on JD: 2452982.48 was excluded. Abscissa axis has dimensions of $(percentage\ of\ contamination) \times (m/s)$.

2005). The RV difference between the visual components is then variable in the range (-4, 10) $\mathrm{km\,s^{-1}}$.
Eight spectra of HD 8071B were acquired between September 2000 and August 2004. The correlation between BVS and RV found for all spectra has Spearman rank correlation coefficient of 0.81 and significance of 98.5%. The analysis of the IP did not show any critical trend acting on the RV computation, leading us to consider contamination as the cause of the observed correlation. The spectrum with RV $\sim 600\,\mathrm{m\,s^{-1}}$ and very different line profile is likely heavily contaminated by the companion, because of the occurrence of technical problems related to telescope tracking that night. Our study of the line bisector allows us to clearly identify the problematic spectrum and to exclude it from the analysis of the RV curve.
Nevertheless a correlation still persists even without considering the highly discrepant spectrum, with a Spearman rank correlation coefficient of 0.86 and significance of 98.6%, the best fitting straight line corresponds to:

$$(V_T - V_B) = (0.66 \pm 0.3) \times V_r + (71.92 \pm 14.78)\mathrm{m/s}\,. \tag{8.4}$$

This is likely due to some residual contamination (of a few percent at most) by the companion, compatible with the small separation of the pair and the actual observing conditions. Figure 8.5 shows the two cases and the eight line bisectors

computed for all spectra of HD 8071B, corrected for their RV and plotted on a common reference frame. The contamination of the spectra by light from the companion star produces an asymmetry in the red wings of the profiles with a consequent inclination of the line bisectors toward positive values of RV. Values of bisector velocity span and RV for individual spectra appear in Table 8.4.
To confirm our hypothesis of contamination as the source of observed BVS-RV correlation, we performed a simple modeling of the expected contamination, excluding the highly discrepant spectrum from JD: 2452982.48. We first determined the light contamination expected on the spectrum of HD 8071B on the basis of the seeing conditions (given by the FWHM of the spectrum measured along a direction perpendicular to the dispersion). RV and BVS of HD 8071B do not show significant correlation with such contamination. We then considered an "effective contamination" as the product of the light contamination and the variable RV difference between HD 8071 A and B. The Spearman rank correlation coefficient of RV and BVS vs. such "effective contamination" is 0.85 with a significance of more than 96%, supporting our hypothesis of light contamination as the origin of the RV and BVS variability of HD 8071B. The relation between RV perturbation and BVS is not linear likely because the RV perturbation due to contamination is expected to be a non-linear function of the position of the contamination across the line profile (See Figure 8.6).

8.1.5 HD 76037A

The star HD 76037A, of spectral type F8, visual magnitude $m_V = 7.5$ and separation of 753 AU between components. Is member of a visual binary system and sixteen spectra were acquired between November 2000 and January 2005.
This is a very peculiar object in which the average absorption profiles, from which the line bisectors were computed, display a dip toward the red wing leading to think of an additional absorption component from an unresolved companion. If this is the correct interpretation, HD 76037A is itself a spectroscopic binary and we will call C the fainter component.
The line bisectors appear deviated toward the red wing and the plot of BVS vs. RV shows a correlation with positive slope (as in the case of HD 8071B) due to contamination by light from the unresolved companion C, responsible for the asymmetry introduced on the average absorption profiles (see lower panel of Figure 8.7). The best fit to a straight line is expressed by:

$$(V_T - V_B) = (1.60 \pm 0.32) \times V_r + (1620.51 \pm 32.25)\mathrm{m/s}\,. \tag{8.5}$$

The Spearman rank correlation coefficient is of 0.7 and significance of 99.7% (see upper panel of Figure 8.7). Values of bisector velocity span and RV for individual

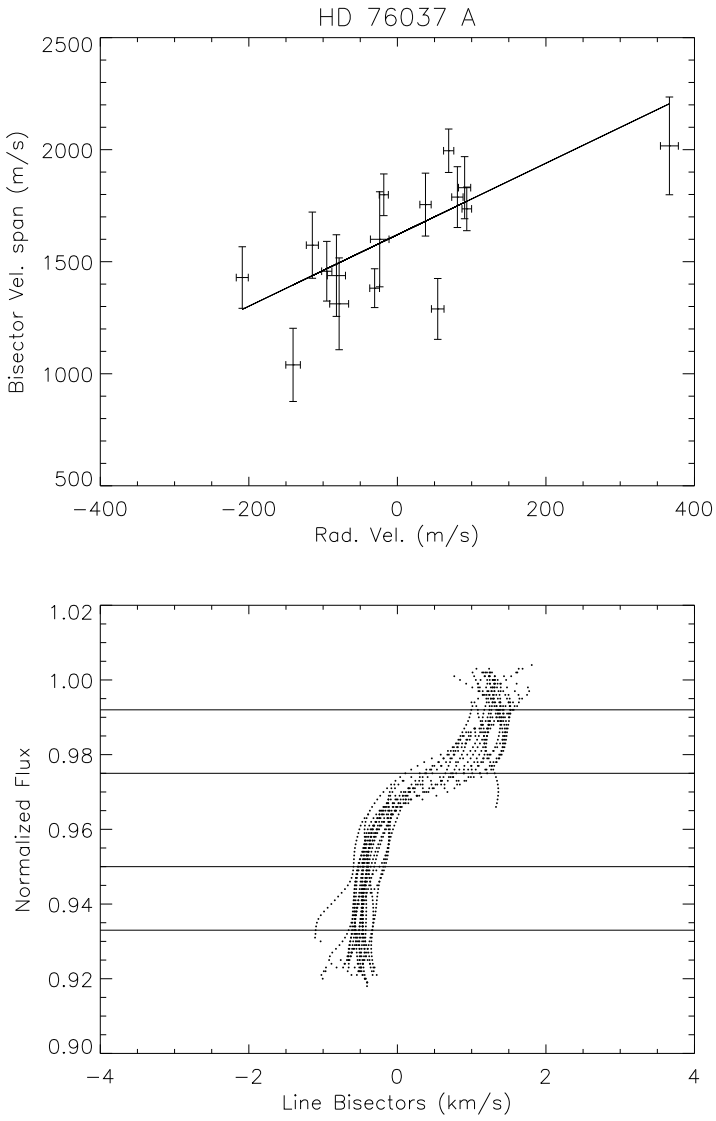

Figure 8.7: Upper panel: plot of BVS vs. RV for HD 76037A and the best fit to a straight line. Lower panel: line bisectors for individual spectra adjusted to their corresponding RV. The horizontal lines enclose the Top and Bottom zones considered in the fitting analysis.

Table 8.5: Bisector velocity span from spectra of HD 76037A.

JD − 2450000	$(V_T - V_B)$ $\mathrm{m\,s^{-1}}$	V_r $\mathrm{m\,s^{-1}}$	S/N
1853.77	1312.0 ± 204.9	-78.4 ± 12.8	65
1985.46	1438.0 ± 182.2	-82.1 ± 12.2	65
2012.41	1457.5 ± 133.1	-95.1 ± 6.9	97
2216.69	1573.9 ± 147.7	-114.5 ± 8.1	81
2327.39	1600.1 ± 212.1	-23.8 ± 12.5	63
2605.78	1429.4 ± 137.3	-208.9 ± 8.1	92
2684.45	1754.9 ± 140.4	37.8 ± 7.6	91
2953.76	1798.7 ± 93.1	-18.3 ± 6.1	132
3017.64	2016.9 ± 218.2	366.2 ± 12.1	65
3018.58	1995.2 ± 97.1	69.0 ± 6.9	127
3072.54	1039.5 ± 163.3	-140.4 ± 9.8	72
3128.42	1735.9 ± 97.3	93.5 ± 6.4	131
3129.43	1830.4 ± 138.6	90.5 ± 8.2	91
3131.36	1788.4 ± 135.7	80.8 ± 7.6	88
3344.63	1381.9 ± 86.5	-30.6 ± 6.6	145
3371.65	1289.3 ± 135.8	54.3 ± 8.5	90

spectra appear in Table 8.5.
This object has a rather low false alarm probability (2.1% for a period of 121.23 days as explained in Section 5.4) in the SARG exoplanet sample, hence there is a high probability that the observed RV periodicity are not casual but caused by a substellar companion to either component A or C. However, it should be noticed that the scatter of individual radial velocity measurements is large likely due to the complexity of the spectra.
A careful inspection of the line bisectors reveals important characteristics of this system. The portion of line bisectors roughly centered at RV $= -0.5$ km/s, slightly above and below the Bottom zone, give information on the stellar component A which displays the deeper average absorption. These line bisectors appear more or less crowded indicating a low dispersion of the spectral line centroids, therefore a low dispersion of RVs for component A.
The portion of line bisectors lying roughly in the interval 0.75–1.5 km/s of RV and mostly enclosed in the Top zone, provide information on both the brighter component A and the fainter component C which displays the shallower average absorption. These line bisectors show a spread in comparison with those of component A, leading to think about a higher dispersion of the spectral line centroids with consequent higher dispersion of RVs of component C. The correlated variations in RVs and BVS seen on the HD 76037A spectra seem then most likely due to variations of the RV of the component C, with a period of 121.23 days, but an amplitude considerably larger than that derived by a simple fit to the RV curve, possibly indicating a rather massive substellar object (HD 76037d). If this is the case, the inner AC triple would be somewhat similar to the HD 41004 system studied by Zucker et al. (2004); a hierarchical system with a brown dwarf that accompanies the faint M component, and a planet of 2.5 M_J that orbits the brighter K component.
A few new RV measurements together with line bisectors analysis, are needed to completely characterize this system. We plan a detailed modeling of the spectra, in order to better constrain the masses of the various objects present in the system as well as we plan an attempt to visually resolve the components using adaptive optics.

8.1.6 51 Peg

The star 51 Peg (HD 217014), of spectral type G2.5IVa and visual magnitude $m_V = 5.5$, is the first discovered solar-type object to host a planet, with $M_p \sin i = 0.47\, M_J$, $a = 0.052$ AU and period of 4.23 days (Mayor and Queloz 1995).
The star lies in a zone of the Hertzsprung-Russell diagram of stable (very low variability) objects (Eyer and Grenon 1997). Indeed, according to Henry et al.

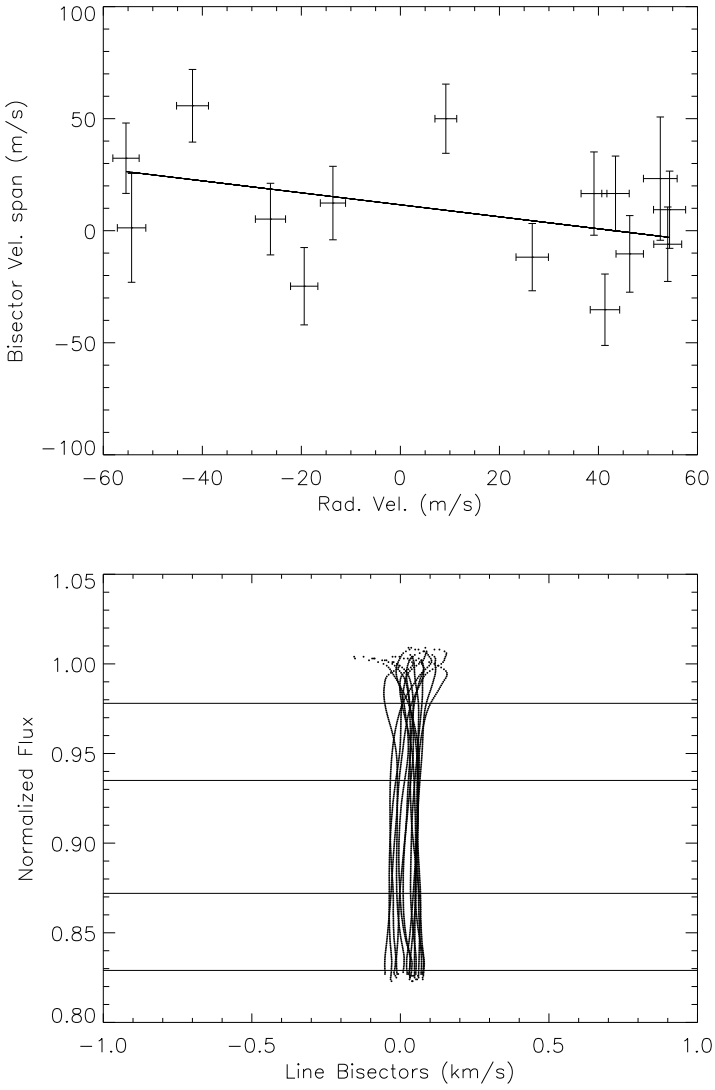

Figure 8.8: Upper panel: plot of BVS vs. RV for 51 Peg and the best fit to a straight line. Lower panel: line bisectors for individual spectra adjusted to their corresponding RV. The horizontal lines enclose the Top and Bottom zones considered for the fitting analysis.

Table 8.6: Bisector velocity span from spectra of 51 Peg.

JD − 2450000	$(V_T - V_B)$ $\mathrm{m\,s^{-1}}$	V_r $\mathrm{m\,s^{-1}}$	S/N
2070.73	50.0 ± 15.4	9.2 ± 2.2	242
2116.73	16.6 ± 18.6	39.1 ± 2.6	204
2145.68	-6.0 ± 16.6	54.0 ± 2.8	221
2189.33	12.4 ± 16.4	-13.6 ± 2.5	225
2190.46	32.4 ± 15.7	-55.4 ± 2.7	227
2216.38	5.2 ± 16.0	-26.2 ± 3.0	223
2245.32	1.3 ± 24.3	-54.3 ± 2.9	154
2423.73	-24.8 ± 17.2	-19.4 ± 2.8	220
2424.72	-10.3 ± 17.1	46.3 ± 2.8	221
2445.73	16.6 ± 16.7	43.4 ± 2.8	227
2446.73	-35.3 ± 15.9	41.3 ± 3.0	228
2539.35	23.3 ± 27.5	52.5 ± 3.4	135
2605.30	55.8 ± 16.2	-42.0 ± 3.2	233
2945.34	9.4 ± 17.2	54.4 ± 3.2	218
2953.32	-11.8 ± 15.0	26.6 ± 3.3	247

(2000a), no measurable change in mean magnitude (over 5 years) was seen and the Ca II record displayed a signal essentially constant despite some season-to-season jitter and a general indication of a low activity level.
Fifteen spectra of 51 Peg were acquired between June 2001 and November 2003. There is no significant correlation between BVS and RV (Spearman rank correlation coefficient of -0.28 and significance of 56%), confirming the results by Hatzes et al. (1998) and Povich et al. (2001). Values of bisector velocity span and RV for individual spectra appear in Table 8.6. The line bisector shape (see Figure 8.8) seems to be constant.

8.1.7 ρ CrB

The star ρ CrB (HD 143761), of spectral type G0Va and visual magnitude $m_V = 5.4$, is known to host a planet with $M_p \sin i = 1.04\, M_J$, $a = 0.22$ AU and a period of 39.95 days (Noyes et al. 1997).
Twenty six spectra of ρ CrB were acquired between April 2001 and March 2004. In the plot of BVS against RV the dispersion of the data points shows no correlation (as in Povich et al. 2001) with a Spearman rank correlation coefficient of 0.15 and significance of 52%.
Values of bisector velocity span and RV for individual spectra appear in Table 8.7. The line bisectors and its behaviour, similar to those for 51 Peg, are shown in Figure 8.9. The typical "C" shape of line bisectors is more evident for ρ CrB in agreement with the warmer temperature of the star.

8.1.8 HD 219542B

The star HD 219542B is member of a wide binary system, with spectral type G7V and visual magnitude $m_V = 8.6$. It was considered in Desidera et al. (2003) as a candidate to host a planet, but ultimately discarded after further analysis; the small RV variations are more likely related to a moderate stellar activity (Desidera et al. 2004b).
For the present analysis of the line bisectors, only the data of the 2002 season were considered, twelve spectra, because the RV scatter and chromospheric activity were greater in this season (see Desidera et al. 2004b). Therefore it should be easier to find a correlation between BVS and RV from these data alone.
Values of bisector velocity span and RV for individual spectra appear in Table 8.8. The plot of BVS against RV and the line bisectors are shown in Figure 8.10. No significant correlation appears in this case: the Spearman rank correlation coefficient is of -0.37 and the significance of 76%. This lack of correlation is due

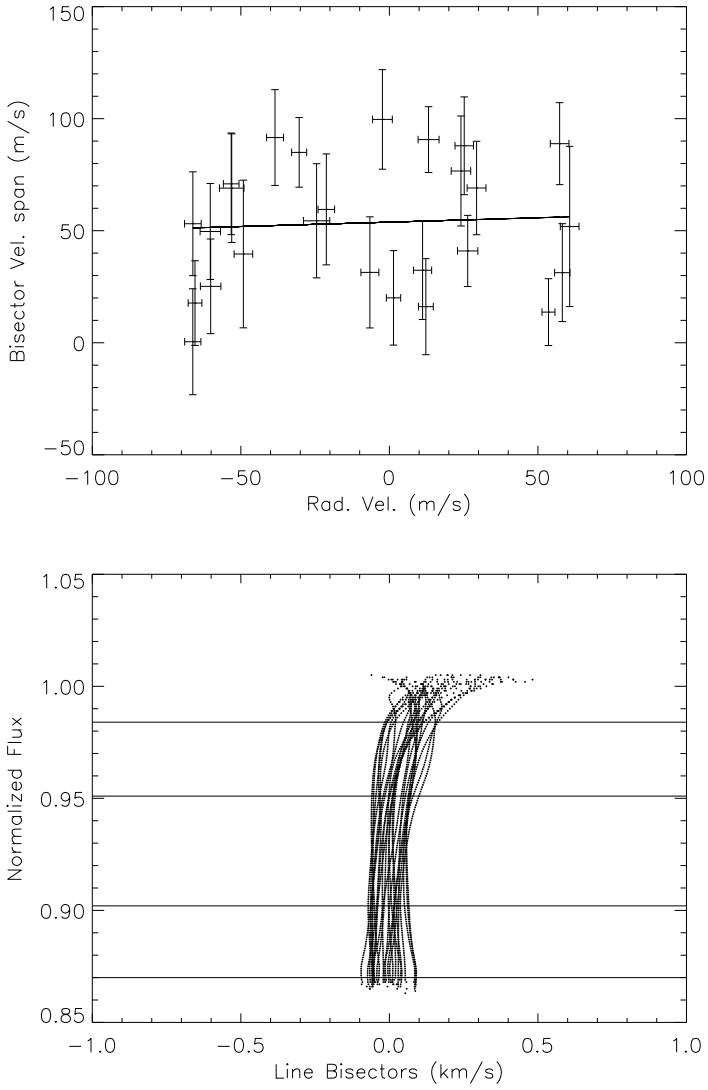

Figure 8.9: Upper panel: plot of BVS vs. RV for ρ CrB and the best fit to a straight line. Lower panel: line bisectors for individual spectra adjusted to their corresponding RV. The horizontal lines enclose the Top and Bottom zones considered for the fitting analysis.

Table 8.7: Bisector velocity span from spectra of ρ CrB.

JD − 2450000	$(V_T - V_B)$ $\mathrm{m\,s^{-1}}$	V_r $\mathrm{m\,s^{-1}}$	S/N
2012.72	16.1 ± 21.4	12.3 ± 2.5	216
2012.74	32.4 ± 22.0	11.2 ± 3.0	210
2013.76	31.4 ± 24.8	-6.6 ± 3.0	178
2040.74	13.7 ± 14.9	53.5 ± 2.2	282
2042.71	31.3 ± 21.9	58.2 ± 2.6	197
2043.73	51.9 ± 35.7	60.7 ± 3.1	124
2071.37	85.2 ± 15.5	-30.4 ± 2.5	288
2115.39	87.9 ± 21.8	25.2 ± 3.1	204
2145.37	17.7 ± 18.9	-65.4 ± 2.3	229
2146.38	0.5 ± 23.6	-66.2 ± 2.7	186
2297.80	91.6 ± 21.4	-38.5 ± 2.8	213
2394.72	41.0 ± 15.9	26.4 ± 3.4	275
2412.43	99.7 ± 22.2	-2.3 ± 3.3	209
2415.49	59.5 ± 24.8	-21.2 ± 2.8	180
2423.36	25.2 ± 21.1	-60.2 ± 3.5	208
2424.37	49.7 ± 21.4	-60.3 ± 3.4	207
2445.39	88.9 ± 18.3	57.3 ± 3.1	248
2457.54	39.6 ± 32.9	-49.1 ± 3.1	133
2463.39	53.1 ± 23.2	-66.2 ± 2.8	187
2472.37	20.0 ± 21.1	1.4 ± 2.4	205
2538.36	70.9 ± 22.7	-53.3 ± 2.6	198
2655.80	54.4 ± 25.5	-24.5 ± 4.4	177
2776.37	69.0 ± 24.2	-53.1 ± 4.1	188
2809.39	90.7 ± 14.7	13.2 ± 3.5	304
3071.77	57.1 ± 21.1	29.3 ± 3.2	213
3071.78	76.7 ± 24.5	24.1 ± 3.3	181

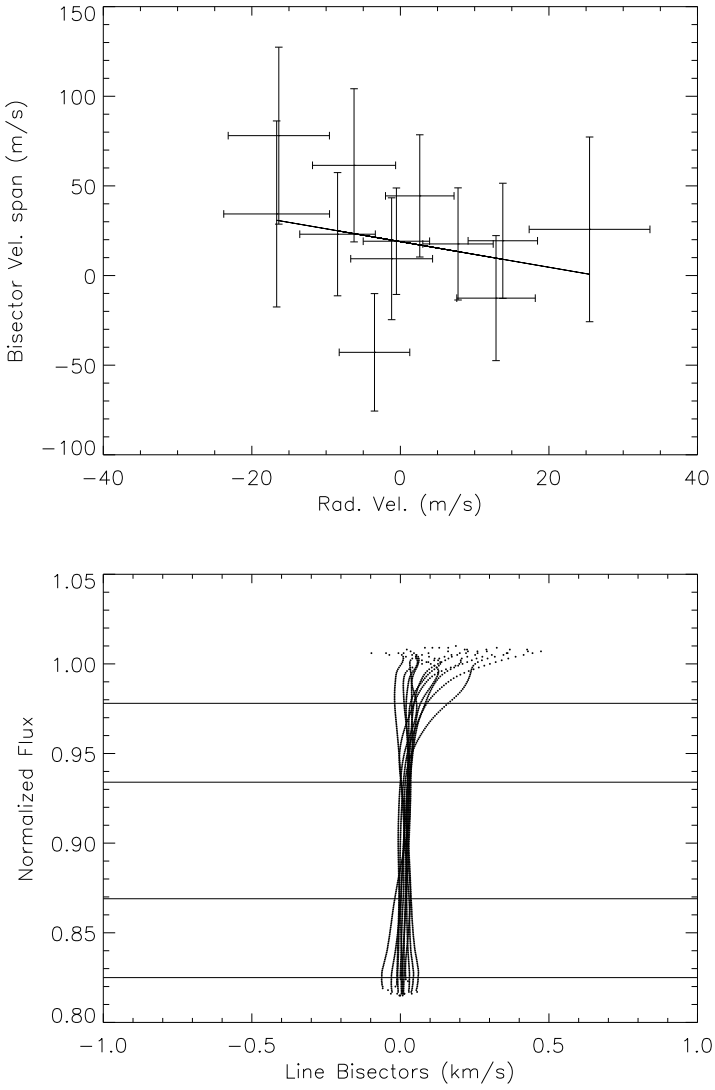

Figure 8.10: Upper panel: plot of BVS vs. RV for HB 219542B and the best fit to a straight line. Lower panel: line bisectors for individual spectra adjusted to their corresponding RV. The horizontal lines enclose the top and bottom zones considered for the fitting analysis.

Table 8.8: Bisector velocity span from spectra of HD 219542B.

JD − 2450000	$(V_T - V_B)$ $\mathrm{m\,s^{-1}}$	V_r $\mathrm{m\,s^{-1}}$	S/N
2424.71	-12.6 ± 34.9	12.9 ± 5.3	90
2445.71	19.4 ± 32.1	13.8 ± 4.7	99
2472.70	61.5 ± 42.7	-6.2 ± 5.6	82
2538.51	25.8 ± 51.5	25.5 ± 8.1	66
2570.41	23.0 ± 34.4	-8.5 ± 5.1	91
2570.42	44.4 ± 34.1	2.6 ± 4.6	92
2585.44	34.4 ± 51.9	-16.7 ± 7.1	65
2585.45	78.0 ± 49.4	-16.4 ± 6.8	66
2597.33	19.1 ± 29.7	-0.5 ± 4.5	105
2597.34	17.6 ± 31.3	7.8 ± 4.7	100
2605.36	-42.8 ± 32.8	-3.5 ± 4.8	96
2605.37	9.4 ± 34.0	-1.2 ± 5.5	93

to the small velocity amplitude (approximately between -17 and 26 $\mathrm{m\,s^{-1}}$) and to the low S/N of the available spectra of ~ 100.
The special case of HD 219542B shows that the bisector technique does not allow to disentangle the activity origin of low amplitude RV variations ($\sim 20\,\mathrm{m\,s^{-1}}$) using spectra of S/N ~ 100 even at the high resolution of SARG spectra ($R \sim 150000$).

8.2 Other objects observed with trends

Among the stars analyzed, there are some cases displaying trends but these lack of high significance. Anyway it is worth to mention those cases because the new spectra that will be acquired in future observations during the survey, will bring more information about the causes of the present observed trends, if these persist.

HD 209965B
Spectral type F8V, visual magnitude $m_V = 7.6$ and separation from the companion of 194 AU. The BVS-RV plot shows a trend likely due to contamination, it has Spearman non parametric rank correlation coefficient 0.59 with significance of 95.5% for 12 spectra. The possibility of contamination is considered by the very different shape of line bisectors for two spectra taken at the beginning of the

survey, yielding values of RVs very discrepant among the other spectra.
Its companion (component A) shows a trend possibly due to activity, with Spearman non parametric rank correlation coefficient -0.40 with significance of 85.7% for the 15 available spectra.

HD 216122B
Spectral type F8, visual magnitude $m_V = 7.6$ and separation from the companion of 407 AU. The RVs show a linear trend with time and the line bisectors (BVS) appear correlated with the RVs with Spearman non parametric rank correlation coefficient 0.57 and significance of 94.5% for 12 spectra. Removing the linear trend in RVs the correlation with line bisectors disappear. If real this correlation would indicate that the contribution of the companion that causes the RV linear trend to the integrated spectrum is not negligible.

HD 33334B
Spectral type G5, visual magnitude $m_V = 8.0$ and separation from the companion of 221 AU. The observed trend is possibly due to contamination. It has Spearman non parametric rank correlation coefficient 0.39 with significance of 92.8% for the 22 available spectra.

HD 139569A
Spectral type F8, visual magnitude $m_V = 8.2$ and separation from the companion of 423 AU. It shows a high $v \sin i = 7.65$km/s suggesting that the observed trend is possibly due to activity. It has Spearman non parametric rank correlation coefficient -0.40 with significance of 87.5% for the 16 available spectra.

HD 132563A
Spectral type F8, visual magnitude $m_V = 8.2$ and separation from the companion of 410 AU. The observed trend is possibly due to activity. It has Spearman non parametric rank correlation coefficient -0.50 with significance of 86.2% for the 10 available spectra.

HD 66491B
Visual magnitude $m_V = 8.4$. The separation from the companion is 340 AU. The spectral type K0III+ reported in Simbad is clearly wrong, as it is not compatible with the Hipparcos parallax and the atmosphere parameters, that indicate this is a late G main sequence star.
It has Spearman non parametric rank correlation coefficient -0.34 with significance of 78.4% for the 15 available spectra.
Its companion (component A) shows a trend possibly due to activity, with Spearman non parametric rank correlation coefficient -0.32 with significance of 77.8%

for the 16 available spectra.

HD 106515B
Spectral type G5, visual magnitude $m_V = 7.35$ and separation from the companion of 254 AU. The observed trend is possibly due to activity. It has Spearman non parametric rank correlation coefficient -0.30 with significance of 70.4% for the 14 available spectra.

8.3 Discussion

The cases discussed above show the useful information that line bisectors provide in the study of stellar spectra involved in the determination of RVs.
Line bisectors represent a valuable diagnostic tool in the search for substellar companions, to understand the causes of the RV variation observed. In fact, the constancy in shape and orientation of line bisectors and the lack of correlation between BVS and RV seen in the cases discussed above, supports the mechanical nature of the observed RV variation. However, one should be cautious with the results presented above; an anticorrelation (negative slope of the linear fit) not necessary is associated directly with cases of stellar activity and a correlation (positive slope of the linear fit) not necessary arises in cases of light contamination. Before attempting to generalize the presence of these features, it is necessary to enhance the sample of stars to analyze and carry out simultaneous photometric and spectroscopic analyzes, to determine the existence or not of stellar variability and/or activity, and to which extent these are correlated with the RVs observed. In some cases no significant correlation is present, but it results that spectra with discrepant RV show also a different line profile, suggesting the occurrence of some contamination. Our analysis is then a powerful tool to identify single contaminated spectra and clean the RV curve from them.
In conclusion, the spectra acquired using the Iodine cell can be used to study variations of line bisectors. In order to achieve the required accuracy, it is necessary to deal with high quality spectra, in particular high S/N to reduce the error bars in the BVS, or to study spectra where the RV variations are of large amplitude.
The projected rotational velocity, $v \sin i$, is a very important factor in the study of spectral line bisectors (as stated at the end of Sec. 4.2.2) because the rotational broadening exaggerates the curvature of line bisectors (Smith et al. 1987). Indeed, it is clear from the plot in Figure 8.11 that the cases of anticorrelations with high Spearman correlation coefficient (ρ), were found for stars with high $v \sin i$ values, a common feature of active stars. In case of star spots, a larger rotational

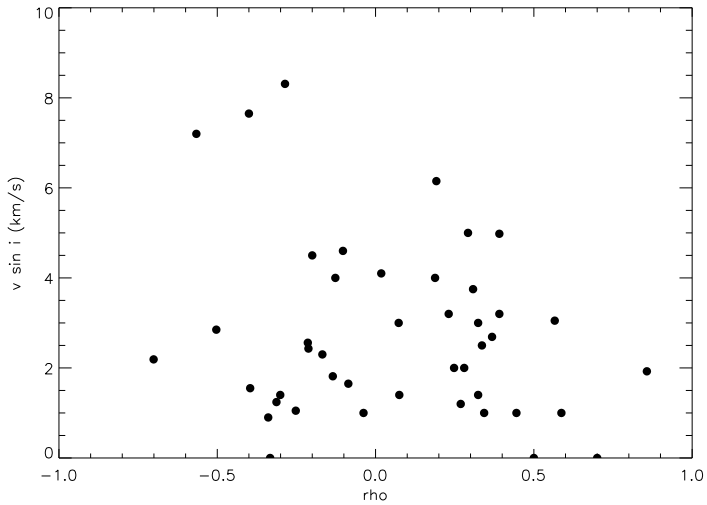

Figure 8.11: Plot of the projected rotation velocity v sin i vs. the Spearman non parametric rank correlation coefficient ρ. Negative values of ρ (anticorrelation due to activity) appear for three cases belonging to stars with the highest v sin i.

velocity also causes a larger slope of the BVS-RV relation (Hatzes 2002), making easier its detection.
In Figure 8.12 the plot of the separation between stellar components against the Spearman correlation coefficient (ρ) shows that for low separations there is a high possibility of spectral contamination, in fact the highest values of ρ, occur for low separations.

8.3.1 Trends observed in more stars

The subject about RV corrections due to activity has been studied by some authors. Saar and Donahue (1997) explore the relation among amplitude RV variations (A'_{max}) due to spots and plages with rotation. They consider a sample of F, G and K dwarfs and plot their maximum velocity amplitudes against (B–V), v sin i and $-log\, R'_{HK}$, observing that the maximum velocity amplitude increases with T_{eff}, v sin i and chromospheric activity.
Later, Saar and Fischer (2000) explore the linear correlation between RV and activity through the Ca II infrared triplet, in particular they measured an index S_{IR} (similar to the Mount Wilson S_{HK}). Considering a sample of F, G and K stars, they plot the absolute value of the slope $\mid dv_r/dS_{IR} \mid$ against (B–V), v sin i and R'_{HK}, observing that the modulus of the slope decreases with (B–V) and increases with v sin i as well as with R'_{HK}.

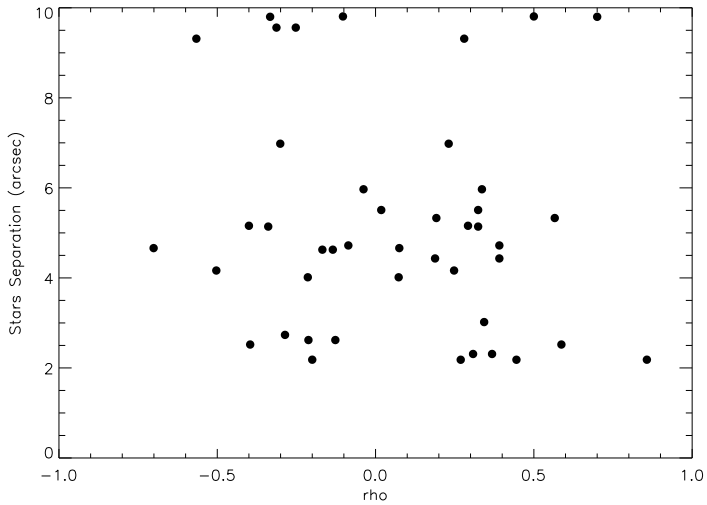

Figure 8.12: Plot of the stellar separation between components (arcsec) vs. the Spearman non parametric rank correlation coefficient ρ. Positive values of ρ (correlation due to spectral light contamination) appear in cases of stars with small separation. The point with high separation and $\rho = 0.7$ corresponds to the special case of the star HD 76037A.

Higher v sin i (Gray 1986 and Smith et al. 1987) or activity (Toner and Gray 1988) can alter bisector shapes.
From Hatzes (2002) it appears that the slope of the correlation BVS-RV increases with v sin i, hence, it will be easier to identify a correlation in the case of stars with high rotation despite the amplitude of the RV variations (note the v sin i of the F-G-K stars in Table 9.1). This trend is similar to that formerly cited from Saar and Fischer (2000) between the RV and the Ca II IR triplet index S_{IR} where the absolute slope ($\mid dv_r/dS_{IR} \mid$) increases as the the v sin i increases.
In the present discussion the relations given by Hatzes (2002) and Saar and Fischer (2000) should be considered as a qualitative description because these were derived for single and specific spectral lines, while we are considering many lines, a different spectral resolution and a different line depth to compute the BVS.
We explore the results presented in Chapter 8 for the case of some stars from the TNG-SARG sample that appear to be active stars, considering its Spearman correlation coeffcient (negative) and significance.
Based on the BVS-RV correlation and some stellar quantities like the rotation v sin i, the color (B-V) and the semiamplitudes of RV and BVS, there are interesting trends like those found by Saar and Donahue (1997) and Saar and Fischer (2000).
We consider three stars with significant linear correlation due to activity presented in Sec. 8.1 and five stars with low significant correlation possibly due to

Table 8.9: These are some basic data of active and possibly active stars from the survey SARG. The considered quantities are the slope of the RV-BVS correlation, the $v \sin i$, the (B–V), the semiamplitude of RV variations and the semiamplitude of BVS variations.

Stars	slope $m\,s^{-1}$	$v \sin i$ $km\,s^{-1}$	(B − V)	Amp RV $m\,s^{-1}$	Amp BVS $m\,s^{-1}$
HD 166435	-1.98 ± 0.21	6.72	0.6330	130.95	206.60
HD 200466B	-3.68 ± 1.22	2.19	0.7851	14.10	180.30
HD 126246A	-1.49 ± 0.19	7.20	0.5385	53.20	204.80
HD 139569A	-3.17 ± 1.52	7.65	0.5377	53.70	289.00
HD 132563A	-1.53 ± 0.81	2.85	0.5377	75.60	255.60
HD 209965A	-0.96 ± 0.97	1.55	0.5501	32.70	103.80
HD 66491A	-1.00 ± 0.87	$\leq$ 0.90	0.7470	51.30	127.10
HD 106515B	-1.37 ± 0.98	$\leq$ 1.40	0.8299	15.25	57.05

activity presented in Sec. 8.2 (see Table 8.9) with different plots in Figure 8.13. The semiamplitude of BVS decreases as (B–V) increases (T_{eff} decreases), the semiamplitude of BVS increases as $v \sin i$ increases. The other plots show less clear trends.

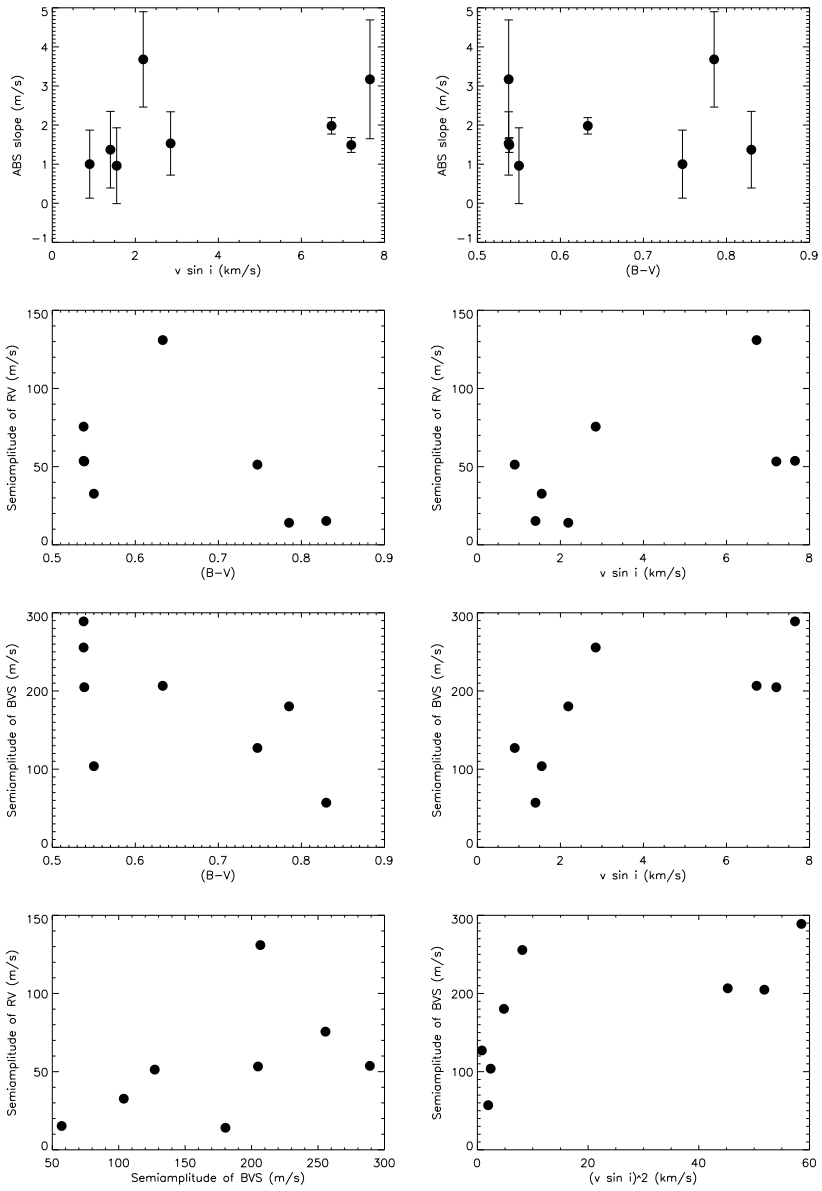

Figure 8.13: Some plots of the computed quantities of stars. From upper to lower panels. Left: modulus of the slope in the BVS-RV correlation vs. v sin i. Right: modulus of the slope in the BVS-RV correlation vs. (B–V). Left: Semiamplitude of RV vs. (B–V). Right: Semiamplitude of RV vs. v sin i. Left: Semiamplitude of BVS vs. (B–V). Right: Semiamplitude of BVS vs. v sin i. Left: Semiamplitude of RV vs. Semiamplitude of BVS. Right: Semiamplitude of BVS vs. $(v \text{ sin } i)^2$.

Chapter 9

Future developments and possible applications

The analysis of line bisectors from stellar spectra may be carried out virtually from any astronomical instrument ensuring high S/N and high resolution. Moreover it is possible to employ the same spectra involved in the RV determination taken with the Iodine cell superposed, after removing their features as explained in Chapter 6.
The study of BVS and RVs is essential in the analyzes of stars surveyed in the search for exoplanets, not only to understand the nature of the observed variations, but to determine the existence and, if is the case, the significance of any correlation. Any trend observed may be characterized by the appropriate equation, a linear one for the cases previously discussed, and it may be exploited as an analytical tool to correct RVs, in order to remove the undesired effect responsible of the variations.
In the following sections we explore the particular case of HD 166435, an attempt to apply corrections to the observed RVs, the limits of masses for possible substellar companions and discuss the viability of such a procedure to search for exoplanets around young and/or active stars.

9.1 The importance of young and active stars in surveys

The radial velocity technique is very sensitive to intrinsic stellar "noise" or jitter in the RV determination, caused by stellar magnetic activity (spots, plages) as well as by photometric variations (Saar and Donahue 1997).
Most of the extrasolar planets discovered to date belong to stars mainly from the

main sequence, spectral type F, G, K and older than about 1-2 Gyr; a distribution which is in part the result of selection effects.
The observational bias against young stars that are generally quite active, represents a severe limitation in studies of planetary systems; including such stars in the RVs surveys would be crucial to better understand the mechanisms of formation and evolution of planetary systems. Furthermore it would provide optimal candidates for direct imaging of extrasolar planets, since planet-star contrast is expected to be more favorable to observations for younger planets, which are intrinsically brighter than old plantes.
The development of techniques for RV correction to reduce the effects of intrinsic stellar processes altering the observed RV values, would improve the measurements of low amplitude RV variations, leading possibly to the detection of low masses or very separated (large semimajor axis) substellar companions. This would enable the search for exoplantes around young (early-type) and active stars, to study the evolution of planetary systems (Saar and Fischer 2000), to study whether the properties of planets change with age (planet evolution), to test theoretical models of orbital migration in protoplanetary disks, to set targets for imaging missions due to the intrinsic brighter properties of young planets (Burrows and et al. 1997), e.g., ϵ Eri (Hatzes et al. 2000).
The study of planets around active stars would also allow to study the interaction processes between the star and the companion due to tidal forces and magnetic fields, to learn about exoplanets atmospheres, and to understand how rare or frequent are extreme scenarios.

9.2 An attempt to correct radial velocities

Attempts to correct RVs must concentrate in the study of stellar phenomena like: spots, plages, active regions, non uniform convection, rotation and magnetic activity; together with the record of many observable features like: temperature T_{eff}, color (B-V), rotation velocity v sin i, CaII H & K indices and spectral line bisectors; to study how these quantities correlate with observed stellar features and set the appropriate strategies of correction. In Table 9.1 we listed a few objects for which a correlation of some of the above quantities with RVs have been determined.
Paulson et al. (2002) estimate the correlation between RV and H K chromospheric emission for all their targets. The stars with possible correlation not included in the successive study (Paulson et al. 2004) are not included in the Table.
Hatzes (1999) and (2002) showed that in stars with spots randomly located the variations in the velocity span (given by bisectors) and RV are linearly correlated,

Table 9.1: These are some basic data of stars for which correlation of activity indicators with RVs have been observed. The observed features correlated with RV appear in the seventh column, these are: bisectors variation (B), photometry variation (P), R' index of Ca II variation (HK) and Hα line strength variation.

Stars	Spectral type	(B − V)	P_{rot} days	$v \sin i$ km/s	$\log R'_{HK}$	RV correlation	Reference
F, G, K, main sequence							
HD 166435	G0V	0.633	3.8	7.5	−4.26	B, P, HK	Queloz et al. 2001
HD 49933	F5V	0.39[b]	8.0	9.5	–	B	Mosser et al. 2005
PW And (HD 1405)	K2V	1.04	1.75	22.6	–	B	Lopez−Santiago et al. 2003
ξ Boo A (HD 131156)	G8V	0.76[c]	6.2[c]	2.7[d]	−4.38[c]	B	Toner & Gray 1988
HIP 13806	G5[b]	0.855	9.4	3.8	−4.38	P	Paulson et al. 2004
HD 26767	G0[b]	0.640	8.7	5.4	−4.44	P	Paulson et al. 2004
HD 26736	G5[b]	0.657	8.2	5.4	−4.42	P, Hα	Paulson et al. 2004
HD 126246A	G0V	0.54	–	7.3	−4.40	B	This Thesis
M dwarfs							
Barnard (GJ 699)	M4Ve	1.73[a]	130.4[a]	$\leq$ 0.31	–	Hα	Kürster et al. 2003
Giants							
HD 81797	K3II − III	1.44	–	$\leq$ 1.4	–	B	Setiawan et al. 2005
HD 27536	G8IV − III	0.91[b]	306.09	1.0	−4.33	B, HK	Dall et al. 2005

[a] Benedict et al. 1998

[b] Simbad database

[c] Noyes et al. 1984

[d] Gray 1984

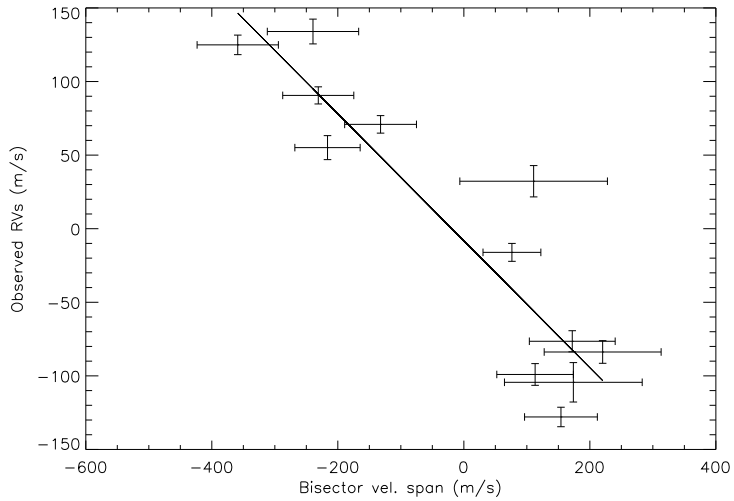

Figure 9.1: Plot of observed RVs Vs. BVS for HD 166435 and the best fit to a straight line, given by equation 9.1.

a relationship confirmed by observations of the star HD 166435 and discussed in Chapters 7 and 8.
A former study to correct RVs of HD 166435 was carried out by Els et al. (2003), based on the width and skewness of its spectral absorption profiles. Here we present the description of a procedure to correct RVs through line bisector analysis, the errors determination and some interesting constraints on possible substellar companions, following a procedure similar to that discussed in Desidera et al. (2003).

9.2.1 The linear correlation

The linear correlation determined between RV and BVS in HD 166435, may be exploited to correct the RVs observed, through the line bisectors computed from the spectra. Figure 9.1 displays the plot of RV against BVS and the best fitting straight line, with:

$$\mathrm{RV} = (-0.43 \pm 0.01) \times \mathrm{BVS} + (-8.22 \pm 2.13)\mathrm{m/s}\,. \tag{9.1}$$

Values of bisector velocity span and RVs for individual spectra are listed in Table 9.2.

Table 9.2: BVS and RVs from spectra of HD 166435. In the third and fourth columns are the observed and corrected RVs, respectively.

JD − 2450000	$(V_T - V_B)$ $m\,s^{-1}$	Obs. V_r $m\,s^{-1}$	Cor. V_r $m\,s^{-1}$	S/N
2775.65	-231.1 ± 56.4	90.6 ± 5.8	-0.8 ± 27.5	164
2776.68	154.1 ± 57.8	-127.9 ± 6.6	-53.3 ± 24.3	156
2809.62	-216.4 ± 51.8	55.1 ± 8.2	-30.0 ± 26.0	178
2818.62	173.8 ± 109.3	-104.4 ± 13.4	-21.2 ± 47.2	86
2860.40	220.3 ± 92.8	-83.8 ± 7.7	19.4 ± 38.5	98
2861.42	110.8 ± 117.1	32.3 ± 10.6	88.2 ± 50.5	81
2862.42	-358.8 ± 64.5	124.9 ± 6.6	-21.6 ± 32.4	140
2891.37	172.0 ± 68.1	-76.5 ± 7.2	5.9 ± 28.5	138
2892.35	-239.4 ± 72.5	134.0 ± 8.4	39.0 ± 34.9	126
3129.74	113.1 ± 60.8	-99.0 ± 7.4	-42.1 ± 26.2	149
3130.73	76.3 ± 45.9	-16.1 ± 6.1	25.0 ± 20.0	201
3131.74	-132.2 ± 57.0	70.9 ± 6.0	22.1 ± 26.8	164

9.2.2 The correction of RVs

Equation 9.1 was employed to compute RVs through the BVS of every spectrum. The corrections were then calculated by:

$$\mathrm{RV_{cor}} = \mathrm{RV_{obs}} - \mathrm{RV_{com}}, \tag{9.2}$$

where $\mathrm{RV_{obs}}$ are the RVs measured from the spectra, and $\mathrm{RV_{com}}$ are the RVs computed from eq. 9.1. Error bars come from applying the equation of error propagation to eq. 9.2. Figure 9.2 shows the plot of the observed and corrected RVs along time. The RV dispersion diminishes from an rms = 91.8 m/s to an rms = 37.9 m/s; values of corrected RVs are listed in the fourth column of Table 9.2.

The periodograms computed with the observed and corrected RVs, can be seen in Figure 9.3. For the observed data, a period of 3.796 days arise with a FAP = 0.041, in agreement with that found by Queloz et al. (2001). With the corrected data, a less confident period of 2.783 days appears with FAP = 0.462.

The different period found for $\mathrm{RV_{cor}}$ after the removal of the line bisector effect (RV-BVS correlation due to spots), indicates that there is no signal consistent with a period of 3.796 days caused by the observed RV variation.

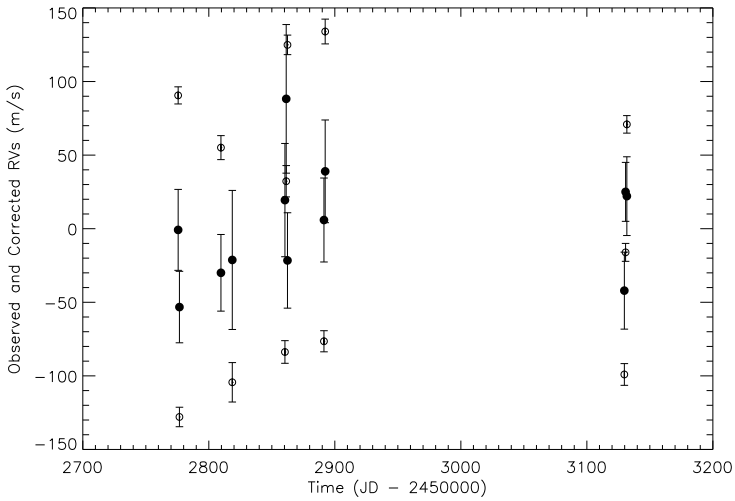

Figure 9.2: RVs of HD 166435. Empty circles with error bars represent observed RVs, with rms = 91.8 m/s, filled circles are the corrected RVs by eq. 9.2 with rms = 37.9 m/s.

9.2.3 Upper limits on substellar companions

Constraints on the masses of possible substellar companions may be set following the approach described in Desidera et al. (2003).
Briefly, a Monte-Carlo method is applied based on a grid of mass and semimajor axis values, ranging from 0.01 to 20.0 M_J and 0.1 to 1.5 AU. For each couple of mass and semimajor axis, 10000 random combinations of orbital phase T_0, eccentricity e and longitude of the periastron ω (this for the eccentric case) are generated. For the eccentricity we assume $e < 0.56\times$ log(P)-0.12 for P < 80 days (a conservative upper limit to the eccentricity of known exoplanets as a function of period).
This method is based on the evaluation of the excess of RV variability due to the presence of possible substellar companions and allows a complete exploration of the possible orbital parameters for eccentric orbits; a possibility not viable when dealing with methods like the periodogram analysis (see Endl et al. 2002).
The curves showed in Figures 9.4 and 9.5, represent confidence limits on the mass (in M_J) of a possible companion for different values of the semimajor axis (in AU). Dashed curves were computed with RV_{obs} and solid curves with RV_{cor}. The high peaks for small values of a may correspond to poor sampling of the few data points available (12); the maximum at 1 AU corresponds to rephasing observations with a period of one year.
Through this approach, we try to explore if possible substellar companions above the curve (i.e., if the limits at given a) may cause scatter incompatible with our

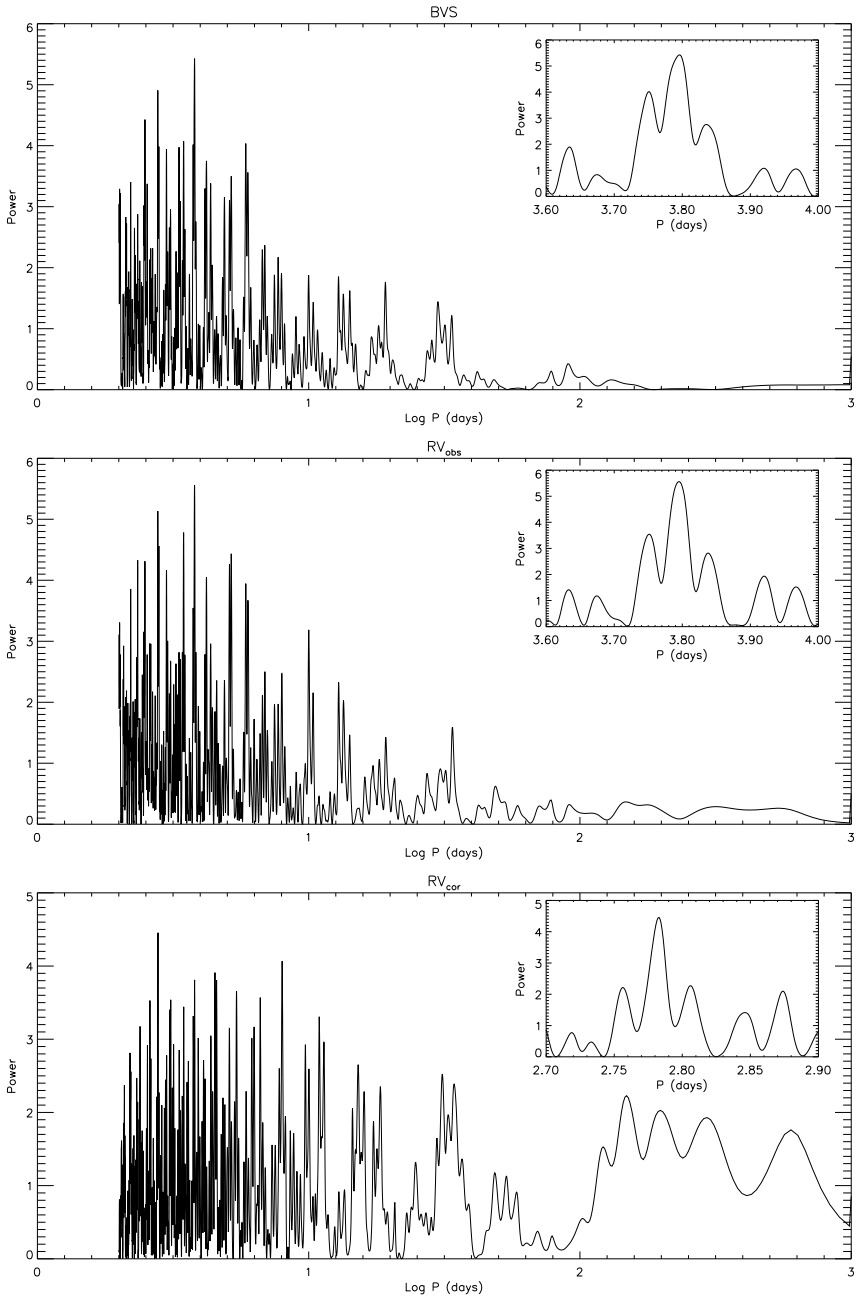

Figure 9.3: These are Scargle periodograms of HD 166435. In the upper panel is the periodogram computed for the values of BVS with P = 3.796 and FAP = 0.066. In the middle panel is the periodogram computed for the values of observed RVs with P = 3.796 and FAP = 0.041. In the lower panel is the periodogram computed for the values of corrected RVs with P = 2.783 and FAP = 0.462.

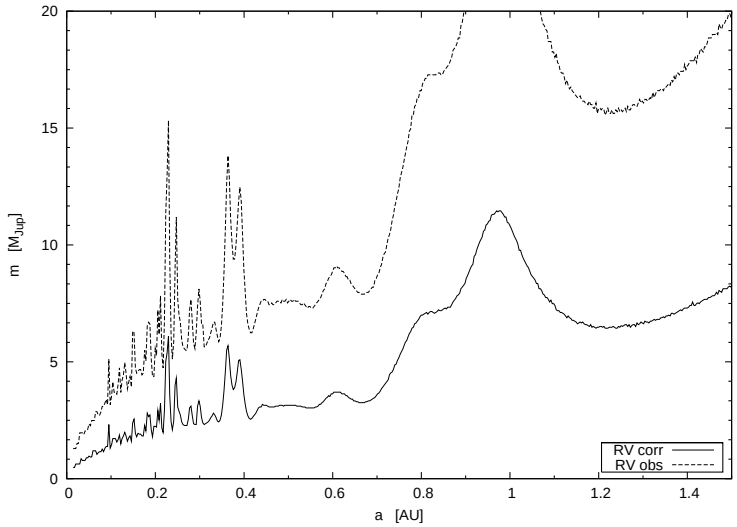

Figure 9.4: Upper limits for masses of possible substellar companions around HD 166435 in circular orbits. The dashed curve was computed with values of RV observed, the solid curve with the corrected RVs.

observed, then corrected, data.
Is worth to note that the corrected RVs, give much smaller confidence limits for the masses. As expected, on the basis of the lower dispersion, the corrected RVs allow to improve the exclusion limits typically by a factor 2÷3.

9.3 Discussion about corrections

If RV variability due to activity and a Keplerian motion with similar amplitude are present in a star, it would be more difficult to correct RVs due to a large scatter in the RV-BVS correlation. A larger number of measurements would be required to determine the correlation caused by stellar activity. In the case of HD 166435 it is possible to correct RVs for the effect of stellar activity, using the tight correlation between RVs and line bisectors. Moreover the small dispersion of the RV-BVS correlation, suggest that the activity is the dominant source of RV variability.
The usefulness of this procedure to search for planets around young or active stars depends on whether other young or active stars have similar characteristics as HD 166435 or not.
From the stellar characteristics of the stars with BVS-RV correlation and the models of RV and BVS variations in case of star spots (e.g., Hatzes 2002) it appears that in general the stars that are most suitable to correct the observed RVs

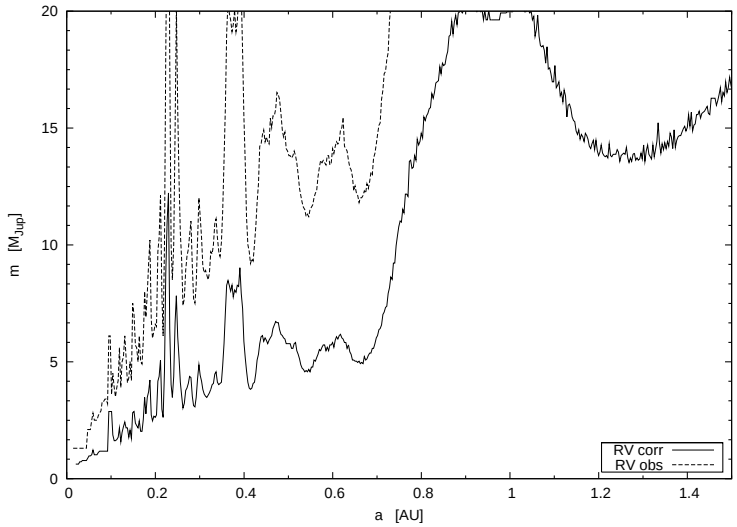

Figure 9.5: Upper limits for masses of possible substellar companions around HD 166435 in eccentric orbits. The dashed curve was computed with values of RV observed, the solid curve with the corrected RVs.

for the effects of the deformation of line profiles induced by stellar activity are those with v sin i in the range 5-15 km/s. In fact, it is difficult to find unblended spectral lines for stars with larger rotational velocity, while at lower rotational velocities the amplitude of the RV jitter and the slope of the BVS-RV relation should be lower. However, the case of HD 200466B with low v sin i and low residual spread in RV jitter, showing a significant correlation likely due to activity, indicate that the full picture is more complicated and further studies are required.

Chapter 10

Conclusions

We presented the analysis of high resolution stellar spectra, employed in the measurement of high precision radial velocities of wide binaries components from the italian planet search program ongoing at the "Telescopio Nazionale Galileo".
We explained in detail the procedure to remove the Iodine absorption lines from the stellar spectra involved in the radial velocity determination and the utility of the B star spectra to accomplish this task. Is the first time, to our knowledge, that high resolution spectra with Iodine lines employed for RV measurements is analyzed for spectral line asymmetries through line bisectors, after removal of Iodine.
With the spectra free of Iodine, we computed cross correlations with masks to obtain average absorption profiles to measure line bisectors, which are the middle points at constant flux between the blue and red sides of the profile. The masks were constructed with suitable lines (sharp, clean and weak wings) from a solar catalog.
Spectral line asymmetries were studied quantitatively through the bisector velocity span, given by the average velocity values of the line bisectors in precise zones (Bottom and Top) along the absorption profile. The relation between bisector velocity span and radial velocity was then studied in the search for trends to determine possible correlations.
We found three interesting cases in the plots of bisector velocity span against radial velocities, namely: a linear correlation with negative slope due to stellar activity likely due to spots crossing the stellar surface as the star rotates, for the stars HD 166435 (not belonging to the planet survey), HD 200466B and HD 126246A. A linear correlation with positive slope due to contamination of the spectra by light from the stellar companion for the stars HD 8071B and HD 76037A, and finally, the lack of correlation for stars known to host planets like 51 Peg and ρ CrB, together with the constancy of shape and orientation of their line bisectors, further supporting the conclusion that in these cases the observed

variation of radial velocities are due to Keplerian motion.
These results shows spreads fully consistent with internal errors, as determined from photon statistics, spectral resolution and intrinsic line profiles.
We are able to distinguish cases of spectral light contamination, to accurately treat the critical RV values and deal with reliable radial velocity curves of stars.
The very particular case of HD 76037A shows the usefulness of the analysis of line bisectors together with radial velocities to try to disentangle the nature of the correlation observed. The dispersion observed for the line bisectors suggest the presence of a companion around the fainter companion of the observed component A, however more spectra are needed to improve the velocity curve to attempt to characterize this possible hierarchical quadruple system.
We explored a procedure to apply corrections in the case of correlation due to activity. The equation given by the linear trend was employed to remove the activity effect in the observed radial velocities for the specific case of HD 166435.
The Monte Carlo method employed to explore the masses of possible substellar companions with the corrected velocities give smaller confidence limits on the basis of the lower dispersion of the corrected velocities which allow to improve the exclusion limits by a factor $2 \div 3$.
The success of such correction technique resides in the behaviour of active stars, if a correlation is found in more cases of stellar activity it would represent a powerful analytic tool to improve the measurements, to enhance the sample of surveyed stars to young or active ones in the study of planetary systems formation and set targets for imaging instruments like Planet Finder at VLT considering the intrinsic high brightness of young exoplanets.

Appendix A

List of lines for the mask

The lines employed in the mask were selected from the solar catalog by Moore et al. (1966). The information of interest appears in the following table of four columns. The first column contains the wavelenght, where the separation between lines is $\gtrsim 0.1$ Å. The second column has the reduced width expressed in F (Fraunhofer), which is defined as the dimensionless quantity $\Delta\lambda/\lambda \times 10^6$, where $\Delta\lambda$ is the equivalent width. The third column corresponds to the element of every wavelenght as appear in the original catalog. The fourth column is our classification of the lines to construct the masks for the CCF, it was made by inspecting the "The Sacramento Peak Atlas of the Solar Flux Spectrum" (Beckers et al. 1976) and labels correspond to: "y" (*very good*): sharp, clear, with weak wings; "y:" (*good*): clear but near other lines altering their wings; "?" (*not very good*): with small blends or strong wings. The total number of lines is 412 and the lines labeled as *very good* are 113.
An ascii file with all values appearing in the hardcopy catalog can be download from `ftp://nsokp.nso.edu/pub/atlas/linelist/`

Table A.1: List of lines employed in the masks.

Wavelength Å	Reduded widht Fraunhofer	Element	Label
6053.693	3	$NI1$	y
6056.013	12	$FE1$	y
6062.856	3	$ZR1$	?
6065.494	19	$FE1$	y
6078.499	15	$FE1$	y
6078.499	15	$FE1$	y
6081.448	3	$V1$	y
6082.718	6	$FE1$	y
6084.105	4	$FE2$	y
6085.257	7	$TI1$	y
6086.288	7	$NI1$	y
6089.574	5	$FE1$	y
6090.216	5	$V1$	y
6093.649	5	$FE1$	y
6094.377	3	$FE1$	?
6096.671	6	$FE1$	y
6098.250	3	$FE1P$	y :
5991.378	5	$FE2$	y
5996.740	3	$NI1$	y
6003.022	15	$FE1$	y
6005.551	4	$FE1$	y
6007.317	4	$NI1$	y
6007.968	10	$FE1$	y
6012.229	4	$NI1$	?
6013.497	14	$MN1$	?
6016.647	15	$MN1$	y
6021.803	16	$MN1$	y
6024.068	20	$FE1$	y
6027.059	11	$FE1$	y
5922.123	3	$TI1$	?
5929.682	7	$FE1$	y
5930.191	15	$FE1$	y
5934.665	13	$FE1$	y
5948.548	15	$SI1$	y :
5952.726	11	$FE1$	y :
5953.170	6	$TI1$	y :
5956.706	10	$FE1$	y
5965.835	4	$TI1$	?
5978.549	4	$TI1$	y :
5978.549	4	$TI1$	y :
5866.461	7	$TI1$	y :
5877.797	3	$FE1$	y :
5905.680	10	$FE1$	y
5916.257	9	$FE1-$	y :
5922.123	3	$TI1$	?
5929.682	7	$FE1$	y
5930.191	15	$FE1$	y
5809.224	9	$FE1$	y :
5831.606	4	$NI1$	y :
5838.381	3		?
5852.228	7	$FE1$	y
5853.688	10	$BA2$	y
5855.086	3	$FE1$	y
5855.086	3	$FE1$	y
5856.096	5	$FE1$	y
5859.596	13	$FE1$	y
5862.368	15	$FE1$	y
5866.461	7	$TI1$	y :
5754.666	13	$NI1$	?
5756.828	5		y
5760.841	6	$NI1$	y :
5772.149	9	$SI1$	y :
5772.149	9	$SI1$	y :
5775.088	9	$FE1$	y
5778.463	3	$FE1$	y
5783.073	5	$CR1$	y
5783.866	7	$CR1$	y :
5784.666	4	$FE1$	y :
5784.976	5	$CR1$	y :
5787.926	7	$CR1$	y
5793.079	7	$SI1$	y :
5793.922	5	$FE1$	y :
5805.226	7	$NI1$	y
5806.732	9	$FE1$	y
5809.224	9	$FE1$	y :
5809.224	9	$FE1$	y :
5701.108	7	$SI1$	y :
5701.557	16	$FE1$	y :
5702.328	5	$CR1$	y :
5711.095	19	$MG1$	y
5711.884	14	$/FE1$	?
5712.138	10	$FE1$	?
5715.094	13	$NI1$	y

Wavelength Å	Reduded width Fraunhofer	Element	Label
5717.841	11	$FE1$	?
5717.841	11	$FE1$	?
5731.772	10	$FE1$	y
5732.304	3	$FE1P$	y :
5741.856	6	$FE1$	y
5748.361	5	$NI1$	y
5752.042	10	$FE1$	y
5754.666	13	$NI1$	?
5754.666	13	$NI1$	?
5756.828	5		y
5760.841	6	$NI1$	y :
5649.996	6	$FE1$	y :
5650.694	7	$FE1$	?
5651.477	4	$FE1P$	y
5653.874	7	$FE1$	y :
5655.500	12	$FE1$	?
5655.500	12	$FE1$	?
5657.880	12	$SC2$	y
5659.593	4		y
5661.354	4	$FE1$	y
5662.524	17	$FE1$	y :
5662.939	9	$/FE1$	y :
5664.009	6	$NI1$	y :
5665.563	7	$SI1$	y
5667.524	9	$FE1$	y :
5669.040	6	$SC2$	?
5670.858	3	$V1$	y
5671.826	3	$SC1$	y :
5679.032	11	$FE1$	y
5682.208	10	$NI1$	y :
5682.208	10	$NI1$	y :
5684.493	11	$SI1$	y :
5690.433	10	$SI1$	y :
5691.505	7	$NI1-$	?
5691.505	7	$NI1-$	?
5693.650	9	$FE1$	y
5694.744	3	$CR1$	?
5694.991	8	$NI1$	?
5701.108	7	$SI1$	y :
5701.108	7	$SI1$	y :
5701.557	16	$FE1$	y :
5702.328	5	$CR1$	y :
5618.642	8	$FE1$	y
5619.609	6	$FE1$	y :
5625.328	7	$NI1$	?
5628.354	3	$NI1$	?
5628.650	3	$CR1$	y
5633.953	12	$FE1$	?
5635.831	6	$FE1$	y
5636.705	4	$FE1$	y :
5637.123	6	$NI1$	y :
5637.414	8	$FE1$	y :
5638.271	14	$FE1$	y
5641.448	12	$FE1$	y :
5643.087	3	$NI1$	y :
5649.996	6	$FE1$	y :
5650.694	7	$FE1$	?
5651.477	4	$FE1P$	y
5653.874	7	$FE1$	y :
5655.500	12	$FE1$	?
5543.944	11	$FE1$	y :
5546.514	10	$FE1$	y :
5562.716	9	$FE1$	y :
5569.631	30	$FE1$	?
5569.631	30	$FE1$	?
5576.099	22	$FE1$	?
5578.729	9	$NI1$	y :
5578.729	9	$NI1$	y :
5581.979	17	$CA1$	?
5584.773	6	$FE1$	?
5587.581	6	$FE1$	y :
5587.868	10	$NI1$	y :
5587.581	6	$FE1$	y :
5587.868	10	$NI1$	y :
5589.366	5	$NI1$	y :
5593.746	8	$NI1$	?
5494.474	5	$FE1$	y :
5494.888	3	$NI1$	y :
5497.526	22	$FE1$	y :
5501.477	22	$FE1$	?
5501.477	22	$FE1$	?
5505.889	9	$//MN$	y :
5506.791	23	$FE1$	?
5512.989	17	$CA1$	y :
5517.075	3	$FE1$	y :
5517.552	3	$SI1$	y
5522.454	8	$FE1$	y

Wavelength Å	Reduded width Fraunhofer	Element	Label
5525.552	18	$FE1$	?
5526.821	14	$SC2$	y
5534.848	11	$FE2$	?
5538.522	7	$FE1$	y
5539.291	4	$FE1$	y
5543.944	11	$FE1$	y :
5546.514	10	$FE1$	y :
5546.514	10	$FE1$	y :
5444.588	3	$CO1-$	y :
5445.053	23	$FE1$	y :
5452.850	3	$NI1$	y
5452.850	3	$NI1$	y
5461.559	4	$FE1$	y
5461.559	4	$FE1$	y
5462.501	7	$NI1$	y
5464.288	6	$FE1$	y :
5466.405	14	$FE1$	y
5466.993	5	$FE1$	y :
5470.093	4	$FE1$	y :
5470.093	4	$FE1$	y :
5472.713	7	$TI1-$	y
5473.168	3	$FE1$	y :
5483.108	8	$FE1$	y :
5483.364	8	$CO1$	y :
5487.153	6	$FE1$	?
5487.153	6	$FE1$	?
5488.170	3	$FE1P$	?
5490.703	3		y :
5494.474	5	$FE1$	y :
5494.888	3	$NI1$	y :
5497.526	22	$FE1$	y :
5501.477	22	$FE1$	?
5395.222	4	$FE1$	y :
5397.623	4	$FE1$	?
5398.287	14	$FE1$	y
5399.479	7	$MN1$	y :
5401.271	4	$FE1$	y :
5406.779	7	$FE1$	y :
5409.139	11	$FE1$	y :
5412.791	4	$FE1P$	y :
5412.791	4	$FE1P$	y :
5414.075	6	$FE2$	y :
5417.042	7	$FE1$	y
5418.775	9		y
5425.259	9	$FE2$	y
5432.548	9	$MN1$	y :
5432.955	13	$FE1-$	y :
5435.866	9	$NI1$	y :
5436.302	7	$FE1$	y :
5436.596	7	$FE1$	y :
5444.588	3	$CO1-$	y :
5445.053	23	$FE1$	y :
5452.850	3	$NI1$	y
5348.326	18	$CR1$	?
5352.049	4	$CO1$	y :
5364.880	25	$FE1$	?
5365.407	15	$FE1$	?
5364.880	25	$FE1$	?
5365.407	15	$FE1$	?
5367.476	29	$FE1$	y :
5373.714	11	$FE1$	y :
5373.714	11	$FE1$	y :
5379.581	10	$FE1$	y
5380.322	5	$C1$	?
5381.028	10	$//TI$	y :
5382.277	4		y
5382.277	4		y
5386.340	6	$FE1$	y
5386.971	4	$FE1-$	y :
5389.486	17	$FE1$	y :
5392.330	3	$NI1$	?
5395.222	4	$FE1$	y :
5397.623	4	$FE1$	?
5398.287	14	$FE1$	y
5399.479	7	$MN1$	y :
5399.479	7	$MN1$	y :
5401.271	4	$FE1$	y :
5406.779	7	$FE1$	y :
5300.751	11	$CR1$	y :
5301.047	4	$CO1$	y :
5304.185	3	$CR1$	y :
5305.866	5	$CR2$	y
5308.429	5	$CR2$	y :
5310.697	3	$CR2$	?
5312.863	4	$CR1$	?
5313.585	7	$CR2-$	y
5318.776	3	$CR1$	y :

Wavelength Å	Reduded width Fraunhofer	Element	Label
5320.040	3	$FE1$	$y:$
5321.114	8	$FE1$	$y:$
5322.049	11	$FE1$	$y:$
5325.560	8	$FE2$	$y:$
5326.149	6	$FE1$	$y:$
5329.147	13	$CR1$	?
5340.454	3	$CR1$	?
5342.708	5	$CO1$	y
5348.326	18	$CR1$	?
5352.049	4	$CO1$	$y:$
5352.049	4	$CO1$	$y:$
5256.933	3	$FE2$	?
5257.645	4	$CO1$	y
5260.390	5	$CA1$	$y:$
5261.708	20	$CA1$	?
5262.887	4	$FE1P$	$y:$
5265.964	10	$TI1$	?
5267.275	5	$FE1P$	?
5271.054	6		?
5272.003	4	$CR1$	$y:$
5272.003	4	$CR1$	$y:$
5279.877	3	$CR2$	?
5280.072	3	$FE1-$	?
5280.633	4	$CO1$	$y:$
5280.633	4	$CO1$	$y:$
5281.798	30	$FE1$	$y:$
5282.402	4	$TI1$	y
5284.112	13	$FE2$	?
5284.428	4	$FE1$	?
5284.615	4	$FE1P$	?
5285.130	5	$FE1P$	?
5288.533	10	$FE1$	$y:$
5292.590	7	$FE1$	y
5293.963	6	$FE1$	$y:$
5295.321	5	$FE1$	y
5296.702	18	$CR1$	y
5300.751	11	$CR1$	$y:$
5301.047	4	$CO1$	$y:$
5304.185	3	$CR1$	$y:$
5305.866	5	$CR2$	y
5305.866	5	$CR2$	y
5308.429	5	$CR2$	$y:$
5310.697	3	$CR2$	?
5312.863	4	$CR1$	?
5313.585	7	$CR2-$	y
5210.392	17	$TI1$	?
5211.535	6	$FE1-$	$y:$
5212.691	4	$CO1$	$y:$
5214.130	4	$CR1$	$y:$
5217.396	21	$FE1$	$y:$
5218.209	10	$CU1$	$y:$
5218.209	10	$CU1$	$y:$
5219.706	5	$TI1$	$y:$
5221.763	5	$/CR1$	y
5223.190	5	$FE1$	y
5224.310	7	$TI1$	?
5224.551	5	$CR1-$	?
5225.534	12	$FE1$	$y:$
5228.103	4	$CR1$	$y:$
5228.383	12	$FE1$	$y:$
5230.216	5	$//CO$	$y:$
5234.630	16	$FE2$	y
5237.325	9	$CR2$	y
5238.969	3	$CR1$	y
5242.500	16	$FE1$	y
5247.058	11	$FE1$	$y:$
5247.574	15	$CR1$	$y:$
5247.923	3	$/CO1$	$y:$
5250.216	12	$FE1$	?
5253.033	3	$FE1P$	$y:$
5253.468	15	$FE1$	?
5256.933	3	$FE2$	?
5257.645	4	$CO1$	y
5260.390	5	$CA1$	$y:$
5260.390	5	$CA1$	$y:$
5261.708	20	$CA1$	?
5262.887	4	$FE1P$	$y:$
5265.964	10	$TI1$	?
5267.275	5	$FE1P$	?
5176.565	11	$NI1$	$y:$
5178.801	5	$FE1$	$y:$
5180.069	9	$FE1$	$y:$
5186.557	3	$NI1$	?
5192.978	16	$TI1$	$y:$
5194.949	25	$FE1$	$y:$
5195.480	22	$FE1$	$y:$
5196.065	15	$FE1$	$y:$
5197.170	5	$NI1$	$y:$

Wavelength Å	Reduded width Fraunhofer	Element	Label
5197.576	15	$FE2$	y :
5197.942	7	$FE1$	y :
5198.718	18	$FE1$	y :
5198.718	18	$FE1$	y :
5200.185	4	$CR1$	?
5210.392	17	$TI1$	?
5211.535	6	$FE1-$	y :
5212.691	4	$CO1$	y :
5214.130	4	$CR1$	y :
5217.396	21	$FE1$	y :
5218.209	10	$CU1$	y :
5219.706	5	$TI1$	y :
5221.763	5	$/CR1$	y
5223.190	5	$FE1$	y
5224.310	7	$TI1$	?
5224.551	5	$CR1-$	?
5123.470	3	$CR1$	?
5126.199	15	$FE1$	?
5127.368	18	$FE1$	?
5127.688	4	$FE1P$	y :
5130.588	3	$C2-$	?
5130.588	3	$C2-$	?
5132.674	5	$FE2P$	?
5136.099	4	$FE1$	?
5137.080	18	$NI1$	?
5137.579	4	$C2$	?
5140.823	3	$FE1$	y
5145.468	6	$TI1$	?
5151.917	20	$FE1$	?
5152.190	7	$TI1$	?
5154.075	14	$TI2$	?
5155.132	9	$NI1$	y :
5155.132	9	$NI1$	y :
5157.984	4	$NI1$	y
5159.065	13	$FE1$	?
5176.565	11	$NI1$	y :
5178.801	5	$FE1$	y :
5180.069	9	$FE1$	y :
5082.349	12	$NI1$	?
5087.426	8	$Y2$	y :
5087.426	8	$Y2$	y :
5088.543	5	$NI1-$	?
5094.418	6	$NI1$	y
5100.656	3	$FE2$	?
5102.973	8	$NI1$	?
5108.394	4		?
5109.657	14	$FE1$	?
5113.447	5	$TI1$	y :
5123.470	3	$CR1$	?
5126.199	15	$FE1$	?
5127.368	18	$FE1$	?
5127.688	4	$FE1P$	y :
5130.588	3	$C2-$	?
5132.674	5	$FE2P$	?
5136.099	4	$FE1$	?
5137.080	18	$NI1$	?
5044.218	14	$FE1$	y :
5051.905	4	$CR1$	?
5052.151	8	$C1$	?
5054.647	7	$FE1$	y
5056.846	5	$FE1$	?
5067.155	14	$FE1$	y
5074.753	23	$FE1$	?
5082.349	12	$NI1$	?
5087.426	8	$Y2$	y :
5088.543	5	$NI1-$	?
5094.418	6	$NI1$	y

Bibliography

R. Alonso. Detección y caracterización de exoplanetas mediante el método de los tránsitos. *Ph.D. Thesis*, 2006. 2.2, 2.3

R. Alonso, T. M. Brown, G. Torres, D. W. Latham, A. Sozzetti, G. Mandushev, J. A. Belmonte, D. Charbonneau, H. J. Deeg, E. W. Dunham, F. T. O'Donovan, and R. P. Stefanik. TrES-1: The Transiting Planet of a Bright K0 V Star. *ApJ*, 613:L153–L156, October 2004. doi: 10.1086/425256. 2.2.2

P. Artymowicz. Dynamics of Gaseous Disks with Planets. In *ASP Conf. Ser. 324: Debris Disks and the Formation of Planets*, pages 39–+, December 2004. 2.1

S. L. Baliunas, R. A. Donahue, W. H. Soon, J. H. Horne, J. Frazer, L. Woodard-Eklund, M. Bradford, L. M. Rao, O. C. Wilson, Q. Zhang, W. Bennett, J. Briggs, S. M. Carroll, D. K. Duncan, D. Figueroa, H. H. Lanning, T. Misch, J. Mueller, R. W. Noyes, D. Poppe, A. C. Porter, C. R. Robinson, J. Russell, J. C. Shelton, T. Soyumer, A. H. Vaughan, and J. H. Whitney. Chromospheric variations in main-sequence stars. *ApJ*, 438:269–287, January 1995. doi: 10.1086/175072. 4.3.2

A. Baranne, D. Queloz, M. Mayor, G. Adrianzyk, G. Knispel, D. Kohler, D. Lacroix, J.-P. Meunier, G. Rimbaud, and A. Vin. ELODIE: A spectrograph for accurate radial velocity measurements. *A&AS*, 119:373–390, October 1996. 3.2

J. M. Beckers, C. A. Bridges, and L. B. Gilliam. *A high resolution spectral atlas of the solar irradiance from 380 to 700 nanometers. Volume 2: Graphical form.* Unknown, June 1976. 6.1.2.1, A

G. F. Benedict, B. McArthur, E. Nelan, D. Story, A. L. Whipple, P. J. Shelus, W. H. Jefferys, P. D. Hemenway, O. G. Franz, L. H. Wasserman, R. L. Duncombe, W. van Altena, and L. W. Fredrick. Photometry of Proxima Cen-

tauri and Barnard's Star Using Hubble Space Telescope Fine Guidance Sensor 3: A Search for Periodic Variations. *AJ*, 116:429–439, July 1998. doi: 10.1086/300420. 9.1

G. F. Benedict, B. E. McArthur, T. Forveille, X. Delfosse, E. Nelan, R. P. Butler, W. Spiesman, G. Marcy, B. Goldman, C. Perrier, W. H. Jefferys, and M. Mayor. A Mass for the Extrasolar Planet Gliese 876b Determined from Hubble Space Telescope Fine Guidance Sensor 3 Astrometry and High-Precision Radial Velocities. *ApJ*, 581:L115–L118, December 2002. doi: 10.1086/346073. 2.2.4

I. A. Bond, A. Udalski, M. Jaroszyński, N. J. Rattenbury, B. Paczyński, I. Soszyński, L. Wyrzykowski, M. K. Szymański, M. Kubiak, O. Szewczyk, K. Żebruń, G. Pietrzyński, F. Abe, D. P. Bennett, S. Eguchi, Y. Furuta, J. B. Hearnshaw, K. Kamiya, P. M. Kilmartin, Y. Kurata, K. Masuda, Y. Matsubara, Y. Muraki, S. Noda, K. Okajima, T. Sako, T. Sekiguchi, D. J. Sullivan, T. Sumi, P. J. Tristram, T. Yanagisawa, and P. C. M. Yock. OGLE 2003-BLG-235/MOA 2003-BLG-53: A Planetary Microlensing Event. *ApJ*, 606: L155–L158, May 2004. doi: 10.1086/420928. 2.2.3, 2.5

X. Bonfils, X. Delfosse, S. Udry, N. C. Santos, T. Forveille, and D. Ségransan. Metallicity of M dwarfs. I. A photometric calibration and the impact on the mass-luminosity relation at the bottom of the main sequence. *A&A*, 442:635–642, November 2005. doi: 10.1051/0004-6361:20053046. 2.3.1

A. P. Boss. Formation of gas and ice giant planets. *Earth and Planetary Science Letters*, 202:513–523, September 2002a. 2.1

A. P. Boss. Stellar Metallicity and the Formation of Extrasolar Gas Giant Planets. *ApJ*, 567:L149–L153, March 2002b. doi: 10.1086/340108. 2.3.1

F. Bouchy and P. Connes. Autoguider locked on a fiber input for precision stellar radial velocities. *A&AS*, 136:193–204, April 1999. 3.2

F. Bouchy, F. Pepe, and D. Queloz. Fundamental photon noise limit to radial velocity measurements. *A&A*, 374:733–739, August 2001. doi: 10.1051/0004-6361:20010730. 3

F. Bouchy, S. Udry, M. Mayor, C. Moutou, F. Pont, N. Iribarne, R. da Silva, S. Ilovaisky, D. Queloz, N. C. Santos, D. Ségransan, and S. Zucker. ELODIE metallicity-biased search for transiting Hot Jupiters. II. A very hot Jupiter transiting the bright K star HD 189733. *A&A*, 444:L15–L19, December 2005. doi: 10.1051/0004-6361:200500201. 2.2.2

A. Burrows and et al. Extra-Solar Giant Planet and Brown Dwarf Models. In *ASP Conf. Ser. 119: Planets Beyond the Solar System and the Next Generation of Space Missions*, pages 9–+, 1997. 2.2.5, 2.7, 9.1

R. P. Butler, G. W. Marcy, E. Williams, C. McCarthy, P. Dosanjh, and S. S. Vogt. Attaining Doppler Precision of 3 M s-1. *PASP*, 108:500–+, June 1996. 3, 3.1, 5.3.2

R. P. Butler, S. S. Vogt, G. W. Marcy, D. A. Fischer, J. T. Wright, G. W. Henry, G. Laughlin, and J. J. Lissauer. A Neptune-Mass Planet Orbiting the Nearby M Dwarf GJ 436. *ApJ*, 617:580–588, December 2004. doi: 10.1086/425173. 2.2.1

D. Charbonneau, T. M. Brown, D. W. Latham, and M. Mayor. Detection of Planetary Transits Across a Sun-like Star. *ApJ*, 529:L45–L48, January 2000. doi: 10.1086/312457. 2.2.2, 2.4

D. Charbonneau, L. E. Allen, S. T. Megeath, G. Torres, R. Alonso, T. M. Brown, R. L. Gilliland, D. W. Latham, G. Mandushev, F. T. O'Donovan, and A. Sozzetti. Detection of Thermal Emission from an Extrasolar Planet. *ApJ*, 626:523–529, June 2005. 2.2, 2.2.5

G. Chauvin, A.-M. Lagrange, C. Dumas, B. Zuckerman, D. Mouillet, I. Song, J.-L. Beuzit, and P. Lowrance. A giant planet candidate near a young brown dwarf. Direct VLT/NACO observations using IR wavefront sensing. *A&A*, 425: L29–L32, October 2004. 2.2

G. Chauvin, A.-M. Lagrange, C. Dumas, B. Zuckerman, D. Mouillet, I. Song, J.-L. Beuzit, and P. Lowrance. Giant planet companion to 2MASSW J1207334-393254. *A&A*, 438:L25–L28, August 2005a. doi: 10.1051/0004-6361:200500116. 2.2.5

G. Chauvin, A.-M. Lagrange, B. Zuckerman, C. Dumas, D. Mouillet, I. Song, J.-L. Beuzit, P. Lowrance, and M. S. Bessell. A companion to AB Pic at the planet/brown dwarf boundary. *A&A*, 438:L29–L32, August 2005b. doi: 10.1051/0004-6361:200500111. 2.2

R. U. Claudi, A. Bonanno, S. Leccia, R. Ventura, S. Desidera, R. Gratton, R. Cosentino, L. Paternò, and M. Endl. Asteroseismology of Procyon A with SARG at TNG. *A&A*, 429:L17–L20, January 2005. doi: 10.1051/0004-6361: 200400106. 2

D. Deming, S. Seager, L. J. Richardson, and J. Harrington. Infrared radiation from an extrasolar planet. *Nature*, 434:740–743, March 2005. 2.2, 2.2.5

S. Desidera. *Ph.D. Thesis*, 1996. 3.2

S. Desidera, R. G. Gratton, M. Endl, M. Barbieri, R. U. Claudi, R. Cosentino, S. Lucatello, F. Marzari, and S. Scuderi. A search for planets in the metal-enriched binary HD 219542. *A&A*, 405:207–221, July 2003. doi: 10.1051/0004-6361:20030531. 5.3.2, 5.4, 8.1.8, 9.2, 9.2.3

S. Desidera, R. G. Gratton, R. U. Claudi, E. Carretta, S. Lucatello, A. Martinez-Fiorenzano, G. Bonanno, R. Cosentino, S. Scuderi, M. Barbieri, M. Endl, F. Marzari, E. Brocato, M. Dolci, and G. Valentini. Searching for Planets around Stars in Wide Binaries. In *ASP Conf. Ser. 321: Extrasolar Planets: Today and Tomorrow*, pages 103–+, December 2004a. 5

S. Desidera, R. G. Gratton, M. Endl, R. U. Claudi, and R. Cosentino. No planet around HD 219542 B. *A&A*, 420:L27–L30, June 2004b. doi: 10.1051/0004-6361:20040155. 8.1.8

S. Desidera, R. G. Gratton, S. Scuderi, R. U. Claudi, R. Cosentino, M. Barbieri, G. Bonanno, E. Carretta, M. Endl, S. Lucatello, A. F. Martinez Fiorenzano, and F. Marzari. Abundance difference between components of wide binaries. *A&A*, 420:683–697, June 2004c. doi: 10.1051/0004-6361:20041242. 5.1, 5.2.2

J. R. Dormand and M. M. Woolfson. The capture theory and planetary condensation. *MNRAS*, 151:307–+, 1971. 2.1

J. R. Dormand and M. M. Woolfson. *Modelling the capture theory*, pages 371–383. The Physics of the Planets, 1988. 2.1

A. Eggenberger, S. Udry, and M. Mayor. Statistical properties of exoplanets. III. Planet properties and stellar multiplicity. *A&A*, 417:353–360, April 2004. doi: 10.1051/0004-6361:20034164. 2.3.2, 5.1

S. G. Els, M. Kürster, M. Endl, A. P. Hatzes, and G. Porto de Mello. Precision Radial Velocities of Active Stars. In *ASP Conf. Ser. 294: Scientific Frontiers in Research on Extrasolar Planets*, pages 55–58, 2003. 9.2

M. Endl, M. Kürster, and S. Els. The planet search program at the ESO Coudé Echelle spectrometer. I. Data modeling technique and radial velocity precision tests. *A&A*, 362:585–594, October 2000. 3.1, 5.3.2

M. Endl, M. Kürster, S. H. A. P. Els, W. D. Cochran, K. Dennerl, and S. Döbereiner. The planet search program at the ESO Coudé Echelle spectrometer. III. The complete Long Camera survey results. *A&A*, 392:671–690, September 2002. doi: 10.1051/0004-6361:20020937. 9.2.3

L. Eyer and M. Grenon. Photometric Variability in the HR Diagram. In *ESA SP-402: Hipparcos - Venice '97*, pages 467–472, 1997. 8.1.6

D. A. Fischer and J. Valenti. The Planet-Metallicity Correlation. *ApJ*, 622: 1102–1117, April 2005. doi: 10.1086/428383. 2.3.1, 2.8, 5.4

D. A. Fischer, G. W. Marcy, R. P. Butler, and S. S. Vogt. Characteristics of Extrasolar Planets. In *ASP Conf. Ser. 324: Debris Disks and the Formation of Planets*, pages 133–+, December 2004. 2.3.2

J. Ge. Fixed Delay Interferometry for Doppler Extrasolar Planet Detection. *ApJ*, 571:L165–L168, June 2002. doi: 10.1086/341226. 3

K. Goździewski, M. Konacki, and A. Wolszczan. Long-Term Stability and Dynamical Environment of the PSR 1257+12 Planetary System. *ApJ*, 619:1084–1097, February 2005. 2

R. G. Gratton, E. Carretta, G. Clementini, and C. Sneden. Metal Abundances of One Hundred HIPPARCOS Dwarfs. In *ESA SP-402: Hipparcos - Venice '97*, pages 339–342, 1997. 5.2.2

R. G. Gratton, G. Bonanno, P. Bruno, A. Cali, R. U. Claudi, R. Cosentino, S. Desidera, F. Diego, G. Farisato, G. Martorana, M. Rebeschini, and S. Scuderi. SARG: the high resolution spectrograph of TNG. *Experimental Astronomy*, 12:107–143, 2001. 5

D. F. Gray. Measurements of rotation and turbulence in F, G, and K dwarfs. *ApJ*, 281:719–722, June 1984. doi: 10.1086/162149. 9.1

D. F. Gray. The rotation effect - A mechanism for measuring granulation velocities in stars. *PASP*, 98:319–324, March 1986. 8.3.1

D. F. Gray. *Lectures on spectral-line analysis: F,G, and K stars*. Arva: Ontario Gray, 1988, 1988. 4.2.1, 4.2.2, 4.3.3, 6.4

D. F. Gray. *The observation and analysis of stellar photospheres*. Cambridge Astrophysics Series, Cambridge: Cambridge University Press, 1992, 2nd ed., ISBN 0521403200., 1992. 4.2.2, 5.2.2, 6.6

D. F. Gray. Shapes of Spectral Line Bisectors for Cool Stars. *PASP*, 117:711–720, July 2005. doi: 10.1086/430412. 4.1, 4.2.2

A. P. Hatzes. Radial-Velocity Variations from Starspots. In *ASP Conf. Ser. 185: IAU Colloq. 170: Precise Stellar Radial Velocities*, pages 259–+, 1999. 9.2

A. P. Hatzes. Starspots and exoplanets. *Astronomische Nachrichten*, 323:392–394, July 2002. doi: 10.1002/1521-3994(200208)323:3/4. 8.3, 8.3.1, 9.2, 9.3

A. P. Hatzes and G. Wuchterl. Astronomy: Giant planet seeks nursery place. *Nature*, 436:182–183, July 2005. doi: 10.1038/436182a. 5.1

A. P. Hatzes, W. D. Cochran, and E. J. Bakker. The Lack of Spectral Variability in 51 Pegasi: Confirmation of the Planet Hypothesis. *ApJ*, 508:380–386, November 1998. doi: 10.1086/306404. 8.1.6

A. P. Hatzes, W. D. Cochran, B. McArthur, S. L. Baliunas, G. A. H. Walker, B. Campbell, A. W. Irwin, S. Yang, M. Kürster, M. Endl, S. Els, R. P. Butler, and G. W. Marcy. Evidence for a Long-Period Planet Orbiting ϵ Eridani. *ApJ*, 544:L145–L148, December 2000. doi: 10.1086/317319. 9.1

A. P. Hatzes, W. D. Cochran, M. Endl, B. McArthur, D. B. Paulson, G. A. H. Walker, B. Campbell, and S. Yang. A Planetary Companion to γ Cephei A. *ApJ*, 599:1383–1394, December 2003. doi: 10.1086/379281. 5.1

B. Hauck and M. Mermilliod. Uvbybeta photoelectric photometric catalogue. *A&AS*, 129:431–433, May 1998. 5.2.2

W. D. Heacox. Wavelength-precise slit spectroscopy with optical fiber image scramblers. In *ASP Conf. Ser. 3: Fiber Optics in Astronomy*, pages 204–235, 1988. 3.2

G. Hébrard and A. Lecavelier Des Etangs. A posteriori detection of the planetary transit of HD 189733 b in the Hipparcos photometry. *A&A*, 445:341–346, January 2006. doi: 10.1051/0004-6361:20054308. 2.2.2

A. Hempelmann, J. H. M. M. Schmitt, and K. Stcepien. Coronal X-ray emission of cool stars in relation to chromospheric activity and magnetic cycles. *A&A*, 305:284–+, January 1996. 4.3.3

G. W. Henry, S. L. Baliunas, R. A. Donahue, F. C. Fekel, and W. Soon. Photometric and Ca II H and K Spectroscopic Variations in Nearby Sun-like Stars with Planets. III. *ApJ*, 531:415–437, March 2000a. doi: 10.1086/308466. 8.1.6

G. W. Henry, G. W. Marcy, R. P. Butler, and S. S. Vogt. A Transiting "51 Peg-like" Planet. *ApJ*, 529:L41–L44, January 2000b. doi: 10.1086/312458. 2.2.2

G. Hill. Intep - an Effective Interpolation Subroutine. *Publications of the Dominion Astrophysical Observatory Victoria*, 16:67–+, 1982. 6.1.1, 6.2

M. J. Holman and P. A. Wiegert. Long-Term Stability of Planets in Binary Systems. *AJ*, 117:621–628, January 1999. doi: 10.1086/300695. 5.1, 5.2.1

J. H. Jeans. The part played by rotation in cosmic evolution. *MNRAS*, 77: 186–199, January 1917. 2.1

M. Konacki. An extrasolar giant planet in a close triple-star system. *Nature*, 436: 230–233, July 2005. doi: 10.1038/nature03856. 2.3.2, 5.1

M. Kürster, M. Endl, F. Rouesnel, S. Els, A. Kaufer, S. Brillant, A. P. Hatzes, S. H. Saar, and W. D. Cochran. The low-level radial velocity variability in Barnard's star (= GJ 699). Secular acceleration, indications for convective redshift, and planet mass limits. *A&A*, 403:1077–1087, June 2003. doi: 10.1051/0004-6361:20030396.

Pierre Laplace. *Exposition du Sistème du Monde Paris*. Imprimiere Cercle-Social, 1796. 2.1

J. L. Linsky. Stellar chromospheres. *ARA&A*, 18:439–488, 1980. doi: 10.1146/annurev.aa.18.090180.002255. 4.3.3

J. López-Santiago, D. Montes, M. J. Fernández-Figueroa, and L. W. Ramsey. Rotational modulation of the photospheric and chromospheric activity in the young, single K2-dwarf PW And. *A&A*, 411:489–502, December 2003. doi: 10.1051/0004-6361:20031377.

G. Marcy, R. P. Butler, D. Fischer, S. Vogt, J. T. Wright, C. G. Tinney, and H. R. A. Jones. Observed Properties of Exoplanets: Masses, Orbits, and Metallicities. *Progress of Theoretical Physics Supplement*, 158:24–42, 2005. 2.3.1, 2.9, 2.3.2

G. W. Marcy and R. P. Butler. Precision radial velocities with an iodine absorption cell. *PASP*, 104:270–277, April 1992. 3.3

A. F. Martínez Fiorenzano, R. G. Gratton, S. Desidera, R. Cosentino, and M. Endl. Line bisectors and radial velocity jitter from SARG spectra. *A&A*, 442:775–784, November 2005. doi: 10.1051/0004-6361:20052888. 4.3.4, 7.2

F. Marzari and S. J. Weidenschilling. Eccentric Extrasolar Planets: The Jumping Jupiter Model. *Icarus*, 156:570–579, April 2002. doi: 10.1006/icar.2001.6786. 2.1

F. S. Masset and J. C. B. Papaloizou. Runaway Migration and the Formation of Hot Jupiters. *ApJ*, 588:494–508, May 2003. 2.1

M. Mayor and D. Queloz. A Jupiter-Mass Companion to a Solar-Type Star. *Nature*, 378:355–+, November 1995. 2, 8.1.6

M. Mayor, F. Pepe, D. Queloz, F. Bouchy, G. Rupprecht, G. Lo Curto, G. Avila, W. Benz, J.-L. Bertaux, X. Bonfils, T. dall, H. Dekker, B. Delabre, W. Eckert, M. Fleury, A. Gilliotte, D. Gojak, J. C. Guzman, D. Kohler, J.-L. Lizon, A. Longinotti, C. Lovis, D. Megevand, L. Pasquini, J. Reyes, J.-P. Sivan, D. Sosnowska, R. Soto, S. Udry, A. van Kesteren, L. Weber, and U. Weilenmann. Setting New Standards with HARPS. *The Messenger*, 114:20–24, December 2003. 2.2.1, 3

H. Mizuno. Formation of the Giant Planets. *Progress of Theoretical Physics*, 64: 544–557, August 1980. 2.1

D. Montes, M. J. Fernández-Figueroa, E. De Castro, M. Cornide, A. Latorre, and J. Sanz-Forcada. Multiwavelength optical observations of chromospherically active binary systems. III. High resolution echelle spectra from Ca ii H and K to Ca ii IRT. *A&AS*, 146:103–140, October 2000. 4.3.3

C. E. Moore, M. G. J. Minnaert, and J. Houtgast. *The solar spectrum 2935 A to 8770 A*. National Bureau of Standards Monograph, Washington: US Government Printing Office (USGPO), 1966, 1966. 6.1.2.1, A

B. Mosser, F. Bouchy, C. Catala, E. Michel, R. Samadi, F. Thévenin, P. Eggenberger, D. Sosnowska, C. Moutou, and A. Baglin. Seismology and activity of the F type star HD 49933. *A&A*, 431:L13–L16, February 2005. doi: 10.1051/0004-6361:200500003.

N. Murray, B. Chaboyer, P. Arras, B. Hansen, and R. W. Noyes. Stellar Pollution in the Solar Neighborhood. *ApJ*, 555:801–815, July 2001. doi: 10.1086/321527. 5.1

R. Neuhäuser, E. W. Guenther, G. Wuchterl, M. Mugrauer, A. Bedalov, and P. H. Hauschildt. Evidence for a co-moving sub-stellar companion of GQ Lup. *A&A*, 435:L13–L16, May 2005. 2.2

R. W. Noyes, L. W. Hartmann, S. L. Baliunas, D. K. Duncan, and A. H. Vaughan. Rotation, convection, and magnetic activity in lower main-sequence stars. *ApJ*, 279:763–777, April 1984. doi: 10.1086/161945. 8.1.1, 9.1

R. W. Noyes, S. Jha, S. G. Korzennik, M. Krockenberger, P. Nisenson, T. M. Brown, E. J. Kennelly, and S. D. Horner. A Planet Orbiting the Star Rho Coronae Borealis. *ApJ*, 483:L111+, July 1997. doi: 10.1086/310754. 8.1.7

D. B. Paulson, S. H. Saar, W. D. Cochran, and A. P. Hatzes. Searching for Planets in the Hyades. II. Some Implications of Stellar Magnetic Activity. *AJ*, 124:572–582, July 2002. doi: 10.1086/341171. 9.2

D. B. Paulson, S. H. Saar, W. D. Cochran, and G. W. Henry. Searching for Planets in the Hyades. III. The Quest for Short-Period Planets. *AJ*, 127:1644–1652, March 2004. 4.4, 9.2

F. Pepe, M. Mayor, G. Rupprecht, G. Avila, P. Ballester, J.-L. Beckers, W. Benz, J.-L. Bertaux, F. Bouchy, B. Buzzoni, C. Cavadore, S. Deiries, H. Dekker, B. Delabre, S. D'Odorico, W. Eckert, J. Fischer, M. Fleury, M. George, A. Gilliotte, D. Gojak, J.-C. Guzman, F. Koch, D. Kohler, H. Kotzlowski, D. Lacroix, J. Le Merrer, J.-L. Lizon, G. Lo Curto, A. Longinotti, D. Megevand, L. Pasquini, P. Petitpas, M. Pichard, D. Queloz, J. Reyes, P. Richaud, J.-P. Sivan, D. Sosnowska, R. Soto, S. Udry, E. Ureta, A. van Kesteren, L. Weber, U. Weilenmann, A. Wicenec, G. Wieland, J. Christensen-Dalsgaard, D. Dravins, A. Hatzes, M. Kürster, F. Paresce, and A. Penny. HARPS: ESO's coming planet searcher. Chasing exoplanets with the La Silla 3.6-m telescope. *The Messenger*, 110:9–14, December 2002. 3.2

F. Pepe, F. Bouchy, D. Queloz, and M. Mayor. From CORALIE to HARPS: Towards 1 Meter/Sec RV Precision. In *ASP Conf. Ser. 294: Scientific Frontiers in Research on Extrasolar Planets*, pages 39–42, 2003. 3.3

M. Perryman and O. Hainaut. Extra-solar planets. Technical report, 2005. 2.2.2, 2.2.4

M. A. C. Perryman. Extra-solar planets. *Reports of Progress in Physics*, 63: 1209–1272, 2000. 2.2.1

J. B. Pollack, O. Hubickyj, P. Bodenheimer, J. J. Lissauer, M. Podolak, and Y. Greenzweig. Formation of the Giant Planets by Concurrent Accretion of Solids and Gas. *Icarus*, 124:62–85, November 1996. 2.1

M. S. Povich, M. S. Giampapa, J. A. Valenti, T. Tilleman, S. Barden, D. Deming, W. C. Livingston, and C. Pilachowski. Limits on Line Bisector Variability for Stars with Extrasolar Planets. *AJ*, 121:1136–1146, February 2001. doi: 10.1086/318745. 8.1.6, 8.1.7

D. Queloz. Echelle Spectroscopy with a CCD at Low Signal-To-Noise Ratio. In *IAU Symp. 167: New Developments in Array Technology and Applications*, pages 221–+, 1995. 3.2

D. Queloz, M. Casse, and M. Mayor. The Fiber-Fed Spectrograph, a Tool to Detect Planets. In *ASP Conf. Ser. 185: IAU Colloq. 170: Precise Stellar Radial Velocities*, pages 13–+, 1999. 3.2

D. Queloz, G. W. Henry, J. P. Sivan, S. L. Baliunas, J. L. Beuzit, R. A. Donahue, M. Mayor, D. Naef, C. Perrier, and S. Udry. No planet for HD 166435. *A&A*, 379:279–287, November 2001. 4.3.4, 6.1.2, 7.2, 8.1.1, 8.1.1, 9.2.2

S. Randich. Coronal activity among open cluster stars. In *ASP Conf. Ser. 198: Stellar Clusters and Associations: Convection, Rotation, and Dynamos*, pages 401–+, 2000. 4.3.3

E. J. Rivera, J. J. Lissauer, R. P. Butler, G. W. Marcy, S. S. Vogt, D. A. Fischer, T. M. Brown, G. Laughlin, and G. W. Henry. A $\sim 7.5\ M_{\oplus;}$ Planet Orbiting the Nearby Star, GJ 876. *ApJ*, 634:625–640, November 2005. doi: 10.1086/491669. 2.2.1

S. H. Saar and R. A. Donahue. Activity-related Radial Velocity Variation in Cool Stars. *ApJ*, 485:319–+, August 1997. doi: 10.1086/304392. 2.2.1, 8.3.1, 9.1

S. H. Saar and D. Fischer. Correcting Radial Velocities for Long-Term Magnetic Activity Variations. *ApJ*, 534:L105–L108, May 2000. doi: 10.1086/312648. 8.3.1, 9.1

S. H. Saar, R. P. Butler, and G. W. Marcy. Magnetic Activity-related Radial Velocity Variations in Cool Stars: First Results from the Lick Extrasolar Planet Survey. *ApJ*, 498:L153+, May 1998. doi: 10.1086/311325. 4.4

N. C. Santos, F. Bouchy, M. Mayor, F. Pepe, D. Queloz, S. Udry, C. Lovis, M. Bazot, W. Benz, J.-L. Bertaux, G. Lo Curto, X. Delfosse, C. Mordasini, D. Naef, J.-P. Sivan, and S. Vauclair. The HARPS survey for southern extra-solar planets. II. A 14 Earth-masses exoplanet around μ Arae. *A&A*, 426: L19–L23, October 2004. doi: 10.1051/0004-6361:200400076. 2.2.1

N. C. Santos, G. Israelian, M. Mayor, J. P. Bento, P. C. Almeida, S. G. Sousa, and A. Ecuvillon. Spectroscopic metallicities for planet-host stars: Extending the samples. *A&A*, 437:1127–1133, July 2005. doi: 10.1051/0004-6361:20052895. 2.3.1

B. Sato, D. A. Fischer, G. W. Henry, G. Laughlin, R. P. Butler, G. W. Marcy, S. S. Vogt, P. Bodenheimer, S. Ida, E. Toyota, A. Wolf, J. A. Valenti, L. J. Boyd, J. A. Johnson, J. T. Wright, M. Ammons, S. Robinson, J. Strader,

C. McCarthy, K. L. Tah, and D. Minniti. The N2K Consortium. II. A Transiting Hot Saturn around HD 149026 with a Large Dense Core. *ApJ*, 633:465–473, November 2005. doi: 10.1086/449306. 2.2.2

W. J. Schuster and P. E. Nissen. Uvby-beta photometry of high-velocity and metal-poor stars. II - Intrinsic color and metallicity calibrations. *A&A*, 221: 65–77, August 1989. 5.2.2

B. A. Skiff. The Variability of HD 126246 = ADS 9251. *Informational Bulletin on Variable Stars*, 3919:1–+, August 1993. 8.1.3

M. A. Smith, W. Livingston, and Y.-R. Huang. The amplification of solar-line asymmetries by rotation. *PASP*, 99:297–302, April 1987. 4.2.2, 8.3, 8.3.1

K. Stepien and P. Ulmschneider. X-ray emission from acoustically heated coronae. *A&A*, 216:139–142, June 1989. 4.3.3

C. G. Toner and D. F. Gray. The starpatch on the G8 dwarf XI Bootis A. *ApJ*, 334:1008–1020, November 1988. doi: 10.1086/166893. 4.3.4, 6.3, 8.3.1

S. Tremaine and N. L. Zakamska. Extrasolar Planet Orbits and Eccentricities. In *AIP Conf. Proc. 713: The Search for Other Worlds*, pages 243–252, June 2004. doi: 10.1063/1.1774531. 2.3.2

A. Udalski, M. Jaroszyński, B. Paczyński, M. Kubiak, M. K. Szymański, I. Soszyński, G. Pietrzyński, K. Ulaczyk, O. Szewczyk, Ł. Wyrzykowski, G. W. Christie, D. L. DePoy, S. Dong, A. Gal-Yam, B. S. Gaudi, A. Gould, C. Han, S. Lépine, J. McCormick, B.-G. Park, R. W. Pogge, D. P. Bennett, I. A. Bond, Y. Muraki, P. J. Tristram, P. C. M. Yock, J.-P. Beaulieu, D. M. Bramich, S. W. Dieters, J. Greenhill, K. Hill, K. Horne, and D. Kubas. A Jovian-Mass Planet in Microlensing Event OGLE-2005-BLG-071. *ApJ*, 628:L109–L112, August 2005. doi: 10.1086/432795. 2.2.3

S. Udry, M. Mayor, and N. C. Santos. Statistical properties of exoplanets. I. The period distribution: Constraints for the migration scenario. *A&A*, 407: 369–376, August 2003. doi: 10.1051/0004-6361:20030843. 2.3.2

J. A. Valenti and D. A. Fischer. Spectroscopic Properties of Cool Stars (SPOCS). I. 1040 F, G, and K Dwarfs from Keck, Lick, and AAT Planet Search Programs. *ApJS*, 159:141–166, July 2005. doi: 10.1086/430500. 2.3.1

J. C. van Eyken, J. Ge, S. Mahadevan, and C. DeWitt. First Planet Confirmation with a Dispersed Fixed-Delay Interferometer. *ApJ*, 600:L79–L82, January 2004. doi: 10.1086/381574. 3

W. R. Ward. Survival of Planetary Systems. *ApJ*, 482:L211+, June 1997. 2.1

S. J. Weidenschilling, B. D. Donn, and P. Meakin. The physics of planetesimal formation. In *The Formation and Evolution of Planetary Systems*, pages 131–146, 1989. 2.1

G. W. Wetherill. Formation of the earth. *Annual Review of Earth and Planetary Sciences*, 18:205–256, 1990. 2.1

A. Wolszczan and D. A. Frail. A planetary system around the millisecond pulsar PSR1257 + 12. *Nature*, 355:145–147, January 1992. 2

M. Woolfson. The origin and evolution of the solar system. *Astronomy and Geophysics*, 41:12–+, February 2000. 2.1

Y. Wu and N. Murray. Planet Migration and Binary Companions: The Case of HD 80606b. *ApJ*, 589:605–614, May 2003. doi: 10.1086/374598. 5.1

S. Zucker and T. Mazeh. On the Mass-Period Correlation of the Extrasolar Planets. *ApJ*, 568:L113–L116, April 2002. doi: 10.1086/340373. 5.1

S. Zucker, T. Mazeh, N. C. Santos, S. Udry, and M. Mayor. Multi-order TOD-COR: Application to observations taken with the CORALIE echelle spectrograph. II. A planet in the system ¡ASTROBJ¿HD 41004¡/ASTROBJ¿. *A&A*, 426:695–698, November 2004. doi: 10.1051/0004-6361:20040384. 8.1.5

CURRICULUM VITÆ

PERSONAL DETAILS

- **Name:** Aldo Fabricio Martínez Fiorenzano
- **Place and date of birth:** Bogotá, Colombia. September 16th 1975
- **Nationality:** Colombian - Italian
- **Address (work):** Osservatorio Astronomico di Padova,
  Vicolo Osservatorio, 5
  35122 Padova, Italy
  (tel. +39 049 8293442/3529)
  (fax. +39 049 8759840)
- **E-mail:** fiorenzano@pd.astro.it

LANGUAGES

Spanish: mother tongue
Italian: very good
English: good

EDUCATION

Sept. 1990 – July 1994: Scuola italiana "Leonardo da Vinci" (High School)
Bogotá, Colombia.

Aug. 1994 – Sept. 1999: Universidad de los Andes. Bogotá, Colombia.
Degree title: Physicist
Dissertation: "Gravitational Waves"
Supervisor: Prof. B. Oostra
Jury: Prof. B. Gómez.

Nov. 2002 – present: University of Padova and
Padova Astronomical Observatory, Italy
Current PhD in Astronomy
Supervisors: Dr. R. Gratton, Dr. G. Piotto

ADDITIONAL TRAINING

11-17 May 2003: National School of Astrophysics
1) The galaxies of the local group
2) The new generation telescopes

27 Sep. – 3 Oct. 2003: National School of Astrophysics
1) Astrophysics of the Interstellar Medium
2) Compact Objects and Pulsars

16-21 May 2004: National School of Astrophysics
1) Gravitational lensing
2) Chaos in astrophysics

5-11 Sep 2004: National School of Astrophysics
1) Cosmological Parameters
2) Extrasolar Planets

INFORMATICS

Languages: C,
O.S.: Windows, Unix, Linux
Packages: IDL, IRAF, MIDAS, Mathematica

TEACHING EXPERIENCE

Teaching Assistant: Physics Department Universidad de los Andes
Aug. – Dec. 1998: Problems in Mechanics (General Physics I).

Cathedratic: Physics Department Universidad de los Andes
Jan. – May 2000: Experimental course: General Physics I.

RESEARCH EXPERIENCE

Sep. 2005 – present: Instituto de Astrofisica de Canarias
Doctoral research fellowship "Marie Curie EARA-EST"

Feb. – Sep. 2004: INAF-Padova Astronomical Observatory
Research Contract in "Spectral analysis of stars in dwarf spheroidal galaxies", as part of the research program: "Evolution of the local group galaxies: star formation history and chemical enrichment".

Nov. 2000 – Apr. 2003: INAF-Trieste Astronomical Observatory
Research scholarship supported by "Ministero degli Affari Esteri" Italy.

Sept. 2001: Participation in a survey mission at the 1.5m G.D. Cassini telescope, Loiano (Bologna), Italy.

CONGRESSES

-Tenth Anniversary of 51 Peg-b: status and prospects for hot Jupiter studies. Observatoire de Haute-Provence, France. August 22-25, 2005.

-Ringberg Workshop on Planet Formation: Theory meets Obsevation, Ringberg Germany, December 19-22, 2004.

-XLVII Annual Meeting of the Italian Astronomical Society, Trieste Italy, April 14-17, 2003.

PUBLICATIONS

REFEREED ARTICLES

Clementini G., Gratton R. G., Ripepi V., Bragaglia A., **Martinez Fiorenzano A. F.**, Held E. V., Carretta E.
Metal abundances of RR Lyrae stars in the metal rich globular cluster NGC 6441
Astrophysical Journal v. 630 I. 2 p.L145-L148 (2005) (astro-ph/0508079)

Martinez Fiorenzano A. F., Gratton R. G., Desidera S., Cosentino R., Endl M.
Line bisectors and radial velocity jitter from SARG spectra
Astronomy and Astrophysics v. 442, p.775-784 (2005) (astro-ph/0508096)

Clementini G., Ripepi V., Bragaglia A., **Martinez Fiorenzano A. F.**, Held E. V., Gratton R. G.
The metal abundance distribution of the oldest stellar component in the Sculptor dwarf spheroidal galax
MNRAS v. 363, I. 3 p.734-748 (2005) (astro-ph/0506206)

Desidera S., Gratton R. G., Endl M., Claudi R. U., Cosentino R., Barbieri M., Bonanno G., Lucatello S., **Martinez Fiorenzano A. F.**, Marzari F., Scuderi S.
No planet around HD 219542 B
Astronomy and Astrophysics, v.420, p.L27-L30 (2004)

Desidera, S., Gratton, R. G., Scuderi, S., Claudi, R. U., Cosentino, R., Barbieri, M., Bonanno, G., Carretta, E., Endl, M., Lucatello, S., **Martinez Fiorenzano, A. F.**, Marzari, F.
Abundance difference between components of wide binaries,
Astronomy and Astrophysics, v.420, p.683-697 (2004)

CONGRESS PROCEEDINGS

Martinez Fiorenzano A. F., Gratton R. G., Desidera S., Cosentino R., Endl M.
Line bisectors and radial velocity jitter from SARG spectra
Tenth anniversary of 51 Peg-b: status and prospects for hot Jupiter studies. Proceedings of Haute Provence Observatory Colloquium (22-25 august 2005). Edited by L. Arnold, F. Bouchy and C. Moutou.

Martínez Fiorenzano, A. F., Vladilo, G., Bonifacio P.,
Search for alpha variation in UVES spectra: Analysis of C IV and Si IV doublets towards QSO 1101-264
Memorie della Società Astronomica Italiana – Supplementi Vol. 3, p.252, (2003) Eds. Girardi, L., Zaggia, S.
Paper available at: *http://sait.oat.ts.astro.it/MSAIS/3/PDF/252.pdf*
astro-ph/0312270
Poster available at: *http://sait.oat.ts.astro.it/MSAIS/3/POST/MartinezF_poster.pdf*

The Astrophysical Journal, 630:L145–L148, 2005 September 10

METAL ABUNDANCES OF RR LYRAE STARS IN THE METAL-RICH GLOBULAR CLUSTER NGC 6441[1]

Gisella Clementini,[2] Raffaele G. Gratton,[3] Angela Bragaglia,[2] Vincenzo Ripepi,[4]
Aldo F. Martinez Fiorenzano,[3,5] Enrico V. Held,[3] and Eugenio Carretta[2]
Received 2005 June 9; accepted 2005 August 2; published 2005 August 26

ABSTRACT

Low-resolution spectra have been used to measure individual metal abundances of RR Lyrae stars in NGC 6441, a Galactic globular cluster known to have very unusual horizontal-branch morphology and periods of the RR Lyrae stars for its high metallicity. We find an average metal abundance of [Fe/H] = -0.69 ± 0.06 (rms = 0.33 dex) and [Fe/H] = -0.41 ± 0.06 (rms = 0.36 dex) on Zinn & West and Carretta & Gratton metallicity scales, respectively, consistent with the cluster metal abundance derived by Armandroff & Zinn. Most of the metallicities were extrapolated from calibration relations defined for [Fe/H] ≤ -1; however, they are clearly high and contrast with the rather long periods of the NGC 6441 variables, thus confirming that the cluster does not fit in the general Oosterhoff classification scheme. The rms scatter of the average is larger than observational errors (0.15–0.16 dex), possibly indicating some spread in metallicity. However, even the metal-poor variables, if confirmed to be cluster members, are still more metal-rich than those commonly found in the Oosterhoff type II globular clusters.

Subject headings: globular clusters: individual (NGC 6441) — stars: abundances — stars: horizontal-branch — stars: variables: other — techniques: spectroscopic

1. INTRODUCTION

NGC 6441 as well as its twin NGC 6388 are metal-rich, massive globular clusters ([Fe/H] = -0.53 ± 0.11 and -0.60 ± 0.15, respectively; Armandroff & Zinn 1988) with very unusual horizontal branches (HBs) extending from stubby red, as expected for their high metallicities, to extremely blue, and with the red HBs sloping upward as one moves blueward in the $V, B - V$ color-magnitude diagram (Rich et al. 1997; Pritzl et al. 2001, 2002, 2003). Given their high metallicities, we would expect them to have very few RR Lyrae stars with the short periods typical of the Oosterhoff type I systems (Oosterhoff 1939). Rather unexpectedly, large numbers of RR Lyrae stars with unusually long periods, even longer than those commonly observed in the Oosterhoff type II systems, have been discovered in both clusters (Layden et al. 1999; Pritzl et al. 2001, 2002, 2003). Indeed, NGC 6441 and NGC 6388 seem to violate the trend of decreasing period with increasing metallicity followed by the Galactic globular clusters (GCs), and stand apart in the mean period versus [Fe/H] diagram (Pritzl et al. 2001). The clusters have been suggested to be a further and extreme manifestation of the so-called second-parameter effect, meaning that metallicity is not the only factor governing the morphology of the HB, but that other parameters such as age, helium or CNO abundances, core rotation, or dynamical interactions are at work. Some of these possibilities (e.g., a high helium abundance, higher interaction rates, etc.) are not supported by observations of NGC 6441 and NGC 6388 (Rich et al. 1997; Layden et al. 1999; Raimondo et al. 2002; Moehler et al. 1999). Thus, we still lack a satisfactory explanation for the cluster's peculiar HBs and for the unusual properties of their RR Lyrae stars.

A metallicity spread, as first argued by Piotto et al. (1997) from the intrinsic spread in color of the red giant branch, with the RR Lyrae stars and the blue HB stars being at the metal-poor tail ([Fe/H] $\lesssim -1.6$) of the cluster's metallicity distributions, could in principle explain their anomalous HBs (Sweigart 2002; Ree et al. 2002). In this scenario, NGC 6441 and NGC 6388, the two most massive Galactic GCs after ω Cen and M54, have been suggested to be the relics of disrupted dwarf galaxies (Ree et al. 2002), similar to ω Cen, which has a metallicity spread, and to M54, which is considered the nucleus of the Sagittarius galaxy (Layden & Sarajedini 2000). However, even the metallicity spread does not completely explain the unusual nature of NGC 6441 and NGC 6388 RR Lyrae stars (see discussions in Pritzl et al. 2001, 2002). On the other hand, if the RR Lyrae stars in NGC 6388 and NGC 6441 are metal-rich, they would form a new, distinct subclass of long-period, metal-rich RR Lyrae stars (Layden et al. 1999) that has no counterpart among the field and cluster RR Lyrae stars known so far, except perhaps V9 in 47 Tuc (Carney et al. 1993).

No direct measure of the metal abundance of the RR Lyrae stars in either cluster existed so far. Pritzl et al. (2001, 2002) derived metallicities for some of the *ab*-type RR Lyrae stars in the two clusters, using the parameters of the Fourier decomposition of the light curve and the Jurcsik-Kovács method (Jurcsik & Kovács 1996; Kovács & Jurcsik 1997). They estimated average metal abundances of [Fe/H] = -0.99 and -1.21 for NGC 6441 and NGC 6388, respectively, that according to Jurcsik (1995) correspond to -1.3 and -1.4 on the Zinn & West (1984, hereafter ZW84) metallicity scale. These metallicities are much lower than the cluster metal abundances derived by Armandroff & Zinn (1988) but are close to the metallicity of Sweigart (2002) models, which yield a best-fitting model of NGC 6441 HB for a [Fe/H] ~ -1.4 and an α-enhancement of [α/Fe] = $+0.3$. However, given the uncertainty of the Jurcsik-Kovács method (see discussions in Di Fabrizio et al. 2005; Gratton et al. 2004, hereafter G04; and Clementini et al. 2005, hereafter C05), and the unusual nature of the NGC 6441 and NGC 6388 RR Lyrae

[1] Based on data collected at the Very Large Telescope of the European Southern Observatory, Paranal, Chile, program number 71.B-0621.

[2] INAF, Osservatorio Astronomico di Bologna, via Ranzani 1, I-40127 Bologna, Italy; gisella.clementini@bo.astro.it, angela.bragaglia@bo.astro.it, eugenio.carretta@bo.astro.it.

[3] INAF, Osservatorio Astronomico di Padova, vicolo dell'Osservatorio 5, I-35122 Padua, Italy; gratton@pd.astro.it, held@pd.astro.it, fiorenzano@pd.astro.it.

[4] INAF, Osservatorio Astronomico di Capodimonte, via Moiarello 16, I-80131 Naples, Italy; ripepi@na.astro.it

[5] Dipartimento di Astronomia, Università di Padova, vicolo dell'Osservatorio 2, I-35122 Padua, Italy.

TABLE 1
LINE INDICES AND METAL ABUNDANCES OF RR LYRAE STARS IN THE GLOBULAR CLUSTER NGC 6441

STAR[a]	HJD (−2,400,000)	TYPE	K	Hδ	Hγ	Hβ	⟨H⟩	MI	[Fe/H] ZW84	[Fe/H] CG97	V_r (km s^{-1})	[Fe/H][b]
V37	52,850.6112	*ab*	0.325	0.216	0.213	0.193	0.207	1.66	−0.71	−0.44	+18	−0.95
V38	52,850.6112	*ab*	0.405	0.157	0.155	0.191	0.167	1.69	−0.68	−0.41	−7	−1.14
V41[c]	52,849.6208	*ab*	0.473	0.056	0.030	0.096	0.060	0.91	−1.37	−1.15	+4	...
V43	52,850.6112	*ab*	0.513	0.098	0.119	0.122	0.113	1.60	−0.76	−0.49	−4	−1.16
V49[d]	52,850.6112	*c*	0.202	0.253	0.220	0.199	0.224	0.90	−1.37	−1.15	+22	...
V51	52,850.6112	*ab*	0.283	0.265	0.270	0.236	0.257	1.94	−0.46	−0.11	−16	−0.84
V69	52,849.6208	*c*	0.300	0.294	0.260	0.260	0.271	2.29	−0.15	+0.16	−10	...
V71	52,850.6112	*c*	0.358	0.222	0.187	0.192	0.200	1.80	−0.58	−0.30	+10	...
V72	52,850.6112	*c*	0.191	0.340	0.349	0.275	0.321	1.72	−0.65	−0.38	−6	...
V74	52,849.6208	*c*	0.147	0.331	0.312	0.289	0.311	1.17	−1.14	−0.90	−7	...
V77	52,849.6208	*c*	0.284	0.275	0.298	0.220	0.264	2.05	−0.36	−0.07	−12	...
V78	52,849.6208	*c*	0.188	0.347	0.356	0.286	0.329	1.75	−0.63	−0.36	−12	...

[a] Identifiers are from the Sawyer-Hogg online catalog of variable stars in Galactic globular clusters, published by Clement et al. (2001).
[b] Pritzl et al. (2001).
[c] Layden et al. (1999) find that this star is ~0.7 mag brighter and ~0.3 mag redder than the other RR Lyrae stars and suggest its image is blended with a red companion. Pritzl et al. (2001) agree on this hypothesis. The star is in the cluster central region, and from our spectrum it looks cooler than a normal RR Lyrae star (see Fig. 1), as also demonstrated by its rather small ⟨H⟩ value, thus supporting the blend hypothesis.
[d] This star is a suspected binary system for Layden et al. (1999). However, Pritzl et al. (2001) find it is a slightly overluminous *c*-type RR Lyrae. The star spectrum shows typical features of an RR Lyrae star (see Fig. 1) confirming Pritzl et al. (2001) classification.

stars, there is some question as to the validity of these metallicity determinations.

In this Letter we present the first direct measure of metallicity for RR Lyrae stars in NGC 6441 through spectroscopy, and provide the first quantitative assessment that the cluster variables are indeed metal-rich, with a few outliers possibly suggesting some spread in metallicity.

2. THE DATA

Spectra of 12 RR Lyrae stars in NGC 6441 were obtained in 2003 July in the course of a spectroscopic survey of RR Lyrae stars in the Sculptor dwarf spheroidal galaxy (C05). Observations were performed using the FORS2 spectrograph at the ESO Very Large Telescope (VLT; Paranal, Chile). We observed two 6′.8 × 6′.8 FORS2 subfields of NGC 6441, centered at $\alpha_{2000} = 17^h50^m19^s.9$, $\delta_{2000} = -37°05'21''.9$ and $\alpha_{2000} = 17^h50^m24^s.5$, $\delta_{2000} = -37°00'06''.3$, and comprising five and seven RR Lyrae stars, respectively. Spectra were collected using slits 1″ wide and about 14″ long to allow for sky subtraction. With this configuration, each pixel corresponds to 0.75 Å. Our wavelength range contains both the Ca II K and the hydrogen Balmer lines up to Hβ. Exposure time was 300 s, as an optimal compromise between signal-to-noise ratio and time resolution of the light curve. Details on the observations and data-reduction procedures can be found in C05.

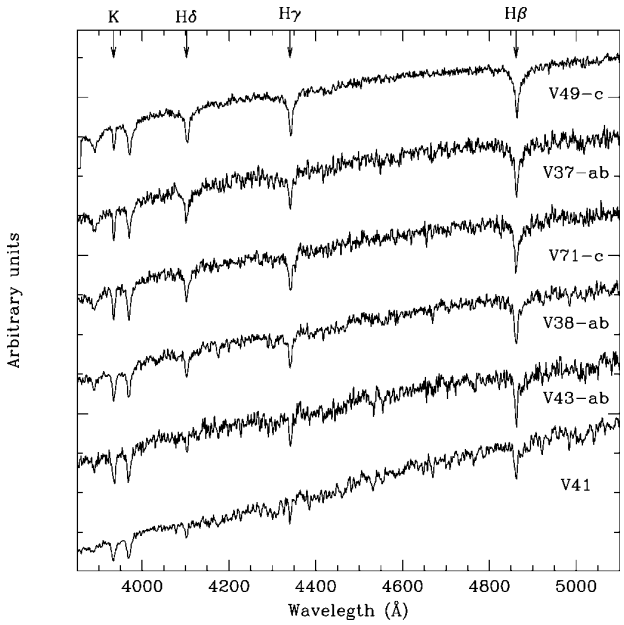

FIG. 1.—Examples of spectra of variable stars in NGC 6441 obtained using FORS2. The spectra have been offset for clarity, and the main spectral lines are indicated. They all correspond to variable stars having ⟨H⟩ < 0.25. V41 is very likely the blend of an RR Lyrae star with a cooler companion.

Time-series photometry for all the target stars, and the classification in types, has been published by Layden et al. (1999) and Pritzl et al. (2001). Accordingly, our sample includes five *ab*-type and seven *c*-type RR Lyrae stars; their identification is provided in Table 1. Figure 1 shows examples of spectra for some of the variable stars in the cluster.

We estimated radial velocities from our spectra; they are given in column (12) of Table 1. According to C05, typical errors of these radial velocity determinations are of about 15 km s^{-1}. Our radial velocity estimates do not exclude the cluster membership for any of the RR Lyrae stars we have analyzed. The 12 stars have $\langle v_r \rangle = -1$ km s^{-1} (rms = 12 km s^{-1}, and a zero-point error of ±7 km s^{-1}). Our average radial velocity differs somewhat from the value of +16.4 km s^{-1} (Harris 1996, online catalog).[6] A reason for part of this discrepancy is that our mean value includes the phase-dependent contributions due to the star pulsations. Further residual differences may be due to systematic offsets possibly caused by offcentering of the cluster variables on the slits.

3. MEASURE OF THE METAL ABUNDANCES

Metal abundances for the RR Lyrae stars in NGC 6441 were derived using a modified (and improved) version of the ΔS method (Preston 1959). Our technique is fully described in G04 and is based on the definition of hydrogen and Ca II spectral indices, ⟨H⟩ and K, for each variable star by directly integrating

[6] Available at http://www.physics.mcmaster.ca/Globular.html.

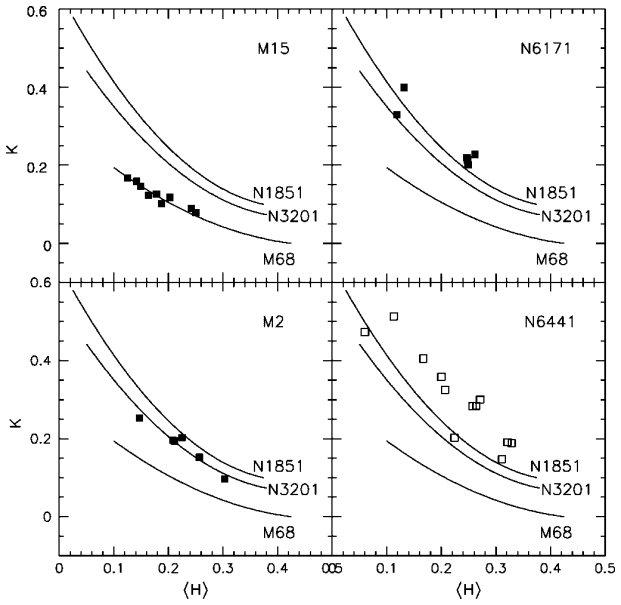

FIG. 2.—Correlations between K and ⟨H⟩ spectral indices for the calibrating clusters M15, M2, and NGC 6171 (from C05; *filled squares*) and M68, NGC 3201, and NGC 1851 (from G04; *solid lines*). For a definition of the spectral indices, see G04.

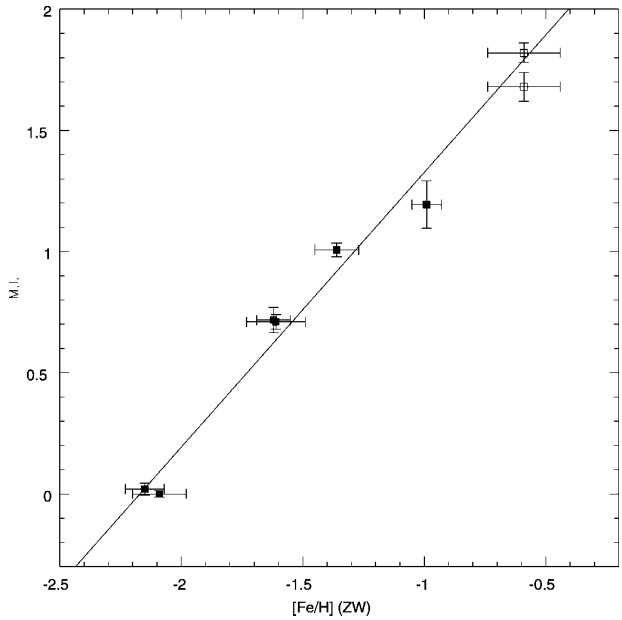

FIG. 3.—Calibration of the metallicity index on the ZW84 metallicity scale. Open squares represent NGC 6441, which is plotted according to its metallicity from ZW84 ([Fe/H] = −0.59) and the MI values obtained, both averaging all the 11 variable stars (*lower open square*) and discarding the two metal-poor objects V49 and V74 (*upper open square*). In both cases the cluster lies very close to the calibration line, which is based on the other clusters only, and perfectly falls on it if V49 and V74 are disregarded.

the instrumental fluxes in spectral bands centered on the Hδ, Hγ, Hβ, and Ca II K lines. These spectral indices are then used to measure metallicities by a comparison to the same quantities for variable stars in a number of globular clusters with known metal abundances. A summary of the method and an update of the metallicity calibration procedure can be found in C05. An advantage of our technique is that we do not need to know the phases of our spectra. On the other hand, the accuracy of our [Fe/H] may be a function of phase, as represented by the strength of the H lines. According to Figure 12 of G04, most accurate metallicity determinations are obtained for values of $\langle H\rangle < 0.20$ and 0.25 for *ab*- and *c*-type RR Lyrae stars, respectively. Outside these ranges, metal-abundance determinations may be more uncertain, depending on the actual value of ⟨H⟩. However, metallicities of individual stars in the calibrating clusters (see Tables 3 and 4 in G04, and Tables 5, 6, and 7 in C05) show this effect to be small, if present. This point is particularly relevant for the NGC 6441 RR Lyrae stars for which, based on the available photometric data (Layden et al. 1999; Pritzl et al. 2001) it may be difficult to reliably define the pulsation phase at the epochs of the observations. Line indices measured for the RR Lyrae stars in NGC 6441 are provided in columns (4) to (8) of Table 1. The stellar K values were not corrected for the interstellar K-line contribution, since we estimated it to be much less than 0.1 dex in [Fe/H]. In fact, given the small absolute value of the cluster radial velocity, interstellar lines are expected to lie in the core of the stellar K lines, where there is almost no flux, and then they can subtract only a negligible fraction of flux.[7] This would not be the case for halo stars where, due to the high velocities, the interstellar absorptions occur outside the line cores.

The calibration of the line indices of the variable stars in terms of metal abundances [Fe/H] was obtained using RR Lyrae stars observed in the clusters M15, M2, and NGC 6171 (C05) and M68, NGC 1851, and NGC 3201 (G04). For all these clusters, precise metal abundances are available on both the ZW84 and the Carretta & Gratton (1997, hereafter CG97) metallicity scales. Figure 2 shows the correlation between K and ⟨H⟩ indices for the calibrating clusters, and in the bottom right panel, the position on the K versus ⟨H⟩ plane of the NGC 6441 variable stars. The figure shows that there are three objects lying near the ridge line of NGC 1851 at an average metallicity of [Fe/H] ≃ −1.3 on the ZW84 scale, while all the remaining stars define a tight correlation at higher metallicity. However, one of the deviating objects, star V41, is probably blended with a cooler companion, as suggested by its spectrum (see Fig. 1). Thus, its metallicity is uncertain, and we drop it from any further consideration. V49 was observed in the safe range in which metal abundance determinations are most reliable. The spectrum of this star is shown in Figure 1, along with spectra of all the variables having $\langle H\rangle < 0.25$, and it clearly shows that the star has a shallower K line. Finally, V74 was observed at $\langle H\rangle = 0.311$, thus its metallicity may be slightly more uncertain.

Metallicity indices (MIs) for the program stars were derived from their K and ⟨H⟩ values using equations (3), (4), and (5) of G04. They are listed in column (9) of Table 1. Metal abundances [Fe/H] were then deduced from the MI values using the metallicity calibrations defined by C05. These are described by linear regressions, namely equations (4) and (5) of C05, between the average ⟨MI⟩ values of RR Lyrae stars in the calibrating clusters M15, M2, NGC 6171, M68, NGC 1851, and NGC 3201 and the cluster's metal abundances on the ZW84 and CG97 metallicity scales, respectively. In Figure 3 we show the calibration relation of the metallicity indices on the ZW84 metallicity scale. We note that the calibrating clusters have metallicities that do not extend higher than [Fe/H] ∼ −1; thus,

[7] We checked this point on the spectra of a few NGC 6441 giants we recently observed with UVES at the VLT. We estimated that according to the definition of the spectral indices used in the present study, the interstellar K-line contribution may cause a systematic offset <0.02 dex in the metal abundance of the NGC 6441 variable stars.

the metal abundance we derive for NGC 6441 is an extrapolation of the calibration equations. However, the cluster is found to fall well on the extrapolation to higher metallicities of the linear relation defined by the calibrating clusters. This result is in agreement with the original Preston's ΔS method, which appears to have a linear calibration up to about solar metallicity.

Individual metal abundances derived with this procedure are given in columns (10) and (11) of Table 1. According to C05, we attach internal errors of 0.15 and 0.16 dex to individual abundance determinations on the ZW84 and CG97 scales, respectively. However, to take into account any additional uncertainty that might affect the spectra corresponding to $\langle H \rangle$ values outside the safest range, below we divide the stars in three groups corresponding to $\langle H \rangle \leq 0.224$, $0.257 \leq \langle H \rangle \leq 0.271$, and $0.311 \leq \langle H \rangle \leq 0.329$, and all averages are computed, giving different weights to the three groups of stars (i.e., 1, 0.75, and 0.5).

For comparison, in the last column of Table 1, we report the metal abundances derived by Pritzl et al. (2001) from the Fourier decomposition of the light curve for four of the *ab*-type RR Lyrae stars analyzed here. The average of Pritzl et al. (2001) values for the four stars is [Fe/H] $= -1.02$ (rms $= 0.15$), on the Jurcsik (1995) metallicity scale. According to equation (4) in Jurcsik (1995), this corresponds to [Fe/H] $= -1.33$ on the ZW84 scale. The average of our metal abundances for these four stars is [Fe/H] $= -0.67$ (rms $= 0.11$) on the ZW84 scale (i.e., much more metal-rich). This result seems to suggest that the Jurcsik-Kovács method may not be reliable when applied to the anomalous RR Lyrae stars in NGC 6441.

Adopting the averaging scheme described above, the mean metal abundance of our RR Lyrae sample in NGC 6441 is [Fe/H] $= -0.69 \pm 0.06$ (rms $= 0.33$ dex, 11 stars) and -0.41 ± 0.06 (rms $= 0.36$ dex) on the ZW84 and CG97 scales, respectively. The scatter of the average is larger than expected from measurement errors alone (<0.2 dex), thus suggesting that if the 11 variables are all cluster members, there is some spread in metallicity with two more metal-poor objects at an average metal abundance around [Fe/H] ~ -1.3, and the remaining nine more metal-rich stars around [Fe/H] ~ -0.6 dex (on the ZW84 scale). If the two metal-poor stars are disregarded, the mean metal abundances become [Fe/H] $= -0.57 \pm 0.04$ (rms $=$ 0.19 dex, nine stars), and -0.28 ± 0.04 (rms $= 0.21$ dex). The former value is in excellent agreement with both ZW84 and Armandroff & Zinn (1988) metallicity estimates for the cluster.

4. SUMMARY AND CONCLUSIONS

Metal abundances from low-resolution spectroscopy obtained with FORS2 at the ESO VLT have revealed that the NGC 6441 RR Lyrae stars are metal-rich, with an average metal abundance of [Fe/H] $= -0.69 \pm 0.06$ on the ZW84 scale. The spectroscopic analysis also reveals that there are 2 variables (out of 11) having metallicities around [Fe/H] ~ -1.3. However, the metal-poor stars, if confirmed cluster members, are a minor component of our sample. Even allowing for measurement errors, we do not find in this cluster RR Lyrae stars as metal-poor as the variables commonly found in the Galactic Oosterhoff type II GCs, as instead one would expect from the extraordinarily long periods and the position near the Oosterhoff type II line of the NGC 6441 variables in the period-amplitude diagram (see Fig. 6 of Pritzl et al. 2003). Clearly, metal abundances and memberships for a larger number of variable stars are needed to better assess the metallicity distribution of the NGC 6441 stars and the relevance of the metal-poor component, if any. Nevertheless, the existence of extremely long period RR Lyrae stars with extraordinarily high metal abundances, as exhibited by some of the variables in our sample, demonstrates that the NGC 6441 variable stars are different from the RR Lyrae stars known so far both in the Milky Way GCs and in the field, and confirms that this cluster does not conform to the Oosterhoff dichotomy described by the other Galactic GCs.

Which mechanism may be able to produce such metal-rich variables with pulsation characteristics similar to the Oosterhoff type II ones remains unexplained. For instance, Pritzl et al. (2002) show that it is difficult to model NGC 6441 as an Oosterhoff type II system under the hypothesis that its variables are evolved from a position on the blue zero-age HB as a result of the small number of progenitors on the blue HB. As suggested by Layden et al. (1999) and Pritzl et al. (2001), the theoretical reproduction of the observed light curves with pulsation models may shed some light on the physical properties responsible for the anomalous properties of the NGC 6441 RR Lyrae stars. Such modeling for the variables analyzed in the present Letter is currently under way (G. Clementini & M. Marconi 2005, in preparation).

This research was funded by MIUR, under the scientific project 2003029437, "Continuity and Discontinuity in the Milky Way Formation" (PI: R. Gratton).

REFERENCES

Armandroff, T. E., & Zinn, R. 1988, AJ, 96, 92
Carney, B. W., Storm, J., & Williams, C. 1993, PASP, 105, 294
Carretta, E., & Gratton, R. G. 1997, A&AS, 121, 95 (CG97)
Clement, C., et al. 2001, AJ, 122, 2587
Clementini, G., Ripepi, V., Bragaglia, A., Martinez Fiorenzano, A., Held, E. V., & Gratton, R. G. 2005, MNRAS, in press (astro-ph/0506206) (C05)
Di Fabrizio, L., Clementini, G., Maio, M., Bragaglia, A., Carretta, E., Gratton, R., Montegriffo, P., & Zoccali, M. 2005, A&A, 430, 603
Gratton, R. G., Bragaglia, A., Clementini, G., Carretta, E., Di Fabrizio, L., Maio, M., & Taribello, E. 2004, A&A, 421, 937 (G04)
Harris, W. E. 1996, AJ, 112, 1487
Jurcsik, J. 1995, Acta Astron., 45, 653
Jurcsik, J., & Kovács, G. 1996, A&A, 312, 111
Kovács, G., & Jurcsik, J. 1997, A&A, 322, 218
Layden, A. C., & Ritter, L. A., Welch, D. L., Webb, T. M. A. 1999, AJ, 117, 1313
Layden, A. C., & Sarajedini, A. 2000, AJ, 119, 1760
Moehler, S., Sweigart, A. V., & Catelan, M. 1999, A&A, 351, 519
Oosterhoff, P. Th. 1939, Observatory, 62, 104
Piotto, G., et al. 1997, in Advances in Stellar Evolution, ed. R. T. Rood & A. Renzini (Cambridge: Cambridge Univ. Press), 84
Preston, G. W. 1959, ApJ, 130, 507
Pritzl, B. J., Smith, H. A., Catelan, M., & Sweigart, A. V. 2001, AJ, 122, 2600
———. 2002, AJ, 124, 949
Pritzl, B. J., Smith, H. A., Stetson, P. B., Catelan, M., Sweigart, A. V., Layden, A. C., & Rich, R. M. 2003, AJ, 126, 1381
Raimondo, G., Castellani, V., Cassisi, S., Brocato, E., & Piotto, G. 2002, ApJ, 569, 975
Ree, C. H., Yoon, S.-J., Lee, S.-C., & Lee, Y.-W. 2002, in ASP Conf. Ser. 265, Omega Centauri: A Unique Window into Astrophysics, ed. F. van Leeuwen, J. D. Hughes, & G. Piotto (San Francisco: ASP), 101
Rich, R. M., et al. 1997, ApJ, 484, L25
Sweigart, A. V. 2002, Highlights Astron., 12, 292
Zinn, R., & West, M. J. 1984, ApJS, 55, 45 (ZW84)

A&A 442, 775–784 (2005)
DOI: 10.1051/0004-6361:20052888

Astronomy & Astrophysics

Line bisectors and radial velocity jitter from SARG spectra⋆

A. F. Martínez Fiorenzano[1,2], R. G. Gratton[2], S. Desidera[2], R. Cosentino[3,4], and M. Endl[5]

[1] Dipartimento di Astronomia, Università di Padova, Vicolo dell'Osservatorio 2, 35122 Padova, Italy
e-mail: fiorenzano@pd.astro.it
[2] INAF – Osservatorio Astronomico di Padova, Vicolo dell'Osservatorio 5, 35122 Padova, Italy
[3] INAF – Osservatorio Astrofisico di Catania, Via S. Sofia 78, Catania, Italy
[4] INAF – Centro Galileo Galilei, Calle Alvarez de Abreu 70, 38700 Santa Cruz de La Palma (TF), Spain
[5] McDonald Observatory, The University of Texas at Austin, Austin, TX 78712, USA

Received 16 February 2005 / Accepted 11 July 2005

ABSTRACT

We present an analysis of spectral line bisector variations for a few stars observed in the SARG high precision radial velocity planet survey, and discuss their relationship with differential radial velocities. The spectra we consider are the same used for determining radial velocities. The iodine cell lines employed in the measurement of radial velocities were removed before bisector analysis. The line bisectors were then computed from average absorption profiles obtained by cross correlation of the stellar spectra with a mask made from suitable lines of a solar catalog. Bisector velocity spans were then determined: errors in these quantities compare well with theoretical expectations based on resolution, *S/N* and line shape. The plot of bisector velocity span against radial velocity was studied to search for correlations between line asymmetries and radial velocity variations. A correlation was seen for HD 166435 due to stellar activity, and for HD 8071B due to spectral contamination by the companion. No correlation was seen for 51 Peg and ρ CrB, stars hosting planets. We conclude that this technique may be useful to separate radial velocity variations due to barycenter motion from spurious signals in spectra acquired with the iodine cell.

Key words. stars: atmospheres – stars: activity – stars: planetary systems – techniques: spectroscopic – techniques: radial velocities – line: profiles

1. Introduction

The study of activity jitter is mandatory in the search for exoplanets using the radial velocity (*RV*) technique, because it represents an important source of noise and a proper analysis is necessary to discard false alarms (e.g., HD 166435: Queloz et al. 2001; HD 219542B: Desidera et al. 2003, 2004a). The differential *RV* variations induced by stellar activity are due to changes in the profile of spectral lines caused by the presence of spots and/or the alteration of the granulation pattern in active regions (Saar & Donahue 1997; Hatzes 2002; Saar 2003; Kürster et al. 2003). The activity jitter of a star may be predicted by means of statistical relations from its chromospheric emission, rotational velocity or amplitude of photometric variations (Saar et al. 1998; Paulson et al. 2004). Simultaneous determination of *RV*, chromospheric emission and/or photometry is even more powerful in disentangling the origin of the observed *RV* variations Keplerian vs. stellar activity. However these techniques cannot be considered as a direct measurement of the alterations of the spectral line profiles that are the origin of the spurious *RV* variations.

This type of study can be carried out by considering variations of line bisectors, that may be thought of as direct measure of activity jitter (Queloz et al. 2001) through the evidence of variations of the asymmetries which appear in spectral lines. Line bisectors are employed in the analysis of asymmetries (Gray 1982, 1988) due to stellar atmospheric phenomena like granulation (Dravins et al. 1981), turbulence or pulsation that sometimes are responsible for the *RV* variations observed in stars.

The reason for studying simultaneously the variations of the *RV* and of the (average) line bisector of a star is to determine if any variation of the measured *RV*s are caused by a center of mass motion due to celestial bodies orbiting a star (see Queloz et al. 2001; and Desidera et al. 2003).

The analysis of spectral line asymmetries also has an important application for the follow-up of transit surveys. An eclipsing binary in a hierarchical triple system and a transiting planetary companion might produce similar photometric signature; but very different line bisector variations, allowing one to disentangle the characteristics of the system (Torres et al. 2004, 2005). In addition, asymmetries of spectral lines may arise due to contamination of the spectrum by a nearby star. This point

⋆ Based on observations made with the Italian Telescopio Nazionale Galileo (TNG) operated on the island of La Palma by the Centro Galileo Galilei of INAF (Istituto Nazionale di Astrofisica) at the Spanish Observatorio del Roque del los Muchachos of the Instituto de Astrofísica de Canarias.

is of particular relevance for the targets we are studying in the SARG survey (Desidera et al. 2004b), because by design all of them are visual binaries. In this case a companion near the line of sight may contaminate the spectral features of the star being observed. Finally, spurious line profile asymmetries may be due to instrumental causes, e.g., non symmetric illumination of the slit.

Line bisector variations may be studied quite easily in spectra acquired using fibers (see e.g., Queloz et al. 2001). The fibers provide a constant, roughly symmetric illumination of the slit. Furthermore, spectra are generally acquired with simultaneous wavelength calibration lamps, rather than imprinting absorption cell features on the stellar spectral lines. No attempt has been made to our knowledge to study line bisectors on spectra obtained through an iodine cell. One disadvantage is the necessity to remove the iodine lines from the stellar spectra; but on the other hand, the iodine lines allow a fine wavelength calibration and the possibility of monitoring the instrumental profile.

In this paper we present such an attempt; line bisectors and radial velocities are determined for SARG stellar spectra, to study possible trends between spectral line shapes (line bisectors) and *RV*s.

This paper describes the procedure followed to handle the spectra, to remove iodine lines, the construction of a mask made from selected lines of a solar catalogue, the cross correlation function (CCF) computed between mask and stellar spectra, the determination of the line bisector and the calculation of the bisector velocity span. We present results obtained for five stars: we found a clear correlation between the line bisector velocity span and *RV* for HD 166435, likely due to stellar activity, consistent with previous published work by Queloz et al. (2001). A similar correlation was found for HD 8071B due to contamination by light from the companion. We did not find any correlation for stars known to host planets like 51 Peg and ρ CrB, and the false alarm (inconclusive) case of HD 219542B.

In the next section we describe some aspects of the observations; Sect. 3 explains the procedure employed in the analysis with results presented in Sect. 4. The last two sections are devoted to a discussion of the error analysis and conclusions.

2. Observations and data reduction

The data discussed in the present paper are part of the *RV* survey aimed to find planets around stars in wide binaries (Desidera et al. 2004b), ongoing at TNG using the high resolution spectrograph SARG (Gratton et al. 2001). The spectra have a resolution of $R \sim 150\,000$, covering the spectral range 4580 Å–7900 Å in 55 echelle orders, with *S/N* values in the range 70–400 and were taken from September 2000 until August 2004. Slit width was set at 0.27″, much smaller than the typical seeing Full Width Half Maximum (FWHM). Furthermore, an autoguider system, viewing the slit by means of a detector with its wavelength response peaked at the wavelength of the iodine cell lines, was employed, keeping the instrumental profile stable and fairly independent of illumination effects. Guiding was generally done using the image of the binary companion on the slit viewer.

Data reduction was performed in a standard way using IRAF[1]. High precision *RV*s were measured on these spectra with the AUSTRAL code (Endl et al. 2000) as described in Desidera et al. (2003).

The iodine cell technique includes the acquisition of spectra from a featureless source (a fast rotating B-star or the flat field lamp) taken with the iodine cell inserted in the optical path (Butler et al. 1996). This kind of spectra is necessary only for the deconvolution of stellar templates (taken without the cell), but they were acquired also in most of the observing nights of our survey to monitor instrument performances. These featureless source spectra were used to remove the iodine lines from the science spectra, as explained in the next section.

3. Data analysis

3.1. Handling of the spectra

The iodine lines, superimposed on the stellar spectrum for wavelength calibration and *RV* determination, were eliminated because the line bisector is intended to study the asymmetries of the stellar spectral lines alone. For this task, spectra of fast rotating ($V \sin i \geq 200\,\mathrm{km\,s^{-1}}$) B-stars were employed. The analysis was made only for the wavelength range where the iodine lines appear in the spectra (5036 Å–6108 Å) along 21 orders. We used only this spectral region because there the wavelength calibration is more accurate, because of the iodine lines themselves.

To handle the spectra, each order was divided in 7 pieces of 500 spectral points each, corresponding to a wavelength width of ∼10 Å, overlapped by 60 points (∼1 Å) to eventually recover any absorption lying at the edges of the chunks. This procedure of cutting the spectra in pieces was clearly advantageous, while the division of complete orders displayed not optimal results, related to errors in the wavelength calibration of the spectra (see Fig. 1). A cross correlation computed between the spectral chunks of the B-star and the program star determined the offset in wavelength between the iodine lines common to both spectra. The B-star spectrum was adjusted using a Hermite spline interpolation (INTEP, see Hill 1982) to the wavelength scale defined by the program star spectrum after application of the appropriate offset and finally divided to the program star spectrum (see Fig. 2; details will appear elsewhere: Martínez Fiorenzano 2005). The success of this procedure depends on the stability of the instrumental profile over time, since the B-star spectra were usually acquired at the beginning or the end of each night.

In a few cases, the cross correlation procedure used to determine the wavelength offset of chunks did not provide a reasonable value; in these cases the division of the star flux by the B-star flux added noise rather than removing the iodine lines. These noisy chunks were rejected from further analysis.

Spikes due to cosmic rays or hot pixels were removed by replacing the spectral values within them with the averaged flux of adjacent spectral points. This procedure was only

[1] IRAF is distributed by the National Optical Observatory, which is operated by the Association of Universities for research in Astronomy, Inc., under contract with the National Science Fundation.

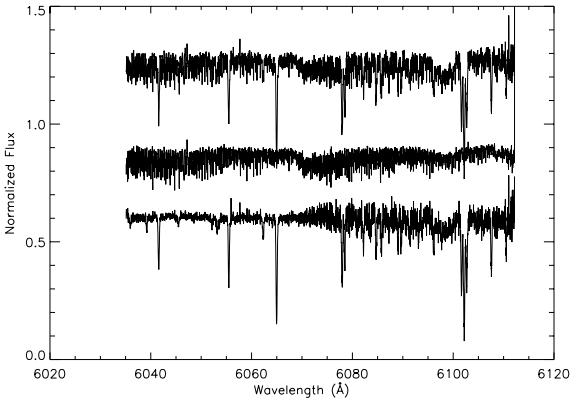

Fig. 1. Portion of a spectrum from HD 166435. The top spectrum corresponds to the program star with iodine lines, in the middle is the spectrum of the B-star with iodine lines and on the bottom is the program star spectrum after the division by the B-star spectrum. The division was computed for the whole order: the poor result is due to errors in the wavelength calibration along one order. In this case the iodine lines are better removed in the left half than in the right half of the order.

applied to those cases where spikes occurred far from the line centers. In the very rare cases where the spikes occurred near the centers of the lines used in our analysis, possibly affecting the line bisector analysis described below, the relevant chunks were simply removed from further analysis, from all spectra of the same star.

3.2. The cross correlation function (CCF)

3.2.1. The solar catalogue and line selection for the mask

The list of spectral lines by Moore et al. (1966) was used to prepare the spectral mask needed for the computation of the CCF. A preliminary line list was obtained by selecting those lines that do not have possible contaminants (wavelength separation $\gtrsim$0.1 Å), and have reduced width between 3 and 30 F. F (Fraunhofer) is defined as the dimensionless quantity $\Delta\lambda/\lambda \times 10^6$, where $\Delta\lambda$ is the equivalent width (see Moore et al. 1966). The range of reduced width chosen here corresponds to a range of central line depths from 0.14 to 0.75 in continuum units (in the solar spectrum). The CCFs we derived thus represent average profile for lines of intermediate strength.

Once a preliminary list of lines was determined for the wavelength range of interest (5036 Å to 6108 Å), a further selection was made by inspecting the "The Sacramento Peak Atlas of the Solar Flux Spectrum" (Beckers et al. 1976). Lines were labeled according to their appearance: "y" (*very good*): sharp, clear, with weak wings; "y:" (*good*): clear but near other lines altering their wings; "?" (*not very good*): with small blends or strong wings. Many other lines, blended or too close to other spectral lines, were removed from the list at this step.

The mask used to compute the CCF is a sum of δ-function profiles corresponding to 1 for the line wavelength, with a base of two (spectral) points, and 0 elsewhere. The extensive line

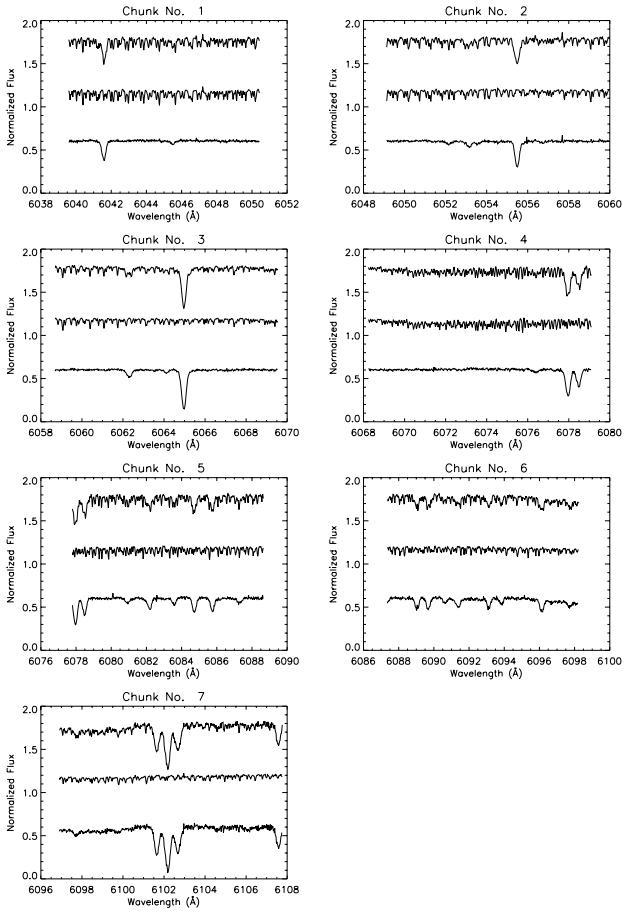

Fig. 2. An order of a spectrum of HD 166435 (wavelength range 6039 Å–6107 Å) shown in Fig. 1. The order has been divided into 7 chunks, as described in the text. The spectra are shifted arbitrarily in flux to show: on top the stellar spectra with iodine lines, in the middle the B-star spectra (adjusted to the wavelength offset) with the iodine lines and on the bottom the clean stellar spectra after dividing the program star spectrum by the B-star spectrum.

list (including *very good*, *good* and *not very good* lines: a total of about 300 lines) served to determine the *RV*; this gave the centroid value of the average absorption profile obtained by the CCF. Once this point was established, which helps to properly locate the profiles for the addition, a new computation of the CCF was performed only with the *very good* lines to obtain an improved average profile, used to calculate reliable average line bisectors (see Fig. 3).

3.2.2. The cross correlation and addition of profiles

A cross correlation between the mask and the stellar spectrum was computed for each chunk; the addition of all these cross correlations gave the average profile. Due to the relatively low *S/N* of some spectra, use of the average of many lines is appropriate for this study (the variations of line bisectors with time). On the other hand, the actual line bisector depends on the line depth, so that our "average" line bisector does not rigorously correspond to the line bisector of a line with similar depth of

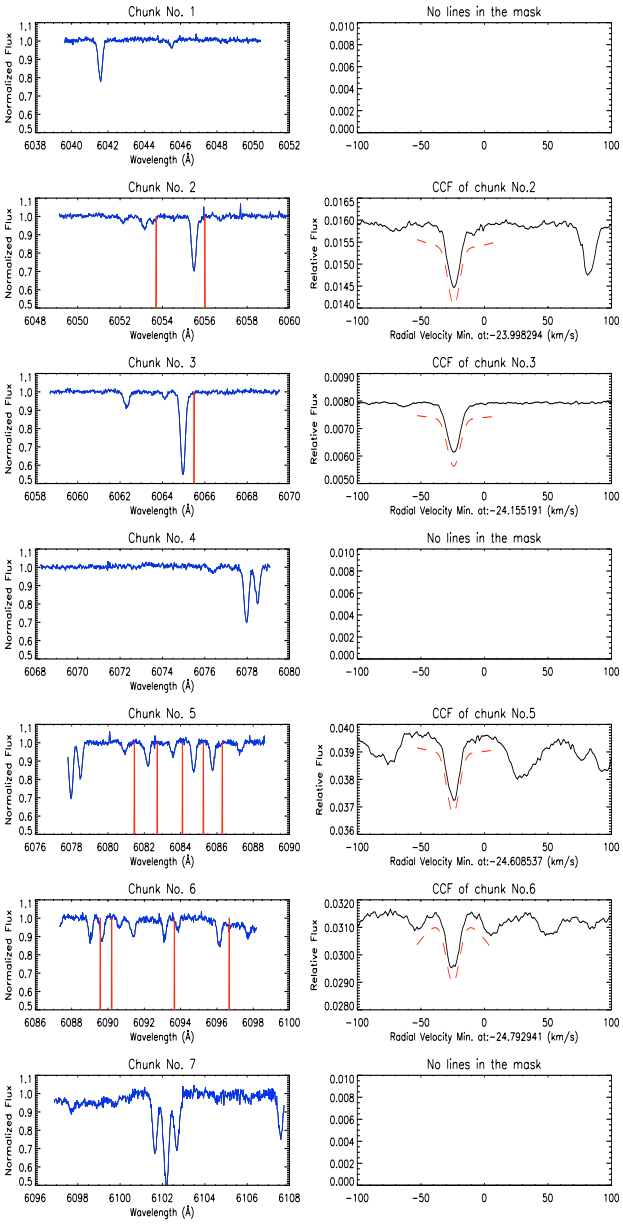

Fig. 3. An order of a spectrum of HD 166435. The left column shows individual chunks of the spectrum (blue lines), after removal of the iodine cell lines (see Fig. 1). Overimposed (as red lines) is the mask used for the determination of the CCF (only lines classified as *very good* are shown here). It is made of a sum of δ-functions centered on the rest wavelengths of the selected lines. Note the wavelength shifts between the stellar lines and the mask peaks due to the non-zero radial velocity of the star. The CCF for individual chunks computed by cross-correlating the spectra with the masks given on the left panels are shown in the right panels. The dashed line, shifted slightly below the profiles for clarity, represent the Gaussian fit computed to determine the local minimum of the CCF for each chunk. There are no CCF profiles for chunks 1, 4 and 7 due to the lack of suitable lines for the mask in these wavelength ranges.

the CCF. Therefore, the use of our average profile would be misleading for some scientific goals such as the study of convection in stellar atmospheres.

Due to different illumination of the CCD, each chunk along an order has different flux values, those close to the center of the orders being more luminous and yielding then results of higher *S/N*. To account for this, before summing the individual cross correlations, each of them was multiplied by an appropriate weight, proportional to the instrumental flux at the center of the chunk.

Once adjusted to a common reference frame, which may be thought of as a centering procedure, and multiplied by its weight, all CCF profiles were added to get the final profile for the spectrum. This was normalized to determine the finally adopted average line profiles using the reference continuum determined in the IRAF reduction. This was obtained by interpolating a polynome throughout the spectra with a suitable clipping rejection procedure. Note that this reference continuum may contain significant errors, so that there may be points in the normalized CCFs that are well above unity. However, we kept our procedures strictly uniform throughout the analysis of different spectra; we then expect that these errors in the location of the reference continuum mainly affect absolute profiles and bisector estimates, but only marginally their spectrum-to-spectrum variations, which are of interest for the present discussion.

3.3. The line bisector calculation

The bisector of an absorption line is the middle point of the horizontal segment connecting points on the left and right sides of the profile with the same flux level. The line bisector is obtained by combining bisector points ranging from the core toward the wings of the line.

For the bisector determination, it is necessary to adjust the ordinate axis of the profile to a convenient scale and to determine the values in velocity belonging to the left and right points for a given flux value. This is accomplished by interpolating (using INTEP, see Hill 1982) the absorption profile to the desired scale (details will appear in Martínez Fiorenzano 2005).

3.4. The bisector velocity span

To quantify the asymmetry of the spectral lines and look for correlation with *RV* it is useful to introduce the bisector velocity span (Toner & Gray 1988). This is determined by considering a top zone near the wings and a bottom zone close to the core of the lines, which represent interesting regions to study the velocity given by the bisector (see Fig. 4). The difference of the average values of velocities in the top and bottom zones, $V_{\rm T}$ and $V_{\rm B}$ respectively, determine the bisector velocity span (BVS for short).

The location of the top and bottom zones, as well as their width ΔF, were determined as percentages along the absorption profiles. They were defined using as templates the spectra of HD 166435; the same zones were then employed in the study of the other objects to be consistent in the analysis procedure.

The Spearman nonparametric rank correlation coefficient was computed to establish the significance of the linear correlation between BVS and *RV* for each star.

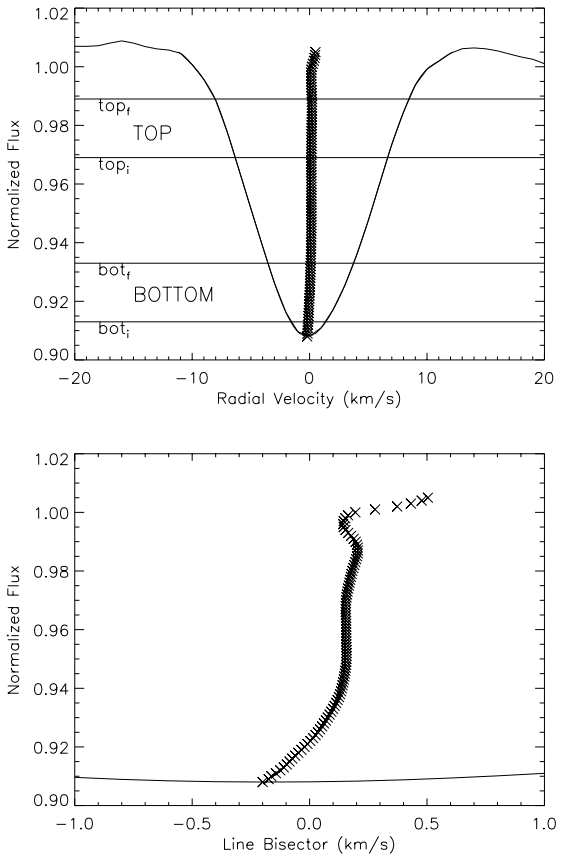

Fig. 4. Spectrum of HD 166435. In the top panel we show the normalized cross correlation profile, the line bisector, the top and bottom zones (both with $\Delta F = 0.02$; $\Delta F = \mathrm{top_f} - \mathrm{top_i} = \mathrm{bot_f} - \mathrm{bot_i}$). In the bottom panel we show a zoom of the profile with the *RV* scale increased to better display the asymmetries of the line bisector.

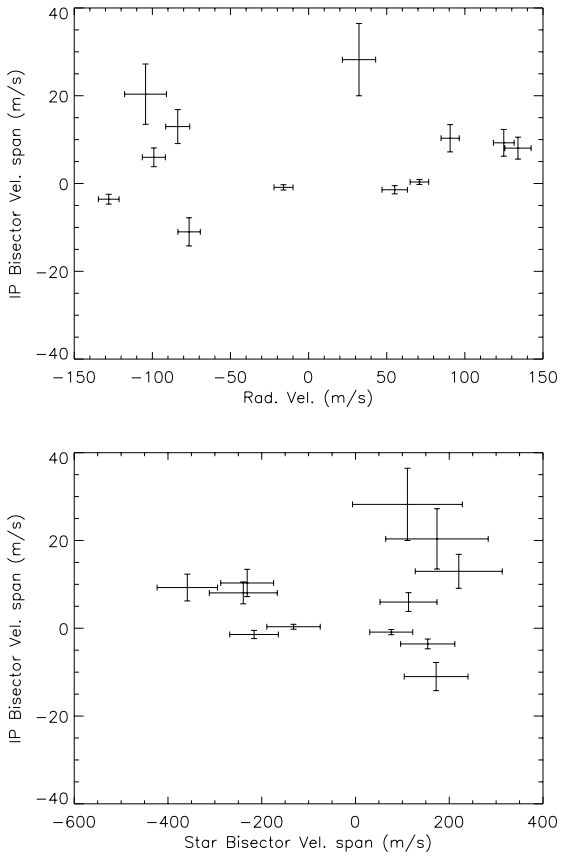

Fig. 5. Instrumental profile (IP) analysis. *Top panel*: plot of IP BVS vs. *RV*s of HD 166435. *Bottom panel*: plot of IP BVS vs. BVS of HD 166435. No evidence of trends were found.

3.5. Error determination

The expression given by Gray (1983) for the bisector error due to photometric error was employed to establish the error for the bisector velocity span. The photon noise error, determined for the specific case of SARG using Gray's equation, yields the expression:

$$\delta V = \left(\frac{S}{N}\right)^{-1} \left(2nF\frac{\Delta F}{x}\frac{\mathrm{d}F}{\mathrm{d}V}\right)^{-1/2}, \quad (1)$$

where S/N is the signal-to-noise of the spectrum, including the contribution of the B-star spectrum and it is given by: $((N/S)^2_{\mathrm{star}} + (N/S)^2_{\mathrm{B-star}})^{-1/2}$, with values between 65–300. The B-star spectra employed in the analysis were acquired on the same observing nights of the target spectra and have typical *S/N* values $\gtrsim$250. In Eq. (1) n is the number of lines in the mask for the CCF; F is the central flux of the zone of analysis; ΔF is the interval of flux determining the zone; x is the scale of the spectrum based on the linear dispersion of the instrument (1.04 km s^{-1} pix^{-1} for SARG) and $\mathrm{d}F/\mathrm{d}V$ gives the slope of the profile in the zone being analyzed (see Fig. 4).

Error bars for the BVS were then determined by adding quadratically the errors for the top and bottom zones.

3.6. Instrument Profile asymmetries

Line bisector variations may arise from variations of the stellar spectra as well as from variations of the instrumental profile (IP). We studied the IP determined by AUSTRAL as part of the *RV* determination and computed line bisectors for it as for stellar spectra.

Generally the line bisector variations of IP are significant, but they are typically much lower than the errors in the line bisectors determined from the stellar spectra. Corrections due to asymmetries of line profiles require complex convolution, which should take into account the real stellar profile. Actually, since the IP is much narrower than the intrinsic stellar line profile (the case of SARG spectra), corrections due to IPs are much smaller than the IP asymmetries themselves; therefore we did not apply corrections to the stellar BVS.

In Fig. 5 we show the run of the BVS of the IP with *RV* and the IP BVS with the stellar BVS in the analysis of HD 166435. No clear trend could be discerned.

4. Results

4.1. HD 166435

The dwarf star HD 166435, of spectral type G0 and visual magnitude $m_V = 6.8$, shows evidence of *RV* variations, photometric

Table 1. Bisector velocity span from spectra of HD 166435. 53 lines were employed in the mask for the CCF.

JD − 2 450 000	$(V_T - V_B)$ m s^{-1}	V_r m s^{-1}	S/N
2775.65	−231.1 ± 56.4	90.6 ± 5.8	164
2776.68	154.1 ± 57.8	−127.9 ± 6.6	156
2809.62	−216.4 ± 51.8	55.1 ± 8.2	178
2818.62	173.8 ± 109.3	−104.4 ± 13.4	86
2860.40	220.3 ± 92.8	−83.8 ± 7.7	98
2861.42	110.8 ± 117.1	32.3 ± 10.6	81
2862.42	−358.8 ± 64.5	124.9 ± 6.6	140
2891.37	172.0 ± 68.1	−76.5 ± 7.2	138
2892.35	−239.4 ± 72.5	134.0 ± 8.4	126
3129.74	113.1 ± 60.8	−99.0 ± 7.4	149
3130.73	76.3 ± 45.9	−16.1 ± 6.1	201
3131.74	−132.2 ± 57.0	70.9 ± 6.0	164

variability and magnetic activity. Furthermore, previous analysis of the variation of the line bisectors revealed a correlation between *RV* and line bisector orientation (Queloz et al. 2001).

The large amplitude of the activity-induced variations and their stability make this star an ideal target to test new procedures like those presented in this paper.

Twelve spectra of HD 166435 were acquired between May 2003 and May 2004. The line bisectors, derived from the spectra, were used to study the correlation between the BVS and the *RV*s. The plot of BVS against *RV* ($(V_T - V_B)$ vs. V_r) was fitted to a straight line.

In principle, the location and extension of top and bottom zones of the line profiles used in the derivation of the BVS are arbitrary. In order to optimize detection of variations of the BVS correlated with *RV* variations, we maximized the m/σ ratio (where m is the slope of the straight line fitting of BVS against *RV*, and σ its uncertainty) over different choices of the location and amplitude of the line profile regions used to derive the BVS. The m/σ ratio is an indicator of the significance of the linear term in the straight line fitting.

The top and bottom zones were determined according to the relative absorption percentages in which the highest significance was found: top centered at 25% of the maximum absorption, bottom at 87%; in both cases the width ΔF was of 25%. For consistency, these percentage values were then considered for the analysis of all the stars.

The upper panel of Fig. 6 displays the plot of BVS against *RV*; superimposed is the best fitting straight line, with:

$$(V_T - V_B) = (-1.98 \pm 0.21) \times V_r + (-29.03 \pm 18.45). \quad (2)$$

The rank correlation coefficient is −0.89 and the significance is of 99.99%. The lower panel of the same figure shows the line bisectors computed for all spectra of HD 166435, corrected for their *RV* and plotted on a common reference frame. Values of bisector velocity span and *RV* for individual spectra are listed in Table 1. The trend of the BVS obtained in this work is similar to that of Queloz et al. (2001); the larger value we found for the slope can be attributed to the higher resolution of the SARG spectra.

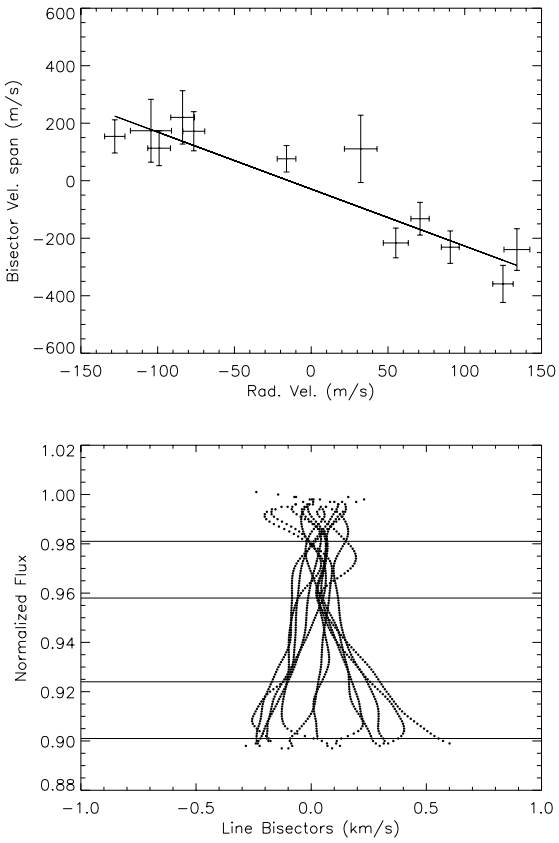

Fig. 6. *Upper panel*: plot of BVS vs. *RV* for HD 166435 and the best fit to a straight line. *Lower panel*: line bisectors for individual spectra adjusted to their corresponding *RV*. The horizontal lines enclose the top and bottom zones considered for the fitting analysis.

4.2. HD 8071B

The star HD 8071B of spectral type G0V and visual magnitude $m_V = 7.6$ is a member of a visual binary system. The primary HD 8071A is brighter by 0.3 mag and has a projected separation of 2.1″, the smallest in the sample of the SARG survey. Pairs with such small separation are typically not observed in cases of bad seeing; furthermore the slit was oriented perpendicularly to the separation of the components. Nevertheless, some contamination of the spectra is still possible, especially for the secondary component. Our velocity measures show that HD 8071A is itself a single lined spectroscopic binary with semiamplitude of ∼7 km s^{-1}. The *RV* difference between the visual components is then variable in the range (−4, 10) km s^{-1}.

Eight spectra of HD 8071B were acquired between September 2000 and August 2004. The correlation between BVS and *RV* found for all spectra has rank correlation coefficient of 0.81 and significance of 98.5%. The analysis of the IP did not show any critical trend acting on the *RV* computation, leading us to consider contamination as the cause of the observed correlation. The spectrum with $RV \sim 600$ m s^{-1} and very different line profile is likely heavily contaminated by the companion, because of the occurrence of technical problems related to telescope tracking that night. Our study of the line

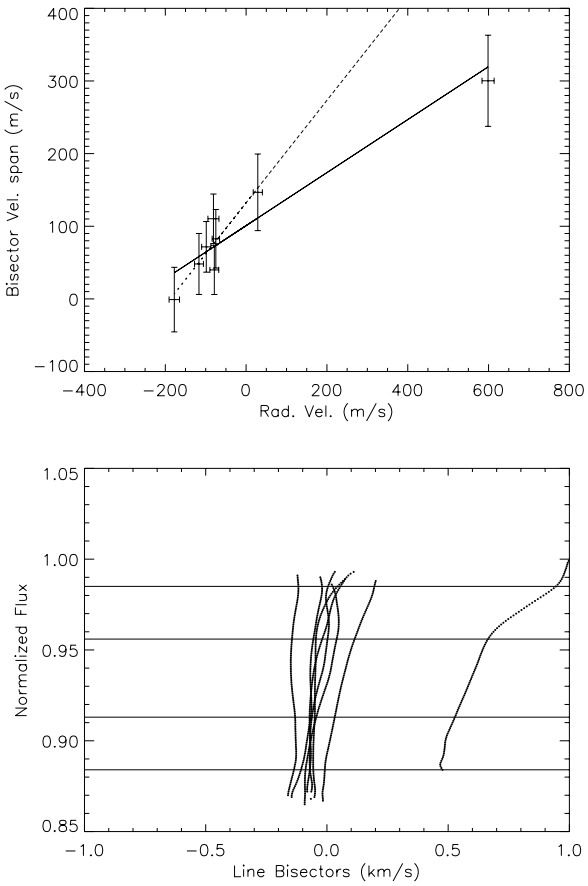

Fig. 7. *Upper panel*: plot of BVS vs. *RV* for HD 8071B and the best fit to a straight line. The dotted line corresponds to the best fit discarding the spectrum with higher *RV*. *Lower panel*: line bisectors for individual spectra adjusted to their corresponding *RV*. The horizontal lines enclose the top and bottom zones considered in the fitting analysis.

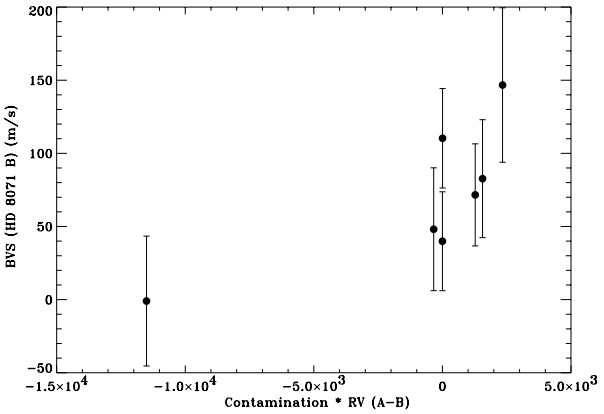

Fig. 8. BVS of HD 8071B vs. the "effective contamination" of *RV*, defined as the product of the light contamination from the companion HD 8071A and the *RV* difference between the components, variable with time because HD 8071A is itself a spectroscopic binary. The highly discrepant spectrum from JD: 2452982.48 was excluded. Abscissa axis has dimensions of (*percentage of contamination*) × (m/s).

Table 2. Bisector velocity span from spectra of HD 8071B. 87 lines were employed in the mask for the CCF.

JD − 2450000	$(V_T - V_B)$ m s^{-1}	V_r m s^{-1}	S/N
1797.64	110.3 ± 34.0	−80.9 13.7 ± 137	
1854.54	146.7 ± 52.8	28.8 ± 11.3	91
2145.71	71.6 ± 34.9	−98.7 ± 11.4	140
2297.38	−1.0 ± 44.4	−177.7 ± 12.9	110
2892.61	48.1 ± 42.0	−116.6 10.9 ± 112	
2982.48	300.3 ± 62.8	598.7 ± 15.0	92
3216.73	39.9 ± 33.8	−78.7 ± 11.0	141
3246.68	82.7 ± 40.3	−74.9 ± 9.2	121

bisector allows us to clearly identify the problematic spectrum and to exclude it from the analysis of the radial velocity curve.

Nevertheless a correlation still persists even without considering the highly discrepant spectrum, with a rank correlation coefficient 0.71 and significance of 92.9%. This is likely due to some residual contamination (of a few percent at most) by the companion, compatible with the small separation of the pair and the actual observing conditions. Figure 7 shows the two cases and the eight line bisectors computed for all spectra of HD 8071B, corrected for their *RV* and plotted on a common reference frame. Values of bisector velocity span and *RV* for individual spectra appear in Table 2.

To confirm our hypothesis of contamination as the source of observed BVS-*RV* correlation, we performed a simple modeling of the expected contamination, excluding the highly discrepant spectrum from JD: 2452982.48. We first determined the light contamination expected on the spectrum of HD 8071B on the basis of the seeing conditions (given by the FWHM of the spectrum measured along a direction perpendicular to the dispersion). *RV* and BVS of HD 8071B do not show significant correlation with such contamination. We then considered an "effective contamination" as the product of the light contamination and the variable *RV* difference between HD 8071 A and B. The Spearman rank correlation coefficient of *RV* and BVS vs. such "effective contamination" is 0.85 with a significance of more than 96%, supporting our hypothesis of light contamination as the origin of the *RV* and BVS variability of HD 8071B. The relation between *RV* perturbation and BVS is not linear likely because the *RV* perturbation due to contamination is expected to be a non-linear function of the position of the contamination across the line profile (see Fig. 8).

4.3. 51 Peg

The star 51 Peg (HD 217014) of spectral type G2.5IVa and visual magnitude $m_V = 5.5$ is the first discovered solar-type object to host a planet, with $M_2 \sin i = 0.47\, M_J$, $a = 0.052$ AU and period of 4.23 days (Mayor & Queloz 1995).

The star lies in a zone of the Hertzsprung-Russell diagram of stable (very low variability) objects (Eyer & Grenon 1997). Indeed, according to Henry et al. (2000), no measurable change in mean magnitude (over 5 years) was seen and the Ca II record displayed a signal essentially constant despite some season-to-season jitter and a general indication of a low activity level.

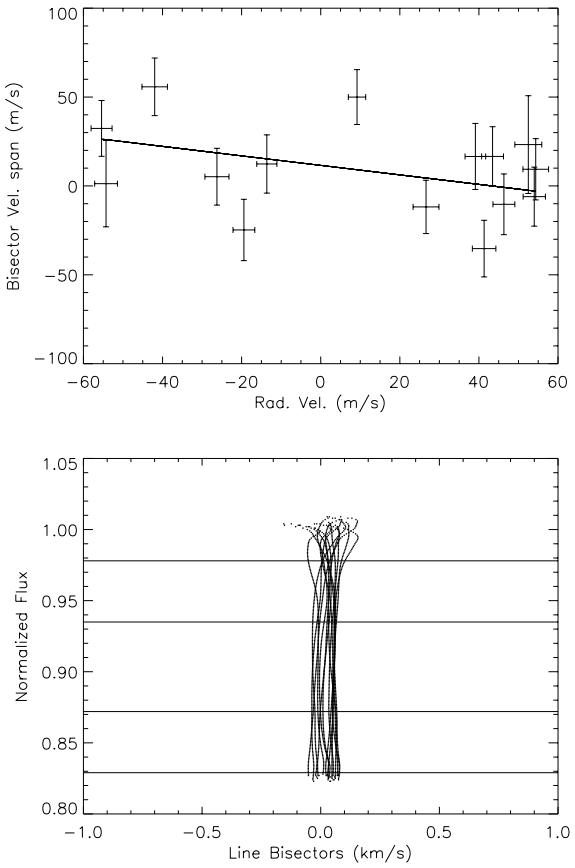

Fig. 9. *Upper panel*: plot of BVS vs. *RV* for 51 Peg and the best fit to a straight line. *Lower panel*: line bisectors for individual spectra adjusted to their corresponding *RV*. The horizontal lines enclose the top and bottom zones considered for the fitting analysis. 74 lines were employed in the mask for the CCF.

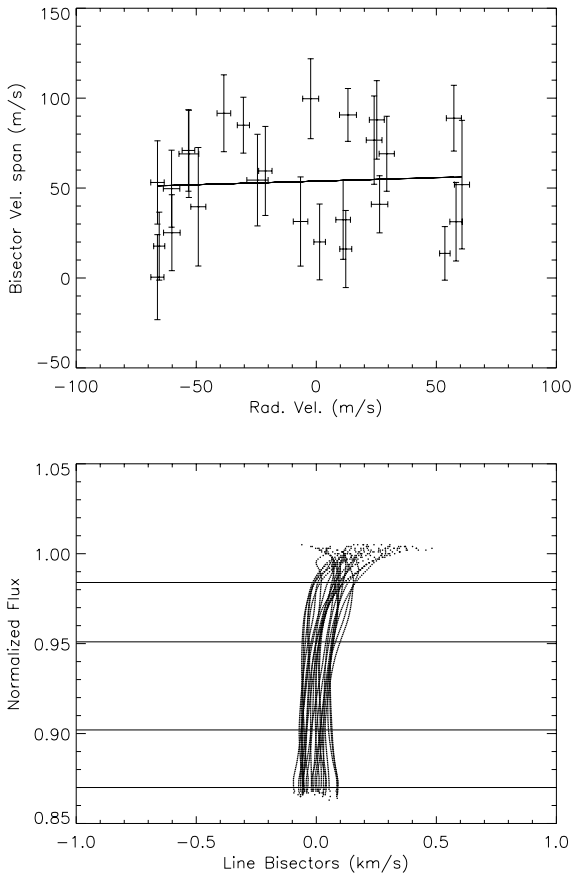

Fig. 10. *Upper panel*: plot of BVS vs. RV for ρ CrB and the best fit to a straight line. *Lower panel*: line bisectors for individual spectra adjusted to their corresponding *RV*. The horizontal lines enclose the top and bottom zones considered for the fitting analysis. 85 lines were employed in the mask for the CCF.

Fifteen spectra of 51 Peg were acquired between June 2001 and November 2003. There is no significant correlation between BVS and *RV* (rank correlation coefficient of −0.28 and significance of 56%), confirming the results by Hatzes et al. (1998) and Povich et al. (2001). The line bisector shape (see Fig. 9) seems to be constant.

4.4. ρ CrB

The star ρ CrB (HD 143761) of spectral type G0Va and visual magnitude $m_V = 5.4$ is known to host a planet with $M_2 \sin i = 1.04\, M_J$, $a = 0.22$ AU and a period of 39.95 days (Noyes et al. 1997).

Twenty six spectra of ρ CrB were acquired between April 2001 and March 2004. In the plot of BVS against *RV* the dispersion of the data points shows no correlation (as in Povich et al. 2001) with a rank correlation coefficient of 0.15 and significance of 52%.

The line bisectors and its behaviour, similar to those for 51 Peg, are shown in Fig. 10. The typical "C" shape of line bisectors is more evident for ρ CrB in agreement with the warmer temperature of the star.

4.5. HD 219542B

The star HD 219542B is member of a wide binary system, with spectral type G7V and visual magnitude $m_V = 8.6$. It was considered in Desidera et al. (2003) as a candidate to host a planet, but ultimately discarded after further analysis; the small *RV* variations are more likely related to a moderate stellar activity (Desidera et al. 2004a).

For the present analysis of the line bisectors, only the data of the 2002 season were considered, twelve spectra, because the *RV* scatter and chromospheric activity were greater in this season (see Desidera et al. 2004a). Therefore it should be easier to find a correlation between BVS and *RV* from these data alone.

The plot of BVS against *RV* and the line bisectors are shown in Fig. 11. No correlation appears in this case: the rank correlation coefficient is of −0.37 and the significance of 76%. This lack of correlation is due to the small velocity amplitude (approximately between −17 and 26 m s^{-1}) and to the low *S/N* of the available spectra ∼100.

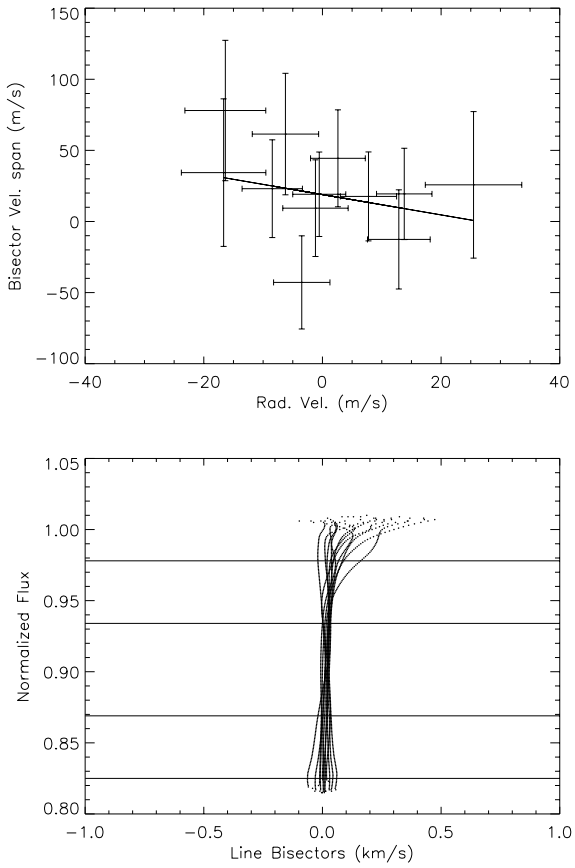

Fig. 11. *Upper panel*: plot of BVS vs. *RV* for HB 219542B and the best fit to a straight line. *Lower panel*: line bisectors for individual spectra adjusted to their corresponding *RV*. The horizontal lines enclose the top and bottom zones considered for the fitting analysis. 86 lines were employed in the mask for the CCF.

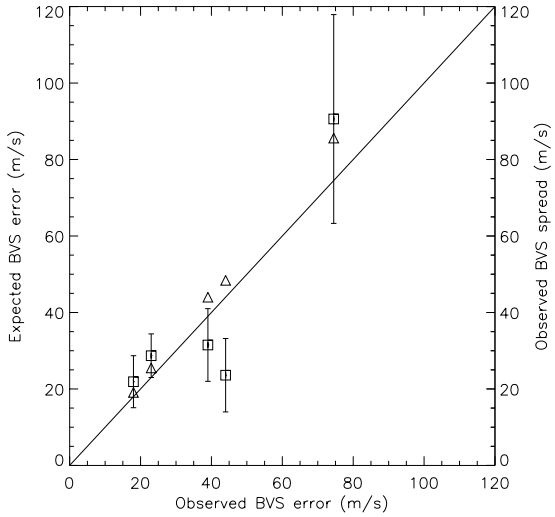

Fig. 12. The expected against observed errors of BVS (triangles: quadratic mean of error bars). Squares correspond to observed BVS spread against the measured BVS errors with spread errors as error bars.

Table 3. BVS errors: computed by Eq. (1) in convolved profiles (expected) and measured from CCF profiles (observed).

Star	BVS error observed (rms) m s^{-1}	BVS error expected m s^{-1}	BVS spread observed m s^{-1}
HD 166435	74.5	85.6	90.6[a] ± 27.3
HD 8071B	44.0	48.4	30.9[a] ± 11.7
51 Peg	18.0	19.1	25.3 ± 6.8
ρ CrB	23.0	25.5	28.7 ± 5.7
HD 219542B	39.0	44.0	31.5 ± 9.5

[a] These values correspond to the rms of residuals from the linear correlation.

5. Error analysis

An analytic study of errors was performed starting by considering the internal BVS errors. The expected errors of BVS were computed for absorption profiles obtained by convolution of Gaussian and rotational profiles. The former were determined with a thermal broadening factor estimated by colors and temperatures of each star and the latter with a $V \sin i$ factor determined by the Fast Fourier Transform (FFT) analysis of each star's absorption profile (Gray 1992).

The observed errors of BVS were the quadratic mean of the error bars of the single spectra. The observed BVS spread was the rms average of the individual BVS for the stars that do not show a significant BVS vs. *RV* correlation (51 Peg, ρ CrB and HD 219542B), and the rms of residuals from the linear correlation for HD 166435 and HD 8071B.

The values of errors estimated by these procedures are given in Table 3. The plot in Fig. 12 compares the observed spread of data with expectations based on internal errors alone. These two set of values are fully consistent with each other, indicating that our procedure is not affected by large systematic errors.

6. Conclusions

We studied the variation of line bisectors in the same spectra acquired through the iodine cell, employed also for high precision *RV* measurements. We found that such variation, as measured by the BVS, shows spreads fully consistent with internal errors, as determined from photon statistics, spectral resolution and intrinsic line profiles. We correlated the variation of the bisector span with high precision *RV*s for five stars.

A significant correlation was established in two cases: an anticorrelation for HD 166435, as found by Queloz et al. (2001). This is due to the stellar variability and magnetic activity, which makes the core of the profiles change from positive to negative values of *RV*. A positive correlation for HD 8071B was due to contamination of the spectra by light from the companion star producing an asymmetry in the red wings of the profiles with a consequent inclination of the line bisectors toward positive values of *RV*.

For the stars known to host exoplanets, 51 Peg and ρ CrB, no correlation was found, further supporting the conclusion that in these two cases *RV* variations are due to Keplerian motion.

The special case of HD 219542B shows that the bisector technique does not allow us to disentangle the activity origin of low amplitude *RV* variations ($\sim$20 m s^{-1}) using spectra of *S/N* $\sim$100 even at the high resolution of SARG spectra ($R \sim$ 150 000).

We conclude that spectra acquired using the iodine cell may be used to study variations of line bisectors. In order to achieve the required accuracy, it is necessary to deal with high quality spectra, in particular high *S/N* to reduce the error bars in the BVS, or to study spectra where the *RV* variations are of large amplitude.

Acknowledgements. We thank the referee Dr. Steven H. Saar for his very detailed report that helped to improve the paper. A. F. Martínez Fiorenzano thank Mikhail Varnoff for support and advice. This work was partially funded by COFIN 2004 "From stars to planets: accretion, disk evolution and planet formation" by Ministero Università e Ricerca Scientifica Italy.

References

Beckers, J., Bridges, C., & Gilliam, L. 1976, Atlas of the Solar Flux Spectrum 3800–7000 Å, Sacramento Peak Solar Observatory, DOC. AFGL-TR-76-0126
Butler, R. P., Marcy, G. W., Williams, E., et al. 1996, PASP, 108, 500
Desidera, S., Gratton, R. G., Endl, M., et al. 2003, A&A, 405, 207
Desidera, S., Gratton, R. G., Endl, M., et al. 2004a, A&A, 420, L27
Desidera, S., Gratton, R. G., Claudi, R. U., et al. 2004b, in Extrasolar Planets Today and Tomorrow, ASP Conf. Ser., 321, 103
Dravins, D., Lindegren, L., & Nordlund, Å. 1981, A&A, 96, 345
Endl, M., Kürster, M., & Els, S. 2000, A&A, 362, 585
Eyer, L., & Grenon, M. 1997, ESA SP-402, 467
Gratton, R. G., Bonanno, G., Bruno, P., et al. 2001, Exp. Astron., 12, 107
Gray, D. F. 1982, ApJ, 255, 200
Gray, D. F. 1983, PASP, 95, 252
Gray, D. F. 1988, Lectures on Spectral-Lines Analysis: F, G and K stars (Arva, ON: The Publisher)
Gray, D. F. 1992, The Observation and Analysis of Stellar Photospheres (Cambridge: Cambridge University Press)
Hatzes, A., Cochran, W. D., & Bakker, E. J. 1998, ApJ, 508, 380
Hatzes, A. 2002, Astron. Nachr., 323, 392
Hill, G. 1982, Publ. Dominion, Ap. Obs., 16, 67
Henry, G. W., Baliunas, S. L., Donahue, R. A., et al. 2000, ApJ, 531, 415
Kürster, M., Endl, M., Rouesnel, F., et al. 2003, A&A, 403, 1077
Martínez Fiorenzano, A. F. 2005, Ph.D. Thesis, in preparation
Mayor, M., & Queloz, D. 1995, Nature, 378, 355
Moore, C. E., Minnaert, M. G. J., & Houtgast, J. 1966, The solar spectrum 2935 Å to 8770 Å (National Bureau of Standards Monograph, Washington: US Government Printing Office, USGPO)
Noyes, R. W., Jha, S., Korzennik, S. G., et al. 1997, ApJ, 483, L111
Paulson, D., Saar, S. H., Cochran, W. D., & Henry, G. W. 2004, AJ, 127, 1644
Povich, M. S., Giampapa, M. S., Valenti, J. A., et al. 2001, AJ, 121, 1136
Queloz, D., Henry, G. W., Sivan, J. P., et al. 2001, A&A, 379, 279
Saar, S. H., & Donahue, R. A. 1997, ApJ, 485, 319
Saar, S. H., Butler, R. P., & Marcy, G. W. 1998, ApJ, 498, L153
Saar, S. H. 2003, in Scientific Frontiers in Research on Extrasolar Planets, ed. D. Deming, & S. Seager, ASP Conf. Ser., 294, 65
Toner, C. G., & Gray, D. F. 1988, ApJ, 334, 1008
Torres, G., Konacki, M., Sasselov, D. D., et al. 2004, ApJ, 614, 979
Torres, G., Konacki, M., Sasselov, D. D., et al. 2005, ApJ, 619, 558

Mon. Not. R. Astron. Soc. **363,** 734–748 (2005) doi:10.1111/j.1365-2966.2005.09478.x

The metal abundance distribution of the oldest stellar component in the Sculptor dwarf spheroidal galaxy⋆

G. Clementini,[1]† V. Ripepi,[2]† A. Bragaglia,[1]† A. F. Martinez Fiorenzano,[3,4]† E. V. Held[3]† and R. G. Gratton[3]†

[1]*INAF – Osservatorio Astronomico di Bologna, via Ranzani 1, I-40127 Bologna, Italy*
[2]*INAF – Osservatorio Astronomico di Capodimonte, via Moiarello 16, I-80131 Napoli, Italy*
[3]*INAF – Osservatorio Astronomico di Padova, vicolo dell'Osservatorio 5, I-35122 Padova, Italy*
[4]*Dipartimento di Astronomia, Università di Padova, vicolo dell'Osservatorio 2, I-35122 Padova, Italy*

Accepted 2005 July 27. Received 2005 July 15; in original form 2005 April 21

ABSTRACT

Low-resolution spectroscopy obtained with FORS2 at the Very Large Telescope (VLT) has been used for the measurement of individual metal abundances ([Fe/H]) for 110 variable stars, including 107 RR Lyrae stars and one anomalous Cepheid, and to trace the metal distribution of the oldest stellar component in the Sculptor dwarf spheroidal galaxy. The RR Lyrae stars are spread over a 15×15 arcmin^2 area around the galaxy centre. Their metallicities have an average value of [Fe/H] $= -1.83 \pm 0.03$ (rms $= 0.26$ dex) and cover the metallicity range $-2.40 <$ [Fe/H] < -0.85 (on the scale of Zinn & West), but there is only one variable that has [Fe/H] > -1.3. The star-to-star scatter is larger than typical errors on individual metallicities ($\pm$0.15–0.16 dex), indicating a real spread in metal abundances. The radial velocities measured from the RR Lyrae spectra have a dispersion of 12.9 km s^{-1}. This value is consistent with the dispersion derived by Tolstoy et al. for metal-poor red giants associated with the blue horizontal branch stars in Sculptor. Along with the metallicity distribution these results suggest that most of the RR Lyrae stars in Sculptor arise from the same burst of stellar formation that produced the metal-poor component, originating the galaxy blue horizontal branch. The metal-rich red horizontal branch population found to be centrally concentrated only produced a few (if any) of the RR Lyrae stars in our sample. The spectroscopic metallicities were used along with the apparent luminosities to study the luminosity–metallicity relation followed by the RR Lyrae stars in Sculptor, for which we derive a shallow slope of 0.09 mag dex^{-1}. This result can be due to a high level of evolution off the zero-age horizontal branch of the RR Lyrae stars in this galaxy, again in agreement with their origin from the blue horizontal branch population.

Key words: stars: abundances – stars: evolution – stars: Population II – stars: variables: other – galaxies: individual: Sculptor.

1 INTRODUCTION

In hierarchical merging scenarios dwarf galaxies are thought to be the bricks from which larger galaxies were assembled. The study of the star formation history (SFH) and the chemical evolution of presently existing dwarf galaxies is then extremely important for a proper understanding of the formation and evolution of the larger systems that this type of galaxies may have contributed to build in the past. Colour magnitude diagrams (CMDs) reaching the faint main-sequence turn-off (TO) of the oldest stellar components are the most traditional and reliable ways to derive the SFH of any individual dwarf galaxy. However, these detailed studies, possible so far mainly for the dwarf members of the Local Group (LG), require very time-consuming observations.

The RR Lyrae variables, being about 3 mag brighter than coeval TO stars ($t > 10$ Gyr), are much easier to observe. They offer an excellent tool for tracing the oldest stellar populations, and therefore the epoch of galaxy formation, in composite systems such as the resolved LG dwarf galaxies. Recent work by several groups has lead to the discovery of RR Lyrae stars in increasing numbers of LG dwarf galaxies (e.g. Leo I and II, IC 1613, Fornax, And VI, NGC 6822:

⋆Based on data collected at the European Southern Observatory, proposal number 71.B-0621.

†E-mail: gisella.clementini@bo.astro.it (GC); ripepi@na.astro.it (VR); angela.bragaglia@bo.astro.it (AB); fiorenzano@pd.astro.it (AFMF); held@pd.astro.it (EVH); gratton@pd.astro.it (RGG)

Table 1. Log of the observations.

Field	RA (JD2000)	Dec. (JD2000)	Date (UT)	Exp. time (s)	N
M15	21:30:13.4	12:11:50.4	2003 July 31	150	9
M2	21:33:40.4	−00:50:45.7	2003 August 05	150	6
NGC 6171	16:32:34.6	−13:06:46.8	2003 July 29	150	6
NGC 6441A	17:50:19.9	−37:05:21.9	2003 July 29	300	5
NGC 6441B	17:50:24.5	−37:00:06.3	2003 July 30	300	7
SCL 1	01:00:30.7	−33:38:18.4	2003 August 01	1860	15
SCL 2	01:00:08.7	−33:38:18.5	2003 August 01	1860	18
SCL 3	00:59:51.2	−33:38:18.5	2003 August 02	1860	15
SCL 4	01:00:34.8	−33:42:43.1	2003 August 02	1860	15
SCL 5	01:00:10.3	−33:42:43.5	2003 August 02	1860	19
SCL 6	00:59:49.1	−33:42:45.0	2003 August 03	1860	18
SCL 7	01:00:32.0	−33:47:18.5	2003 August 03	1860	15
SCL 8	01:00:09.5	−33:47:15.5	2003 August 05	1860	19
SCL 9	00:59:47.8	−33:47:53.8	2003 August 05	1860	13

Siegel & Majewski 2000; Dolphin et al. 2001; Held et al. 2001; Bersier & Wood 2002; Pritzl et al. 2002; Clementini et al. 2003a, just to mention a few of them). An early stellar population, nearly coeval to the old Galactic globular clusters, has been found in the majority of LG galaxies, irrespective of their SFHs. This indicates that all LG dwarfs started forming stars at an early epoch, ∼13 Gyr ago (e.g. Held et al. 2000).

The Sculptor dwarf spheroidal (dSph) galaxy is no exception to this general trend. Two hundred twenty-six RR Lyrae stars and three anomalous Cepheids have been detected in a 15×15 arcmin^2 area around the galaxy centre by Kaluzny et al. (1995), who published multi-epoch photometry for all of them. Kaluzny et al. (1995) also found that the period distribution of the RRab stars shows a sharp cut-off at $P = 0.475$ d, implying a metallicity of [Fe/H] $\leqslant -1.7$ (on the Zinn & West 1984 scale), and that the dispersion of the average V magnitudes is most likely due to the metallicity spread exhibited by the stars in this galaxy. Similarly, Kovács (2001) found $\langle$[Fe/H]$\rangle \sim -1.5$ with a large dispersion from about -2.0 to -0.8 dex (on the metallicity scale by Jurcsik 1995), from the Fourier decomposition of the light curves of the RRab stars.

Indeed, Sculptor dSph has long been known, from photometric studies, to have a large metallicity spread and bimodality in the metallicity and spatial distribution of its horizontal branch (HB) stars (Hurley-Keller, Mateo & Grebel 1999; Majewski et al. 1999; Harbeck et al. 2001; Rizzi et al. 2004; Babusiaux, Gilmore & Irwin 2005). Very few spectroscopic determinations of the metal abundance of Sculptor stars existed so far (Norris & Bessell 1998; Tolstoy et al. 2001, 2003). Geisler et al. (2005), from high-resolution spectroscopy of red giants, find [Fe/H] values in the range from -2.10 to -0.97 dex, confirming a large metallicity spread in Sculptor. Two distinct ancient populations showing an abrupt change in the [Fe/H] distribution at about 12 arcmin from the galaxy centre are found in Sculptor by Tolstoy et al. (2004) based on FLAMES@VLT low-resolution spectroscopy and Wide Field imaging of the galaxy. The two components have also different spatial distribution and velocity dispersion.

In this paper, we present metal abundance determinations based on multislit low-resolution spectroscopy obtained with FORS2 at the Very Large Telescope (VLT) for more than a hundred RR Lyrae stars in Sculptor. The variables are spread over a 15×15 arcmin^2 area around the galaxy centre, thus being almost coincident with the internal region of Sculptor where Tolstoy et al. (2004) find segregation of red HB stars. The knowledge of the *metal distribution* of the RR Lyrae population allows putting important constraints on the early star formation and chemical evolution histories of the host galaxy, by removing the age–metallicity degeneracy: the earliest measurable data point for the chemical enrichment history of Sculptor can be determined with accuracy.

Observations and data reduction are discussed in Section 2. Metal abundances are presented in Section 3. The luminosity–metallicity relation and the radial velocities we determined for the RR Lyrae stars in Sculptor are discussed in Sections 4 and 5, respectively. In Section 6, the metallicity distribution of the Sculptor RR Lyrae stars is compared to that of other old stellar populations in the galaxy. A summary and some final remarks in Section 7 close the paper.

2 OBSERVATIONS AND DATA REDUCTIONS

Observations of 110 variable stars (107 RR Lyrae, 1 anomalous Cepheid, 1 binary system and 1 variable of unknown type) in Sculptor and of RR Lyrae stars in four Galactic globular clusters (namely, M2, M15, NGC 6171 and NGC 6441) were carried out using FORS2 (Focal Reducer/low-dispersion Spectrograph 2), mounted on the European Southern Obseratory (ESO) VLT (Paranal, Chile). The data were collected in service mode during the period 2003 July 29 to August 5. Typical seeing values during the observations were in the range 0.7–1.7 arcsec and on average of about 1.2 arcsec. We used the MXU (Mask Exchange Unit) configuration, which allows one to observe many objects simultaneously, with more freedom in choosing the location, size and shape of individual slitlets with respect to the standard Multiple Object Spectroscopy (MOS) mode. The detector is a mosaic of two MIT CCDs with 15-μm pixel size.

Spectra were collected using the blue grism GRIS_600B covering the 3450–5900 Å wavelength range, with a dispersion of 50 Å mm^{-1} with slits 1 arcsec wide, and usually 14 arcsec long to allow for sky subtraction. With this configuration, each pixel corresponds to 0.75 Å. An effort was made to cover the relevant wavelength range for each star (∼3900–5100 Å), containing both the Ca II K and the hydrogen Balmer lines up to Hβ. We have used an instrumental set-up similar [i.e. same spectral range, resolution and typical signal-to-noise ratio (S/N)] to that employed in our study of the RR Lyrae stars in the Large Magellanic Cloud (LMC; Gratton et al. 2004), so that RR Lyrae variables in some calibrating GCs are already available (namely, in clusters NGC 1851, NGC 3201 and M68). Exposure times on the Sculptor variables were of 31 min, as an optimal compromise between S/N and time-resolution of the light curve of the RR Lyrae targets. We employed nine masks in Sculptor, two in NGC 6441, one in M2, one in NGC 6171 and one in M15. The nine Sculptor fields were slightly overlapped, so that for 25 variables we have more than one spectrum. A detailed log of the observations is given in Table 1, where N is the number of variable stars observed in each mask. The complete listing of the variables observed in Sculptor is provided in Table 2, where we have adopted Kaluzny et al. (1995) identification numbers. Their location on a 16×16 arcmin^2 map of the central region of Sculptor dSph galaxy is shown in Fig. 1. Finding charts corresponding to the nine 6.8×6.8 arcmin^2 FORS2 subfields are given in Appendix A. Centre-of-field coordinates are provided in Table 1. Equatorial coordinates for all our targets can be found in table 2 of Kaluzny et al. (1995).

Data reduction was performed using the standard IRAF[1] routines. Images have been trimmed, corrected for bias and for the normalized

[1] IRAF is distributed by the National Optical Astronomy Observatories (NOAO), which are operated by the Association of Universities for Research (AURA), under contract with the National Science Foundation (NSF).

Table 2. Line indices and metal abundances of variable stars in Sculptor.

Star (a)	Type (b)	P (b)	Epoch (b)	$\langle V\rangle$ (b)	HJD (c)	ϕ	K	H_δ	H_γ	H_β	$\langle H\rangle$	MI	$[Fe/H]_{ZW}$	$[Fe/H]_{CG}$	V_r (km s^{-1})	Notes
33	c	0.309 071	9168.9087	20.110	6.7675	0.088	0.002	0.352	0.347	0.300	0.333	−0.280	−2.42	−2.26	89	
37	ab	0.508 709	9162.9151	20.189	6.7675	0.230	0.161	0.168	0.199	0.164	0.177	0.239	−1.96	−1.78	68	
59	c	0.359 681	9168.9359	20.176	6.7675	0.073	0.073	0.277	0.253	0.226	0.252	0.035	−2.14	−1.97	111	(d)
71	c	0.434 922	9228.8270	20.015	6.7675	0.589	0.104	0.196	0.159	0.176	0.177	−0.127	−2.28	−2.12	105	
321	ab	0.601 783	9167.9003	20.137	4.7959	0.616	0.234	0.120	0.133	0.148	0.134	0.386	−1.77	−1.57	101	
					6.7675	0.892	0.224	0.172	0.141	0.172	0.162	0.528			99	
368	c	0.358 962	9184.8696	20.133	4.7959	0.727	0.096	0.269	0.249	0.245	0.254	0.252	−1.95	−1.76	108	
439	ab	0.496 115	8809.6429	20.146	4.7959	0.658	0.215	0.141	0.161	0.152	0.152	0.401	−1.81	−1.62	109	
737	c/d?	0.338 614	8809.8469	20.061	4.7959	0.612	0.083	0.308	0.294	0.252	0.285	0.328	−1.88	−1.69	96	(e)
763	c	0.293 114	8830.8675	20.139	3.7485	0.615	0.128	0.280	0.239	0.176	0.232	0.370	−1.84	−1.65	102	
786	c	0.279 088	8809.7457	20.179	3.7485	0.048	0.072	0.362	0.377	0.328	0.356	0.601	−1.64	−1.43	111	
793	c	0.359 921	8809.9129	20.135	3.7485	0.339	0.118	0.268	0.264	0.228	0.253	0.442	−1.91	−1.72	107	
					4.7959	0.249	0.092	0.253	0.250	0.230	0.244	0.150			140	
803	ab	0.573 658	8809.8060	20.061	3.7485	0.394	0.222	0.135	0.131	0.167	0.144	0.392	−1.82	−1.63	92	
811	c	0.363 134	8809.8517	20.131	3.7485	0.098	0.092	0.308	0.283	0.268	0.287	0.420	−1.93	−1.75	131	
					4.7959	0.982	0.090	0.265	0.229	0.232	0.242	0.120			140	
860	c	0.359 517	9158.9314	20.206	4.7959	0.071	0.140	0.299	0.208	0.185	0.231	0.464	−1.76	−1.56	129	(f)
1139	ab	0.518 930	8809.5982	20.060	3.7485	0.245	0.075	0.299	0.262	0.269	0.277	0.194	−2.00	−1.82	127	
1164	ab	0.606 190	8809.6323	20.185	3.7485	0.367	0.261	0.152	0.113	0.113	0.126	0.473	−1.75	−1.56	126	
1261	ab	0.630 359	8809.4200	20.172	3.7485	0.912	0.323	0.106	0.134	0.137	0.125	0.782	−1.48	−1.26	148	
1439	c	0.356 043	9168.9196	20.152	6.8001	0.952	0.115	0.292	0.230	0.199	0.240	0.324	−1.88	−1.70	104	(d)
1457	ab	0.717 799	8827.8527	19.919	6.8001	0.915	0.085	0.341	0.295	0.243	0.293	0.398	−1.82	−1.63	74	
1491	c	0.357 866	8809.7866	20.135	6.8001	0.727	0.153	0.350	0.225	0.223	0.266	0.854	−1.41	−1.20	84	(g)
1519	c	0.356 859	9169.9083	20.173	6.7675	0.414	0.127	0.228	0.193	0.182	0.201	0.161	−2.03	−1.85	79	
1546	ab	0.531 239	9174.9206	20.151	6.8001	0.737	0.143	0.076	0.158	0.129	0.121	−0.153	−2.31	−2.14	92	
1555	ab	0.527 243	8823.8298	20.089	6.7675	0.112	0.078	0.312	0.301	0.286	0.300	0.372	−1.84	−1.65	81	
1558	c/d?/Bl	0.243 016	8833.9116	20.203	6.8001	0.006	0.102	0.296	0.250	0.198	0.248	0.267	−1.65	−1.45	94	(h)
					6.7675	0.872	0.175	0.259	0.265	0.225	0.250	0.913			107	
1566	ab	0.570 272	8809.9982	20.053	6.8001	0.266	0.177	0.175	0.210	0.193	0.193	0.458	−1.77	−1.57	107	
1823	c	0.298 462	9189.8649	20.255	4.7959	0.373	0.152	0.294	0.230	0.235	0.253	0.743	−1.52	−1.30	107	
1830	ab	0.517 855	8809.2712	20.224	3.8132	0.181	0.145	0.180	0.165	0.160	0.168	0.089	−2.09	−1.92	112	
1875	ab	0.499 773	8823.9437	20.028	3.8132	0.400	0.188	0.153	0.151	0.113	0.139	0.174	−2.02	−1.84	95	(f)
1899	ab	0.646 664	9182.9074	19.978	4.7959	0.201	0.071	0.240	0.219	0.210	0.223	−0.137	−2.29	−2.13	74	
1910	ab	0.572 828	9189.9080	20.083	3.8132	0.172	0.111	0.183	0.185	0.177	0.182	−0.059	−2.11	−1.93	97	
					6.8001	0.386	0.209	0.133	0.128	0.118	0.126	0.208			77	
1914	ab	0.570 540	8829.8781	20.220	6.8001	0.084	0.195	0.120	0.106	0.194	0.140	0.213	−1.87	−1.68	98	
					6.7675	0.027	0.248	0.137	0.133	0.138	0.136	0.478			78	
1930	ab	0.611 160	9188.9162	20.251	3.8132	0.626	0.141	0.251	0.235	0.206	0.231	0.473	−1.79	−1.59	103	
					6.8001	0.514	0.165	0.220	0.170	0.190	0.193	0.380			119	(g)
1932	ab	0.506 044	9174.9206	20.155	4.7959	0.848	0.275	0.143	0.152	0.155	0.150	0.731	−1.53	−1.32	118	
					6.8001	0.809	0.257	0.228	0.141	0.113	0.160	0.716			90	
1940	ab	0.692 975	9224.7748	20.117	4.7959	0.312	0.332	0.127	0.137	0.091	0.118	0.769	−1.49	−1.28	98	
					6.7675	0.157	0.333	0.109	0.126	0.117	0.118	0.769			104	
1941	c	0.365 674	9166.8670	20.152	6.7675	0.689	0.157	0.258	0.253	0.250	0.254	0.789	−1.47	−1.26	107	
1943	ab	0.551 149	9169.9100	20.146	3.8132	0.045	0.203	0.172	0.131	0.127	0.143	0.281	−1.54	−1.32	89	
					6.8001	0.464	0.248	0.235	0.222	0.184	0.214	1.159			103	(i)
1997	ab	0.626 766	8823.9437	20.136	3.8132	0.625	0.179	0.165	0.101	0.138	0.134	0.097	−2.08	−1.91	125	
2058	ab	0.503 415	9226.9053	20.238	3.8132	0.610	0.133	0.224	0.212	0.204	0.214	0.288	−1.92	−1.73	96	
2423	c	0.358 540	9167.9003	20.010	3.8132	0.328	0.202	0.170	0.149	0.157	0.159	0.372	−1.84	−1.65	120	(f)
2424	c	0.348 780	8809.8058	20.145	4.7959	0.527	0.166	0.215	0.227	0.178	0.207	0.482	−1.75	−1.55	118	
2450	ab	0.617 962	8810.1279	20.071	2.7656	0.886	0.252	0.141	0.141	0.126	0.136	0.500	−1.84	−1.65	113	
					3.8132	0.581	0.238	0.123	0.135	0.133	0.130	0.383			92	
					4.7959	0.172	0.192	0.136	0.157	0.146	0.146	0.239			108	
2455	ab	0.636 250	9184.8700	20.156	3.7485	0.413	0.247	0.160	0.135	0.112	0.136	0.467	−1.76	−1.56	113	
2458	c	0.357 686	8809.6823	20.156	2.7656	0.446	0.118	0.260	0.208	0.187	0.218	0.199	−1.73	−1.53	85	
					3.8132	0.375	0.201	0.228	0.208	0.205	0.214	0.802			102	
2470	ab	0.693 447	8809.4598	20.073	3.8132	0.245	0.168	0.183	0.220	0.207	0.203	0.467	−1.76	−1.56	94	
2482	c	0.365 865	9167.8931	20.191	4.7959	0.233	0.108	0.337	0.250	0.279	0.289	0.600	−1.64	−1.44	135	(f)
2502	ab	0.487 474	9185.8606	20.238	4.7959	0.419	0.123	0.268	0.300	0.258	0.275	0.645	−1.60	−1.39	140	(f)
2545	ab	0.674 059	8809.0126	20.016	2.7656	0.104	0.168	0.224	0.231	0.220	0.225	0.644	−1.60	−1.39	116	
2566	ab	0.583 517	9190.8800	20.234	4.7959	0.018	0.180	0.248	0.235	0.247	0.243	0.901	−1.38	−1.15	88	
2627	ab	0.575 091	9166.8885	20.130	4.7959	0.733	0.192	0.136	0.157	0.146	0.146	0.239	−1.96	−1.78	108	
2689	ab	0.511 352	8809.5668	20.139	3.7485	0.805	0.270	0.155	0.206	0.159	0.173	0.909	−1.37	−1.15	99	
3004	ab	0.715 496	8809.5055	20.044	2.7656	0.990	0.187	0.199	0.183	0.192	0.191	0.514	−1.72	−1.52	129	

Table 2 – *continued*

Star (a)	Type (b)	P (b)	Epoch (b)	$\langle V\rangle$ (b)	HJD (c)	ϕ	K	H_δ	H_γ	H_β	$\langle H\rangle$	MI	$[Fe/H]_{ZW}$	$[Fe/H]_{CG}$	V_r (km s^{-1})	Notes
3016	c	0.360 325	8809.8443	20.117	2.7656	0.220	0.139	0.279	0.227	0.172	0.226	0.414	−1.81	−1.61	131	(d)
3019	ab	0.732 965	9162.9250	19.978	3.7485	0.472	0.202	0.112	0.094	0.138	0.115	0.109	−2.07	−1.90	105	
3024	ab/Bl?	0.572 818	9223.7730	20.059	3.7485	0.052	0.179	0.197	0.229	0.216	0.214	0.641	−1.61	−1.40	143	(f)
3043	ab	0.623 908	8810.0604	20.192	2.7656	0.650	0.178	0.201	0.199	0.204	0.201	0.529	−1.70	−1.50	129	
3044	d	0.354 271	8810.0791	20.126	3.7485	0.044	0.092	0.319	0.283	0.227	0.276	0.355	−1.86	−1.67	133	(j)
3104	d	0.356 984	8809.9225	20.209	2.7656	0.982	0.243	0.182	0.171	0.169	0.174	0.745	−1.51	−1.30	124	(j)
3113	ab	0.593 260	8809.6681	20.098	2.7656	0.049	0.121	0.296	0.244	0.256	0.265	0.556	−1.79	−1.59	130	
					3.7485	0.706	0.216	0.152	0.134	0.130	0.139	0.319			116	
3125	ab	0.533 130	8809.9264	20.120	2.7656	0.220	0.201	0.179	0.160	0.154	0.164	0.404	−1.81	−1.62	134	
3143	d	0.354 531	9184.9270	20.188	2.7656	0.607	0.170	0.276	0.236	0.251	0.255	0.914	−1.36	−1.14	140	(j)
3302	AC	1.346 056	9227.8700	18.560	4.8256	0.506	0.295	0.101	0.116	0.124	0.114	0.553	−1.78	−1.58	81	
					6.8001	0.975	0.089	0.289	0.294	0.251	0.278	0.340			84	
3318	ab	0.640 243	9169.8898	20.148	4.8256	0.530	0.221	0.086	0.108	0.131	0.108	0.165	−2.02	−1.85	79	
3319	ab/Bl	0.564 984	9223.8400	20.012	4.8256	0.703	0.229	0.172	0.148	0.153	0.158	0.524	−1.71	−1.51	89	
3320	c	0.282 469	9192.9040	20.119	4.8256	0.954	0.067	0.341	0.338	0.300	0.326	0.403	−1.94	−1.76	84	
					6.8001	0.944	0.039	0.358	0.338	0.290	0.329	0.115			66	
3346	c	0.357 547	9168.9247	20.125	4.8256	0.857	0.088	0.244	0.216	0.189	0.216	−0.043	−2.02	−1.84	96	
					6.8001	0.379	0.141	0.214	0.243	0.203	0.220	0.394			120	
3365	ab	0.668 088	9235.8929	20.105	6.8001	0.807	0.196	0.126	0.157	0.119	0.134	0.187	−2.01	−1.82	99	
3413	c	0.359 537	9167.9120	20.132	4.8256	0.607	0.194	0.247	0.206	0.181	0.211	0.727	−1.72	−1.52	90	
					6.8001	0.098	0.103	0.299	0.230	0.220	0.250	0.285			85	
3710	Bin?	0.473 839	9192.9030	19.856	3.8132	0.070	0.046	0.215	0.205	0.182	0.201	−0.420	−2.56	−2.42	73	(f)
					4.8256	0.207	0.077	0.201	0.159	0.194	0.185	−0.270			85	
					6.8001	0.374	0.029	0.159	0.186	0.140	0.162	−0.646			89	
3827	ab	0.587 708	9226.7339	20.135	6.8001	0.644	0.212	0.147	0.071	0.122	0.114	0.152	−2.04	−1.86	67	
3834	c	0.375 237	9189.9150	20.003	3.7809	0.125	0.169	0.179	0.158	0.172	0.170	0.245	−1.84	−1.65	96	
					4.8256	0.909	0.164	0.204	0.205	0.184	0.198	0.400			85	
					6.8001	0.171	0.195	0.184	0.164	0.184	0.177	0.463			90	
3862	c	0.294 092	9188.9188	20.219	3.7809	0.622	0.087	0.307	0.318	0.268	0.298	0.442	−1.78	−1.58	121	
3907	ab	0.583 204	9169.9000	20.203	3.8132	0.683	0.269	0.126	0.093	0.137	0.119	0.464	−1.76	−1.56	112	
4263	c	0.284 768	8820.7399	20.229	2.7333	0.861	0.208	0.284	0.283	0.268	0.279	1.493	−0.85	−0.60	111	
4277	c	0.306 303	8809.7972	20.172	2.7333	0.136	0.113	0.332	0.254	0.251	0.279	0.576	−1.79	−1.60	115	
					3.8132	0.661	0.100	0.245	0.277	0.239	0.253	0.284			96	
4291	c	0.387 992	8810.1654	20.057	2.7656	0.282	0.185	0.209	0.238	0.202	0.217	0.700	−1.64	−1.43	105	
					3.8132	0.982	0.186	0.206	0.191	0.180	0.192	0.514			106	
4308	c	0.358 956	8809.7147	20.123	2.7656	0.364	0.112	0.229	0.240	0.170	0.213	0.122	−1.83	−1.64	118	
					3.8132	0.283	0.169	0.230	0.220	0.226	0.225	0.649			130	
4313	ab	0.731 064	8820.6952	20.111	2.7333	0.298	0.231	0.202	0.150	0.152	0.168	0.617	−1.63	−1.42	119	
4385	ab	0.487 413	8809.8949	20.191	2.7656	0.550	0.200	0.108	0.190	0.183	0.160	0.376	−1.87	−1.68	117	
					3.8132	0.699	0.076	0.328	0.298	0.253	0.293	0.311			103	
4689	ab	0.639 202	8809.9119	20.024	2.7656	0.843	0.178	0.150	0.137	0.183	0.157	0.221	−1.98	−1.79	108	
4747	ab	0.591 979	9166.9255	20.181	2.7333	0.246	0.168	0.234	0.201	0.198	0.211	0.534	−1.70	−1.50	120	
4780	?	0.391 270	8810.1007	19.958	2.7656	0.164	0.252	0.061	0.081	0.103	0.082	0.160	−2.03	−1.85	110	(k)
4785	ab	0.506 109	8809.4911	20.139	2.7656	0.935	0.069	0.267	0.179	0.136	0.194	−0.283	−2.42	−2.27	63	
4786	ab	0.537 290	9226.9054	20.102	2.7333	0.365	0.263	0.146	0.172	0.185	0.168	0.817	−1.45	−1.23	138	
4793	ab	0.559 834	8809.1465	20.059	2.7333	0.839	0.131	0.163	0.158	0.142	0.155	−0.068	−2.23	−2.06	133	
5000	c	0.323 261	9166.8850	20.158	4.8256	0.543	0.136	0.192	0.222	0.182	0.199	0.207	−1.99	−1.81	93	
5049	ab	0.648 752	8825.8195	20.076	4.8256	0.392	0.234	0.151	0.115	0.160	0.142	0.444	−1.78	−1.58	96	
5065	c	0.380 212	9222.7846	19.989	3.7809	0.931	0.101	0.322	0.275	0.231	0.276	0.440	−1.74	−1.54	125	
					4.8256	0.678	0.176	0.251	0.197	0.167	0.205	0.547			116	
5105	ab	0.556 682	9166.8930	20.154	4.8256	0.847	0.255	0.162	0.108	0.168	0.146	0.588	−1.65	−1.45	132	
5123	c	0.325 323	8810.9530	20.162	4.8256	0.327	0.074	0.325	0.323	0.312	0.320	0.441	−1.78	−1.59	95	
5155	ab	0.567 457	8823.8298	20.090	4.8256	0.611	0.241	0.081	0.104	0.167	0.117	0.316	−1.89	−1.70	108	
5330	ab	0.645 766	8809.3652	20.136	3.7809	0.976	0.210	0.170	0.202	0.214	0.195	0.704	−1.55	−1.34	110	(f)
5343	ab/Bl?	0.546 964	9164.9231	20.181	4.8256	0.149	0.190	0.158	0.147	0.162	0.156	0.282	−1.92	−1.74	108	
5359	ab	0.670 952	8809.7021	19.972	3.7809	0.375	0.121	0.108	0.115	0.150	0.124	−0.247	−2.39	−2.23	93	
5364	c	0.394 203	9168.9185	19.943	3.7809	0.624	0.044	0.238	0.268	0.231	0.246	−0.248	−2.39	−2.23	135	(f)
5376	c	0.389 520	9187.8882	20.079	3.7809	0.315	0.074	0.224	0.167	0.164	0.185	−0.287	−2.42	−2.27	137	
5382	ab	0.595 937	9191.9233	20.171	3.7809	0.708	0.249	0.121	0.136	0.111	0.123	0.389	−1.83	−1.63	99	
5393	c	0.322 741	9166.9255	20.081	3.7809	0.587	0.153	0.221	0.185	0.183	0.196	0.313	−1.89	−1.71	144	
5492	ab	0.528 786	8833.9145	20.161	3.7809	0.065	0.171	0.222	0.205	0.190	0.206	0.515	−1.72	−1.52	115	
5710	c	0.355 803	9227.7927	20.132	3.7809	0.997	0.133	0.234	0.205	0.171	0.203	0.219	−1.98	−1.79	141	
5714	c	0.292 913	8809.7224	20.221	2.7333	0.747	0.113	0.267	0.280	0.228	0.258	0.434	−1.79	−1.59	84	
5723	ab	0.566 020	9166.9255	20.250	2.7333	0.801	0.248	0.138	0.135	0.147	0.140	0.505	−1.73	−1.53	112	

Table 2 – *continued*

Star (a)	Type (b)	P (b)	Epoch (b)	$\langle V\rangle$ (b)	HJD (c)	ϕ	K	H_δ	H_γ	H_β	$\langle H\rangle$	MI	[Fe/H]$_{ZW}$	[Fe/H]$_{CG}$	V_r (km s^{-1})	Notes
5724	ab	0.498 508	8809.8649	–	2.7333	0.400	0.009	0.326	0.333	0.298	0.319	−0.265	−2.40	−2.25	104	(f,l)
5747	ab	0.559 848	8833.9264	20.040	2.7333	0.388	0.176	0.172	0.145	0.153	0.156	0.206	−1.99	−1.81	126	
5751	c	0.397 328	8809.6162	20.083	2.7333	0.756	0.112	0.267	0.191	0.208	0.222	0.177	−1.99	−1.81	97	
					3.7809	0.393	0.072	0.340	0.276	0.245	0.287	0.233			118	
5773	ab	0.508 760	8823.9310	20.223	3.7809	0.931	0.084	0.272	0.256	0.223	0.250	0.116	−2.07	−1.89	91	
5802	ab	0.514 632	8810.9385	20.244	3.7809	0.788	0.215	0.107	0.121	0.142	0.123	0.221	−1.98	−1.79	150	
6031	c	0.326 878	9168.9123	20.124	2.7333	0.709	0.172	0.244	0.216	0.203	0.221	0.637	−1.61	−1.40	140	(f)
6048	ab	0.626 791	9224.8920	20.168	2.7333	0.964	0.167	0.229	0.221	0.220	0.223	0.623	−1.62	−1.41	117	
6050	c	0.305 175	8809.7002	20.121	2.7333	0.227	0.151	0.248	0.228	0.180	0.219	0.462	−1.76	−1.57	139	
6085	c	0.361 528	9235.7159	20.146	2.7333	0.808	0.165	0.293	0.243	0.228	0.255	0.869	−1.40	−1.18	139	

[a]Identifiers are from Kaluzny et al. (1995). [b]Epochs are −244 0000. Along with types, periods and mean magnitudes (in intensity average) they were redetermined from the study of the light curves based on data from Kaluzny et al. (1995). In a number of cases (marked with notes) they differ significantly from values published in Kaluzny et al. (1995). [c]HJDs are −245 2850, they correspond to the HJD at half exposure. [d]Kovács (2001) classifies star 59, 1439 and 3016 as suspected double-mode RR Lyrae stars, with periodicities of 0.359 68/0.4837; 0.356 04/0.478 09 and 0.360 33/0.484 01 d, respectively. Our study of the light curves does not confirm these findings, we think these stars are monoperiodic *c*-type variables with noisy light curves. [e]We think this is a double-mode RR Lyrae, we list the first overtone period. [f]Classification and periods differ significantly from Kaluzny et al. (1995), who published aliases of the periodicities preferred here. Star 3710 is a suspected binary system ('Bin'). [g]Noisy spectrum. [h]We think this RR Lyrae could either be a double-mode or be affected by the Blazhko effect (Bl, Blazhko 1907). [i]*G*-band visible. [j]Kovács (2001) classifies these variables as double-mode RR Lyrae stars, respectively, with periodicities of 0.354 27/0.475 46 (3044), 0.356 99/0.479 75 (3104) and 0.354 53/0.476 30 (3143) d. [k]Variable star of unknown type. [l]Incomplete light curve.

flat field. Then we used the IRAF command LINECLEAN to reduce the contamination by cosmic rays. Up to 19 spectra were present in each pointing, and were extracted with the optimal extraction and automated cleaning options switched on. The sky contribution was subtracted making use of the slit length. The contamination of targets from nearby stars was reduced to a minimum, except for a few objects. For each science mask a HeCdHg lamp was acquired, and used to calibrate in wavelength the spectra, each one covering a different spectral range, depending on the target position. Not less than 10 lines of the calibration lamp were visible for each aperture, and the resulting dispersion solutions have rms of about 0.03 Å. Further cleaning of cosmic ray hits and bad sky subtractions was done using the clipping option in the IRAF SPLOT task. Fig. 2 shows examples of the final spectra.

3 DERIVATION OF THE METAL ABUNDANCES

We obtained the spectra for 110 of the variable stars identified in Sculptor by Kaluzny et al. (1995), and for 25 of them we have multiple observations. These authors published photometry in the *V*-band for all our targets. Periods and epochs of maximum light were determined from their time series data (kindly made available by Dr J. Kaluzny), using the period search package Graphycal Analyser of Time Series (GRATIS, Di Fabrizio 1999; Clementini et al. 2000). The new ephemerides are provided in Table 2. We found that our periods are in general slightly different from those published by Kaluzny et al. (1995); differences are in most cases around the fourth or fifth digit. However, there are a number of cases where our periods and type classifications significantly differ from those of Kaluzny et al. (1995), who published aliases of the periodicities preferred here. All these objects have been flagged in the last column of Table 2, where we provide comments on individual stars. We used our new periods to phase the spectra of our target stars in Sculptor since the scatter in the light curves appears to be significantly reduced than using the published values. Phases corresponding to the heliocentric Julian day (HJD) at half exposure are listed in column 3 of Table 2; for the double-mode RR Lyrae stars they correspond to the first overtone pulsation period. We also computed intensity-averaged luminosities for all the variables in our study, which are given in column 5 of Table 2. Based on our study of the light curves, our sample contains 62 *ab*-type, 40 *c*-type, three confirmed and two suspected *d*-type RR Lyrae stars, one anomalous Cepheid, one suspected binary system and one variable of unknown type.

3.1 Metallicities and metal abundance distribution of the variable stars in Sculptor

Precise and homogeneous metal abundances for the target stars in Sculptor were measured using the revised version of the ΔS method (Preston 1959) devised by Gratton et al. (2004). We do not actually measure ΔS values, but rather estimate metallicities for individual variables by comparing the strength of the H lines and of the Ca II K line with analogous data for variables in GCs of known metallicity. A detailed description of our method can be found in Gratton et al. (2004). A summary of the technique, and an update of the calibration procedures are provided in Appendix B, to which the interested reader is referred for details. Spectral line indices measured for the variables in Sculptor following Gratton et al. (2004), are given in columns 8–12 of Table 2. The correlation between K and $\langle H\rangle$ spectral indices is shown in Fig. 3. In this figure, the solid lines represent the mean relations of the calibrating clusters M68 and NGC 1851 (see Appendix B). The variables in Sculptor fall almost entirely below the mean line of NGC 1851 indicating that they are metal poorer than this cluster ([Fe/H]$_{ZW} = -1.36$), and also extend below the mean line of M68, showing that there is a number of variables in Sculptor metal poorer than [Fe/H]$_{ZW} = -2.09$. Metallicity indices MI defined according to equations (B1)–(B3), are listed in column 13 of Table 2. Individual metallicities were derived from the calibration equations (B4) and (B5) in the Zinn & West (1984, hereafter ZW84) and in the Carretta & Gratton (1997, hereafter CG97) metallicity scales separately; they are listed in columns 14 and 15 of Table 2. For different observations of the same star the [Fe/H] values are averages of all the available measurements. From the objects with multiple observations, we

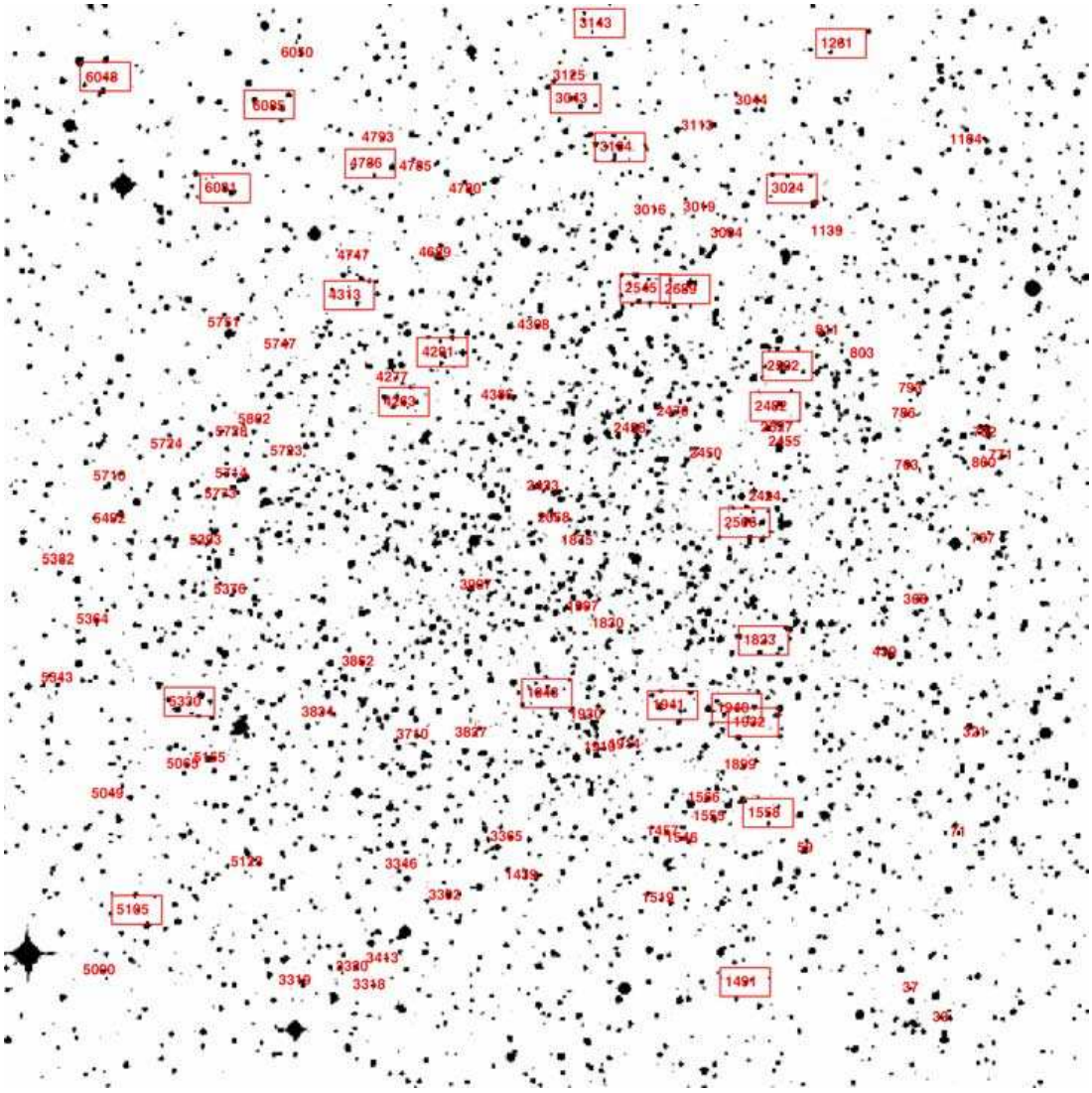

Figure 1. Position of the observed variables on a 16 × 16 arcmin^2 map of the centre of Sculptor dSph galaxy. North is up and east is to the left. Variables are identified according to Kaluzny et al. (1995) identifiers. Boxes mark the RR Lyrae stars for which we measured metallicites [Fe/H] > -1.70 dex (see Section 3.1).

estimate that errors of individual abundance determinations are 0.15 and 0.16 dex in ZW84 and CG97 metallicity scales, respectively.

The average metal abundance of the 107 RR Lyrae stars in our sample is [Fe/H] $= -1.83 \pm 0.03$ (rms $= 0.26$ dex) with a total metallicity range of $-2.42 <$ [Fe/H] < -0.85 in ZW84 scale, and an offset of about 0.2 dex to higher metallicity in CG97 scale. The star-to-star scatter inferred from the rms dispersions is about 0.19–0.23 dex, hence larger than typical measurement errors. If we adopt 0.23 dex as the measured metallicity spread, and quadratically subtract a [Fe/H] measurement error of 0.16 dex, we obtain $\sim$0.16 dex as our estimate of the intrinsic spread in the metal abundance of the Sculptor RR Lyrae stars.

The observed metallicity distribution of the Sculptor RR Lyrae stars (uncorrected for the measurement errors) in the ZW84 metallicity scale is shown in Fig. 4. Variable stars are divided by type. We find that the different types follow the same metallicity distributions. As is well known, the CG97 scale provides systematically higher metallicities than ZW84. In the following we will adopt ZW84 values, unless explicitly noted. However, independently of the adopted metallicity scale there are only very few metal-rich stars in our RR Lyrae sample. Based on the period distribution of the *ab*-type pulsators, Kaluzny et al. (1995) conclude that the bulk of the RR Lyrae stars in Sculptor have metallicities equal to or lower than [Fe/H] $= -1.7$. Indeed, there are only 26 stars with [Fe/H] > -1.7 in our sample. This is also the metallicity at which Tolstoy et al. (2004) find the break between metal-poor and metal-rich old populations in Sculptor. We will come back to this point in Section 6.

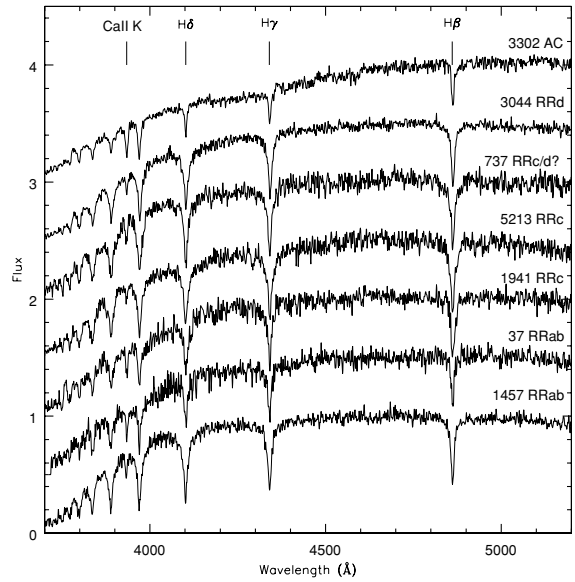

Figure 2. Examples of spectra of variable stars in Sculptor obtained using FORS2. The stars are identified according to Kaluzny et al. (1995). The six lower plots are RR Lyrae variables (from bottom to top: two fundamental mode, two first overtone, one suspected and one confirmed double-mode pulsator observed at different phases). The upper plot is an anomalous Cepheid (star 3302). The spectra have been offset for clarity, and the main spectral lines are marked.

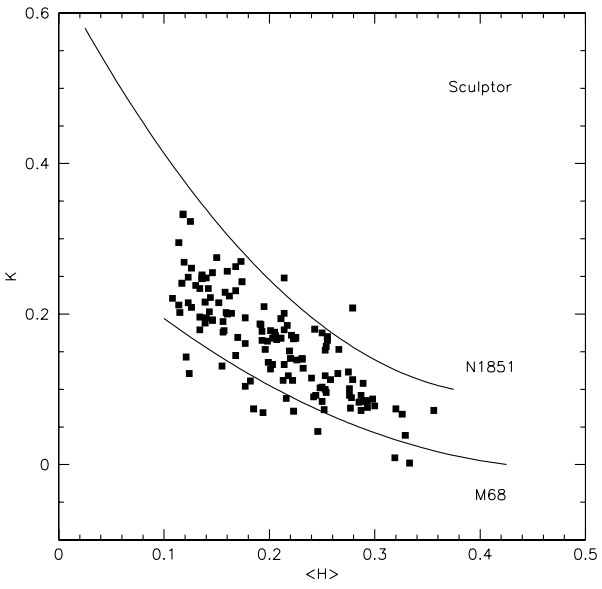

Figure 3. Correlation between K and $\langle H \rangle$ spectral indices for the variable stars in Sculptor. Solid lines represent the mean lines for M68 and NGC 1851 from Gratton et al. (2004).

3.2 Comparison with metallicities from the Fourier parameters of the light curve and the pulsation equations

Metal abundances for the *ab*-type RR Lyrae stars in Sculptor have been estimated by Kovács (2001) using the parameters of the Fourier decomposition of the light curves and the Jurcsik & Kovács (1996) method. Derived metallicities are in the range from ~ -0.8 to -2.0 dex, with an average value of [Fe/H] ~ -1.5 dex in the Jurcsik (1995) metallicity scale. Based on the frequency analysis of Kaluzny et al. (1995) data, Kovács (2001) also identified 15 confirmed and three suspected double-mode pulsators in Sculptor and estimated their metal abundance using the pulsation equations. He found that, similarly to the RRab stars, the bulk of the double-mode RR Lyrae stars in Sculptor have [Fe/H] ~ -1.5, with only two RRd stars (stars 1168 and 5354 in Kaluzny et al. 1995) at [Fe/H] $= -1.9$. The metallicity distributions of RRab and RRd stars separately are shown in fig. 5 of Kovács (2001), and can be compared to our distribution in Fig. 4. We recall that the Jurcsik (1995) metallicity scale is on average 0.2 dex more metal rich than the ZW84 scale at [Fe/H] ~ -1.5. This partially accounts for the difference between average values in Kovács (2001) and in our distribution in Fig. 4, but there still is a residual difference of 0.17 dex between the average values, and our distribution appears to cover a metallicity range larger than in Kovács (2001).

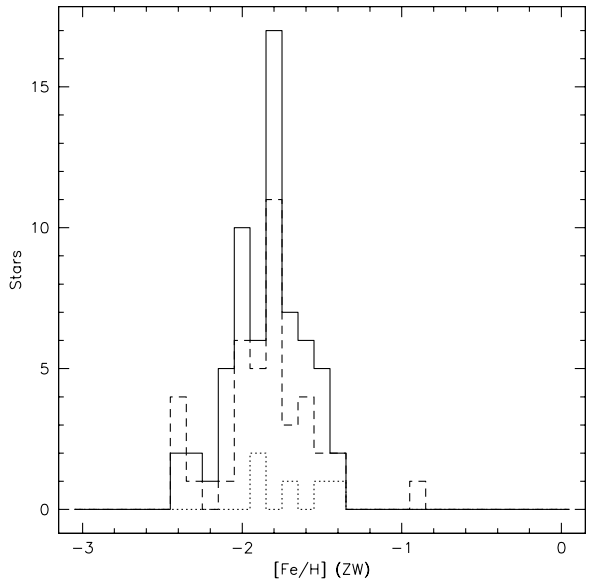

Figure 4. Metallicity distribution of the RR Lyrae stars in Sculptor using metal abundances in ZW84 metallicity scale. Variables are divided by type, solid line: RRab pulsators, dashed line: RRc pulsators, dotted line: RRd pulsators.

We determined metallicities for six of the RRd variables discovered by Kovács (2001), three of which are actually only suspected RRd stars. From our re-analysis of the light curves we think that these stars are monoperiodic *c*-type RR Lyraes with noisy light curves. The comparison between individual metallicity values is shown in Table 3, where the range given in column 4 was evaluated from the metallicity distribution of the RRd stars in fig. 5 of Kovács (2001). Unfortunately, we did not observe the two most metal-poor RRd stars in Kovács (2001).

As with the RRab stars, the metallicity range spanned by the RRd stars we analysed is larger than that obtained by Kovács (2001) for the same stars.

4 THE LUMINOSITY–METALLICITY RELATION

The luminosity–metallicity relation followed by the RR Lyrae stars in Sculptor was derived using the intensity-averaged mean

Table 3. Comparison of the metallicities for RRd variable stars in Sculptor.

Star	[Fe/H] this paper, ZW84	[Fe/H] this paper, CG97	[Fe/H] Kovács (2001)	Type Kovács (2001)	Type this paper
59	−2.14	−1.97	$-1.6 \leqslant$ [Fe/H] $\leqslant -1.4$	RRd	RRc
1439	−1.88	−1.70	$-1.6 \leqslant$ [Fe/H] $\leqslant -1.4$	RRd	RRc
3016	−1.81	−1.61	$-1.6 \leqslant$ [Fe/H] $\leqslant -1.4$	RRd	RRc
3044	−1.86	−1.67	$-1.6 \leqslant$ [Fe/H] $\leqslant -1.4$	RRd	RRd
3104	−1.51	−1.30	$-1.6 \leqslant$ [Fe/H] $\leqslant -1.4$	RRd	RRd
3143	−1.36	−1.14	$-1.6 \leqslant$ [Fe/H] $\leqslant -1.4$	RRd	RRd

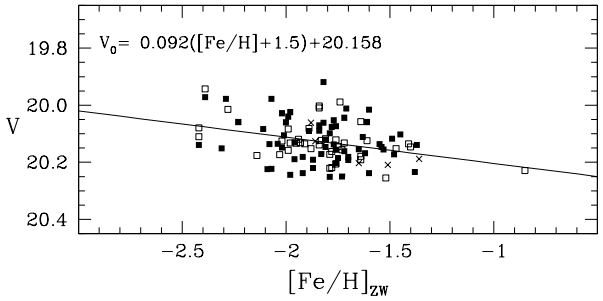

Figure 5. Luminosity–metallicity relation of the RR Lyrae stars in Sculptor; variables are divided by type, filled squares: RRab pulsators, open squares: RRc pulsators, crosses: RRd pulsators.

magnitudes and the metal abundances in Table 2. We first discarded all objects that are not RR Lyrae stars or have incomplete light curves (stars 3302, 3710, 4780 and 5724). We also eliminated the most metal-rich variable in our sample (star 4263), even if this star falls extremely well on the mean relations we derive. Following the procedure applied by Gratton et al. (2004) to the LMC RR Lyrae stars, we divided the Sculptor variables into six metallicity bins 0.1 dex wide; the corresponding average apparent magnitudes are given in Table 4 in the two metallicity scales, respectively. A least-squares fit weighted by the errors in both variables gives

$$\langle V \rangle = (0.092 \pm 0.027)([\mathrm{Fe/H}]_{\mathrm{ZW}} + 1.5) + (20.158 \pm 0.009),$$

where the errors in the slopes were evaluated via Monte Carlo simulations. The same slope is found for metallicities in CG97 scale.

The luminosity–metallicity relation of the Sculptor RR Lyrae stars is shown in Fig. 5. It is based on 105 stars covering the metallicity range [Fe/H] from −1.36 to −2.42, and we used different symbols for the various types of RR Lyrae stars. All variables seem to follow the same luminosity–metallicity relation independent of type. Gratton et al. (2004) found that the LMC double-mode RR Lyrae stars are offset to brighter luminosities in the luminosity–metallicity plane and explain this evidence with the LMC RRd stars being more evolved than the single-mode pulsators. The lack of a similar difference in luminosity between single- and double-mode Sculptor RR Lyrae stars suggests that in this galaxy also the single-mode variables are evolved.

A more striking difference is the slope of the luminosity–metallicity relation, significantly shallower than that obtained for the LMC variables by Gratton et al. (2004).[2] On the other hand, we note that also the scatter in the average apparent luminosity of the RR Lyrae stars in Sculptor is less than half of that observed for the variables in the LMC: σ_V(Sculptor) = 0.07 mag, compared to the 0.15–0.16 mag in the LMC (Clementini et al. 2003b). This scatter is almost entirely accounted for by photometric errors and the dispersion in metallicity of the Sculptor RR Lyrae stars, thus indicating that these variables have a very similar degree of evolution off the zero-age HB. The shallow slope of the luminosity–metallicity relation in Sculptor could thus be explained with the Sculptor RR Lyrae stars being all rather evolved stars arising from the old metal-poor population that also gives origin to the blue HB in the galaxy. Some support to this suggestion arises from the comparison of the average luminosity of the RR Lyrae stars with that of non-variable HB stars in Sculptor.

From the colour–magnitude diagram of Sculptor, values of $\langle V_{\mathrm{HB}} \rangle \simeq 20.18$–$20.20$ mag, $\langle V_{\mathrm{blue\,HB}} \rangle \simeq 20.20$ and $\langle V_{\mathrm{red\,HB}} \rangle \simeq 20.29$ mag are obtained by Kaluzny et al. (1995), Babusiaux et al. (2005) and Rizzi (2003), respectively. This is at least $\simeq$0.06–0.08 mag fainter than the average luminosity of the RR Lyrae stars, which, for the 106 RR Lyrae with full light curve coverage, is $\langle V \rangle = 20.127$ with a dispersion of $\sigma = 0.072$ (this value agrees well with the estimate by Kaluzny et al. 1995, based on the total sample of 226 RR Lyrae stars in Sculptor).

5 RADIAL VELOCITY DETERMINATIONS

Radial velocities were measured from the spectra of the Sculptor RR Lyrae stars, and are given in column 16 of Table 2. Multiple observations of the same stars show that our estimates have typical errors of about $\pm 15\,\mathrm{km\,s^{-1}}$, with no systematic differences for different masks. This error includes the contribution of measurement uncertainties, errors related to the centring of the stars in the slit and uncertainties due to the poor sampling of the radial velocity curves of the variable stars.

The average heliocentric radial velocity of all our variable stars in Sculptor is $\langle V_{\mathrm{r}} \rangle = 109.1 \pm 1.9\,\mathrm{km\,s^{-1}}$ (rms = $19.9\,\mathrm{km\,s^{-1}}$, 110 stars, having preliminarily averaged individual values for stars with multiple observations). The average radial velocity of the RR Lyrae stars alone is $\langle V_{\mathrm{r}} \rangle = 109.6 \pm 1.9\,\mathrm{km\,s^{-1}}$ (rms = $19.8\,\mathrm{km\,s^{-1}}$, 107 stars). These values are in excellent agreement with the estimate obtained from K-giants in Sculptor by Queloz, Dubath & Pasquini (1995: $\langle V_{\mathrm{r}} \rangle = 109.9 \pm 1.4\,\mathrm{km\,s^{-1}}$) and are consistent with the value of $\langle V_{\mathrm{r}} \rangle = 107 \pm 2.0\,\mathrm{km\,s^{-1}}$ previously derived by Armandroff & Da Costa (1986).

The good agreement with the literature values suggests that the off-centring problems noted for the calibrating cluster variables (see Appendix B) do not seem to affect the variables in Sculptor, and that the undersampling of the variable star's radial velocity curves does not significantly bias our estimates of the average V_{r} value.

[2] However, we note that in both the studies the slopes of the RR Lyrae luminosity–metallicity relations could be slightly underestimated by a few hundredths of magnitude, because of the relatively large errors of the individual [Fe/H] values.

Table 4. Metallicity distribution and average magnitudes of the RR Lyrae stars in Sculptor.

$[Fe/H]_{ZW}$ bin	No. stars	$\langle V \rangle$	$\langle [Fe/H]_{ZW} \rangle$	$\langle [Fe/H]_{CG} \rangle$
$[Fe/H] \leqslant -2.0$	22	20.093 ± 0.017	-2.175 ± 0.034	-2.005 ± 0.036
$-2.0 < [Fe/H] < -1.9$	14	20.139 ± 0.017	-1.957 ± 0.008	-1.773 ± 0.008
$-1.9 < [Fe/H] < -1.8$	19	20.099 ± 0.016	-1.846 ± 0.006	-1.656 ± 0.007
$-1.8 < [Fe/H] < -1.7$	23	20.140 ± 0.015	-1.757 ± 0.005	-1.559 ± 0.006
$-1.7 < [Fe/H] \leqslant -1.6$	13	20.144 ± 0.018	-1.638 ± 0.009	-1.432 ± 0.010
$-1.6 < [Fe/H]$	14	20.163 ± 0.012	-1.461 ± 0.018	-1.245 ± 0.019

To further check this point we extracted from the data base of the Galactic field RR Lyrae stars analysed with the Baade–Wesselink method (Liu & Janes 1990; Cacciari, Clementini & Fernley 1992; Jones et al. 1992; Skillen et al. 1993; Fernley 1994) template radial velocity curves of *ab*- and *c*-type RR Lyrae stars with metal abundance comparable to that of the variable stars in Sculptor, and estimated phase-dependent radial velocity corrections for each spectrum of RR Lyrae star. Using this procedure we found that the average correction to apply to the radial velocity mean value of the 107 RR Lyrae stars in our sample is less than $\sim 0.1\,\mathrm{km\,s^{-1}}$ and can be safely neglected.

The difference between rms scatter of the RR Lyrae stars ($19.8\,\mathrm{km\,s^{-1}}$) and typical measurement errors ($15\,\mathrm{km\,s^{-1}}$) implies an intrinsic radial velocity dispersion of $\sigma = 12.9\,\mathrm{km\,s^{-1}}$ for the RR Lyrae stars. This value is larger than the $6.3 + 1.1$, -1.3 and $6.2 \pm 1.1\,\mathrm{km\,s^{-1}}$ found for the K-giants by Armandroff & Da Costa (1986) and Queloz et al. (1995), and for Sculptor metal-rich red giant stars by Tolstoy et al. (2004; $\sigma_{\text{metal-rich}} = 7 \pm 1\,\mathrm{km\,s^{-1}}$), but is consistent with the $11 \pm 1\,\mathrm{km\,s^{-1}}$ dispersion observed by these same authors for the metal-poor red giants in Sculptor. This result gives further support to the hypothesis that the RR Lyrae stars in Sculptor arise from the old, metal-poor population, giving origin to the galaxy blue HB, although our value for their velocity dispersion needs to be confirmed by higher resolution spectroscopy.

6 METALLICITY DISTRIBUTIONS OF THE DIFFERENT OLD STELLAR COMPONENTS IN SCULPTOR

The average metallicity, metal abundance distribution and range in metal abundance spanned by the RR Lyrae stars can be compared with the analogous quantities for other old stellar components in Sculptor, namely, with the metallicity spread inferred from the width of the red giant branch (e.g. Kaluzny et al. 1995; Majewski et al. 1999; Rizzi 2003; Babusiaux et al. 2005), and with the abundances directly measured for red giants in Sculptor by Geisler et al. (2005) and Tolstoy et al. (2004), respectively.

The metallicity distribution in Fig. 4 shows that the RR Lyrae stars in Sculptor cover a full metallicity range of about 1.6 dex, which however reduces to $\sim$1 dex if the single most metal-rich star in the sample is discarded. This range is larger than that inferred from the spread of the red giant stars ($\Delta[Fe/H] \simeq 0.6$ dex, Kaluzny et al. 1995; Rizzi 2003; $\simeq$0.8 dex, Majewski et al. 1999; $\simeq$0.7 dex, Babusiaux et al. 2005), and is consistent with the spectroscopic study of red giants in Sculptor by Geisler et al. (2005: $\simeq$1.1 dex) and Tolstoy et al. (2004) in the galaxy inner region (see upper panel of their fig. 3).

Tolstoy et al. (2004) find that the ancient stellar component ($\geqslant$10 Gyr old) in Sculptor is divided into two distinct groups having different metal abundance, kinematics and spatial distribution. The metal-rich population is concentrated within the $r = 0.2^\circ$ central region, has metallicities in the range $-1.7 < [Fe/H] < -0.9$, velocity dispersion of $\sigma_{\text{metal-rich}} = 7 \pm 1\,\mathrm{km\,s^{-1}}$ and is related to the Sculptor red HB. The metal-poor population is more spatially extended, has metallicities in the range $-2.8 < [Fe/H] < -1.7$, velocity dispersion of $\sigma_{\text{metal-poor}} = 11 \pm 1\,\mathrm{km\,s^{-1}}$ and is related to the Sculptor blue HB.

Our RR Lyrae stars are located in the central region of Sculptor, virtually coincident with the region where Tolstoy et al. (2004) find segregation of red HB stars. However, their metallicity distribution is dominated by the metal-poor objects with an average value of $[Fe/H] = -1.83$. The 26 stars with $[Fe/H] > -1.7$ are marked by boxes in Fig. 1. Their average luminosity $\langle V_{[Fe/H]>-1.7} \rangle = 20.154$ ($\sigma = 0.060$, 26 stars) is marginally fainter than the average of the remaining 80 stars with $[Fe/H] \leqslant -1.7$ ($\langle V_{[Fe/H]\leqslant-1.7} \rangle = 20.118$, $\sigma = 0.075$, 80 stars), as expected given the shallow slope of the Sculptor RR Lyrae luminosity–metallicity relation, and is anyway brighter than both the blue and red HBs of the non-variable stars, thus indicating that they are evolved objects, like their metal-poor counterpart. The average radial velocity of the two samples is only marginally different: $\langle v_r \rangle = 117.5$ (rms = 18.5, 26 stars) for the metal-rich sample and $\langle v_r \rangle = 107.0$ (rms = 19.6, 80 stars) for the metal-poor stars. The rms scatters are very similar and, once deconvolved for the measurement errors ($15\,\mathrm{km\,s^{-1}}$), lead to very similar velocity dispersions of 10.8 and $12.6\,\mathrm{km\,s^{-1}}$ in agreement with the velocity dispersion measured by Tolstoy et al. (2004) for the metal-poor component associated to Sculptor blue HB.

7 SUMMARY AND CONCLUSIONS

Low-resolution spectra obtained with FORS2 at the VLT have been used to measure individual metal abundances ([Fe/H]) and radial velocities for 107 RR Lyrae stars in the Sculptor dSph galaxy. Metallicities were derived using a revised version of the ΔS method (Gratton et al. 2004). The RR Lyrae stars in Sculptor are predominantly metal poor with an average metal abundance of $[Fe/H] = -1.83 \pm 0.03$ (rms = 0.26 dex) on the ZW84 metallicity scale, and only a few outliers having metallicities larger than -1.4 dex. The observed metallicity dispersion is larger than the observational errors, thus showing that these variables have a real metallicity spread.

The RR Lyrae stars in Sculptor are found to follow a luminosity–metallicity relation with a slope of 0.09 mag $\mathrm{dex^{-1}}$, which is shallower than in the LMC (Gratton et al. 2004). This is explained with the Sculptor variable stars being rather evolved from the zero-age HB, as also supported by their brighter luminosity compared to the non-variable HB stars.

From our spectra we measured an intrinsic velocity dispersion $12.9\,\mathrm{km\,s^{-1}}$ for the RR Lyrae stars, which appears to be in agreement

with the dispersion derived by Tolstoy et al. (2004) for metal-poor red giants associated to the blue-HB stars in Sculptor.

All these evidences suggest that our RR Lyrae sample, and the RR Lyrae stars in Sculptor in general, are connected to the blue-HB population and arise from the first burst of star formation that produced the galaxy blue metal-poor HB. They allow to trace and distinguish this older component in the internal regions of the galaxy, which are otherwise dominated by the metal-rich and younger red-HB stars. Indeed, this component only produced a few, if any, of the Sculptor RR Lyrae stars since average luminosity and kinematic properties of the few metal-rich objects in our sample suggest that they are more likely the high-metallicity tail of the metal-poor star population rather than objects associated with Sculptor red-HB stars.

ACKNOWLEDGMENTS

Special thanks go to J. Kaluzny for providing us the time-series photometry of the Sculptor variables. We thank an anonymous referee for his/her comments and suggestions. This research was funded by MIUR, under the scientific projects 2002028935, 'Stellar Populations in the Local Group' (principal investigator: Monica Tosi) and 2003029437, 'Continuity and Discontinuity in the Milky Way Formation' (principal investigator: Raffaele Gratton).

REFERENCES

Armandroff T. E., Da Costa G. S., 1986, AJ, 92, 777
Babusiaux C., Gilmore G., Irwin M., 2005, MNRAS, 359, 985
Bersier D., Wood P. R., 2002, AJ, 123, 840
Blazhko S., 1907, Astron. Nachr., 175, 325
Cacciari C., Clementini G., Fernley J., 1992, ApJ, 396, 219
Carretta E., Gratton R. G., 1997, A&AS, 121, 95 (CG97)
Clement C. M., Shelton I., 1997, AJ, 113, 171
Clement C. M. et al., 2001, AJ, 122, 2587
Clementini G. et al., 2000, AJ, 120, 2054
Clementini G., Held E. V., Baldacci L., Rizzi L., 2003a, ApJ, 588, L85
Clementini G., Gratton R. G., Bragaglia A., Carretta E., Di Fabrizio L., Maio M., 2003b, AJ, 125, 1309
Clementini G., Gratton R. G., Bragaglia A., Ripepi V., Martinez Fiorenzano A. F., Held E. V., Carretta E., 2005, ApJ, 630 L145
Coutts C. M., Sawyer Hogg H., 1971, Publ. David Dunlap Obs. 3, 62
Di Fabrizio L., 1999, Laurea Degree thesis, Univ. Bologna
Dolphin A. E. et al., 2001, ApJ, 550, 554
Fernley J., 1994, A&A, 284, L16
Geisler D., Smith V. V., Wallerstein G., Gonzales G., Charbonnel C., 2005, AJ, 129, 1428
Gratton R. G., Bragaglia A., Clementini G., Carretta E., Di Fabrizio L., Maio M., Taribello E., 2004, A&A, 421, 937
Harbeck D. et al., 2001, AJ, 122, 3092
Held E. V., Saviane I., Momany Y., Carraro G., 2000, ApJ, 530, L85
Held E. V., Clementini G., Rizzi L., Momany Y., Saviane I., Di Fabrizio L., 2001, ApJ, 562, L39
Hurley-Keller D., Mateo M., Grebel E. K., 1999, ApJ, 523, L25
Jones R. V., Carney B. W., Storm J., Latham D. W., 1992, ApJ, 386, 646
Jurcsik J., 1995, Acta Astron., 45, 653
Jurcsik J., Kovács G., 1996, A&A, 312, 111
Lee J.-W., Carney B. W., 1999, AJ, 117, 2868
Liu T., Janes K. A., 1990, ApJ, 354, 273
Kaluzny J., Kubiak M., Szymański M., Udalski A., Krzemiński W., Mateo M., 1995, A&AS, 112, 407
Kovács G., 2001, A&A, 375, 469
Majewski S., Siegel M. H., Patterson R. J., Rood R. T., 1999, ApJ, 520, L33
Norris J., Bessell M. S., 1978, ApJ, 225, L49
Preston G. W., 1959, ApJ, 130, 507
Pritzl B. J., Armandroff T. E., Jacoby G. H., Da Costa G. S., 2002, AJ, 124, 1464
Queloz D., Dubath P., Pasquini L., 1995, A&A, 300, 31
Rizzi L., 2003, PhD thesis, Univ. Padua
Rizzi L., Held E. V., Bertelli G., Saviane I., 2004, Mem. Soc. Astron. Ital., 75, 110
Siegel M., Majewski S., 2000, AJ, 120, 284
Silbermann N. A., Smith H. A., 1995, AJ, 110, 704
Skillen I., Fernley J., Stobie R. S., Jameson R. F., 1993, MNRAS, 265, 301
Tolstoy E., Irwin M. J., Cole A. A., Pasquini L., Gilmozzi R., Gallagher J. S., 2001, MNRAS, 327, 918
Tolstoy E., Venn K. A., Shetrone M., Primas F., Hill V., Kaufer A., Szeifert T., 2003, AJ, 125, 707
Tolstoy E. et al., 2004, ApJ, 617, L119
Zinn R., West M. J., 1984, ApJS, 55, 45 (ZW84)

APPENDIX A: FINDING CHARTS

We present in this Section finding charts (Figs A1a–c) for all the variable stars we observed in Sculptor. They correspond to the nine 6.8×6.8 arcmin^2 FORS2 subfields used to map the central 15×15 arcmin^2 area of the galaxy. Centre-of-field coordinates are provided in Table 1. In each map, north is up and east to the left, and variables are identified according to Kaluzny et al. (1995) identifiers. The RR Lyrae stars are marked by open circles (in red in the electronic edition of the journal), and other types of variables are marked by (blue) open squares. The complete listing of the variables observed in Sculptor is provided in Table 2. Equatorial coordinates for all our targets can be found in table 2 of Kaluzny et al. (1995).

APPENDIX B: THE METALLICITY CALIBRATION

Following the procedure devised by Gratton et al. (2004), line indices for RR Lyrae stars are computed from the spectra shifted to rest wavelength by directly integrating the instrumental fluxes in spectral bands centred on the Ca II K, Hδ, Hγ and Hβ lines (see table 2 and fig. 10 of Gratton et al. 2004 for the definition of the spectral bands). Then a $\langle H \rangle$ index is defined as the average of the indices of the three hydrogen lines, and K as the index of the Ca II K line. Metallicities are derived by comparing the $\langle H \rangle$ and K indices measured for the target stars to the same quantities for variables in a number of globular clusters of known metal abundance.

The calibration of the line indices of the Sculptor variables in terms of metal abundances ([Fe/H]) was obtained using RR Lyrae stars in the newly observed clusters M15, M2 and NGC 6171, and in the calibrating clusters used in Gratton et al. (2004), namely, M68, NGC 1851 and NGC 3201. For all these clusters, precise metal abundances are available on both the ZW84 and CG97 metallicity scales. NGC 6441, a metal-rich cluster ([Fe/H] $= -0.59$ according to ZW84 metallicity scale) having RR Lyrae stars with anomalously long periods, was not used for calibration purposes and is discussed elsewhere (see Clementini et al 2005).

Line indices measured for RR Lyrae stars in the calibrating clusters analysed in the present paper are provided in Tables B1–B3 for M15, M2 and NGC 6171, respectively. The calibrating clusters define monometallic correlations in the K versus $\langle H \rangle$ plane. These relations are shown in Fig. B1, where filled squares represent stars in M15, M2 and NGC 6171, and solid lines are the mean relations defined by M68, NGC 1851 and NGC 3201 taken from Gratton et al. (2004). RR Lyrae stars in M15 fall precisely on the mean line of

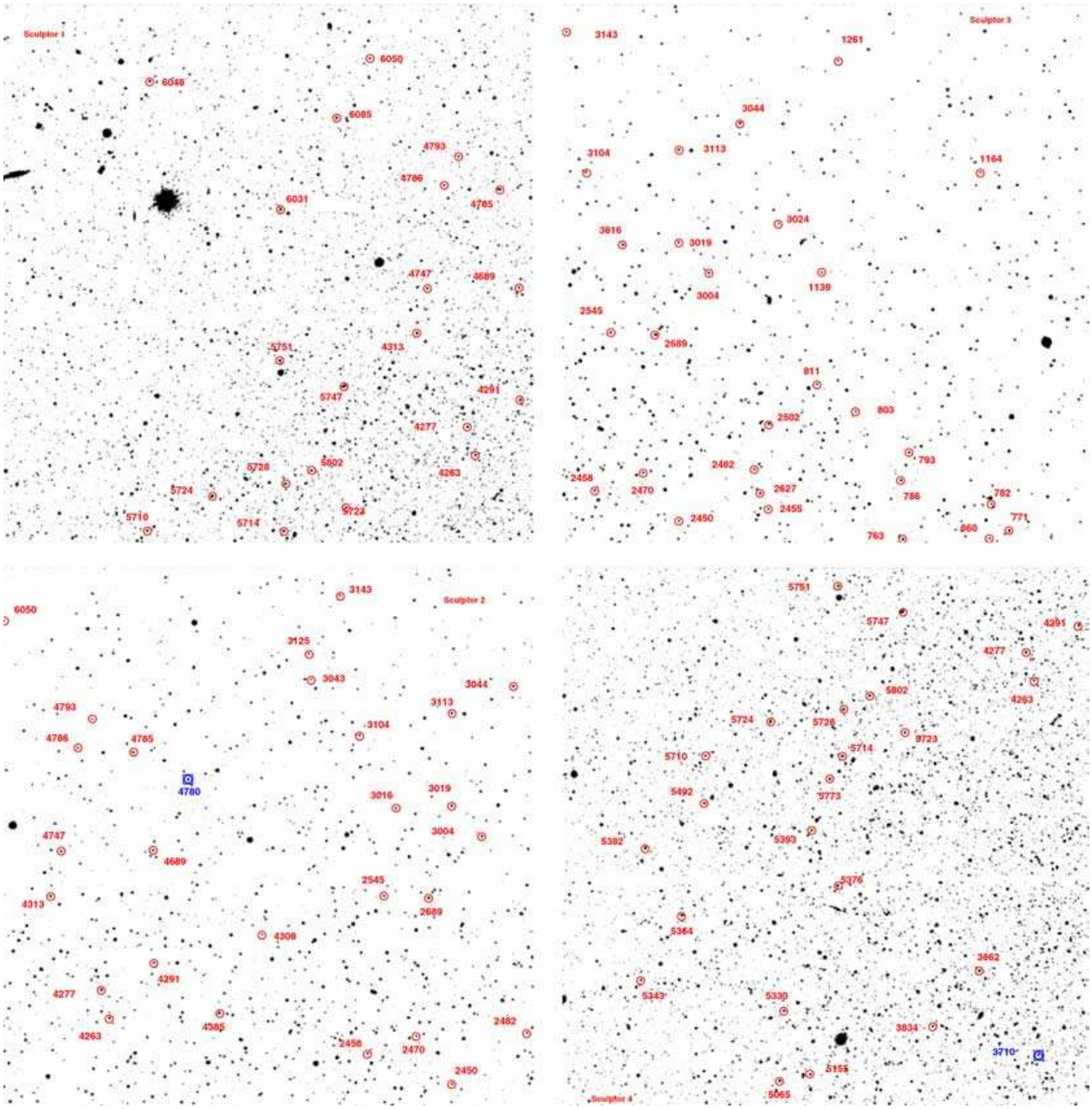

Figure A1. (a) Finding charts of the variable stars in Sculptor fields 1–4. (b) Finding charts of the variable stars in Sculptor fields 5–8. (c) Finding chart of the variable stars in Sculptor field 9.

M68, and those in M2 closely follow the mean line of NGC 3201, confirming the good agreement between metal abundances of these two pairs of clusters. Stars in NGC 6171 generally fall slightly above the mean line of NGC 1851, in agreement with the slightly higher metallicity of NGC 6171 with respect to NGC 1851.

According to Gratton et al. (2004) the mean relations drawn in Fig. B1 by M68 and NGC 1851 are

$$K_1 = 0.3093 - 1.2815\langle H\rangle + 1.3045\langle H^2\rangle \quad \text{(B1)}$$

(valid for $\langle H\rangle$ between 0.12 and 0.40) for M68, and

$$K_2 = 0.6432 - 2.6043\langle H\rangle + 3.0820\langle H^2\rangle \quad \text{(B2)}$$

(valid for $\langle H\rangle$ between 0.04 and 0.34) for NGC 1851. We thus defined MI as

$$MI = (K - K_1)/(K_2 - K_1) \quad \text{(B3)}$$

where K is the Ca II K line index of the star, and K_1, K_2 are derived entering the $\langle H\rangle$ index measured for the star into equations (B1) and

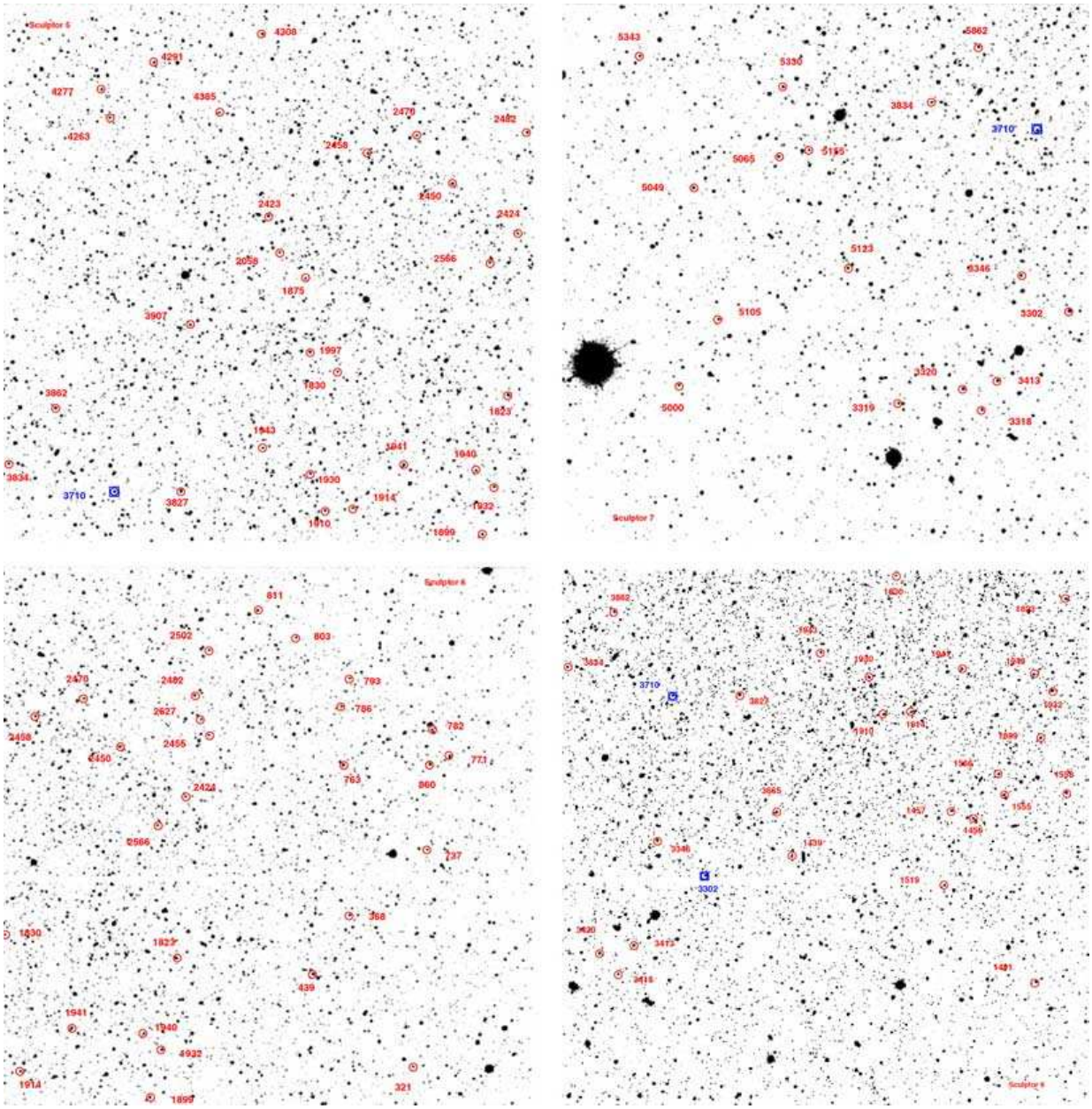

Figure A1 – *continued*

(B2). *MI* values derived by this procedure for the RR Lyrae stars in the calibrating clusters analysed in the present paper are listed in column 10 of Tables B1–B3.

The calibration of the metallicity index in terms of metal abundance ([Fe/H]) was derived by computing average $\langle MI \rangle$ values for the M15, M2 and NGC 6171 variables from the individual *MI*s in Tables B1–B3 and from the *MI* values in column 9 of tables 3–5 of Gratton et al. (2004) for M68, NGC 1851 and NGC 3201, and correlating these $\langle MI \rangle$ values with the metal abundances of the clusters on the ZW and CG metallicity scales, respectively. The average $\langle MI \rangle$ values and their dispersions are summarized in columns 6 and 7 of Table B4 along with the cluster metallicities (and their uncertainties) in the two metallicity scales (columns 2–5).

The correlation between [Fe/H] and $\langle MI \rangle$ values is very well represented by linear regressions with scatter typically within the error of measure. These linear regressions are described by the following equations:

$$[\mathrm{Fe/H}]_{\mathrm{ZW}} = 0.882\langle MI \rangle - 2.170 \quad \text{(B4)}$$

$$[\mathrm{Fe/H}]_{\mathrm{CG}} = 0.941\langle MI \rangle - 2.000 \quad \text{(B5)}$$

and are shown in Fig. B2 for the ZW84 and CG97 metallicity scales, respectively.

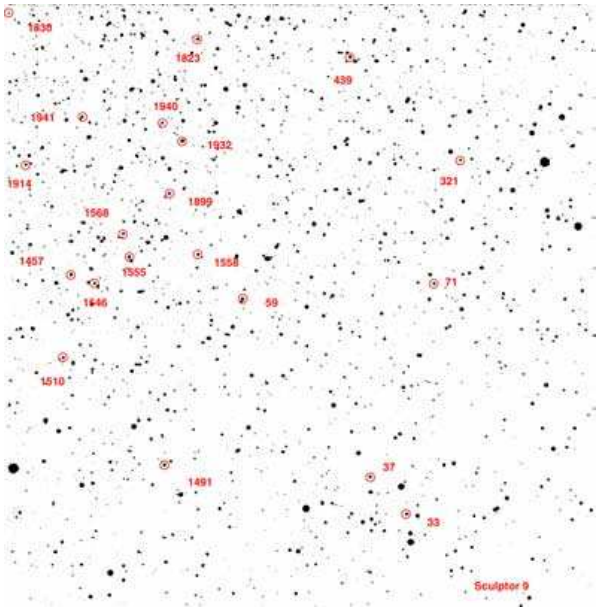

Figure A1 – *continued*

Individual metal abundances for the RR Lyrae stars in the calibrating clusters analysed in the present paper were derived from the above calibration equations. They are listed in Tables B1–B3, respectively, while the mean metallicities derived from the averages of these individual values and their respective dispersions are given in Table B4.

The last column in each of Tables B1–B3 gives individual radial velocities measured from the spectra of the stars observed in the calibrating clusters. Averages of these values are listed in Table B4. We note that these average radial velocities differ somewhat from the literature values, particularly for NGC 6171, suggesting the presence of systematic offsets possibly caused by off-centring of the cluster variables in the slit. These systematic differences are not found in the case of the Sculptor variables, for which the average radial velocity we measured is perfectly consistent with the literature values (see Section 5). This suggests that we are simply seeing an effect of the small samples in the Galactic clusters, while the one in Sculptor is large enough to average away the off-centring effects.

Table B1. Line indices and metal abundances of RR Lyrae stars in the globular cluster M15.

						M15						
Star (a)	HJD (−240 0000)	Type	ϕ (b)	K	H_δ	H_γ	H_β	$\langle H \rangle$	MI	$[Fe/H]_{ZW}$	$[Fe/H]_{CG}$	V_r (km s^{-1})
V10	52851.6744	c	0.781	0.126	0.195	0.192	0.147	0.178	0.025	−2.15	−1.98	−83
V12	52851.6744	ab	0.645	0.159	0.148	0.155	0.122	0.142	0.027	−2.15	−1.98	−92
V17	52851.6744	d	0.429	0.123	0.181	0.151	0.158	0.163	−0.073	−2.23	−2.07	−96
V19	52851.6744	ab	0.592	0.090	0.272	0.247	0.208	0.242	0.121	−2.06	−1.89	−122
V23	52851.6744	ab	0.024	0.118	0.218	0.208	0.184	0.203	0.108	−2.08	−1.90	−118
V25	52851.6744	ab	0.492	0.167	0.141	0.107	0.126	0.125	−0.015	−2.18	−2.01	−99
V29	52851.6744	ab	0.967	0.146	0.170	0.145	0.133	0.149	−0.002	−2.17	−2.00	−114
V42	52851.6744	c	0.818	0.102	0.228	0.171	0.163	0.187	−0.092	−2.25	−2.09	−99
V50	52851.6744	c	0.298	0.079	0.272	0.253	0.225	0.250	0.078	−2.10	−1.93	−104

[a]Star identifiers are from Sawyer Hogg on line catalogue of variable stars in Galactic globular clusters published by Clement et al. (2001). [b]Phases were calculated from the HJD of observation using epochs and periods corrected according to the rates of period changes published by Silbermann & Smith (1995).

Table B2. Line indices and metal abundances of RR Lyrae stars in the globular cluster M2.

						M2						
Star (a)	HJD (−240 0000)	Type	ϕ (b)	K	H_δ	H_γ	H_β	$\langle H \rangle$	MI	$[Fe/H]_{ZW}$	$[Fe/H]_{CG}$	V_r (km s^{-1})
V10	52856.7503	ab	0.758	0.194	0.221	0.219	0.193	0.211	0.722	−1.53	−1.32	−38
V15	52856.7503	c/d	0.345	0.097	0.319	0.308	0.281	0.303	0.583	−1.66	−1.45	−25
V26[c]	52856.7503	c	0.428	0.196	0.224	0.223	0.177	0.208	0.716	−1.54	−1.33	−21
V32[c]	52856.7503	c	0.350	0.152	0.266	0.257	0.249	0.257	0.774	−1.49	−1.27	−34
V7	52856.7503	ab	0.621	0.203	0.221	0.217	0.238	0.225	0.923	−1.36	−1.13	−36
V3[d]	52856.7503	ab	0.191	0.253	0.150	0.144	0.147	0.147	0.585	−1.65	−1.45	−15

[a]Star identifiers are from Sawyer Hogg on line catalogue of variable stars in Galactic globular clusters published by Clement et al. (2001). [b]Phases of the spectra were derived from the HJD of observation and the ephemerides published by Lee & Carney (1999). [c]Variable stars V26 and V32 correspond to stars LC608 and LC864 of Lee & Carney (1999), respectively. [d]Doubtful identification.

Table B3. Line indices and metal abundances of RR Lyrae stars in the globular cluster NGC 6171.

						NGC 6171						
Star (a)	HJD (−240 0000)	Type	ϕ (b)	K	H_δ	H_γ	H_β	$\langle H \rangle$	MI	$[Fe/H]_{ZW}$	$[Fe/H]_{CG}$	V_r (km s^{-1})
V2	52 849.5952	ab	0.746	0.330	0.113	0.128	0.117	0.119	0.771	−1.49	−1.27	−77
V4	52 849.5952	c	0.385	0.220	0.283	0.241	0.219	0.247	1.280	−1.04	−0.80	−91
V6	52 849.5952	c	0.570	0.214	0.256	0.284	0.205	0.248	1.239	−1.08	−0.83	−87
V7	52 849.5952	ab	0.683	0.399	0.124	0.129	0.142	0.132	1.234	−1.08	−0.84	−86
V9	52 849.5952	c	0.793	0.201	0.277	0.238	0.231	0.249	1.133	−1.17	−0.93	−96
V21	52 849.5952	c	0.774	0.228	0.267	0.295	0.222	0.262	1.504	−0.84	−0.59	−77

[a]Star identifiers are from Sawyer Hogg on line catalogue of variable stars in Galactic globular clusters published by Clement et al. (2001). [b]Phases were derived from the HJD of observation, the periods published by Clement & Shelton (1997) and the epochs we estimated from the study of the light curves published from the same authors. V2 was not observed by Clement & Shelton (1997), for this star the adopted ephemerides, from Coutts & Sawyer Hogg (1971), may be no longer valid.

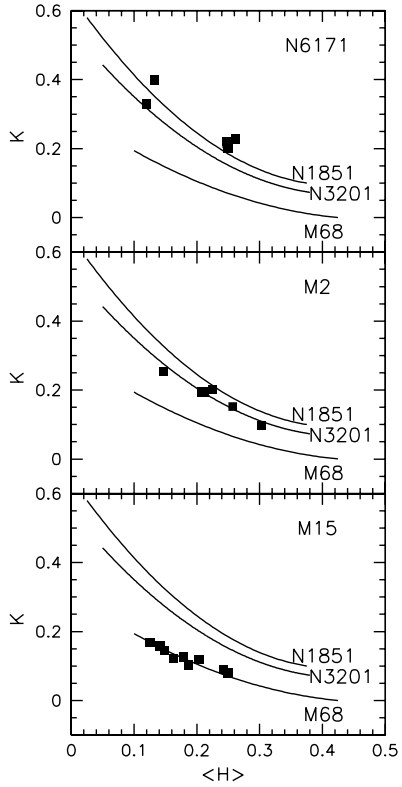

Figure B1. Correlation between K and $\langle H \rangle$ spectral indices for the calibrating clusters M15, M2 and NGC 6171 observed in the present run. Solid lines represent the mean lines for the calibrating clusters M68, NGC 3201 and NGC 1851, from Gratton et al. (2004).

Table B4. Calibration of the metallicity index.

Cluster	$[Fe/H]_{ZW}$	Err	$[Fe/H]_{CG}$	Err	$\langle MI \rangle$	Err	$\langle$[Fe/H]$\rangle$ this paper, ZW scale	σ	$\langle$[Fe/H]$\rangle$ this paper, CG scale	σ	$\langle V_r \rangle$ (km s^{-1})
NGC 1851	−1.36	0.09	−1.03	0.06	1.007	0.028	-1.36 ± 0.02^a	0.10	–	–	–
NGC 3201	−1.61	0.12	−1.24	0.03	0.710	0.030	-1.56 ± 0.02^a	0.08	–	–	–
NGC 4590 (M68)	−2.09	0.11	−2.00	0.03	0.000	0.014	-2.09 ± 0.01^a	0.05	–	–	–
NGC 6171	−0.99	0.06	−0.95	0.04	1.194	0.098	-1.12 ± 0.09	0.21	-0.88 ± 0.09	0.22	-86 ± 3
NGC 7078 (M15)	−2.15	0.08	−2.02	0.04	0.020	0.025	-2.15 ± 0.02	0.06	-1.98 ± 0.02	0.07	-103 ± 4
NGC 7089 (M2)	−1.62	0.07	−1.31	0.04	0.717	0.052	-1.54 ± 0.05	0.11	-1.33 ± 0.05	0.12	-28 ± 4

Note. [a]Averages of the values in tables 3–5 of Gratton et al. (2004) corrected downward, respectively, by 0.10, 0.07 and 0.03 dex to account for systematic differences between ZW84 and the metallicity scale adopted in Gratton et al. (2004).

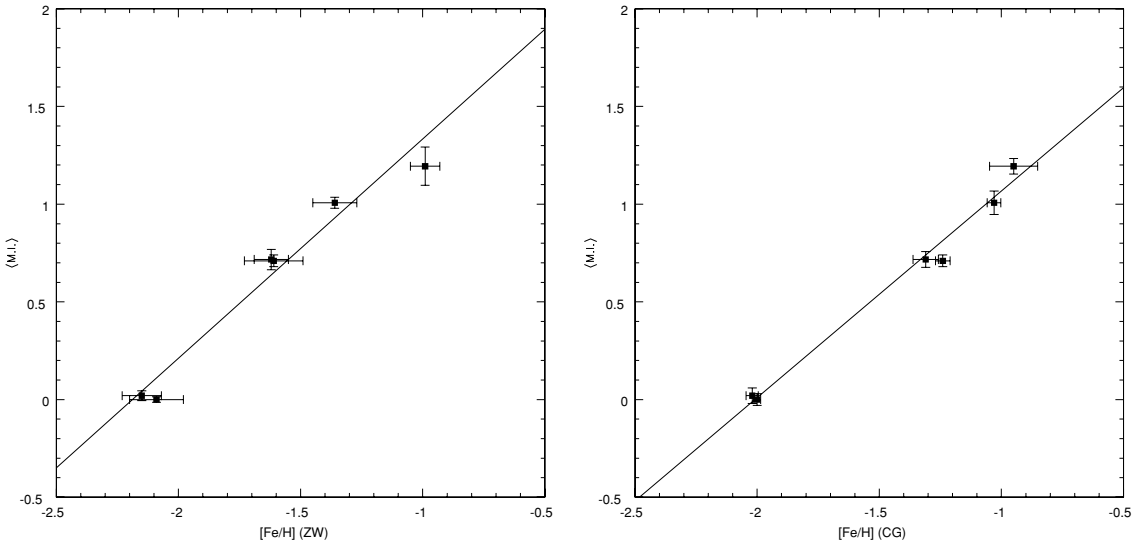

Figure B2. Calibration of the metallicity index (*MI*) on ZW84 (left-hand panel) and CG97 (right-hand panel) metallicity scales.

This paper has been typeset from a TEX/LATEX file prepared by the author.

A&A 420, L27–L30 (2004)
DOI: 10.1051/0004-6361:20040155

Astronomy & Astrophysics

Letter to the Editor

No planet around HD 219542 B⋆

S. Desidera[1], R. G. Gratton[1], M. Endl[2], R. U. Claudi[1], R. Cosentino,[3,4], M. Barbieri[5,6], G. Bonanno[3], S. Lucatello[1,7], A. F. Martinez Fiorenzano[1,7], F. Marzari[8], and S. Scuderi[2]

[1] INAF - Osservatorio Astronomico di Padova, Vicolo dell' Osservatorio 5, 35122 Padova, Italy
[2] McDonald Observatory, The University of Texas at Austin, Austin, TX 78712, USA
[3] INAF - Osservatorio Astrofisico di Catania, Via S. Sofia 78, Catania, Italy
[4] INAF - Centro Galileo Galiei, Calle Alvarez de Abreu 70, 38700 Santa Cruz de La Palma (TF), Spain
[5] CISAS - Università di Padova, c/o Dipartimento di Fisica, Via Marzolo 8, 35131 Padova, Italy
[6] LESIA, Observatoire de Paris, Section de Meudon, 92195 Meudon Principal Cedex, France
[7] Dipartimento di Astronomia - Università di Padova, Vicolo dell'Osservatorio 2, 35131 Padova, Italy
[8] Dipartimento di Fisica - Università di Padova, Via Marzolo 8, 35122 Padova, Italy

Received 5 April 2004 / Accepted 30 April 2004

Abstract. The star HD 219542 B has been reported by us (Desidera et al. 2003) to show low-amplitude radial velocity variations that could be due to the presence of a Saturn-mass planetary companion or to stellar activity phenomena. In this letter we present the results of the continuation of the radial velocity monitoring as well as a discussion of literature determinations of the chromospheric activity of the star (Wright et al. 2004). These new data indicate that the observed radial velocity variations are likely related to stellar activity. In particular, there are indications that HD 219542 B underwent a phase of enhanced stellar activity in 2002 while the activity level has been lower in both 2001 and 2003. Our 2003 radial velocity measurements now deviate from our preliminary orbital solution and the peak in the power spectrum at the proposed planet period is severely reduced by the inclusion of the new data. We therefore dismiss the planet hypothesis as the cause of the radial velocity variations.

Key words. stars: individual: HD 219542 B – stars: planetary systems – stars: binaries: visual – stars: activity – techniques: spectroscopic – techniques: radial velocity

1. Introduction

In Desidera et al. (2003, hereafter Paper I) we presented high precision radial velocity (hereafter *RV*) monitoring of the components of the wide binary system HD 219542. This pair is part of the sample of wide binaries currently under monitoring at TNG using the high resolution spectrograph SARG (Gratton et al. 2001). We have found evidence for the presence of low amplitude *RV* variations on the secondary HD 219542 B with a period of 112 days at a confidence level of 96–97%. These *RV* variations could be due to a Saturn-mass planet orbiting at 0.46 AU or to stellar activity.

The relatively low statistical confidence of the proposed planetary orbit as well as the possible presence of stellar activity indicate that a confirmation is required before we can classify of HD 219542 B as a bona fide planet host star.

It is well known that stellar activity induces distortions of the profile of the spectral lines that could be seen as *RV* variations and then mimic the occurrence of companions orbiting the target (see e.g. Saar et al. 1998). These spurious *RV* variations may have amplitudes and timescales comparable to those induced by giant planets, making challenging the search for planets around active stars. The controversial case of HD 192263 (Henry et al. 2002; Santos et al. 2003) is worth of mention in this context.

Two different components of the magnetic activity phenomena are of concern for planet searches. Star spots alter the profile of spectral lines, as well known from Doppler imaging studies of rapidly rotating spotted stars (see e.g. Rice 2002; Strassmeier 2002). For slowly rotating stars the distortions of line profile are more subtle but nevertheless sufficient to be detected as spurious *RV* variations (Hatzes 2002). The *RV* variations resulting from the presence of surface features typically follow the time scales of the rotational period of the star (a few days for the active stars for which such signal is more easily detectable), but for the long term and sparse sampling typical of planet search surveys no clear periodicities are often present, because of the limited lifetime of such features. *RV* variations caused by star spots are usually correlated to photometric

Send offprint requests to: S. Desidera,
e-mail: desidera@pd.astro.it

⋆ Based on observations made with the Italian Telescopio Nazionale Galileo (TNG) operated on the island of La Palma by the Centro Galileo Galilei of the INAF (Istituto Nazionale di Astrofisica) at the Spanish Observatorio del Roque de los Muchachos of the Instituto de Astrofisica de Canarias.

variations (Paulson et al. 2004; Queloz et al. 2001). The second contribution is represented by plages, that cause a change of the shape of spectral lines, mostly because of the alteration of the granulation pattern (Saar 2003; Kürster et al. 2003). The variations of the area covered by plages along the magnetic cycle and/or the rotational period then cause *RV*s variations, correlated with chromospheric emission. For some low activity stars, for which the effects of rotational modulations are lower than those of the long term magnetic cycle, a fairly good correlation between *RV*s and chromospheric emission can be found (Saar & Fischer 2000).

In order to disentangle the origin of *RV* variations (keplerian orbital motion vs. activity jitter) basically three approaches can be pursued.

1. To directly search for the presence of distortions of line profiles (ideally on the same spectra on which *RV*s are derived), as done by e.g. Hatzes et al. (1998) for 51 Peg and Queloz et al. (2001) for HD 166435
2. To obtain measurements of stellar activity (chromospheric emission, photometry), possibly simultaneous to *RV*s, to search for correlation between *RV*s and activity. Note that one single activity diagnostics may not be enough since photometry and chromospheric emission are mostly sensitive to different components of magnetic activity.
3. To continue the *RV* monitoring of the object. In fact, stellar activity typically is not stable on yearly timescales, so that an activity signal is not expected to maintain the same phase and amplitude with time (see Queloz et al. 2001)

For our candidate we followed the second and third approaches, collecting new *RV* data and considering literature determinations of the chromospheric emission of the star (Wright et al. 2004), published after Paper I, to study the evolution of its activity level. The line bisector variations corresponding to the observed *RV* variations are below our detectability threshold, as discussed in Paper I.

2. Radial velocities

The new *RV*s have been obtained from SARG spectra in the same way as in Paper I, using the AUSTRAL code (Endl et al. 2000). Six new spectra were acquired from June 2003 to January 2004, hereafter referred as 2003 season. Table 1 and Fig. 1 present the full radial velocity data set for HD 219542 B (nightly averages)[1]. As can be seen in Fig. 1, the data taken during the 2003 season do not follow the tentative orbital solution derived in Paper I.

Figure 2 shows the Lomb-Scargle periodogram (Lomb 1976; Scargle 1982) for the data included in Paper I and for the whole dataset presented here. The power at 112 days sharply decreases with the addition of the data of the last observing season.

[1] For the 2000–2002 velocities, there are minor differences with respect to those published in Paper I. These are due to the fact that some trends in the radial velocity of the ∼100 pixel long chunks along a spectral order, due to errors in the wavelength calibration of the stellar template (without iodine lines), are removed considering the average velocity of each chunk for the whole dataset. This correction then slightly changes with the addition of the new data. The differences are much smaller than internal errors. The inclusion of the new data also changes the normalization.

Table 1. Differential radial velocities for HD 219542 B.

JD-2 450 000	*RV* m s^{-1}	Err. m s^{-1}	JD-2 450 000	*RV* m s^{-1}	Err. m s^{-1}
1825.51	−5.0	7.4	2424.71	12.4	5.3
1826.49	−10.7	6.0	2445.71	13.3	4.7
2070.71	1.0	4.0	2472.70	−6.7	5.6
2071.71	7.2	4.2	2538.51	25.0	8.1
2072.69	9.6	6.0	2570.42	−2.9	3.4
2113.71	−0.7	4.6	2585.45	−16.0	4.9
2115.69	6.7	3.9	2597.33	2.9	3.3
2116.68	−5.0	6.0	2605.36	−3.0	3.6
2117.71	−1.4	5.2	2810.69	−2.2	4.9
2120.72	0.9	5.1	2818.66	2.2	8.6
2145.66	0.1	4.7	2891.55	−2.4	5.8
2190.54	3.2	3.8	2953.35	−11.8	6.0
2216.47	10.6	7.0	2982.39	−12.8	8.2
2245.43	−7.7	4.2	3018.35	−5.8	6.3

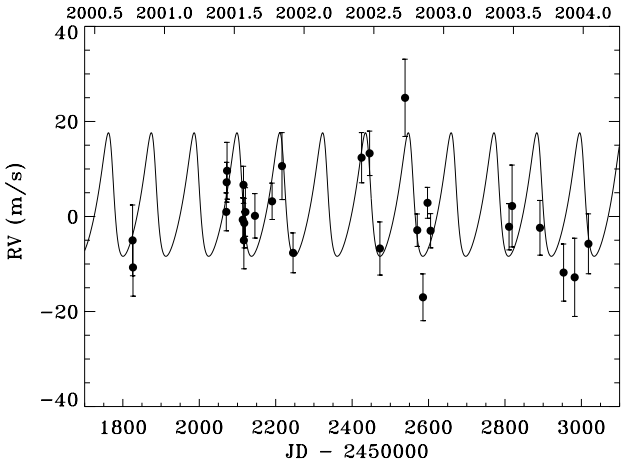

Fig. 1. Radial velocity curve for HD 219542 B. The data taken in the 2003 season do not follow the tentative orbital solution derived in Paper I (overplotted as a solid line).

3. Chromospheric activity

Wright et al. (2004) recently published the measurement of Ca II H and K emission for the whole samples of the Keck and Lick planets searches. HD 219542 A and B were recently added to the Keck planet search sample. Overall, 11 and 15 measurements from June 2002 to July 2003 are presented for the two stars respectively. The mean S index for HD 219542 A and B result of 0.158 and 0.204 respectively. The calibration of Noyes et al. (1994) coupled with the colors of the stars as given by Simbad, i.e. $(B - V) = 0.64$ and 0.69 for HD 219542A and B

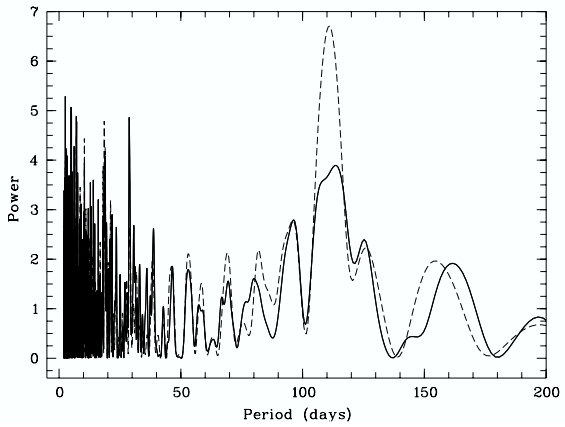

Fig. 2. Lomb-Scargle periodogram of radial velocities for HD 219542 B. The solid line refers to the full data set while dashed line is the periodogram of the data included in Paper I. The inclusion of 2003 data causes a strong decrease of the 112 days peak. Note that for display purposes only the period range 2 to 200 days is shown.

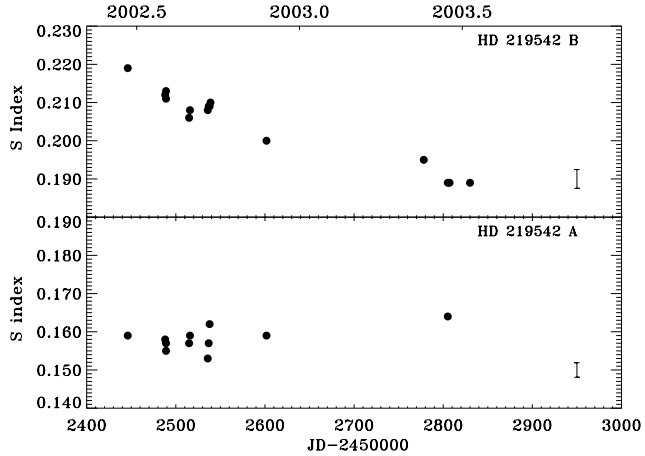

Fig. 3. Ca II H&K emission measurements of HD 219542 A (*lower panel*) and HD 219542 B (*upper panel*) from Keck (Wright et al. 2004). Typical error bars on differential values of S index measured at Keck are shown in the right part of each panel. These results show an enhanced activity in 2002 and a sharp decline over the following year for HD 219542 B. The activity level of component A is fairly constant and lower than component B.

respectively[2] gives $\log R'_{HK} = -5.01$ and -4.80. Our measurement of Paper I was based on a single FEROS spectrum and has a fairly large error because of the low signal and the paucity of available calibrators with low activity level.

Single epoch measurements are also included in Wright et al. (2004) (available at `astro.berkeley.edu/~jtwright/CaIIdata/tab1.tex`). These were obtained using the differential technique described in their paper, reaching errros of 1.2%. They are plotted in Fig. 3.

4. Discussion

The differential Ca II H&K measurements by Wright et al. (2004) indicate a much higher activity level for HD 219542 B during the 2002 season with respect to 2003. The activity level of HD 219542 A is instead lower and nearly constant, with a possible small increase in the 2003 season. When considering the radial velocity curve, it should be noticed that the dispersion of *RV*s of HD 219542 B is larger during the 2002 season. Table 2 shows the seasonal mean and dispersion of *RV*s and Ca II H&K emission, the measured *RV* dispersion excess (calculated as the quadratic difference between the observed dispersion and the mean internal errors) as well as the radial velocity jitter expected on the basis of the calibration by Marcy (2002, private communication).

These results strongly suggest that HD 219542 B underwent a phase of enhanced activity during 2002, while the activity decreased significantly in 2003. On the basis of the low *RV* scatter, the activity level could have been low also in June–July 2001.

We note that the seasonal variations of rms *RV* dispersion are much larger than those predicted by the jitter calibration. The global scatter on longer timescale (4 years) is instead much better predicted by such relation. This indicates that the estimates on *RV* jitter based on the activity level of the star should be more reliable when considering a fairly long time coverage, while on short time scales the calibration might severely underestimate or overestimate the actual jitter. This fact may be explained considering that during the phases of higher activity the appearance of spots and plages causes short term *RV* (and photometric) variations according to the rotational phases (see e.g. Paulson et al. 2004), while the absolute value of the chromospheric emission might be only moderately affected.

It appears that the high activity phase of HD 219542 B during 2002 was relatively short lived when compared to that of the Sun. The star might have a fairly short and/or irregular activity cycle. Alternatively, its activity behaviour might be similar to that of 15 Sge, that has a cycle with activity enhancements lasting about 1 year every 17 years (Baliunas et al. 1995; Wright et al. 2004) and low activity level at other epochs.

HD 219542 A instead shows no sign of enhanced or variable activity. The age of the two components derived using the relation by Donahue (1993) is 5.7 and 2.7 Gyr for HD 219542 A and B respectively. This age difference is larger than typically obtained in coeval systems (Henry et al. 1996) but similar to that derived for the Sun when using the maximum and minimum *S* values along its magnetic cycle.

In Paper I we noted that the 2002 *RV* data could be fitted quite well by sinusoidal variations with a period of 18.5 days. Both the *RV* and Ca H&K emission data are not sufficient to firmly establish the rotational period of the star[3]. However, a

[2] The colors and absolute magnitudes adopted by Wright et al. ($\Delta(B-V) = 0.014$ mag; HD 219542 B brighter by 0.59 mag), indicate that they probably took the magnitude and colors of HD 219542 A from the Simbad object HD 219542 and those of HD 219542 B from the Simbad object CCDM J23166-0135AB, which is actually the composite HD 219542 A+B, instead that for BD -02 5917B.

[3] The power at 18.5 days decreased with the inclusion of 2003 data, see Fig. 2.

Table 2. Seasonal mean and dispersion of radial velocities and Ca H&K emission for HD 219542 B.

Season	N_{data}	Mean *RV* m s^{-1}	rms *RV*s m s^{-1}	Err. m s^{-1}	log R'_{HK}	Obs. jitter m s^{-1}	Exp. jitter m s^{-1}
2001	12	2.0 ± 1.6	5.6	5.0	–	2.6	–
2002	8	3.0 ± 4.7	13.3	5.1	−4.78	10.1	7.1
2003	6	−5.4 ± 2.6	6.5	6.8	−4.86	0.0	6.1
all	28	0.0 ± 1.7	9.0	5.6	−4.80	7.1	6.8

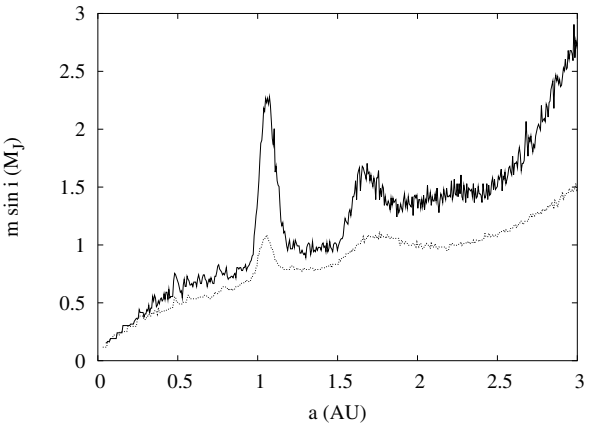

Fig. 4. Limits on planets around HD 219542 B in circular orbits (dotted line) and eccentric orbits (solid line).

period of 18.5 days is compatible within the uncertainties to that obtained using the Noyes et al. (1994) calibration.

In spite of the moderate activity level of the star our *RV*s are anyway of some usefulness for planet search. We derived the upper limits on the planets which are still compatible with our data (Fig. 4). We use the same technique developed in Paper I, that allows the determinations of the upper limits on the mass of companions in eccentric orbits, while most of the upper limits determinations in literature consider only circular orbits. With the exclusion of a small window around 1 year period, planets with $m \sin i > 1 M_J$ can be excluded within 1.5 AU. The peak around 1 year can be explained considering that a planet with period close to 1 year, fairly high eccentricity, and longitude of periastron and orbital phases in suitable ranges would cause a radial velocity curve nearly flat most of the time with *RV* variations concentrated on the times on which the target is not observable.

5. Conclusion

The continuation of the radial velocity monitoring and the multi-epoch measurements of the Ca II H&K emission indicate that the low amplitude *RV* variations of HD 219542 B presented in Paper I are likely due to stellar activity. This star should therefore be removed from the list of extrasolar planet host stars.

The available data suggest that the star underwent a relatively short-lived phase of enhanced activity during the 2002 season.

This study confirms the relevance of the activity-related phenomena in the *RV* planet searches and, on the other hand, the great impact of the high precision Doppler surveys in improving our understanding of the stellar activity cycles. Even for stars with modest activity level, the discovery of planets with amplitude of 10–15 m s^{-1} requires a long term monitoring to check for the stability of the signal as well as ancillary measurements of activity indicators (see e.g. Hatzes et al. 2000).

Acknowledgements. We thank the TNG staff for its help in the observations. We are grateful to G. Marcy for providing us its jitter calibration. We thank the referee, Dr. R. Freire-Ferrero, for his stimulating comments. This research has made use of the SIMBAD database, operated at CDS, Strasbourg, France. M.E. is supported by NASA Grant NAG5-13206

References

Baliunas, S. L., Donhaue, R. A., Soon, W. H., et al. 1995, ApJ, 438, 269
Desidera, S., Gratton, R. G., Endl, M., et al. 2003, A&A, 405, 207 (Paper I)
Donahue, R. A. 1993, Ph.D. Thesis, New Mexico State University
Endl, M., Kürster, M., & Els, S. 2000 A&A, 363, 585
Gratton, R. G., Bonanno, G., Bruno, P., et al. 2001, Exp. Astron., 12, 107
Hatzes, A. P. 2002, Astron. Nachr., 323, 392
Hatzes, A. P., Cochran, W. D., & Bakker, E. J. 1998, Nature, 391, 154
Hatzes, A. P., Cochran, W. D., McArthur, B., et al. 2000, ApJ, 544, L145
Henry, G. W., Donahue, R. A., & Baliunas, S. L. 2002, ApJ, 577, L111
Henry, T. J., Soderblom, D. R., Donahue, R. A., & Baliunas, S. L. 1996, AJ, 111, 439
Kürster, M., Endl, M., Rouesnel, F., et al. 2003 A&A, 403, 1077
Lomb, N. R. 1976, Ap&SS, 39, 477
Noyes, R. W., Hartmann, L. W., Baliunas, S. L., Duncan, D. K., & Vaughan, A. H. 1984, ApJ, 279, 763
Paulson, D., Saar, S. H., Cochran, W. D., & Henry, G. W. 2004, AJ, 127, 1644
Queloz, D., Henry, G. W., Sivan, J. P., et al. 2001, A&A, 379, 279
Rice, J. B. 2002, Astron. Nachr., 323, 220
Saar, S. H. 2003, in Scientific Frontiers in Research on Extrasolar Planets, ed. D. Deming, & S. Seager, ASP Conf. Ser., 294, 65
Saar, S. H., Butler, R. P., & Marcy, G. W. 1998, ApJ, 498, L153
Saar, S. H., & Fischer, D. A. 2000, ApJ, 534, L105
Santos, N. C., Udry, S., Mayor, M., et al. 2003, A&A, 406, 373
Scargle, J. D. 1982, ApJ, 263, 835
Strassmeier, K. G. 2002, Astron. Nachr., 323, 309
Wright, J. T., Marcy, G. W., Butler, R. P., & Vogt, S. S. 2004, ApJS, in press [arXiv:astro-ph0402582]

A&A 420, 683–697 (2004)
DOI: 10.1051/0004-6361:20041242

Astronomy & Astrophysics

Abundance difference between components of wide binaries⋆,⋆⋆

S. Desidera[1], R. G. Gratton[1], S. Scuderi[2], R. U. Claudi[1], R. Cosentino[2,3], M. Barbieri[4], G. Bonanno[2], E. Carretta[1], M. Endl[5], S. Lucatello[1,6], A. F. Martinez Fiorenzano[1,6], and F. Marzari[7]

[1] INAF – Osservatorio Astronomico di Padova, Vicolo dell' Osservatorio 5, 35122 Padova, Italy
[2] INAF – Osservatorio Astrofisico di Catania, via S. Sofia 78, Catania, Italy
[3] INAF – Centro Galileo Galiei, Calle Alvarez de Abreu 70, 38700 Santa Cruz de La Palma (TF), Spain
[4] CISAS – Universitá di Padova, via Venezia 15, Padova, Italy
[5] McDonald Observatory, The University of Texas at Austin, Austin, TX 78712, USA
[6] Dipartimento di Astronomia – Universitá di Padova, Vicolo dell'Osservatorio 2, Padova, Italy
[7] Dipartimento di Fisica – Universitá di Padova, via Marzolo 8, Padova, Italy

Received 16 February 2004 / Accepted 4 March 2004

Abstract. We present iron abundance analysis for 23 wide binaries with main sequence components in the temperture range 4900–6300 K, taken from the sample of the pairs currently included in the radial velocity planet search on going at the Telescopio Nazionale Galileo (TNG) using the high resolution spectrograph SARG. The use of a line-by-line differential analysis technique between the components of each pair allows us to reach errors of about 0.02 dex in the iron content difference. Most of the pairs have abundance differences lower than 0.02 dex and there are no pairs with differences larger than 0.07 dex. The four cases of differences larger than 0.02 dex may be spurious because of the larger error bars affecting pairs with large temperature difference, cold stars and rotating stars. The pair HD 219542, previously reported by us to have a different composition, here is shown to be normal. For non-rotating stars warmer than 5500 K, characterized by a thinner convective envelope and for which our analyis appears to be of higher accuracy, we are able to exclude in most cases the consumption of more than 1 Earth Mass of iron (about 5 Earth masses of meteoritic material) during the main sequence lifetime of the stars, placing more stringent limits (about 0.4 Earth masses of iron) in five cases of warm stars. This latter limit is similar to the estimates of rocky material accreted by the Sun during its main sequence lifetime. Combining the results of the present analysis with those for the Hyades and Pleiades, we conclude that the hypothesis that pollution by planetary material is the only mechanism responsible for the highest metallicity of the stars with planets may be rejected at more than 99% level of confidence if the incidence of planets in these samples is as high as 8% and similar to the field stars included in current radial velocity surveys. However, the significance of this result drops considerably if the incidence of planets around stars in binary systems and clusters is less than a half of that around normal field stars.

Key words. stars: abundances – stars: planetary systems – stars: binaries: visual – techniques: spectroscopic

1. Introduction

The evidence for a high metal content in stars harbouring planets is becoming stronger as planet discoveries cumulate and suitable control samples are studied using strictly the same procedures. It appears that the metal abundance of stars with planets is on average about 0.25 dex larger than that of typical control sample stars (Laws et al. 2003) and that the frequency of planets is a strong function of metallicity (Santos et al. 2004; Fischer et al. 2004).

Two alternative hypotheses have been proposed to explain these observations: either the high metallicity is responsible for the presence of planets, making their formation easier; or the planets are the cause of the high metallicity, because of pollution of metal-rich planetary material onto the (outer region of the) central star (Gonzalez 1997).

Infall of planetesimals on the star during the early phases of planet formation is generally expected on the basis of current models of planet formation. The orbital migration proposed to explain the occurrence of the close-in giant planets found by radial velocity surveys also points to the infall on the star of portions of the proto-planetary disk.

Most of the accretion is expected to take place during the early phases of the evolution of the planetary system. However, when a star is still in the phase of gravitational contraction,

Send offprint requests to: S. Desidera,
e-mail: desidera@pd.astro.it

⋆ Based on observations made with the Italian Telescopio Nazionale Galileo (TNG) operated on the island of La Palma by the Centro Galileo Galilei of the INAF (Istituto Nazionale di Astrofisica) at the Spanish Observatorio del Roque de los Muchachos of the Instituto de Astrofisica de Canarias.

⋆⋆ The equivalent widths are only available in electronic form at the CDS via anonymous ftp to
cdsarc.u-strasbg.fr (130.79.128.5) or via
http://cdsweb.u-strasbg.fr/cgi-bin/qcat?J/A+A/420/683

its convective zone is much thicker than for main sequence stars (see e.g., Murray et al. 2001). In this case, the metal-rich material should be uniformly distributed by convective mixing over a large portion of the star, resulting in a negligible photospheric chemical alteration even for rather large amounts of accreted material. Late accretion, when the star is approaching or has already reached the main sequence, is likely required to produce observable differences. This may happen due to infall of residual planetesimal/asteroids. The age distribution of the main sequence stars hosting debris disks (Habing et al. 2001), and of the impact craters on Solar System solid bodies, indicate that a significant infall of gas-poor material may be present until 300–400 Myr after star formation; at this epoch the convective zone of a solar-mass star has been thinned enough that significant alterations of the surface abundances may be produced. The ingestion of planets scattered toward the star by dynamical interactions (Marzari & Weidenschilling 2002) might also produce metallicity enhancements at late phases.

The signatures of accretion should be more evident for stars with smaller mixing zones, and disappear for evolved stars, when the outer convective region penetrates deeply into the star. The observations of lithium depletion for stars in the range 1.2−1.5 $M_{\odot}$ (the so-called Li-dip, Boesgaard & Tripicco 1986) indicate that an additional mixing mechanism is at work, other than standard convective mixing[1]. It must be further noted that the lithium dip is not present in open clusters as young as Pleiades (Pilachowski et al. 1987), indicating an age dependence. Such an extra-mixing mechanism, besides destroying lithium, should also efficiently flatten the radial abundance profiles of the star, if enrichment of external layers occurred. Therefore the stars that should show the most prominent signatures of accretion are early G-dwarfs and late F-dwarfs, with masses smaller than those in the Li-dip (Murray et al. 2001). The occurrence of "Li-dip" extra-mixing might also help in explaining the lack of F stars with very high metallicity ([Fe/H] > +0.50), predicted by the pollution scenario when considering only the extension of the convective zone.

The metal abundance of planet hosts does not appear to be correlated with the thickness of the convective zone (Pinsonneault et al. 2001; Santos et al. 2004). This seems to indicate that pollution is not the most relevant contribution to the high metallicity of stars with planets. On the other hand, two possible effects might in principle explain such a lack of a trend as a function of the thickness of the convective envelope. The first is the result of Vauclair (2004), who suggests that, when the metallicity difference between the inner and outer parts of a star exceedes a threshold, further mixing is induced in the transition zone, therefore diluting the atmospheric metallicity enhancement. The second effect can be considered if the metal enrichment is dominated by the ingestion of already formed planets. According to the hydrodynamical simulations by Sandquist et al. (1998), a 1.22 $M_{\odot}$ star should be able to only partially consume an engulfed giant planet within its thin convective zone. Depending on the actual distribution of heavy elements within the planet (possibly mostly confined in the planet core), the resulting alteration of chemical composition might be even smaller than for a solar-like star that is able to consume nearly completely a Jupiter-like planet within its convective zone.

On the other hand, several observational results support the occurrence of pollution phenomena.

Smith et al. (2001) found indications of systematic element-to-element differences as a function of the condensation temperature on some planet host stars. This could be explained by the infall of material devoid of light elements, such as rocky planets or asteroids. However, such chemical composition trends can be confused with galactic chemical evolution trends, and can be more easily studied in binaries and clusters. Gratton et al. (2001b), hereafter Paper I, performed a differential analysis of 6 visual main sequence binaries. They found one pair (HD 219542) with a 0.09 dex iron content difference, four pairs with very similar composition and one ambiguous case (HD 200466). Laws & Gonzalez (2001) also found a small difference between the components of 16 Cyg. A similar approach can be pursued to look for chemical anomalies among open cluster stars. Paulson et al. (2003) studied 55 FGK dwarfs in the Hyades. They found two stars with abundances 0.2 dex larger than the cluster mean, but their membership is questionable. The Pleiades were studied by Wilden et al. (2002); they found one possible candidate out of 15 stars with abundance 0.1 dex above the cluster mean and very little scatter for the other stars (0.02 dex). No correlation appears to be present between iron and lithium abundances.

The presence of ^{6}Li might be a strong indication of accretion phenomena, since this element is easily destroyed and cannot be observed in main sequence stars unless recently fallen onto the star from an external source. The presence of ^{6}Li in HD 82943 is controversial (Reddy et al. 2002; Israelian et al. 2003). If confirmed, this would indicate the infall of a giant planet. Anomalies of the most abundant ^{7}Li isotope are instead easier to find (see e.g., Pasquini et al. 1997; King et al. 1997; Martin et al. 2002) but they are more difficult to interpret as they might not be linked to planetary pollution.

Murray et al. (2001) found that the Sun should have ingested some 2 $M_{\oplus}$ of meteoritic material (about 0.4 $M_{\oplus}$ of iron), considering the drop of iron density in the asteroid region and the time distribution of the impact craters. This corresponds to a metallicity enhancement of 0.017 dex. Helioseismology currently does not allow a confirmation of the presence of such a small metal abundance difference between the inner and the outer regions (Winnick et al. 2002), with upper limits on the amount of accreted iron about four times higher than the Murray et al. (2001) estimate[2].

From this discussion, it appears that the comparison of the chemical composition of wide binaries is a very powerful approach to study the occurrence of planetary pollution.

[1] Alternative explanations of Li-dip depletion such as mass loss or gravitational sedimentation do not seem to be supported by observations, see Do Nascimento et al. (2000).

[2] The comparison between the results quoted in the original papers show some inconsistencies because of different assumptions on the composition of meteoritic material. In this paper, we adopt the meteoritic abundances by Lodders (2003). The mass fraction of iron is thus 18.3% of the meteoritic material.

The number of pairs studied in Paper I is too small to allow significant inferences about the frequency and the amount of chemical anomalies in visual binaries. In this paper, we significantly enlarge the number of pairs studied (23), with various improvements in the analysis procedure. We will then combine the results of the present analysis with the literature results for Hyades and Pleaides, to draw tentative conclusions about the impact of planetary material pollution.

2. Observations and data reduction

A radial velocity survey aimed to find planets around stars in wide binaries is on-going at TNG (the Italian Telescopio Nazionale Galileo on La Palms, Canary Islands, Spain) using the high resolution spectrograph SARG (Gratton et al. 2001a). The goals of the project are the study of the dynamical effects due to the presence of the companion on the existence and orbital characteristics of planetary systems, and the study of chemical composition differences possibly caused by the ingestion of planetary material. A recent report describing the status of the survey is given by Gratton et al. (2004).

The radial velocities are determined using the iodine cell technique. A high resolution, high quality spectrum of each star, free of iodine lines, is used as template for the radial velocity analysis. Such observational material is fully suited for a careful abundance analysis, without further observational efforts. All the spectra were acquired with the Yellow Grism, that covers the spectral range 4600–7900 Å without gaps, and the 0.25 arcsec slit. The resulting resolution is $R = 150\,000$ (2 pixel sampling). The insertion of a suitable filter avoids any grism second order contamination in the red extreme of the spectra. During the observations, the slit was usually oriented perpendicularly to the separation of the components to minimize the contamination of the spectra by the companion.

We present in this paper the stellar templates acquired between June 2001 and November 2002. We also reanalyzed the pairs included in Paper I to take into account the modifications in our analysis procedure. The spectra were reduced in the standard way using IRAF[3]. The signal to noise ratio per pixel in most cases exceeds 150.

3. Abundance analysis

The analysis procedure is similar to that performed in Paper I, with some differences outlined in detail below. The unidimensional spectra were analyzed using routines within the ISA code (Gratton 1988). The continuum level was determined by fitting a cubic spline through automatically selected regions of the spectra, excluding discrepant points identified by eye. Then the equivalent widths (*EW*s) were measured using an automatic procedure, that estimates a local continuum level and perform a Gaussian fit to the selected lines (see Bragaglia et al. 2001 for details)[4]. The assumption of a Gaussian line profile fails for stars with rotational velocities larger than about 5–10 km s^{-1} (at the very high resolution of our spectra the contribution of instrument profile becomes small). The resulting *EW*s are overestimated for these stars. We then apply a suitable correction, determined from spectral synthesis of stars with different rotational velocities, to the *EW*s of stars with $v \sin i$ larger than 5 km s^{-1} (HD 8071 A/B, BD+231978A/B, HD 108574/5, HD 216122A/B).

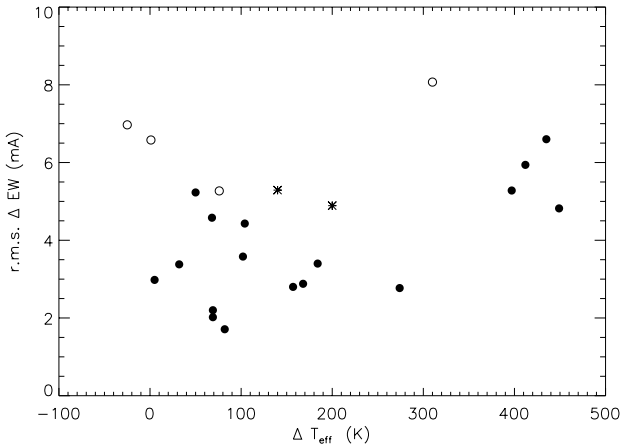

Fig. 1. rms scatter in equivalent width differences ΔEW between the components of the binaries analyzed in this paper as a function of temperature difference $\Delta T_{\rm eff}$. Open circles represent stars with rotational broadening larger than about 5 km s^{-1}, filled circles slowly rotating stars, asterisks the two pairs with slightly evolved primaries.

The line list is the same used in Paper I, with the addition of some vanadium lines from Whaling et al. (1985).

The errors of *EW*s can be estimated by the rms of the difference of *EW*s between the components of pairs whose temperatures differ by less than 200 K, about 2–3 mÅ (Fig. 1). Stars that have significant rotation have larger errors. The increase of the rms of the difference for stars with larger temperature difference and for the pairs whose primary appears to be evolved out of the main sequence may be explained by the intrinsic variations of the line-by-line sensitivity to temperature and gravity changes. The signal to noise ratio seems to play a role in *EW* errors only for the few spectra with S/N lower than about 100–120.

The abundance analysis made use of Kurucz (1995) model atmospheres, computed with the overshooting option switched off (Castelli et al. 1997). The primaries were analyzed differentialy with respect to the Sun, then the line-by-line abundance differences between primaries and secondaries were determined.

Improvements with respect to Paper I concern the inclusion of the damping wings in the analysis of lines with $\log(EW/\lambda) > -5.4$ (in the previous analysis this limit was fixed to −5.1). The calculation of the damping constant is based on the formalism by Barklem et al. (2000), while in Paper I we used an enhancement factor to the Unsold formula (Unsold 1955). These improvements allow a more appropriate treatement of microturbulence (fixed to 0 in Paper I) and an extension toward stronger lines (up to 100 mÅ), while in Paper I we limited ourselves to

[3] IRAF is distributed by the National Optical Observatory, which is operated by the Association of Universities for Research in Astronomy, Inc., under contract with the National Science Fundation.

[4] The equivalent widths are only available in electronic form at the CDS.

Table 1. Visual and absolute magnitudes, $B-V$ color, Hipparcos parallaxes, stellar masses (derived iterativey during the abundance analysis using the spectroscopic temperatures and abundances) and projected binary separation for program stars. As discussed in the text, the formal errors on magnitudes and colors are likely underestimated.

Object	V_A	V_B	$(B-V)_A$	$(B-V)_B$	π	$M_{V(A)}$	$M_{V(B)}$	M_A	M_B	ρ	ρ
					mas			$M_\odot$	$M_\odot$	$''$	AU
HD 8009	8.819 ± 0.007	9.724 ± 0.017	0.64 ± 0.03	0.82 ± 0.07	15.43 ± 2.02	4.61 ± 0.29	5.52 ± 0.29	0.95	0.85	4.7	326
HD 8071	7.312 ± 0.003	7.573 ± 0.004	0.58 ± 0.01	0.60 ± 0.01	19.67 ± 1.58	3.73 ± 0.17	3.99 ± 0.17	1.25	1.22	2.2	115
HD 9911	9.428 ± 0.008	9.448 ± 0.008	0.90 ± 0.04	0.89 ± 0.04	20.40 ± 3.32	5.74 ± 0.36	5.76 ± 0.36	0.85	0.85	3.9	213
HD 13357	8.180 ± 0.006	8.647 ± 0.010	0.67 ± 0.03	0.73 ± 0.05	20.41 ± 1.75	4.67 ± 0.19	5.14 ± 0.19	0.98	0.93	5.9	297
HD 17159	8.775 ± 0.007	8.923 ± 0.007	0.54 ± 0.03	0.53 ± 0.03	14.65 ± 2.24	4.40 ± 0.33	4.55 ± 0.33	1.15	1.12	2.7	203
HD 19440	7.874 ± 0.004	8.574 ± 0.007	0.47 ± 0.01	0.53 ± 0.02	12.55 ± 1.39	3.27 ± 0.24	3.96 ± 0.24	1.25	1.14	6.0	501
HD 30101	8.782 ± 0.009	8.848 ± 0.009	0.82 ± 0.04	0.91 ± 0.03	23.43 ± 2.55	5.53 ± 0.24	5.66 ± 0.24	0.84	0.83	4.6	205
HD 33334	8.023 ± 0.004	8.857 ± 0.009	0.70 ± 0.03	0.80 ± 0.07	21.39 ± 2.18	4.59 ± 0.22	5.42 ± 0.22	1.00	0.89	4.7	229
HD 66491	9.253 ± 0.009	9.312 ± 0.009	0.75 ± 0.05	0.67 ± 0.05	15.11 ± 2.71	4.85 ± 0.39	4.91 ± 0.39	0.96	0.96	5.1	387
BD+23 1978	9.395 ± 0.010	9.530 ± 0.011	0.80 ± 0.06	0.75 ± 0.05	24.04 ± 2.97	6.17 ± 0.27	6.31 ± 0.27	0.84	0.84	2.6	115
HD 106515	7.960 ± 0.005	8.234 ± 0.007	0.79 ± 0.02	0.83 ± 0.03	27.50 ± 1.54	5.13 ± 0.12	5.41 ± 0.12	0.93	0.89	7.0	257
HD 108574/5	7.418 ± 0.005	7.972 ± 0.007	0.56 ± 0.01	0.67 ± 0.02	25.06 ± 1.81	4.37 ± 0.16	4.93 ± 0.16	1.22	1.11	9.8	399
HD 123963	8.758 ± 0.006	9.511 ± 0.010	0.60 ± 0.03	0.54 ± 0.04	13.81 ± 1.74	4.33 ± 0.28	5.08 ± 0.28	1.08	0.96	2.6	200
HD 132563	8.966 ± 0.007	9.472 ± 0.010	0.54 ± 0.03	0.57 ± 0.05	10.15 ± 2.01	3.62 ± 0.44	4.13 ± 0.44	1.13	1.06	4.2	491
HD 132844	9.022 ± 0.006	9.114 ± 0.007	0.55 ± 0.05	0.63 ± 0.05	16.57 ± 2.05	4.99 ± 0.27	5.08 ± 0.27	1.01	0.99	3.0	192
HD 135101	6.656 ± 0.006	7.500 ± 0.009	0.69 ± 0.01	0.75 ± 0.02	34.18 ± 1.78	4.30 ± 0.11	5.15 ± 0.11	0.97	0.95	23.5	694
HD 190042	8.755 ± 0.009	8.778 ± 0.006	0.73 ± 0.03	0.80 ± 0.04	16.52 ± 1.64	4.76 ± 0.22	4.79 ± 0.22	0.96	0.94	4.2	264
HD 200466	8.399 ± 0.005	8.528 ± 0.006	0.71 ± 0.02	0.79 ± 0.03	22.83 ± 1.75	5.14 ± 0.17	5.28 ± 0.17	0.99	0.97	4.7	210
HIP 104687	8.144 ± 0.006	8.189 ± 0.006	0.64 ± 0.06	0.71 ± 0.06	20.87 ± 1.99	4.67 ± 0.21	4.72 ± 0.21	1.09	1.08	4.0	198
HD 213013	8.982 ± 0.008	9.612 ± 0.013	0.81 ± 0.04	0.93 ± 0.08	21.59 ± 2.01	5.58 ± 0.20	6.21 ± 0.20	0.93	0.84	5.5	263
HD 215812	7.275 ± 0.005	7.576 ± 0.006	0.64 ± 0.02	0.70 ± 0.02	31.94 ± 1.66	4.78 ± 0.11	5.08 ± 0.11	0.95	0.92	2.2	70
HD 216122	8.062 ± 0.011	8.186 ± 0.013	0.58 ± 0.02	0.58 ± 0.03	13.11 ± 2.36	3.35 ± 0.40	3.47 ± 0.40	1.23	1.22	5.3	464
HD 219542	8.174 ± 0.006	8.547 ± 0.008	0.64 ± 0.03	0.71 ± 0.04	18.30 ± 1.97	4.39 ± 0.23	4.78 ± 0.23	1.08	1.05	5.3	303

*EW*s < 50 mÅ. The line list is then expanded by about 50%. To remove outliers, we also used an automathic procedure that iteratively cleans the set of lines, disregarding outliers that yield abundances differing more than 2.5σ from the average abundance of the remaining lines, while in Paper I outliers were removed by hand.

3.1. Analysis of primaries

Table 1 reports visual and absolute magnitudes, $B-V$ colours, parallaxes, masses and projected separations for the program stars. V band magnitudes are the weighted average of Tycho and Hipparcos photometries (ESA 1997), corrected to the standard system using the calibrations by Bessell (2000). $B-V$ colours are from Tycho and corrected using Bessell (2000). The parallaxes are from Hipparcos. When separate parallaxes were available for the two components (HD 108574/5, HD 135101A and B), a weighted average was performed. The absolute magnitudes were corrected by the Lutz-Kelker effect following Hanson (1979). The differences with respect to Paper I concern the inclusion of the Hipparcos photometry in the calculation of magnitude differences, the correction to the standard system of the Tycho photometry, the inclusion of some further literature measurements, and the application of the Lutz-Kelker correction to parallaxes.

The stellar masses were determined from the isochrones of Girardi et al. (2002), averaging the masses obtained for 1 Gyr main sequence stars having absolute magnitudes and temperatures equal to those of the program stars for the appropriate metallicity[5]. To take into account the dependences on temperature and metallicity, the masses were determined iteratively during the abundance analysis. For the stars that show significant evolution out of the main sequence (namely HD 135101A and HD 19440A), stellar masses were taken from the suitable isochrone that fits the position of the components on the color–magnitude diagram. In Paper I the mass were derived using Tycho colours instead of the derived temperatures (coupled with absolute magnitudes) and using Gray (1992) tables (therefore neglecting metallicty effects).

Table 2 summarizes the magnitude differences for program stars, including Hipparcos, Tycho and further ground-based photometry when available. Only literature observations reported in the standard system are included. When available, we used the internal errors as estimate of errors. A 0.04 mag error was assigned to the Docobo et al. (2000) magnitudes from the scatter of magnitude difference of pairs with multiple observations; a 0.02 mag error was assigned to the Simbad photometry

[5] The periods of the observed systems are too long for any reliable determination of dynamical masses (see Desidera et al. 2003 for the case of HD 219542).

Table 2. Magnitude difference for program stars.

Object	ΔV Hipparcos	ΔV Tycho	ΔV Other	Ref. Other	ΔV Adopted
HD 8009	0.935 ± 0.021	0.763 ± 0.046			0.905 ± 0.065
HD 8071	0.281 ± 0.006	0.233 ± 0.010			0.268 ± 0.021
HD 9911	0.026 ± 0.013	-0.023 ± 0.033			0.019 ± 0.017
HD 13357	0.465 ± 0.013	0.477 ± 0.034	0.47 ± 0.01	1	0.469 ± 0.010
HD 17159	0.148 ± 0.011	0.166 ± 0.028			0.150 ± 0.010
HD 19440	0.710 ± 0.008	0.631 ± 0.021	0.68 ± 0.01	1	0.692 ± 0.016
HD 30101	0.134 ± 0.013	-0.153 ± 0.032	0.146 ± 0.005	2	0.134 ± 0.025
			0.13 ± 0.01	1	
HD 33334	0.839 ± 0.010	0.700 ± 0.048	0.82 ± 0.01	1	0.827 ± 0.015
HD 66491	0.057 ± 0.013	0.077 ± 0.047			0.058 ± 0.016
BD+23 1978	0.139 ± 0.016	0.092 ± 0.041			0.132 ± 0.019
HD 106515	0.273 ± 0.009	0.263 ± 0.024			0.272 ± 0.011
HD 108574/5	0.554 ± 0.012	0.572 ± 0.015	0.57	3	0.563 ± 0.011
HD 123963	0.773 ± 0.013	0.664 ± 0.034			0.759 ± 0.036
HD 132563	0.511 ± 0.013	0.451 ± 0.039			0.505 ± 0.018
HD 132844	0.095 ± 0.009	0.027 ± 0.044			0.092 ± 0.013
HD 135101	0.894 ± 0.020	0.833 ± 0.012	0.85	3	0.849 ± 0.017
HD 190042	0.021 ± 0.008	0.037 ± 0.031			0.022 ± 0.010
HD 200466	0.133 ± 0.008	0.101 ± 0.021	0.15 ± 0.01	1	0.139 ± 0.009
			0.17	4	
HIP 104687	0.048 ± 0.008	-0.052 ± 0.053	0.00	5	0.045 ± 0.010
			0.06	5	
HD 213013	0.631 ± 0.016	0.627 ± 0.047	0.62	5	0.628 ± 0.017
			0.62	5	
HD 215812	0.307 ± 0.008	0.243 ± 0.019			0.297 ± 0.022
HD 216122	0.123 ± 0.011	0.123 ± 0.024	0.11 ± 0.01	1	0.117 ± 0.009
HD 219542	0.369 ± 0.010	0.412 ± 0.034	0.391 ± 0.007	2	0.387 ± 0.006

References: 1: Nakos et al. (1995); 2: Cuypers & Seggewiss (1999); 3: Simbad; 4: Carney et al. (1994); 5: Docobo et al. (2000).

of HD 108575/5 and HD 135101 and to the Carney et al. (1994) photometry of HD 200466. The adopted magnitude difference is the weighted average of individual determinations. The resulting error is lower than 0.02 mag in most cases.

There is an offset of 0.052 ± 0.016 mag (rms 0.075 mag) between Hipparcos and Tycho magnitude differences. The discrepancy is larger for pairs with a magnitude difference larger than 0.65 mag. There is instead no significant offset between Hipparcos and the literature determinations: the mean offset is 0.005 ± 0.007 mag (rms 0.023 mag). The lower quality of Tycho photometry is also supported by the very large difference of temperatures derived from $B - V$ Tycho colors with those derived from spectroscopy (see Table 5).

The dispersion of Hipparcos and literature differences suggests that quoted errors are underestimated by about 30%. This may be due to the fact that in most cases the two components are not resolved by Hipparcos. The Hipparcos epoch photometry (composite magnitudes) shows a scatter larger than internal errors in many cases (flag "Duplicity induced variability"). Uncertainties in the transformation to the standard system, based on Tycho colors, may also play a role. We include such 30% increase of errors in our adopted error bars.

As in Paper I, effective temperatures were determined from the ionization equilibrium. This method gives robust values for the differences between the temperatures of the two components, since in this case uncertainties in the absolute magnitude (the largest contribution to errors) cancel out, the two components being virtually at the same distance from the Sun. Note however that errors are much larger for the analysis with respect to the Sun (analysis of primaries), since in this case the full error bar in the parallax must be taken into account.

In this paper, we also use vanadium lines, characterized by a temperature sensitivity larger than typical of an iron line. The lack of a suitable number of VII lines forced us to compare VI to Fe II. Intrinsic differences of [V/Fe] might in principle introduce spurious effects on our temperatures. However, vanadium is not known to show peculiar relative abundance with respect to iron for both populations I and II stars (Gratton & Sneden 1991). Possible small intrinsic abundance differences due to chemical evolution are not of concern in the differential analysis of the binary components. Spurious effects due to accretion of chemically fractionated material, more crucial for the goals of this work, are also not expected, since iron and vanadium have very similar condensation temperatures (1334

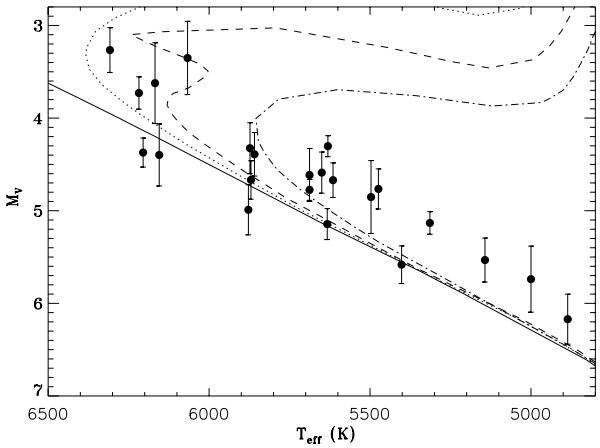

Fig. 2. Color–Magnitude diagram for primaries using Hipparcos and Tycho magnitudes (corrected to the standard system using Bessell 2000) with Hipparcos parallaxes and our spectroscopically determined effective temperatures. The solar metallicity isochrones by Girardi et al. (2002) are overplotted for ages of 1, 2.5, 4 and 8 Gyr.

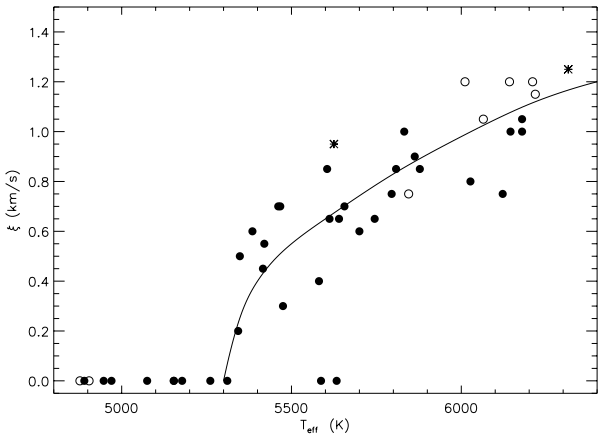

Fig. 3. Microturbulence as a function of effective temperature resulting from the analysis performed leaving the microturbulence as a free parameter. Symbols as in Fig. 1. The relation between temperature and microturbulence adopted in the analysis is shown as a continuous line.

and 1429 K respectively, according to Lodders 2003). The hyperfine splitting of V lines is included in our analysis as in Gratton et al. (2003). For the few lines for which the hyperfine splitting constants are not available, a correction was applied considering the abundance difference of the other lines due to hyperfine splitting as a function of *EW*.

For the line lists we are using, the sensitivity of Fe I–Fe II and VI–Fe II differences on temperature is about 0.0009 and 0.0015 dex/K respectively. Temperatures from iron and vanadium were averaged.

Stellar gravities were calculated using the standard relation

$$\log g = \text{const} + \log M + 0.4\,(M_V + BC) + 4 \log T_{\rm eff} \qquad (1)$$

where the constant term includes the solar quantities. We used the absolute magnitudes from Hipparcos parallaxes, the stellar masses determined from the isochrones of Girardi et al. (2002) and the bolometric corrections by Kurucz (1995). Since the derived masses and gravities depend on temperatures and metallicities, an iterative procedure is required.

The errors in the absolute magnitudes of the primaries are typically 0.2–0.3 mag. These propagate into errors of about 0.10 dex in $\log g$, therefore significantly affecting the derived temperature from the ionization equilibrium (±30 K) and the abundances for the primaries (±0.04 dex)[6]. However, such sources of error are not of concern for the differential analysis between primaries and secondaries, where they cancel out. Only errors in relative photometry (less than 0.05 mag in all but one case) play a role in this case.

Microturbulent velocity was originally fixed by eliminating trends of Fe I abundance with expected equivalent width (see Magain 1984). Residual trends with expected equivalent width are often present for cool stars ($T_{\rm eff} < 5300$ K), even when the microturbulent velocity was set at zero. These residual trends may be due to various causes, the most likely being an incorrect (too large) temperature gradient of the adopted model atmospheres. To reduce the impact of this effect on our differential abundance analyses, in these cases we only considered weak lines, that form deeper in the atmosphere.

As expected for main sequence stars, there is a relation between the temperature and the microturbulence derived as a free parameter from the analysis (Fig. 3). The residuals with respect to a global fitting to the temperature-microturbulence relation (excluding rotating stars and the two slightly evolved stars) show a dispersion of 0.22 km s^{-1}. This is comparable to the errors in determination of individual values of microturbulence, estimated to be about 0.2 km s^{-1}. Since the scatter around the fitting relation appears to be dominated by measurement errors, we adopted the values given by the relation (shown in Fig. 3), iterating the process if the analysis with the revised microturbulence values requires some temperature and abundance changes.

For the evolved stars HD 135101A and HD 19440A we instead adopted the values of microturbulence resulting from the stellar analysis (as expected they are larger than the standard relation by 0.25 and 0.10 km s^{-1} respectively).

Table 3 summarizes the atmospheric parameters adopted in the abundance analysis. Table 4 shows the results of the analysis of the primaries.

3.2. Differential analysis of secondaries

The secondary of each pair was analyzed differentially with respect to the primary, using strictly the same line set. The initial line list for the differential analysis includes the lines not removed as outliers in the analysis of both components. Further iterative clipping is performed to exclude lines that gives abundance differences outside $\pm 2.5\sigma$ with respect to the average of the other lines.

[6] In the case of HD 132844A the procedure used for the other stars gives very high gravities ($\log g = 4.74$), This is likely due to a large error in parallaxes. For this star only, the analysis of the primary was purely spectroscopic, with the temperature derived from the excitation equilibrium and gravity from the ionization equilibrium.

Table 3. Adopted atmospheric parameters.

Object	$T_{\rm eff(A)}$	$T_{\rm eff(B)}$	$\log g_A$	$\log g_B$	$[A/H]_A$	$[A/H]_B$	ξ_A	ξ_B
HD 8009	5688	5291	4.30	4.45	–0.20	–0.14	0.75	0.00
HD 8071	6218	6142	4.24	4.32	+0.26	+0.26	1.10	1.10
HD 9911	5000	4968	4.40	4.39	+0.06	+0.01	0.00	0.00
HD 13357	5615	5341	4.31	4.36	–0.02	–0.01	0.65	0.25
HD 17159	6155	6051	4.46	4.48	+0.02	+0.02	1.10	1.00
HD 19440	6308	6108	4.09	4.27	–0.05	–0.05	1.25	1.05
HD 30101	5143	5061	4.39	4.39	–0.14	–0.14	0.00	0.00
HD 33334	5650	5201	4.30	4.39	+0.02	+0.03	0.70	0.00
HD 66491	5497	5492	4.33	4.35	+0.03	+0.02	0.55	0.55
BD+23 1978	4886	4911	4.51	4.58	+0.22	+0.22	0.00	0.00
HD 106515	5314	5157	4.35	4.37	+0.08	+0.07	0.10	0.00
HD 108574/5	6205	5895	4.49	4.55	+0.23	+0.23	1.10	0.90
HD 123963	5873	5438	4.31	4.39	+0.11	+0.14	0.90	0.45
HD 132563	6168	5985	4.15	4.27	–0.18	–0.19	1.10	0.95
HD 132844	5878	5809	4.12	4.13	–0.18	–0.18	0.90	0.85
HD 135101	5631	5491	4.17	4.44	+0.05	+0.05	0.95	0.55
HD 190042	5474	5406	4.28	4.26	+0.02	+0.02	0.50	0.40
HD 200466	5633	5583	4.51	4.54	+0.06	+0.04	0.70	0.65
HIP 104687	5870	5801	4.45	4.44	+0.11	+0.12	0.90	0.85
HD 213013	5402	4990	4.56	4.58	+0.08	+0.07	0.40	0.00
HD 215812	5688	5586	4.37	4.43	–0.19	–0.21	0.75	0.65
HD 216122	6067	6066	4.04	4.09	+0.25	+0.28	1.05	1.05
HD 219542	5859	5691	4.34	4.42	+0.14	+0.14	0.90	0.75

The differential approach allows us to remove a number of possible systematic errors in the analysis, as indicated by the internal scatter of abundance difference that is lower than expected if the errors of the two components were fully independent (Fig. 4). The degree of correlation between the abundances obtained from individual lines on the spectra of the two components is a function of the difference of the temperature of the stars: we found that the correlation is negligible when this difference is larger than about 300 K. This is likely due to the combination of two factors: (i) for large temperature differences, line strengths are very different, due to the different impact of continuum opacity; and (ii) systematic errors in the determination of the correct continuum level become quite different. It is clear that the differential analysis yields most accurate results when the two components are very similar.

Table 5 shows the temperature differences given by different methods.

The first and second column give the temperature difference from the ionization equilibrium of iron and vanadium respectively and the third column their weighted average. As shown in Fig. 5, for the pairs with temperature of the secondary larger than 5450 K and excluding the rotating stars characterized by much larger error bars, iron and vanadium temperatures agree very well (mean offset -3 ± 7 K, rms 25 K, 10 pairs). A possible trend in the sense of vanadium giving larger temperatures differences may be present for the stars in the range 5100–5450 K, while the situation is less clear for even cooler stars. Systematic trends in cooler stars may be caused by some residual effects of hyperfine splitting or to the fact that most of the lines in our line list become quite strong in the spectra of these stars, for which a trend of abundance as a function of *EW*s still remains for such cool stars, as discussed above. A better evaluation of the existence of systematic trends is postponed to the analysis of further stars for which spectra already have been obtained.

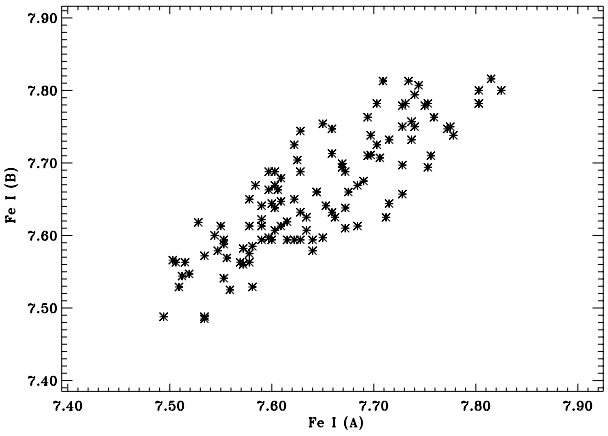

Fig. 4. Iron abundance derived for each line for the components of HIP 104687A and B. A clear correlation is present, indicating that the use of a line-by-line differential analysis significantly reduces the errors on abundance difference between the components.

Table 4. Results of abundance analysis for primaries.

Object	[Fe/H]I	rms	N_{lines}	[Fe/H]II	rms	N_{lines}	[V/H]I	rms	N_{lines}
HD 8009	–0.195	0.084	126	–0.194	0.164	32	–0.195	0.113	28
HD 8071	+0.267	0.133	133	+0.203	0.197	30	+0.085	0.117	12
HD 9911	+0.058	0.082	73	+0.099	0.151	20	+0.177	0.162	27
HD 13357	–0.012	0.130	146	–0.045	0.094	28	–0.109	0.090	32
HD 17159	+0.017	0.104	126	+0.038	0.129	33	+0.068	0.165	20
HD 19440	–0.058	0.111	138	–0.038	0.152	34	–0.003	0.158	22
HD 30101	–0.148	0.079	104	–0.174	0.095	26	–0.229	0.083	25
HD 33334	+0.015	0.078	122	+0.012	0.174	34	+0.013	0.108	32
HD 66491	+0.031	0.079	125	+0.016	0.130	25	–0.013	0.118	30
BD+23 1978	+0.221	0.171	60	+0.282	0.157	14	+0.367	0.150	11
HD 106515	+0.078	0.065	85	+0.094	0.090	25	+0.120	0.092	23
HD 108574/5	+0.214	0.120	128	+0.259	0.198	28	+0.332	0.218	24
HD 123963	+0.111	0.086	140	+0.075	0.102	33	+0.010	0.091	28
HD 132563	–0.185	0.103	139	–0.186	0.109	34	–0.197	0.173	19
HD 132844	–0.182	0.077	130	–0.208	0.153	32	–0.249	0.059	23
HD 135101	+0.068	0.073	136	+0.077	0.125	31	+0.094	0.121	31
HD 190042	+0.045	0.092	130	+0.036	0.074	23	+0.019	0.143	31
HD 200466	+0.050	0.061	82	+0.055	0.137	30	+0.060	0.084	29
HIP 104687	+0.123	0.083	126	+0.106	0.157	31	+0.075	0.103	26
HD 213013	+0.084	0.088	84	+0.112	0.144	26	+0.151	0.129	30
HD 215812	–0.195	0.083	136	–0.198	0.074	29	–0.204	0.094	27
HD 216122	+0.263	0.116	124	+0.263	0.141	23	+0.269	0.159	20
HD 219542	+0.135	0.084	132	+0.122	0.109	27	+0.102	0.143	28

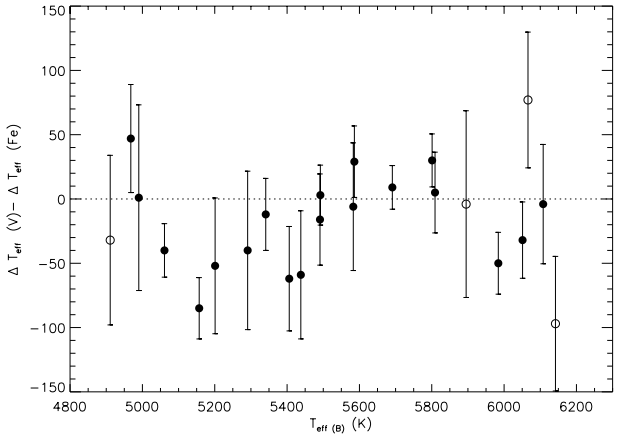

Fig. 5. Differences between the temperatures derived using the iron and vanadium lines as a function of the temperature of the secondary.

The excitation temperatures show an offset of 24 ± 14 K (rms 59 K) for the 19 slow rotating pairs with respect to temperatures based on ionization equlibrium. The residual slopes of abundance difference as a function of excitation potential are correlated with those as a function of equivalent width, suggesting a common origin (likely the inadequacies of the atmospheric models and/or a possible underestimate of equivalent widths of strong lines when using a Gaussian fit). Therefore, the internal errors on the excitation temperature should not represent the full error bar.

Temperature differences from colors are calculated using the calibrations by Alonso et al. (1996). $B - V$ colors are taken from Table 1. $V - I$ of HD 30101 and HD 219542 are from Cuypers & Seggewiss (1999) and those of HD 108584/5 and HD 135101 are from the Hipparcos Catalog. Transformation to the Johnson photometric system was performed following Bessell (1983). 2MASS photometry was transformed to the TCS photometric system using the calibrations provided by Cutri et al. (2003) and those by Alonso et al. (1994). The only pair for which Strömgren photometry is available for both components is HD 135101 (Hauck & Mermilliod 1998). A temperature difference of 160 K is derived. It appears that temperatures based on colors have typically very poor precision, likely because of the photometric errors induced by the small separation of the components.

The temperature difference from ΔV is estimated considering the slope of the main sequence on the 1 Gyr solar metallicity isochrone. It does not include evolutionary effects and therefore represents an upper limit to the actual temperature difference.

When considering the differential analysis between the two components, parallaxes no longer play a role; the same applies to absolute errors on mass estimates. Only errors on relative photometry are relevant. The errors on magnitude difference are less than 0.05 mag in all but one case (HD 8009).

Table 5. Temperature difference using different methods. The weighted average between the temperature difference based on the ionization equilibrium of iron and vanadium was adopted because of its higher accuracy.

Object	Ion. Eq. Fe	Ion. Eq. V	Ion. Eq. mean	Exc. Eq.	$B-V$	$V-I$	$V-K$	$J-K$	$J-H$	ΔV
HD 8009	371 ± 50	411 ± 36	397 ± 29	408 ± 93	563		649			≤503
HD 8071	24 ± 38	121 ± 36	76 ± 28	234 ± 55	75					≤149
HD 9911	62 ± 33	15 ± 26	32 ± 20	−11 ± 60	–44		14	–39	–149	≤11
HD 13357	267 ± 23	279 ± 16	274 ± 13	279 ± 38	188		272	176	488	≤260
HD 17159	87 ± 21	119 ± 21	104 ± 15	17 ± 49	–54					≤83
HD 19440	198 ± 28	202 ± 37	200 ± 22	282 ± 60	239		339	290	214	≤385
HD 30101	55 ± 17	95 ± 12	82 ± 10	126 ± 27	235	123	34	13	–26	≤73
HD 33334	418 ± 42	470 ± 32	449 ± 26	520 ± 82	295		570	262	489	≤460
HD 66491	9 ± 20	6 ± 12	5 ± 10	21 ± 38	–257		76	277	347	≤32
BD+23 1978	−43 ± 50	−11 ± 43	−25 ± 28	106 ± 224	–142					≤73
HD 106515	98 ± 20	183 ± 13	157 ± 11	206 ± 49	106		174	208	90	≤151
HD 108574/5	307 ± 57	311 ± 45	310 ± 35	392 ± 87	412	322	281	343	215	≤313
HD 123963	399 ± 39	458 ± 31	435 ± 24	539 ± 82	–73					≤422
HD 132563	159 ± 17	209 ± 17	184 ± 12	222 ± 38	108					≤281
HD 132844	72 ± 25	67 ± 19	69 ± 15	36 ± 22	308					≤51
HD 135101	131 ± 27	147 ± 23	140 ± 18	211 ± 60	188	158	136	124	–24	≤472
HD 190042	35 ± 32	97 ± 25	68 ± 20	35 ± 60	220		22	–55	120	≤12
HD 200466	38 ± 41	44 ± 28	50 ± 23	17 ± 92	244		161	236	245	≤77
HIP 104687	87 ± 16	57 ± 13	69 ± 11	53 ± 22	257		6	–163	242	≤25
HD 213013	413 ± 58	412 ± 35	412 ± 35	570 ± 109	315		335	112	203	≤349
HD 215812	121 ± 22	92 ± 19	102 ± 14	124 ± 49	200					≤165
HD 216122	50 ± 42	−27 ± 32	1 ± 26	45 ± 71	–10		237	437	257	≤65
HD 219542	173 ± 12	159 ± 15	168 ± 9	206 ± 27	246	238	232	23	220	≤212

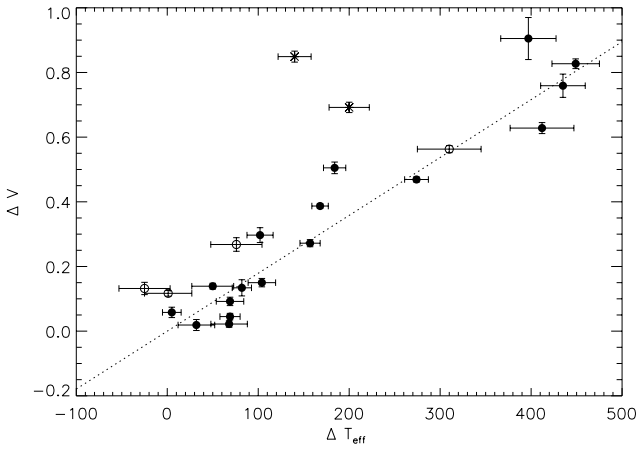

Fig. 6. Magnitude vs. temperature differences. The dotted line represents the typical slope alone the main sequence of a 1 Gyr solar metallicity isochrone. Symbols as in Fig. 1. The two discrepant cases are HD 135101 and HD 19440, that have primaries clearly evolved off of the main sequence.

A 0.05 mag error in magnitude difference produces errors for relative gravities of about 0.02 dex and for 7 K on relative temperatures. The contribution of magnitude difference to the temperature error is therefore very small. The contribution of line-to-line scatter is larger for all the pairs (Table 5).

Table 6 shows the sensitivity of the abundance differences to variations of the atmospheric parameters, changing them one-by-one.

Table 7 shows the results of the differential analysis for Fe I and Fe II and Table 8 summarizes the results of temperature difference, metallicity and iron content differences (Fe I from Table 7). We also give the internal errors (due to the line-to-line scatter) and the global errors that include also the contribution due to the errors on temperature differences. Errors due to microturbulence are not included. The last column of Table 8 lists the estimated amount of iron accreted by the richer in metal component of each pair, derived in Sect. 4.

Our analysis procedure makes use of standard stellar models in the derivation of stellar masses. However, if the outer part of a star is enriched in metals, the model should be systematically wrong. Stellar models with an enriched convective zone have been calculated by e.g. Ford et al. (1999) and Dotter & Chaboyer (2003). In the case of 51 Peg, Ford et al. (1999) found that for a metallicity difference of 0.21 dex, the mass decreases from 1.05 to 0.94 $M_{\odot}$, while for τ Boo

Table 6. Sensitivity to abundance and temperature difference to changes of atmospheric parameters for the pair HD 219542.

Changes	Δ Fe I	Δ Fe II	Δ VI	Δ Fe I–Fe II	Δ VI–Fe II	$\Delta T_{\rm eff}$ (Fe)	$\Delta T_{\rm eff}$ (V)
$\Delta T_{\rm eff}$ +30 K	–0.018 ± 0.008	+0.010 ± 0.013	–0.033 ± 0.024	–0.028 ± 0.016	–0.043 ± 0.027	–32 ± 17	–29 ± 18
$\Delta T_{\rm eff}$ –30 K	+0.017 ± 0.008	–0.012 ± 0.013	+0.028 ± 0.024	+0.029 ± 0.016	+0.040 ± 0.027	+32 ± 17	+27 ± 18
$\Delta \log g$ +0.05 dex	+0.002 ± 0.008	–0.019 ± 0.013	+0.001 ± 0.024	+0.021 ± 0.016	+0.020 ± 0.027	+23 ± 17	+14 ± 18
$\Delta \log g$ –0.05 dex	–0.008 ± 0.008	+0.020 ± 0.013	+0.000 ± 0.024	–0.028 ± 0.016	–0.020 ± 0.027	–31 ± 17	–13 ± 18
Δ [*A*/H] +0.05 dex	–0.006 ± 0.008	–0.016 ± 0.013	-0.001 ± 0.024	+0.010 ± 0.016	+0.015 ± 0.027	+11 ± 17	+10 ± 18
Δ [*A*/H] –0.05 dex	+0.005 ± 0.008	+0.016 ± 0.013	+0.001 ± 0.024	–0.011 ± 0.016	–0.015 ± 0.027	–13 ± 17	–10 ± 18
$\Delta\xi$ +0.15 km s^{-1}	+0.017 ± 0.008	+0.030 ± 0.013	+0.005 ± 0.024	–0.013 ± 0.016	–0.025 ± 0.027	–15 ± 17	–17 ± 18
$\Delta\xi$ –0.15 km s^{-1}	–0.019 ± 0.008	–0.030 ± 0.013	-0.008 ± 0.024	+0.009 ± 0.016	+0.000 ± 0.027	+11 ± 13	+15 ± 18

Table 7. Results of differential analysis.

Object	Δ [Fe/H]I	rms	N_{lines}	Δ [Fe/H]II	rms	$N_{\rm lines}$	Δ [*V*/H]I	rms	$N_{\rm lines}$
HD 8009	–0.067	0.131	85	–0.090	0.212	25	–0.111	0.152	22
HD 8071	+0.001	0.113	116	–0.046	0.133	17	–0.113	0.151	13
HD 9911	+0.051	0.072	71	+0.078	0.104	13	+0.104	0.108	18
HD 13357	–0.016	0.065	117	–0.022	0.105	27	–0.028	0.072	26
HD 17159	+0.012	0.097	102	–0.004	0.085	28	–0.027	0.095	13
HD 19440	+0.001	0.117	106	+0.002	0.113	25	+0.005	0.202	16
HD 30101	–0.003	0.036	83	–0.028	0.067	20	–0.048	0.040	17
HD 33334	–0.015	0.105	78	–0.042	0.194	29	–0.074	0.161	26
HD 66491	+0.006	0.063	112	+0.010	0.080	22	+0.015	0.030	21
BD+23 1978	–0.012	0.145	43	–0.028	0.135	12	–0.049	0.116	5
HD 106515	+0.018	0.060	75	–0.036	0.075	20	–0.075	0.041	17
HD 108574/5	+0.004	0.160	105	+0.002	0.242	24	+0.000	0.190	17
HD 123963	–0.037	0.137	120	–0.070	0.169	27	–0.105	0.150	20
HD 132563	+0.012	0.090	117	–0.011	0.070	30	–0.049	0.079	13
HD 132844	-0.004	0.052	110	–0.008	0.116	27	–0.005	0.059	13
HD 135101	+0.004	0.116	121	–0.004	0.125	30	–0.013	0.119	24
HD 190042	0.000	0.098	118	–0.030	0.142	26	–0.058	0.129	26
HD 200466	+0.020	0.117	70	+0.009	0.180	28	+0.000	0.111	21
HIP 104687	–0.015	0.045	113	+0.001	0.045	9	+0.018	0.056	19
HD 213013	+0.013	0.123	71	+0.013	0.175	12	+0.012	0.154	15
HD 215812	+0.017	0.092	127	+0.034	0.091	25	+0.050	0.084	22
HD 216122	–0.035	0.145	108	+0.009	0.166	22	+0.051	0.123	14
HD 219542	+0.001	0.057	110	+0.006	0.042	20	+0.012	0.081	23

Dotter & Chaboyer (2003) found a mass decrease from 1.36 to 1.32 $M_{\odot}$ for the same abundance difference.

We estimated the effects of studing a polluted star with an abundance difference of 0.21 dex using standard models taking as a reference the result by Ford et al. (1999) that predicts a larger effect and is computed for a star with a temperature more typical of the values of our program stars. For fixed magnitudes, the stellar gravity is overestimated by 0.048 dex. This in turn implies an overestimatation of the temperature derived from the ionization equilibrium by about 25 K (with some further effects of the derived stellar gravity) and then a ∼0.015 dex overestimatation of the abundance. The induced error is then less than 10% of the real metallicity difference. Since we have not found a pair with a large abundance difference, the impact on our result is very small.

3.3. Comparison with Paper I and other literature data

In Paper I we derived an abundance difference of 0.09 dex for the components of HD 219542, with the primary being more metal rich. The present analysis does not confirm this result.

As described above, we made several modifications of our analysis procedure with respect to Paper I. The continuum level and the *EW*s were re-measured on the same

Table 8. Final abundance difference (Fe I from Table 7) and estimates of iron possibly accreted.

Object	$\Delta T_{\rm eff(A)}$ K	[Fe/H](A)	Δ [Fe/H]	Int. Err.	Error	$\Delta M_{\rm Fe}$ $M_\oplus$
HD 8009	397 ± 30	–0.20	–0.067	0.014	0.029	2.83 ± 1.19
HD 8071	76 ± 28	+0.27	+0.001	0.009	0.021	0.03 ± 0.77
HD 9911	32 ± 20	+0.06	+0.051	0.010	0.019	4.63 ± 1.69
HD 13357	274 ± 13	–0.01	–0.016	0.009	0.013	0.80 ± 0.63
HD 17159	104 ± 15	+0.02	+0.012	0.010	0.016	0.20 ± 0.28
HD 19440	200 ± 22	–0.06	+0.001	0.010	0.022	0.01 ± 0.30
HD 30101	82 ± 11	–0.15	–0.003	0.005	0.010	0.16 ± 0.54
HD 33334	449 ± 26	+0.02	–0.015	0.013	0.025	1.10 ± 1.86
HD 66491	6 ± 10	+0.03	+0.006	0.009	0.011	0.27 ± 0.48
BD+23 1978	–25 ± 28	+0.22	–0.012	0.025	0.032	2.64 ± 7.31
HD 106515	157 ± 11	+0.08	+0.018	0.006	0.012	1.21 ± 0.78
HD 108574/5	310 ± 35	+0.21	+0.004	0.015	0.034	0.10 ± 0.78
HD 123963	435 ± 25	+0.11	–0.037	0.012	0.024	2.50 ± 1.60
HD 132563	184 ± 12	–0.19	+0.012	0.007	0.013	0.12 ± 0.13
HD 132844	69 ± 15	–0.18	–0.004	0.004	0.014	0.06 ± 0.20
HD 135101	140 ± 18	+0.07	+0.004	0.010	0.019	0.20 ± 0.96
HD 190042	68 ± 20	+0.05	0.000	0.010	0.019	0.00 ± 0.96
HD 200466	50 ± 23	+0.05	+0.020	0.012	0.024	0.80 ± 0.97
HIP 104687	69 ± 11	+0.12	–0.015	0.005	0.010	0.49 ± 0.33
HD 213013	412 ± 35	+0.08	+0.013	0.012	0.033	0.86 ± 2.26
HD 215812	102 ± 14	–0.20	+0.017	0.008	0.015	0.31 ± 0.27
HD 216122	1 ± 26	+0.26	–0.035	0.013	0.026	0.99 ± 0.73
HD 219542	168 ± 9	+0.14	+0.001	0.006	0.009	0.03 ± 0.31

spectra of Paper I to be fully consistent with the other stars studied in this paper, but without significant differences in the *EW*s with respect to Paper I. We also compared our *EW*s with those of Sadakane et al. (2003). We obtain a mean difference of −0.050 ± 0.074 mÅ and −0.051 ± 0.069 mÅ with an rms of 3.65 and 3.36 mÅ (24 lines) for HD 219542A and B respectively.

We performed several tests to understand the origin of the change in abundance and temperature differences with respect to Paper I, introducing one by one the changes between Paper I and this paper, and starting from both the final solution given here and in Paper I. We were able to explain most of the differences in terms of the modifications of the analysis procedure introduced.

The most relevant contributions come from the adoption of different microturbulences for the two stars and for the changes in the formalism for the damping constant (0.02–0.03 dex each one).

The lines selection also plays a role: using the the set of lines of Paper I (limit about 50 mÅ) with the technique used in this paper causes a temperature difference of about 30 K (in the sense of HD 219542B being colder) and then an abundance difference of about 0.02 dex.

Some further minor differences (less than 0.01 dex) are due to the inclusion of vanadium (for this pair the temperature differences based on iron and vanadium differ by just 9 K) and to the changes in the mass determination (inclusion of the metallicity dependence and exclusion of Tycho colors).

The input metallicity used in the analysis also plays a role: when an abundance difference is present between the components, adopting the same abundance difference in the atmospheric parameters causes a further increase of the measured difference. From Table 6 we see that this effect amounts to about 10% of the input difference (i.e. about 0.01 dex for the case of HD 219542 in Paper I).

We also compared our results with those of Sadakane et al. (2003). They used spectra with a higher signal to noise ratio than ours (about 500) but measured a lower number of spectral lines (46 Fe I and 7 Fe II lines respectively). They determined the atmospheric parameters spectroscopically, fixing the effective temperature and gravity from the excitation and ionization equilibrium respectively. They found ($T_{\rm eff}$, $\log g$, ξ, [Fe/H]) = (5830, 4.45, 0.95, 0.13) and (5600, 4.40, 0.90, 0.08) for HD 219542A and B respectively. Our parameters for the primary are fairly similar to their values, while their temperature differences is larger by 62 K. However, we note that the statistical error quoted by Sadakane et al. (2003) for the temperature difference is 42 K (30 K for each star). Furthermore, we note some inconsistencies in the parameters they derived. Their spectroscopic analysis gives gravities larger for the warmer and

brighter components ($\Delta \log g(A-B) = 0.05$ dex), contrary to expectation for normal main sequence stars ($\Delta \log g(A-B) = -0.06$ dex from the 1 Gyr isochrone).

As a check that the discrepancy is not due to *EW* measurements, we analyzed our data using the Sadakane et al. (2003) atmospheric parameters, and found very similar abundance differences than obtained by them, and the Sadakane et al. (2003) *EW* using our technique. The latter test gives a temperature difference 27 K larger than ours (195 vs. 168 K) and an abundance difference of 0.012 dex.

While we have no indication that the HD 219542 parallax is inaccurate, we checked the effect on the differential analysis of the adoption of different temperatures for the primary. For differences of 100 K with respect to the adopted values, we get effects on the abundance difference at the 0.01 dex level, likely because the relations between $\log g$ and ξ with $T_{\rm eff}$ are not linear.

The temperature difference adopted in this paper is compatible with the position of the stars in the color–magnitude diagram. The primary might be slightly evolved (about 0.1 mag with respect to the main sequence).

Finally, we note that the analysis of HD 219542B published by Santos et al. (2004) gives ($T_{\rm eff}$, $\log g$, ξ, [Fe/H]) = (5732, 4.40, 0.99, 0.17), compatible within errors with our estimates.

One may wonder why the results for the other pairs studied in Paper I do not change as did the values for HD 219542 (note that for HD 200466 we use in this paper a new, higher quality spectrum). We think that this is due to the fact that, with the exception of HD 8071, charactrized by a small temperature difference and thus with little effect on the differential analysis, HD 219542A is the warmest of the stars studied in Paper I. The effect of assumptions about microturbulence (zero for both components in Paper I, different values here) is then largest for this star.

We conclude that the abundance difference between the components of HD 219542 derived in Paper I is likely due the combination of several factors, some random and some systematic, that worked by chance all in the same direction. This signals that caution should be applied when considering abundance differences between pairs of stars, even if they appear to be much larger than the internal errors.

The only other pair for which high resolution spectroscopic analysis is published in the literature is HD 135101, whose components were recently studied individually (i.e. as single stars) by Heiter & Luck (2003). They found ($T_{\rm eff}$, $\log g$, ξ, [Fe/H]) = (5700, 4.20, 0.90, 0.06 ± 0.04) and (5550, 4.24, 0.40, 0.10 ± 0.05) for HD 135101A and B respectively. These parameters are fairly similar to ours. From our analysis there is a much larger gravity difference between the components, derived from the magnitude difference (0.85 mag).

4. Results

Figures 7–9 show the metallicity differences as a function of the temperature difference between the components, the temperature of the primary and that of the secondary. The scatter of abundance difference is larger below 5500 K (Fig. 9). The pattern of Δ [Fe/H] as a function of the temperature of the secondary rensembles that of the difference of temperatures based on iron and vanadium lines but the correlation between Δ [Fe/H] and and $\Delta T_{\rm eff}$(Fe − V) is not statistically significant.

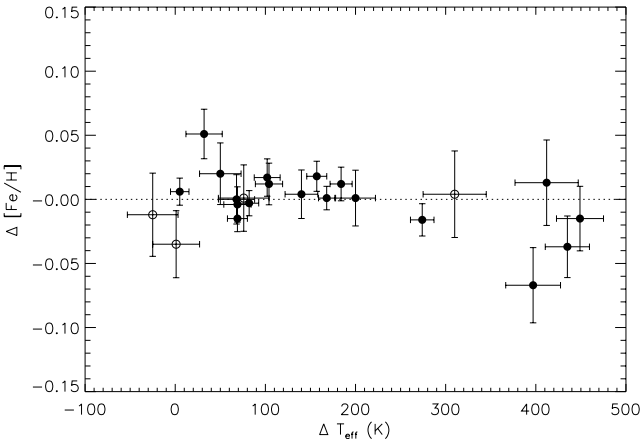

Fig. 7. Iron abundance difference between the components of pairs as a function of temperature difference. Open circles represent stars with rotation broadening larger than about 5 km s^{-1}, filled circles slowly rotating stars.

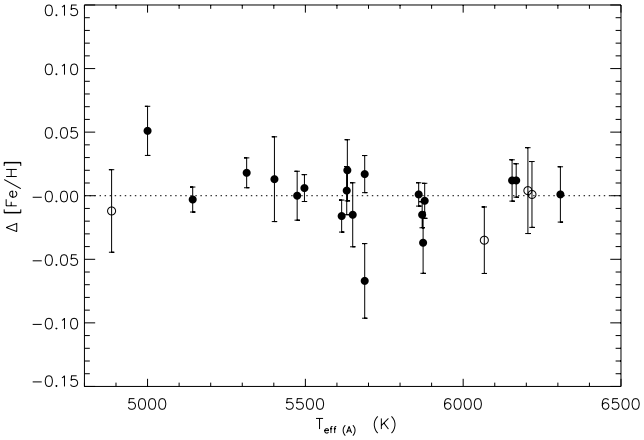

Fig. 8. Iron abundance difference between the components of pairs as a function effective temperature of the primary. Open and filled circles as in Fig. 7.

Four pairs have differences larger than 0.03 dex.

The components of HD 8009 and HD 123963 have a fairly large temperature difference. This causes errors larger than in most cases, making the difference significant to about the 2.5 and 1.5σ level respectively. The magnitude difference between the components is also quite uncertain for these pairs: the values given by Hipparcos and Tycho differ by more than 0.1 mag (see Table 2). The adoption of the Tycho magnitude difference for HD 8009 would imply a decrease of the abundance difference by about 0.01 dex.

The components of HD 9911 are quite cool (with only those of BD+23 1978 being even cooler). We saw that our analysis procedure has some difficulty in handling such stars, likely because of inadequacies of the atmosphere models, so we think the the observed difference (formally significant at about 2.5σ level) is not real.

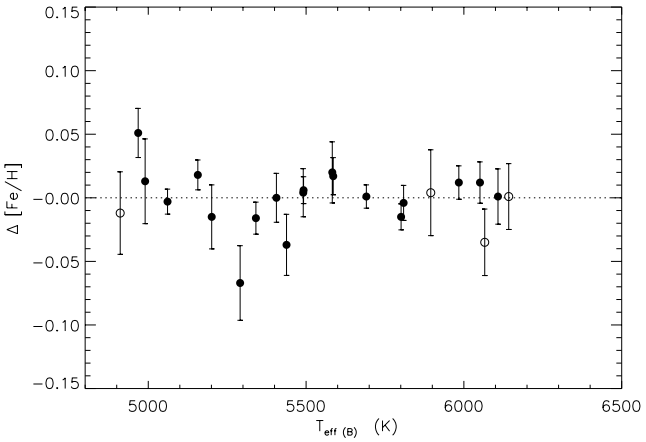

Fig. 9. Iron abundance difference between the components of pairs as a function effective temperature of the secondary. Open and filled circles as in Fig. 7.

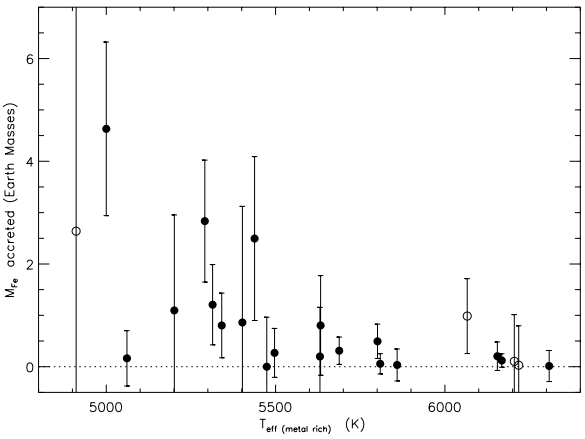

Fig. 10. Estimate of iron accreted by the metal-rich component of each pair as a function of its effective temperature, taking into account the mass of the mixing zone as in Murray et al. (2001). Open and filled circles as in Fig. 7. The mass of meteoritic material is about 5.5 times the mass of iron.

The components of HD 216122 show significant rotational broadening. As for the other rotating stars, internal errors are larger, making the observed difference of low significance. The star is also listed in the Hipparcos catalog as an unsolved variable.

Thus we have performed a differential abundance analysis of 23 wide binaries, with typical errors of about 0.02 dex. The analysis appears more robust for the stars warmer than about 5450 K, while some inconsistencies appear to be present for cooler stars. Such warmer stars are also the most interesting for our science goal, because of their thinner convective envelope. While there are some pairs with a marginal abundance difference (0.03–0.07 dex), we take with caution such differences because of possible problems in the analysis of these pairs (errors due to the large temperature difference: HD 123963 and HD 8009; systematic errors of abundance analysis at low temperature: HD 9911), or large random errors, because of the fast rotational velocity (HD 216122).

The analysis of other elements, the search for trends in abundance difference with condensation temperature and the determination of the lithium abundance will be presented elsewhere.

A large fraction of the pairs have abundance differences lower than 0.02 dex. It is possible to estimate rough upper limits on metal-rich material accreted by the stars after their convective zones have shrunk. We follow the approach by Murray et al. (2001). They consider the extension of the convective zone during the main sequence as a function of stellar mass and metallicity. Furthermore, they add a further mixing in the mass range 1.2–1.5 $M_{\odot}$, scaling the amount of mixing according to the observed lithium depletion in this region[7]. We can then calculate the amount of mass of iron that, accreted on the (nominally) metal richer component of each pair, produces the observed abundance difference (Fig. 10).

We are able to exclude at the 1σ level the consumption of 1 $M_{\oplus}$ of iron for 10 out of 11 slow-rotating stars with stellar temperatures of both components higher than 5400 K. This amount of iron corresponds to less than 5 $M_{\oplus}$ of meteoritic material. The accretion of a quantity of meteoritic material similar to that expected to has been accreted from the Sun after the shrunking of its convective zone (about 0.4 $M_{\oplus}$ of iron, Murray et al. 2001) can be excluded at the 1σ confidence level in five cases.

A more detailed estimate of the amount of iron accreted by stars of given physical properties requires further investigation of the extension of the mixing zone as well as suitable stellar models with enhanced metallicity in the outer convective zone, that are beyond the scope of this paper. The very small abundance difference of the warmest pairs may also be used to constrain the diffusion of heavy elements within the star. From the models of Turcotte et al. (1998) we see that the effect of iron diffusion at the end of the main sequence lifetime should be of 0.02 and 0.10 dex for a 1.1 and 1.3 $M_{\odot}$ star respectively, i.e. within or close to our detection limit. Such investigations are postponed to a future paper, after the abundance determination of further elements, very useful in constraining the diffusion scenario.

5. Discusssion

The frequency of planets is estimated to be about 8% (Butler et al. 2000) and the stars hosting planets appear to have metallicity larger than 0.25 dex with respect to normal field population stars (Laws et al. 2003). We have not found any pair among 23 with such large composition differences[8]. One star out of 15 in Pleiades might have a metallicity enhancement

[7] As noted in Sect. 1, the extra-mixing mechanism producing the Li dip has some dependence on stellar age. This is not taken into account in our estimate of the mass of the mixing zone.

[8] Considering the observed planet frequency, and the differences of the mass of the convective zone between the components, it appears very unlikely that both components of a binary system have accreted such metal rich material that their original composition is alterated by a similar amount.

of about 0.1 dex (Wilden et al. 2002), while two out of 55 in Hyades (with questionable membership) have metallicity difference of about 0.20 dex with respect to the cluster mean (Paulson et al. 2003).

The fraction of stars with metal enrichment comparable to the observed metal overabundance of stars with planets appears to be lower than the fraction of stars with planets. Taken at face value, this indicates that pollution phenomena *alone* cannot explain the planet-metallicity connection. High metallicity then seems to play a role in favouring the presence of planets. Enrichment phenomena might be present, as possibly indicated by the still controversial presence of ^{6}Li in HD 82943, but they should be rare and/or produce only a small composition alteration. Increasing the statistics of wide binaries and stars in clusters in the most suitable temperature range should allow one to constrain the accretion scenario more tightly.

If we consider our sample and those of Pleiades and Hyades, we have 2 possible cases with a metallicity difference comparable to the typical offset between planet hosts and normal field stars (the two Hyades stars) out of 126 stars. With the hypothesis that 8% of these stars have planets (see below for an important caveat) and that the ~0.25 dex metallicity offset is entirely due to planetary pollution, we obtain a probability of less than 1% to observe just two cases out of 126 stars. However, such a probability reaches 13% if the actual planet frequency for these stars is 4%.

Some selection effect may be present considering that the temperature and mass distribution of some of the samples studied for the high-precision differential abundance analysis may be different with respect to the field stars selected for radial velocity planet searches.

A more fundamental caveat to this discussion is that the components of wide binaries considered in this study (typical projected separations of about 100–400 AU, Table 1) as well as stars in open clusters like Pleiades and Hyades might have planet frequencies and pollution histories different from the mostly single field star planets hosts. There are some hints that the properties of planets in binary systems are different with respect to those orbiting single stars (Zucker & Mazeh 2002). This seems to indicate a significant role of orbital interactions in the formation and evolution of planetary systems, whose effects on the accretion of planetary material should be considered. Dedicated searches for planets in various kind of binaries (Desidera et al. 2003; Eggenberger et al. 2003) and in star clusters characterized by different dynamical conditions (see e.g., Gilliland et al. 2000; Bruntt et al. 2003; Street et al. 2003; Piotto et al. 2004) are thus very useful to understand the effects of the dynamical environment on the presence of planets and their orbital properties. This will allow us also to determine whether the pollution properties derived by the study of wide pairs and cluster stars can be extended to single stars (for which this is much more difficult to show).

Acknowledgements. We thank the T.N.G. staff for its help with the observations. This research has made use of the SIMBAD database, operated at CDS, Strasbourg, France, and of data products from the Two Micron All Sky Survey, which is a joint project of the University of Massachusetts and the Infrared Processing and Analysis Center/California Institute of Technology, funded by the National Aeronautics and Space Administration and the National Science Foundation.

References

Alonso, A., Arribas, S., & Martinez-Roger, C. 1994, A&AS, 107, 365
Alonso, A., Arribas, S., & Martinez-Roger, C. 1996, A&A, 313, 873
Barklem, P. S., Piskunov, N., & O'Mara, B. J. 2000, A&AS, 142, 467
Bessell, M. S. 1983, PASP, 95, 480
Bessell, M. S. 2000, PASP, 112, 961
Boesgaard, A. M., & Tripicco, M. J. 1986, ApJ, 302, L49
Bragaglia, A., Carretta, E., Gratton, R., et al. 2001, AJ, 121, 327
Bruntt, H., Grundahl, F., Tingley, B., et al. 2003, A&A, 410, 323
Butler, R. P., Marcy, G. W., Fischer, D. A., et al. 2000, in Planetary Systems in the Universe: Observation, Formation and Evolution, ed. A. J. Penny et al., ASP Conf Ser.
Carney, B. W., Latham, D. W., Laird, J. B., & Aguilar, L. A. 1994, AJ, 107, 2240
Castelli, F., Gratton, R. G., & Kurucz, R. L. 1997, A&A, 318, 504
Cutri, R. M., Skrutskie, M. F., Van Dyk, S., et al. 2003, Explanatory Supplement to the 2MASS All Sky Data Release (`www.ipac.caltech.edu/2mass`)
Cuypers, J., & Seggewiss, W. 1999, A&AS, 139, 425
Desidera, S., Gratton, R. G., Endl, M., et al. 2003, A&A, 405, 207
Docobo, J. A., Alvarez, C., Lahulla, J. F., Lancharesi, V., & Aguirre, A. 2000, Astron. Nachr., 321, 53
Do Nascimento, Jr. J. R., Charbonnel, C., Lebre, A., De Laverny, P., & De Medeiros, J. R. 2000, A&A, 357, 931
Dotter, A., & Chaboyer, B. 2003, ApJ, 596, 496
Eggenberger, A., Udry, S., & Mayor, M. 2003, in Scientific Frontiers in Research on Extrasolar Planets, ed. D. Deming, & S. Seager, ASP Conf. Ser., 294, 43
ESA 1997, The Hipparcos and Tycho Catalogues, ESA SP-1200
Fischer, D., Valenti, J., & Marcy, G. W. 2004, in IAU Symp., 219 Stars as Suns: activity, evolution and planets, ed. A. K. Dupree, ASP Conf. Ser., in press
Ford, E. B., Rasio, F. A., & Sills, A. 1999, ApJ, 514, 411
Gilliland, R. L., Brown, T. M., Guhathakurta, P., et al. 2000, ApJ, 545, L47
Girardi, L., Bertelli, G., Bressan, A., et al. 2002, A&A, 391, 195
Gonzalez, G. 1997, MNRAS, 285, 403
Gratton, R. G. 1988, Rome Obs. Preprint, 29
Gratton, R. G., & Sneden, C. 1991, A&A, 241, 501
Gratton, R. G., Bonanno, G., Bruno, P., et al. 2001a, Exp. Astron., 12, 107
Gratton, R. G., Bonanno, G., Claudi, R. U., et al. 2001b, A&A, 377, 123 (Paper I)
Gratton, R. G., Carretta, E., Claudi, R. U., Lucatello, S., & Barbieri, M. 2003, A&A, 404, 187
Gratton, R. G., Carretta, E., Claudi, R. U., et al. 2004, Mem SAIt, 75, 97
Gray, D. F. 1992, The Observation and Analysis of Stellar Photospheres (Cambridge: Cambridge University Press)
Habing, H. J, Dominik, C., Jourdain de Muizon, M., et al. 2001, A&A, 365, 545
Hanson, R. B. 1979, MNRAS, 186, 875
Hauck, B., & Mermilliod, M. 1998, A&AS, 129, 431
Heiter, U., & Luck, R. E. 2003, AJ, 126, 201
King, J. R., Delyannis, C. P., Hiltgen, D. D., et al. 1997, AJ, 113, 1871
Kurucz, R. L. 1995, CD-ROM, 13
Israelian, G., Santos, N. C., Mayor, M., & Rebolo, R. 2003, A&A, 405, 753

Laws, C., & Gonzalez, G. 2001, ApJ, 533, 405
Laws, C., Gonzalez, G., Walker, K. M., et al. 2003, AJ, 125, 2664
Lodders, K. 2003, ApJ, 591, 1220
Magain, P. 1984, A&A, 134, 189
Martin, E. L., Basri, G., Pavlenko, Y., & Lyubchik, Y. 2002, ApJ, 579, 437
Marzari, F., & Weidenschilling, S. J. 2002, Icarus, 156, 570
Murray, N., Chaboyer, B., Arras, P., Hansen, B., & Noyes, R. W. 2001, ApJ, 555, 801
Nakos, T., Sinachopoulous, D., & Van Dessel, E. 1995, A&AS, 112, 453
Pasquini, L., Randich, S., & Pallavicini, R. 1997, A&A, 325, 535
Paulson, D., Sneden, C., & Cochran, W. D. 2003, AJ, 125, 3185
Pilachowski, C. A., Booth, J., & Hobbs, L. M. 1987, PASP, 99, 1288
Pinsonneault, M. H., De Poy, D. L., & Cofee, M. 2001, ApJ, 556, L59
Piotto, G. P., Montalto, M., Desidera, S., et al. 2004, in XIXth IAP Colloq. Extrasolar Planets, Today and Tomorrow ASP Conf. Ser., in press
Reddy, B. E., Lambert, D. L., Laws, C., Gonzalez, G., & Covey, K. 2002, MNRAS, 335, 1005
Sadakane, K., Ohkubo, M., & Honda, S. 2003, PASJ, 55, 1005
Sandquist, E., Taam, R. E., Lin, D. N. C., & Burkert, A. 1998, ApJ, 506, L65
Santos, N. C., Israelian, G., & Mayor, M. 2004, A&A, 415, 1153
Smith, V. V., Cunha, K., & Lazzaro, D. 2001, AJ, 121, 3207
Street, R. A., Horne, K., Lister, T. A., et al. 2003, MNRAS, 340, 1287
Turcotte, S., Richer, J., & Michaud, G. 1998, ApJ, 504, 559
Unsold, A. 1955, Physik der Sternatmospharen
Vauclair, S. 2004, ApJ, in press [arXiv:astro-ph/0309790]
Whaling, W., Hannaford, P., Lowe, R. M., Biemont, E., & Grevesse, N. 1985, A&A, 153, 109
Wilden, B. S., Jones, B. F., Lin, D. N. C., & Soderblom, D. R. 2002, AJ, 124, 2799
Winnick, R. A., Demarque, P., Basu, S., & Guenther, D. B. 2002, ApJ, 576, 1075
Zucker, S., & Mazeh, T. 2002, ApJ, 568, L113